Calculation of bit error rates of optical signal transmission in nano-scale silicon photonic waveguides

Jie You

A dissertation submitted in partial fulfillment

of the requirements for the degree of

Doctor of Philosophy

of

University College London.

Department of Electronic and Electrical Engineering

University College London

July 11, 2017

I, Jie You, confirm that the work presented in this thesis is my own. Where information has been derived from other sources, I confirm that this has been indicated in the work.

Abstract

In this dissertation, a comprehensive and rigorous analysis of BER performance in the single- and multi-channel silicon optical interconnects is presented. The illustrated computational algorithms and new results can furnish one with insight of how to engineer waveguide dimensions, optical nonlinearity and dispersion, in order to facilitate the design and construction of the ultra-fast and low-cost chip-level communications for next-generation high-performance computing systems.

Two types of optical links have been intensively discussed in this dissertation, namely a strip single-mode silicon photonic waveguide and a silicon photonic crystal waveguide. Different types of optical input signals are considered here, including an ON-OFF keying modulated nonreturn-to-zero continuous-wave signal, a phase-shift keying modulated continuous-wave signal, and a Gaussian pulsed signal, all in presence of white noise. The output signal is detected and analyzed using direct-detection optical receivers. To model the signal propagation in the single- and multi-channel silicon photonic waveguides, we employ both rigorous theoretical models that incorporate all relevant linear and nonlinear optical effects and the mutual interaction between the free carriers and the optical field, as well as their linearized version valid in the low-noise power regime. Particularly, the second propagation model is designed only for optical continuous-wave signals. Equally important, the bit error rate (BER) of the transmitted signal is accurately and efficiently calculated by using the Karhunen-Loève series expansion methods, with these approaches performed via the time-domain, frequency-domain, and Fourier-series expansion, separately.

Based on the theoretical models proposed in this work, a system analysis engine has been constructed numerically. This engine can not only analyze the underlying physics of silicon waveguides, but also evaluate the system performance, which is extremely valuable for the configuration and optimization of the optical networks on chip.

Acknowledgements

I would like to express my deep and sincere gratitude to my supervisor Prof. Nicolae C. Panoiu. He gave me the opportunity to work in the field of silicon photonic interconnects and helped me to solve the research obstacles with his scientific insight and diligence. His talents and unrelenting pursuit for quality make himself the best role model of scientific researchers for me. I will always appreciate his guidance and support.

I would like to thank my second supervisor Dr. Philip Watts for constructive advice, useful discussions and instructions, and for providing the encouragement for my PhD research. I would also like to thank Prof. John Mitchell for providing insightful comments during the transfer viva. It is helpful to improve my research in a wide aspect.

I would also like to show my heartfelt gratitude to my colleagues in Prof. Nicolae C. Panoiu's group (Dr. Spyros Lavdas, Dr. Martin Weismann, Dan Timbrell, Dr. Jianwei You, Qun Ren, Dr. Abiola Oladipo, Dr. Ahmed Al-Jarro, Dr. Wei Wu) for their friendship and help during my PhD years. Especially for Dr. Spyros Lavdas and Dr. Jianwei You, who provided me loads of valuable and practical advice when I encountered difficulties in my study, and who were always ready to support me whenever I needed help during my research.

In the end, I want to thank my family for their precious love and unconditional support throughout my whole life.

I really appreciate China Scholarship Council and UCL Dean's Prize Scholarship for providing the financial support for my PhD.

Journal articles related to the PhD Dissertation

1. J. You and N. C. Panoiu, *"BER in Slow-light and Fast-light Regimes of Silicon Photonic Crystal Waveguides: A Comparative Study,"* IEEE Photon. Technol. Lett. **29**, 1093-1096 (2017).

2. J. You and N. C. Panoiu, *"Exploiting Higher-order Phase-shift Keying Modulation and Direct-detection in Silicon Photonic Systems,"* Opt. Express **25**, 8611-8624 (2017).

3. J. You, S. Lavdas, and N. C. Panoiu, *"Comparison of BER in Multi-channel Systems With Stripe and Photonic Crystal Silicon Waveguides,"* IEEE J. Sel. Topics Quantum Electron. **22**, 4400810 (2016).

4. J. You, S. Lavdas, and N. C. Panoiu, *"Calculation of BER in Multi-channel Silicon Optical Interconnects: Comparative Analysis of Strip and Photonic Crystal Waveguides,"* Proc. of SPIE **989116**, Brussels (2016).

5. J. You and N. C. Panoiu, *"Calculation of Bit Error Rates in Optical Systems with Silicon Photonic Wires,"* IEEE J. Quantum Electron. **51**, 8400108 (2015).

6. S. Lavdas, J. You, R. M. Osgood, and N. C. Panoiu, *"Optical pulse engineering and processing using optical nonlinearities of nanostructured waveguides made of silicon,"* Proc. SPIE **9546**, Active Photonic Materials VII, (2015).

7. J. You and N. C. Panoiu, *"An Efficient BER Calculation Approach in Single-channel Silicon Photonic Interconnects Utilizing Arbitrary RZ-pulse Signals,"* J. Lightw. Technol. (submitted).

Journal articles not directly related to the PhD Dissertation

1. J. W. You, J. You, M. Weismann, and N. C. Panoiu, *"Double-Resonant Enhancement of Third-Harmonic Generation in Graphene Nanostructures,"* Phil. Trans. R. Soc. A **375**, 20160313 (2017).

Conference contributions related to the PhD Dissertation

1. J. You and N. C. Panoiu, *"BER Transmission in Silicon Strip and Photonic Crystal Systems Utilizing Advanced Modulation Formats,"* Photon 16, Leeds (2016).

2. J. You and N. C. Panoiu, *"Analysis of BER in Silicon Photonic Systems Utilizing*

Higher-order PSK Modulation Formats," CLEO: Applications and Technology, San Jose (2016).

3. J. You, S. Lavdas, and N. C. Panoiu, *"Calculation of BER in multi-channel silicon optical interconnects: comparative analysis of strip and photonic crystal waveguides,"* SPIE Photonics Europe, Brussels (2016).

4. J. You, S. Lavdas, and N. C. Panoiu, *"BER Calculation in Photonic Systems Containing Strip or Photonic Crystal Silicon Waveguides,"* Asia Communications and Photonic Conference, HongKong (2015).

5. N. C. Panoiu, S. Lavdas, and J. You, *"Optical pulse engineering using nonlinearities of nanostructured silicon photonic wires,"* 24th International Laser Physics Workshop (LPHYS'15), Shanghai (2015). (Invited)

6. N. C. Panoiu, S. Lavdas, J. You, and R. M. Osgood, *"Optical pulse engineering and processing using nonlinearities of tapered and photonic crystal waveguides made of silicon,"* Active Photonic Materials VII, San Diego (2015).

LIST OF NOTATIONS AND ACRONYMS

4PSK	4-ary phase-shift keying
8PSK	8-ary phase-shift keying
ASK-PSK	combination of intensity and phase modulation
α_{in}	intrinsic loss
α_{FC}	free-carrier loss
BER	bit-error rate
β	mode propagation constant
β_2	group velocity dispersion coefficient
CW	continuous-wave
c	speed of light in vacuum $(2.99792458 \times 10^8\ m/s)$
ε_0	electric permittivity of vacuum $(8.854 \times 10^{-12} F/m)$
e	electron charge $(1.6021766208 \times 10^{-19}\ C)$
FC	free-carrier
FCD	free-carrier dispersion
FCA	free-carrier absorption
FEM	finite-element method
FFT	Fast Fourier Transformation
FWM	four-wave mixing
$\mathscr{F}\{\ \}$	Fourier transform
GV	group velocity
GVD	group-velocity dispersion
HPC	high-performance computing
$\hbar$	reduced Planck constant $(1.05457162853 \times 10^{-34}\ kg/s)$
KLSE	Karhunen-Loève Series Expansion
κ	overlap integral between the waveguide core and optical mode
MZI	Mach-Zehnder interferometer
MGF	moment-generating function
NLSE	nonlinear Schrödinger equation
NoC	networks-on-chip

LIST OF NOTATIONS AND ACRONYMS

NRZ	nonreturen-to-zero
n	refractive index
δn_{FC}	free-carrier induced refractive index charge
OOK	On-Off keying
ODE	ordinary differential equation
PSK	phase-shift keying
PhC	photonic crystal
γ	waveguide nonlinear coefficient
Γ	effective nonlinear susceptibility
Si	silicon
SOI	silicon-on-insulator
Si-PhW	silicon photonic waveguide
Si-PhCW	silicon photonic crystal waveguide
SSFM	Split-step Fourier Method
SL	slow-light
SPM	self phase modulation
TOD	third-order dispersion
TPA	two-photon absorption
VCSEL	vertical-cavity surface-emitting lasers
WDM	wavelength-division multiplexing
XPM	cross-phase modulation
$\chi^{(3)}$	third-order optical susceptibility
ZGVD	zero group velocity dispersion

Contents

List of Figures

List of Tables

Chapter 1

Introduction

Photonics can be viewed as a field that involves light-related technologies and applications, which smoothly blends the subjects of physics and engineering. During the last few decades, photonics has spread into almost all areas of modern life and cutting-edge technologies, including telecommunications, computing, medicine and robotics. Concurrently, with the development of photonics in our knowledge-based society, rapidly increasing growth of data traffic in networks driven by bandwidth-intensive applications, such as the widespread use of social networking, video streaming in mobile applications, and cloud services, is creating increasingly stringent demand for bandwidth, which can be effectively addressed by deploying broadband optical communications solutions [1]. Internet data centers and high-performance computing (HPC) systems are just two examples of markets where photonic technologies can play a major role.

Optical interconnects are viewed as a promising alternative to the commonly used copper wires [2], due to their unique features of high capacity, large transparency window, and fundamentally low energy consumption. Furthermore, the optical communications have already been deployed in the metro and long haul networks during the last two decades [3], and will penetrate into the development of next-generation information networks [4]. In fact, rack-to-rack ($1\,\mathrm{m} \sim 100\,\mathrm{m}$) [5] and board-to-board ($10\,\mathrm{cm} \sim 1\,\mathrm{m}$) [6] communications already contain optical networks in some fastest HPC systems. It is envisioned that this trend of using optical communications at an ever-smaller scale will continue to grow, so that in future HPC platforms will play the main role in node-to-node and even intra-node communications [7, 8].

Then silicon-on-insulator (SOI) material platform is regarded as one of the most appealing approaches to integrate photonics into chip-level networks, due to its unique

characteristics listed below:

1. High index contrast. The relatively large refractive index difference between silicon (Si) ($n_{Si} \sim 3.46$) and cladding, which can be either buried-oxide substrate ($n_{Si0_2} \sim 1.45$) or air ($n_{air} = 1$), makes possible to tightly confine and guide light in optical waveguides with deep-subwavelength transverse dimensions [9–11].

2. Broad-band transparency window. Silicon is transparent beyond 1.2 μm up to the mid-Infrared region, which allows for ultrahigh bandwidth data communications [12].

3. Dispersion and nonlinearity engineering. The strong light confinement enables to greatly engineer the dispersion of Si waveguides, either by changing the transverse size of the waveguides or by nano-patterning them. In addition, Si possesses very large third-order nonlinearities in a broad spectral range, which means that key active optical functionalities, such as Raman amplification, self-phase modulation (SPM), cross-phase modulation (XPM), four-wave mixing (FWM), and pulse self-steepening can be easily implemented by using this optical material [11, 13].

4. Good compatibility with the CMOS electric circuitries [14–16]. All basic components of the desired photonic networks have already been implemented in the SOI platforms, including optical amplifiers [17, 18], modulators [19–21], switches [22–24], receivers [25, 26], and frequency converters [27, 28].

5. High thermal conductivity and high optical damage threshold [29]. Silicon encompasses optical damage threshold of $1-4\,\mathrm{GW\,cm^{-2}}$ and thermal conductivity of 148 $\mathrm{W\,m^{-1}\,K^{-1}}$, facilitating excellent mid-Infrared Raman lasers and amplifiers [30].

Importantly, the recent breakthroughs in the photonic device integration [31, 32] make Si photonics more pervasive for the chip-level information networks.

In addition to the constant drive towards downscaling the size of optical interconnects, an equally daunting challenge pertaining to exascale computing systems is to decrease the per-bit power consumption to levels that allow cost-effective operation.

Photonic structures provide a versatile solution that addresses both these issues, as they allow one to engineer both the linear and nonlinear properties of the optical interconnects. To be more specific, by nano-patterning Si photonic strip waveguides (Si-PhWs) and photonic crystal (PhC) waveguides (Si-PhCWs), optical properties of these structures can be tuned. A salient example of such structure are Si-PhCWs [33, 34], which are commonly implemented by introducing a line defect in a periodic dielectric matrix. In particular, the group-velocity (GV), v_g, of optical signals propagating in PhC waveguides can be reduced by orders of magnitude, which leads to a dramatic change of the linear and nonlinear optical properties of photonic devices [35–37]. One key consequence of this so-called slow-light (SL) effect is that the characteristic dispersion and nonlinear lengths, and implicitly the device footprint, could decrease significantly. On the other hand, optical losses and nonlinear effects, such as SPM, XPM and two-photon absorption (TPA), which impair the quality of transmitted optical signals, are enhanced in the SL regime, too. Moreover, if Si waveguides are employed in wavelength-division-multiplexing (WDM) enabled applications, photogenerated free-carriers (FCs) provide an additional mechanism for inter-channel cross-talk, which is an example of a detrimental effect that is enhanced in the SL regime. The advantages provided by the SL operation of photonic devices are therefore not *a priori* transparent, especially if multi-channel operation is considered, and consequently an in-depth analysis of these ideas is needed.

Furthermore, intensive investigation of main optical phenomena in Si photonic waveguides have been carried out experimentally and theoretically in recent years. Raman scattering in the Si waveguides was firstly observed in 2002 [38], followed by the exploration of anti-Stokes Raman scattering (CARS) in 2003 [39]. Simultaneously, several other important nonlinear phenomena were discovered, i.e., SPM [40], TPA [41], XPM [42], FWM [43], supercontinuum generation [44], and soliton generation [45]. In addition, research efforts have also been devoted to linear effects like optical loss [46], GV dispersion (GVD) [47], and third-order dispersion (TOD) [48].

Up to now, even though almost all components of Si photonics ecosystem exist, including the fundamental study (e.g., UCSB), design (e.g., Photon Design), foundries (e.g., ST), devices (e.g., LIGHTWIRE), systems (e.g, IBM, CISCO, HUAWEI), and end-customers (e.g., Facebook), the large scale manufacturing of Si photonic waveg-

uides for the optical chips is still in its infancy [49]. It will be of critical importance to have a set of tools suitable for estimating the bit error rate (BER) of optical data streams transmitted among different nodes of the nextworks-on-chip (NoC). In particular, a reliable characterization of the performance photonic NoC can be achieved via a bottom-up approach, in which one first determines at the physical layer the optical signal impairments introduced by each of the components of the NoC, are firstly determined at the physical layer, this information being then used to evaluate at the system level the overall performance of the photonic network. Therefore, the aim of this dissertation is to propose a rigorous theoretical and computational software platform, which can not only facilitate the physics of Si photonic waveguides, but also evaluate the BER performance of photonic systems under different circumstance. In the next section, the main objectives of this dissertation will be explained.

1.1 Main Objectives of the Work

The two main objectives of this dissertation will be discussed in this section. Aiming at developing a set of theoretical models and computational tools for the analysis of optical signal transmission in silicon photonic systems, both cases of continuous-wave (CW) and pulsed optical signals will be extensively investigated. Achieving each of the objectives amounts to employing different mathematical algorithms and numerical implementations, which will be explained in details below.

To start with, I will use a rigorous theoretical model to describe the propagation of optical signals in a single-mode silicon-on-insulator strip waveguide. In particular, a superposition of a nonreturn-to-zero (NRZ) ON-OFF keying (OOK) modulated optical signal and an additive white Gaussian noise is selected as the optical input, which can also be analyzed by utilizing a linearized propagation model. These models fully incorporate all essential linear and nonlinear optical effects. The BER of the output signal will be measured via the time-domain Karhunen-Loève series expansion (KLSE) method after direct-detection. For a better understanding of how waveguide dispersion and nonlinearity determine the signal quality, I will present a comparative study of the influence of the normal and anomalous dispersion regimes in Si-PhWs on the system BER.

Subsequently, I will present an in-depth investigation of the NRZ CW optical sig-

nal transmission in the optical system containing PhC Si waveguides operating in the slow- and fast-light regimes. Particularly, SL spectral regions can be accessed by significantly reduced GV, v_g. This results in increased waveguide dispersion and effective waveguide nonlinearity, as these physical quantities scale with v_g as v_g^{-1} and v_g^{-2}, respectively. Correpsondingly, the influence of SL effects on the optical field and carrier dynamics will be also thoroughly explored.

In addition, I will also theoretically and numerically evaluate the BER in Si photonic systems employing high-order phase-shift keying (PSK) modulation formats. Particularly, both Si-PhWs and Si-PhCWs are included in the investigated systems, as well as direct-detection receivers suitable to detect PSK and amplitude-shaped PSK signals. Notably, the system BER will be calculated by applying a frequency-domain approach based on the KLSE. The emphasis of this comprehensive analysis will be on how the optical power, types of PSK modulation, and group-velocity characterize the transmission BER, as well as the relation between the influence of these factors on BER and system nonlinearity.

Furthermore, I will illustrate a multi-wavelength optical signal propagating either in a Si-PhW or in a Si-PhCW, with each channel consisting of a CW NRZ OOK modulated signal. As an extension of the single-wavelength signal transmission case, $\tilde{M}$ sets of coupled linearized equations will be utilized to describe $\tilde{M}$-wavelength signals co-propagation. Both time- and frequency-domain KLSE methods will be employed to calculate the BER of the transmitted signal. The numerical simulations will highlight the importance of carefully selecting the waveguide types and dimensions, number of channels, and optical input power, when taking the system performance into consideration.

The second objective of this dissertation is to extensively study the performance of Si photonic systems operating in the pulsed regimes. To fulfill this goal, I will employ the full theoretical model to characterize the single-wavelength optical pulse propagation in a Si-PhW or a Si-PhCW, and a Fourier-series KLSE method to estimate the system BER. Then, I will demonstrate the impact of signal parameters (pulsewidth, data rate, wavelength, power) and waveguide parameters (dispersion regions, SL regimes) on the quality of transmitted signal. One remarkable feature of the rigorous models mentioned above is that they can account for all types of optical signals and be easily

extended to the multi-channel system evaluation cases.

A related point to consider is that the performance analysis engine, which will be described in this dissertation, is of the capability to characterize more complicated photonic systems. To be more specific, this engine can be easily extended to other types of optical waveguides, waveguide-based devices and chip-scale optical networks of practical interest. Moreover, the formalism of signal propagation theory can be modified to incorporate additional nonlinear effects such as FWM and stimulated Raman scattering, which could become important optical effects in nanoscale waveguides. A brief summary of the whole dissertation will be given in the next section.

1.2 Outline

Chapter 2 presents the literature review of Si photonics, optical characterization of Si waveguides, and the configuration of the photonic systems investigated in this work. Further to that, rigorous theoretical models for the single- and multi-wavelength signal propagation will be presented, aiming at incorporating all relevant linear and nonlinear optical effects and the mutual interaction between FCs and the optical field. Additionally, the linearized version of the full propagation model mentioned above is presented for the case of CW signals, which is validated in the low-noise power regime. Thereafter, the numerical routines regarding the full and linearized propagation models will be described. Specifically, the former models employ the Split-step Fourier Method (SSFM) plus a fifth-order Runge-Kutta method, whereas a Matlab built-in function is used to solve ordinary differential equations (ODEs) in the latter models. This chapter provides the physical background and signal propagation routines for the remaining chapters in this dissertation.

Chapter 3 describes the computational methods for the BER calculation in Si photonic systems. Firstly, a concise literature review of the BER evaluation methods will be introduced. Next, three types of KLSE approaches (the time-domain, frequency-domain and Fourier-series) which are adopted in this dissertation, will be described in details. I will then present a numerical technique called saddle-point approximation, which is applied to derive the system BERs based on the moment-generating function (MGF) calculated with these KLSE methods. This chapter can be viewed as containing all the essential implementation related to the system evaluation models.

Chapter 4 describes the numerical implementation of the system evaluation models, including the signal propagation theory in Chapter 2 and BER calculation methods in Chapter 3. This numerical and computational tool is capable of accounting for different types of Si waveguides, various formats of signal modulation , and varied numbers of transmission channels. The program flow of this system evaluation engine will be illustrated in this chapter, followed by the specification of the key parameters and the characterization of the numerical algorithms utilized in the computer program.

In Chapter 5 and Chapter 6, I discuss the transmission of an OOK modulated optical CW signal in the single-channel optical systems containing a Si-PhW and a Si-PhCW, respectively, in presence of an additive white Gaussian noise. In these two chapters, both full and linearized theoretical single-channel CW models are adopted to describe the propagation of the optical signal in Si waveguides, whereas the time-domain KLSE method is used to evaluate the BER. Importantly, in Chapter 5, I comprehensively investigate the influence of parameters characterizing the Si-PhWs on the transmission BER, while I present and discuss the dependence of BER on the key system parameters in Chapter 6, including group-velocity, input power, and signal-to-noise ratio.

In Chapter 7, I focus on the evaluation of a higher-order PSK modulated optical CW signal transmitted in the single-channel strip and photonic crystal Si systems. The modified nonlinear Schrödinger equation (NLSE) that governs the propagation of the noisy PSK signals in Si waveguides is employed, as well as the frequency-domain KLSE method for BER calculation. Moreover, the description of the advanced modulation formats and the details of direct-detection are also presented in this chapter. The system performance corresponding to several PSK formats is rigorously analyzed, considering varied key system parameters.

For completeness, in Chapter 8, I present a comparative analysis of the performance of the multi-channel photonic systems containing a Si-PhW or a Si-PhCW, with each channel propagating the OOK modulated CW signals. The optical properties of the investigated Si waveguides are described in this chapter. Furthermore, the system of $\tilde{M}$ coupled NLSE equations is applied to measure the propagation of a $\tilde{M}$-wavelength noisy signal in these two Si waveguides, taking into account the nonlinear phenomena like XPM and the overall FCs accumulated from these signals, whereas the time- and

frequency-domain formulation of the KLSE method are used to compute system BER. The impact of white Gaussian noise on BER is thoroughly studied, in presence of Kerr nonlinearity, frequency dispersion, and FCs.

What follows next is the investigation of the single-channel Si photonic interconnects exploiting optical pulsed signals, as discussed in Chapter 9. Firstly, the full single-channel pulse propagation model is utilized to describe the evolution of a single-channel pseudorandom binary sequence (PRBS) noisy Gaussian signal. The details of the investigated Si Photonic waveguides are also exhibited in Chapter 8, considering frequencies (1550 nm, 1300 nm), dispersion regions (normal, anomalous), and GV (SL, FL). Then, the Fourier-series KLSE method is employed to evaluate the system performance. Several simulation results regarding the pulse properties and waveguide parameters are displayed in this chapter as well, in order to provide a reference for the photonic systems operating in the pulsed regime.

In Chapter 10, I summarize the main conclusions of this dissertation, and stresses the main contributions of this dissertation to the field of Si optical interconnects. Future perspectives of this work are also included in this chapter.

Bibliography

[1] Y. A. Vlasov, "Silicon CMOS-Integrated Nano-Photonics for Computer and Data Communications Beyond 100G," Commun. Mag.**50**, S67-S72 (2012).

[2] A. Benner, D. M. Kuchta, P. K. Pepeljugoski, R. A. Budd, G. Hougham, B. V. Fasano, K. Marston, H. Bagheri, E. J. Seminaro, H. Xu, D. Meadowcroft, M. H. Fields, L. McColloch,M. Robinson, F.W. Miller, R. Kaneshiro, R. Granger, D. Childers, and E. Childers, "Optics for High-Performance Servers and Supercomputers," *Optical Fiber Communication Conf. and Expo. (OFC)*, **OTuH1**, 1-3 (2010).

[3] B. Ciftcioglu, "Intra-Chip Free-Space Optical Interconnect: System, Device, Integration and Prototyping," Ph. D. Thesis (University of Rochester, 2012).

[4] R. Ho, K. W. Mai, and M. A. Horowitz, "The future of wires," Proc. IEEE **89**, 490-504 (2001).

[5] J. W. Parker, P. J. Ayliffe, T. V. Clapp, M. C. Geear, P. M. Harrison, and R. G. Peall, "Multifibre Bus for rack-to-rack intreconnects based on opto-hybrid trnamitter/receiver array pair," Electron. Lett. **28**, 801-803 (1992).

[6] D. V. Plant, M. B. Venditti, E. Laprise, J. Faucher, K. Razavi, M. Chteauneuf, A. G. Kirk, and J. S. Aheran, "256-Channel Bidirectional Optical Interconnect Using VCSELs and Photodiodes on CMOS," IEEE J. Lightwave Technol. **19**, 1093-1103 (2002).

[7] W. Green, S. Assefa, A. Rylyakov, C. Schow, F. Horst, and Y. Vlasov, "CMOS integrated silicon nanophotonics: Enabling technology for exascale computation," *Semicon, Tokyo (2010).* Available at www.research.ibm.com/photonics.

[8] J. A. Kash, A. F. Benner, F. E. Doany, D. M. Kuchta, B. G. Lee, P. K. Pepeljugoski, L. Schares, C. L. Schow, and M. Taubenblatt, "Optical Interconnects in Exascale Supercomputers," *23rd Annual Meeting of the IEEE Photonics Society*, 483-484 (2010).

[9] K. K. Lee, D. R. Lim, H. C. Luan, A. Agarwal, J. Foresi, and L. C. Kimerling, "Effect of size and roughness on light transmission in a Si/SiO_2 waveguide: Experiments and model," Appl. Phys. Lett. **77**, 1617-1619 (2000).

[10] R. U. Ahmad, F. Pizuto, G. S. Gamarda, R. L. Espinola, H. Rao, and R. M. Osgood, "Ultracompact cornermirrors and T-branches in silicon-on-insulator," IEEE Photon. Technol. Lett. **14**, 65-67 (2002).

[11] R. M. Osgood, N. C. Panoiu, J. I. Dadap, X. Liu, X. Chen, I-W Hsieh, E. Dulkeit, W. M. J. Green, and Y. A. Vlassov, "Engineering nonlinearities in nanoscale optical systems: physics and applications in dispersion engineered silicon nanophotonics wires," Adv. Opt. Photon. **1**, 162-235 (2009).

[12] B. G. Lee, X. Chen, A. Biberman, X. Liu, I-W. Hsieh, C. Chou, J. I. Dadap, F. Xia, W. M. J. Green, L. Sekaric, Y. A. Vlasov, R. M. Osgood, and K. Bergman, "Ultrahigh-Bandwidth Silicon Photonic Nanowire Waveguides for On-Chip Networks," IEEE Photon. Technol. Lett. **20**, 398-400 (2008).

[13] Q. Lin, Oskar J. Painter, and G. P. Agrawal, "Nonlinear optical phenomena in silicon waveguides: modeling and applications," Opt. Express **15**, 16604-16644 (2007).

[14] T. Barwicz, H. Byun, and F. Gan, C. W. Holzwarth, M. A. Popovic, P. T. Rakich, M. R. Watts, E. P. Ippen, F. X. Kartner, H. I. Smith, J. S. Orcutt, R. J. Ram, V. Stojanovic, O. O. Olubuyide, J. L. Hoyt, S. Spector, M. Geis, M. Grein, T. Lyszczarz, and J. U. Yoon, "Silicon photonics for compact, energy-efficient interconnects," J. Opt. Commun. Netw. **6**, 63-73 (2007).

[15] J. S. Orcutt, A. Khilo, C. W. Holzwarth, M. A. Popovic, H. Li, J Sun, T. Bonifield, R. Hollingsworth, F. X. Kärtner, H. I. Smith, V. Stojanović, R. J. Ram, "Nanophotonic integration in state-of-the-art CMOS foundries," Opt. Express **19**, 2335-2346 (2011).

[16] A. V. Krishnamoorthy, X. Zheng, G. Li, J. Yao, T. Pinguet, A. Mekis, H. Thacker, I. Shubin, Y. Luo, K. Raj, and J. E. Cunningham, "Exploiting CMOS Manufactur-

ing to Reduce Tuning Requirements for Resonant Optical Devices," IEEE Photon. J. **3**, 567–579 (2011).

[17] R. Claps, D. Dimitropoulos, V. Raghunathan, Y. Han, and B. Jalali, "Observation of stimulated Raman amplification in silicon waveguides," Opt. Express **11**, 1731-1739 (2003).

[18] R. Espinola, J. I. Dadap, R. M. Osgood, S. J. McNab, and Y. A. Vlasov, "Raman amplification in ultrasmall silicon-on-insulator wire waveguides," Opt. Express **12**, 3713-3718 (2004).

[19] G. Cocorullo, M. Iodice, I. Rendina, and P. M. Sarro, "Silicon Thermooptic Micromodulator with 700-kHz –3-dB Bandwidth," IEEE Photon. Technol. Lett. **7**, 363-365 (1995).

[20] A. Liu, R. Jones, L. Liao, D. Samara-Rubio, D. Rubin, O. Cohen, R. Nicolaescu, and M. Paniccia, "A high-speed silicon optical modulator based on a metal-oxide-semiconductor capacitor," Nature **427**, 615-618 (2004).

[21] Q. Xu, B. Shmidt, S. Pradhan, and M. Lipson, "Micrometre-scale silicon electro-optic modulator," Nature **435**, 325-327 (2005).

[22] R. L. Espinola, M.-C. Tsai, J. T. Yardley, and R. M. Osgood Jr., "Fast and low-power thermooptic switch on thin silicon-on-insulator," IEEE Photon. Technol. Lett. **15**, 1366-1368 (2005).

[23] O. Boyraz, P. Koonath, V. Raghunathan, and B. Jalali, "All optical switching and continuum generation in silicon waveguides," Opt. Express **12**, 4094-4102 (2004).

[24] B. G. Lee, A. Biberman, P. Dong, M. Lipson, and K. Bergman, "All-optical comb switch for multiwavelength message routing in silicon photonic networks," IEEE Photon. Technol. Lett. **20**, 767-769 (2008).

[25] P. C. P. Chen, A. M. Pappu, and A. B. Apsel, "Monolithic integrated SiGe optical receiver and detector," *Proc. Conf. Lasers and Electro-Optics, Tech. Dig. (CD) (Optical Society of America)* **CTuZ4**, 1-2 (2007).

[26] S. Assefa, F. Xia, W. M. J. Green, C. L. Schow, A. V. Rylyakov, and Y. A. Vlasov, "CMOS-Integrated Optical Receivers for On-Chip Interconnects," IEEE J. Sel. Top. Quantum Electron. **16**, 1376-1385 (2010).

[27] H. Fukuda, K. Yamada, T. Shoji, M. Takahashi, t. Tsuchizawa, T. Watanabe, J. Takahashi, and S. Itabashi, "Four-wave mixing in silicon wire waveguides," Opt. Express **13**, 4629-4637 (2005).

[28] S. Zlatanovic, J. S. Park, S. Moro, J. M. C. Boggio, I. B. Divliansky, N. Alic, S. Mookherjea, and S. Radic, "Mid-infrared wavelength conversion in silicon waveguides using ultracompact telecom-band-derived pump source," Nat. Phot. **4**, 561-564 (2010).

[29] B. Jalali, and S. Fathpour, "Silicon photonics," IEEE J. Lightwave Technol. **24**, 4600-4615 (2006).

[30] G. T. Reed, *Silicon Photonics: The State of the Art* (John Wiley & Sons Ltd, 2008).

[31] C. Gunn, "CMOS Photonics for High-Speed Interconnects," IEEE Micro **26**, 58-66 (2006).

[32] Y. A. Vlasov, "Si CMOS-Integrated Nano-Photonics for Computer and Data Communications Beyond 100G," IEEE. Commun. Mag. **50**, S67-S72 (2012).

[33] A. Mekis, J. C. Chen, I. Kurland, S. Fan, P. R. Villeneuve, and J. D. Joannopoulos, "High Transmission through Sharp Bends in Photonic Crystal Waveguides," Phys. Rev. Lett. **77**, 3787-3790 (1996).

[34] S. Y. Lin, E. Chow, V. Hietala, P. R. Villeneuve, and J. D. Joannopoulos, "Experimental Demonstration of Guiding and Bending of Electromagnetic Waves in a Photonic Crystal," Science **282**, 274-276 (1998).

[35] Marin Soljačić, S. G. Johnson, S. Fan, M. Ibanescu, E. Ippen, and J. D. Joannopoulos, "Photonic-crystal slow-ligh enhancement of nonlinear phase sensitivity," J. Opt. Soc. Am. B. **19**, 2052-2059 (2002).

[36] T F. Krauss, "Why do we need slow light," Nat. Phot. **2**, 448-450 (2008).

[37] T. Baba, "Slow light in photonic crystals," Nat. Phot. **2**, 465-473 (2008).

[38] R. Claps, D. Dimitropoulos, Y. Han, and B. Jalali, "Observation of Raman emission in silicon waveguides at 1.54 μm," Opt. Express **10**, 1305-1313 (2002).

[39] R. Claps, V. Raghunathan, D. Dimitropoulos, and B. Jalali, "Anti-Stokes Raman conversion in silicon waveguides," Opt. Express **11**, 2862-2872 (2003).

[40] H. K. Tsang, C. S. Wong, T. K. Lang, I. E. Day, S. W. Roberts, A. Harpin, J. Drake, and M. Asghari, "Optical dispersion, two-photon absorption and self-phase modulation in silicon waveguides at 1.5 μm wavelength," Appl. Phys. Lett. **80**, 416-418 (2002).

[41] C. Manolatou, and M. Lipson, "All-optical silicon modulators based on carrier injection by two-photon absorption," IEEE J. Lightwave Technol. **24**, 1433-1436 (2006).

[42] T. Liang, L. Nunes, T. Sakamoto, K. Sasagawa, T. Kawanishi, M. Tsuchiya, G. Priem, D. Van Thourhout, P. Dumon, R. Baets, and H. Tsang, "Ultrafast all-optical switching by cross-absorption modulation in silicon wire waveguides," Opt. Express **13**, 7298-7303 (2005).

[43] R. L. Espinola, J. I. Dadap, R. M. Osgood, S. J. McNab, and Y. A. Vlasov, "C-band wavelength conversion in silicon photonic wire waveguides," Opt. Express **13**, 4341-4349 (2005).

[44] I.-W. Hsieh, X. Chen, X. Liu, J. I. Dadap, N. C. Panoiu, C.-Y. Chou, F. Xia, W. M. Creen, Y. A. Vlasov, and R. M. Osgood, "Supercontinuum generation in silicon photonic wires," Opt. Express **15**, 15242-15249 (2007).

[45] J. Zhang, Q. Lin, G. Piredda, R. W. Boyd, G. P. Agrawal, and P. M. Fauchet, "Optical solitons in a silicon waveguides," Opt. Express **15**, 7682-7688 (2007).

[46] Y. Vlasov, and S. McNab, "Losses in single-mode silicon-on-insulator strip waveguides and bends," Opt. Express **12**, 1622-1633 (2004).

[47] E. Dulkeith, F. Xia, L. Schares, W. M. J. Green, and Y. A. Vlasov, "Group index and group velocity dispersion in silicon-on-insulator photonic wires," Opt. Express **14**, 3853-3863 (2006).

[48] X. Chen, N. C. Panoiu, I. Hsieh, J. I. Dadap, and R. M. Osgood, "Third-Order Dispersion and Ultrafast-Pulse Propagation in Silicon Wire Waveguides," IEEE Photon. Technol. Lett. **18**, 2617-2619 (2006).

[49] Jean Louis Malinge, "A view on the Silicon Photonics trends and Market propsective," *2nd Summer School on INtelligent signal processing for FrontlEr Research and Industry*, 2014.

Chapter 2

Background

2.1 Introduction

Silicon photonics denotes as the widespread investigation and utilization of Si medium based photonic systems. To date, various studies of Si devices have been carried out, aiming at constructing telecommunication systems at subwavelength scale. After the Si waveguides were first introduced by Soref in 1985 [1], rapid progress has been made on the Si optical modulators [2], waveguides [3], polarizers [4], interferometers [5], filters [6] and switches [7] in the 1990s. However, it was not until the beginning of 2000s that big breakthroughs were achieved in the Si mode converters [8], receivers [9], couplers [10], splitters [11], amplifiers [12] and photonic integrated circuits [13]. Recent improvements have been made on the Si lasers (i.e., Si Raman lasers), giving rise to the extremely compact Si chips and efficient on-chip amplification. In parallel to that, Si photonics has also been utilized to optical sensing, nonlinear optics engineering and mid-Infrared applications, such as airport security systems, environment monitoring and personalized health care.

Silicon waveguides play a crucial role in the field of Si photonics. With regard to the structure, Si waveguides can generally be divided into four types [14]: (1) Strip waveguides. This type of waveguides is basically a strip core medium surrounded by the cladding materials (see Fig. 2.1(a)), and has wide applications in the Mach-Zehnder interferometers (MZIs), lasers and integrated optical circuits; (2) Rib waveguides. The guiding layers of these waveguides consist of the slabs and with the strip media on top, as shown in Fig. 2.1(b). They are commonly used for light confinement; (3) Slot waveguides. Their main structure comprises two ridges of the core materials, where a

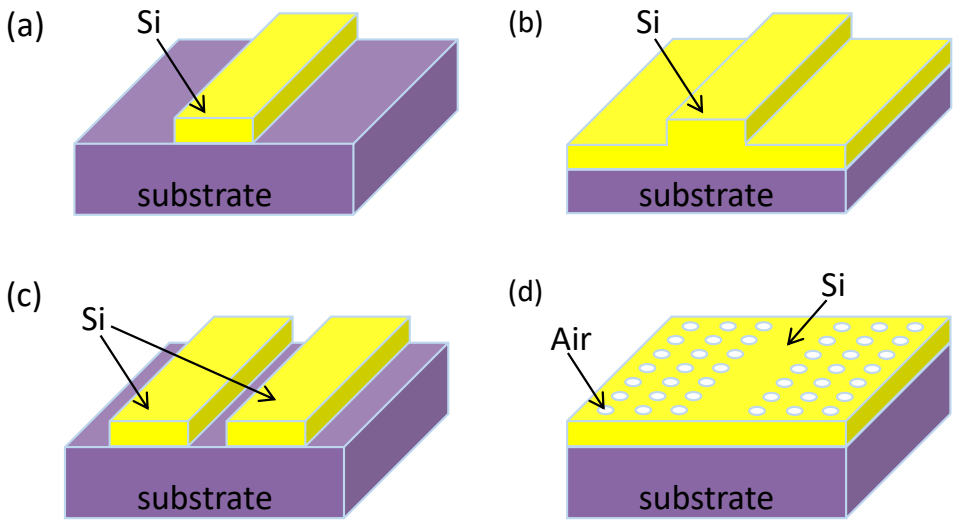

Figure 2.1: Structure of four types of Si waveguides, including (a) a strip waveguide, (b) a rib waveguide, (c) a slot waveguide and (d) a photonic crystal waveguide.

narrow gap exists in between, as illustrated in Fig. 2.1(c). Typically, these waveguides are suitable for the mode field manipulation and optical sensing; (4) Photonic crystal waveguides. They are usually photonic crystal structures containing a constant cross-section region (shown in Fig. 2.1(d)), which allows the light propagation in specific direction. One remarkable feature of this type of waveguides is the SL regimes, where the device size and footprint can be easily downscaled. In this work, our main research interest is in the strip and photonic crystal waveguides.

This chapter describes the background of this dissertation, which provides essential theoretical knowledge for the following chapters. Specifically, Sec. 2.2 introduces the optical phenomena for the Si nanowire waveguides. Sec. 2.3 discusses important linear and nonlinear optical parameters of strip and photonic crystal Si waveguides, which occupies a fundamental part of this dissertation. Moreover, the schematics of the investigated single- and multi-channel Si photonic systems are illustrated in Sec. 2.4. Sec. 2.5 describes the basic types of optical signals used in this work. Next, the signal propagation theory will be presented, which is one of the key aspects in the system evaluation models. In particular, the full propagation theory that incorporates all the essential optical effects in Si waveguides is presented in Sec. 2.6, whereas their linearized version is outlined in Sec. 2.7. In the end, the computational algorithms of both signal propagation models are discussed in Sec. 2.8.

2.2 Optical Properties of Silicon Nanowire Waveguide

Silicon waveguides are generally light guiding devices which are placed on top of the SOI and a oxide layer. A simple example of such waveguide is illustrated in Fig. 2.2. In the last two decades, Si waveguides have become an increasingly important area in the ultra-dense photonic integration [15]. This popularity originates from the fabrication of low loss Si waveguides, in which the waveguide loss can be reduced to $0.026\,\mathrm{dB\,cm^{-1}}$ or even lower [16, 17]. Moreover, Si waveguides exhibit unique optical nonlinearity: (1) their second-order nonlinear optical susceptibility is zero, due to the symmetry property of crystalline Si. (2) the third-order optical susceptibility turns out to be particularly large [18], which allows for the control of the optical nonlinearity within the Si waveguides in order to furnish various functionalities. In this section, we will mainly present the optical characterization of the general Si nanowire, and explain the underlying physics with explicit mathematical formula.

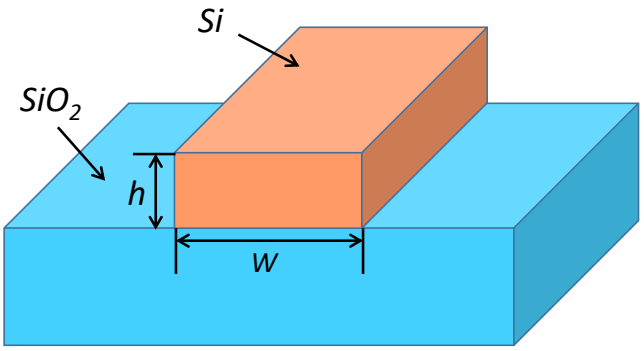

Figure 2.2: The generic structure of strip Si photonic waveguides.

2.2.1 Frequency Dispersion of Silicon Nanowire Waveguide

Optical dispersion, a vital part of linear optical effects, represents the dependence of phase velocity of an electromagnetic wave on the frequency when propagating in an optical waveguide. In this section, a brief introduction regarding the optical dispersion of Si nanowires will be presented. The calculation of optical dispersion in the Si nanowire waveguides was first reported by Chen et al [19]. The successive experimental measurements were carried out on the GVD and TOD effects in the same year [20, 21]. These studies suggest that the waveguide geometry determines the optical dispersion in the Si nanowires, due to the subwavelength cross section and high index

contrast. An analytic expression is used to describe the waveguide dispersion, by expanding the mode propagation constant $\beta(\omega)$ in a Taylor series at the carrier frequency ω_0 [22, 23]:

$$\begin{aligned}\beta(\omega) &= n(\omega)\frac{\omega}{c} \\ &= \beta_0 + (\omega-\omega_0)\beta_1 + \frac{1}{2!}(\omega-\omega_0)^2\beta_2 + \frac{1}{3!}(\omega-\omega_0)^3\beta_3 + + \frac{1}{4!}(\omega-\omega_0)^4\beta_4 ...\end{aligned} \tag{2.1}$$

where $n(\omega)$ is the refractive index, c is the speed of light, $\beta_0 \equiv \beta(\omega_0)$ is the propagation constant at ω_0, and $\beta_m = \left(\frac{d^m\beta}{d\omega^m}\right)_{\omega=\omega_0}$ represents the mth order dispersion coefficient. β_1 is the inverse of the group velocity ($v_g = 1/\beta_1$), which is an important parameter in the multi-wavelength signal co-propagation and several nonlinear phenomena like FWM. β_2 represents the GVD coefficient and determines the degree of pulse broadening. Additionally, the GVD parameter D, with the mathematical definition of $D = \frac{d\beta_1}{d\lambda} = -\frac{2\pi c}{\lambda^2}\beta_2$, is also widely used in the optical communications. β_3 and β_4 are useful parameters for optical pulses with femtosecond pulsewidth or even smaller. To be more specific, the TOD effect would lead to the spectral asymmetry, whereas the fourth dispersion effect has a significant contribution to the nonlinear frequency mixing.

Dispersion engineering offers an effective approach to achieve the integration of ultra-small optical devices on Si chips. Therefore, accurate theoretical description of the dominant dispersive opticals effects (i.e., GVD and TOD) within Si nanowires is indeed necessary to fulfill the goal mentioned above.

Group velocity dispersion means that each frequency component of optical signal propagates at different speed, thus resulting in the optical pulse broadening. In particular, a zero-dispersion (ZGVD) wavelength λ_D usually exists in a Si nanowire [19], which indicates a fact that no GVD effect occurs at $\lambda = \lambda_D$. The wavelength λ_D is often used to separate the normal dispersion ($\beta_2 > 0$) and anomalous dispersion ($\beta_2 < 0$) regimes. Furthermore, the sign of β_2 also influences the nonlinear optical effects in the Si nanowires. A prominent example is the optical soliton, which is only generated in anomalous dispersion regions. Additionally, the characteristic length of GVD is denoted as $L_D = \frac{\tau^2}{|\beta_2|}$ (τ is the pulsewidth, unless otherwise is specified), which is used

to measure the minimum length where the GVD effect begins to strongly influence the pulse evolution. Specifically, when the transmission distance is much larger than L_D ($L \gg L_D$), the GVD effect must be included in the theoretical description of pulse dynamics.

Third-order dispersion effect can be easily observed when the optical pulse possesses the wavelength of λ_D, where no GVD occurs. As mentioned earlier, TOD can also be important for optical signals with femtosecond pulsewidth or smaller. The TOD effect is responsible for the pulse reshaping and distortion. Precisely, the positive (negative) value of β_3 indicates that the oscillatory structure appears at the trailing (leading) edge of the pulse. Similar to GVD, the characteristic length of TOD is denoted as $L_D^{'} = \frac{\tau^3}{|\beta_3|}$, indicating that the TOD affects the pulse propagation when $L_D^{'} \leq L_D$.

With respect to the calculation of these dispersion coefficients, the finite element method (FEM) is applied on Eq. (2.1) in conjunction with the Sellmeier relation, which for Si is written as [24]:

$$n(\lambda) = \varepsilon + \frac{A}{\lambda^2} + \frac{B\lambda_1^2}{\lambda^2 - \lambda_1^2}, \tag{2.2}$$

where $\lambda_1 = 1.1071\,\mu\text{m}$, $\varepsilon = 11.6858$, $A = 0.939816\,\mu\text{m}^2$, $B = 8.10461 \times 10^{-3}$.

2.2.2 Nonlinear Optical Properties of Silicon Nanowire Waveguide

Nonlinear optics represents a significant branch of the light-matter interactions, where the waveguide response to the optical field behaves in a nonlinear manner. Various optical effects are included in this field, namely the frequency-mixing process (e.g., second-harmonic generation, third-harmonic generation, and optical parametric generation), the optical Kerr effect (e.g., SPM and optical solitons), XPM, FWM, and the Raman amplification [18]. In particular, the Si nanowires discussed in this dissertation exhibit a strong anisotropic Kerr effect [25, 26], which is quantified by the third-order susceptibility tensor $\chi^{(3)}$ of Si. Due to the symmetry property of Si crystalline structure, two independent components, $\chi^{(3)}_{1111}$ and $\chi^{(3)}_{1122}$, are selected to represent the 21 nonzero elements of $\chi^{(3)}$. Moreover, $\chi^{(3)}$ can be further simplified to one-component independent variable, according to such relation, $\chi^{(3)}_{1111}/\chi^{(3)}_{1122} = 2.36$ [23, 25]. From physical point of view, both the Kerr effect and TPA govern the third-order susceptibility in Si nanowires.

The nonlinear coefficient γ , a $\chi^{(3)}$ related parameter, is introduced to determine

the waveguide nonlinearity:

$$\gamma = \frac{3\omega\Gamma}{4\varepsilon_0 A_{nl} v_g^2}, \tag{2.3}$$

where Γ measures the effective nonlinear susceptibility, ω is the carrier frequency, A_{nl} is the cross sectional area of the Si waveguides, ε_0 is the permittivity of free space, and v_g represents the GV [27]. Equation (2.3) shows that γ has strong dependence on the operational frequency and the waveguide geometry. Different from silica fibers, the nonlinear coefficient γ in Si nanowires is a complex number, which consists of the real (γ') and imaginary (γ'') part. To be more specific, γ' corresponds to the SPM effects [28] – the nonlinear response of the optical phase shift caused by the Kerr effect, leading to optical spectral broadening. The corresponding nonlinear length is given by $L_{NL} = 1/(\gamma' P)$, where P is the power. γ'' quantifies the TPA effects [29], an optical process describing the absorption of two photons in order to excite a molecule to a higher energy state. Note also that TPA is a strong power-dependent phenomenon. Further to that, possessing the SL spectral regions of the dispersive photonic-guiding structures can increase the effective waveguide nonlinearity [30], since the nonlinearity scales with v_g as v_g^{-2}.

With regard to the multi-wavelength signal co-propagation in the same waveguide, new nonlinear optical processes have to be taken into consideration, such as XPM [31], multi-mode mixing, FWM and stimulated Raman scattering [23]. Among these effects, only the XPM effect is added in the coupled-mode theory utilized in this dissertation. XPM describes an optical process where the refractive index change is induced by one pulse but probed by a second co-propagating pulse [32]. Therefore, two sets of standard nonlinear coefficients γ_i and γ_{ik} are defined, in order to characterize the nonlinear interaction between the co-propagating optical pulses [23]:

$$\gamma_i = \frac{3\omega_i\Gamma_i}{4\varepsilon_0 A_{nl} v_{g,i}^2}, \tag{2.4a}$$

$$\gamma_{ik} = \frac{3\omega_i\Gamma_{ki}}{4\varepsilon_0 A_{nl} v_{g,i} v_{g,k}}, \tag{2.4b}$$

γ_i and γ_{ik} describe SPM and XPM interactions, respectively, with i or k the ith or kth pulse during transmission channel. Γ_i is the effective nonlinear susceptibility for ω_i, while Γ_{ki} measures the nonlinear susceptibility interaction between ω_k and ω_i. The

other relevant coefficients have been defined earlier in this section. More specific cases regarding the nonlinear coefficients are discussed in Sec. 2.6.1 and Sec. 2.6.2.

2.2.3 Free Carrier Dynamics in Silicon Nanowire Waveguide

The carrier mechanism describes the interaction between FCs and the optical field in Si nanowires, by means of including additional linear absorption and changing the refractive index [33]. Apart from SPM, FCs make another contribution to the change of refractive index. In general, the carrier density is a function of the time and distance. The carrier relaxation time t_c is a key parameter in the carrier dynamics, since FCs can significantly influence signal reshaping when the signal pulsewith is larger than t_c. Thus, two relevant nonlinear effects are specified here, namely the FC absorption (FCA) and FC-induced dispersion (FCD), with their mathematical formulas given by [34]:

$$\alpha_{FC} = \frac{e^3 N}{\varepsilon_0 c n \omega^2} \left(\frac{1}{\mu_e m_{ce}^{*2}} + \frac{1}{\mu_h m_{ch}^{*2}} \right), \tag{2.5a}$$

$$\delta n_{FC} = -\frac{e^2}{2\varepsilon_0 n \omega^2} \left(\frac{N}{m_{ce}^{*}} + \frac{N^{0.8}}{m_{ch}^{*}} \right), \tag{2.5b}$$

where δn_{FC} characterizes the refractive index change induced by FCD, α_{FC} stands for the FCA coefficient, N is the FCs density, e is the electric charge of the electron, $m_{ce}^{*} = 0.26\, m_0$ and $m_{ch}^{*} = 0.39\, m_0$ are the effective masses of the electron and the hole, m_0 is the mass of the electron, and $\mu_e(\mu_h)$ is the electron (hole) mobility. Regarding Eq. (2.5b), it is important to mention that this equation is only validated when N is in unit of cm^{-3} [34]. Generally, the FCs relaxation time t_c of Si nanowires is set to be 0.5 *ns* [35]. Additional explanation for the evolution of FCs will be introduced in Sec. 2.6.1 and Sec. 2.6.2.

2.3 Types of Silicon Photonic Waveguides

In this section, we present two specific types of Si waveguides utilized throughout this dissertation: The first waveguide is a single-mode Si photonic waveguide (Si-PhW) with uniform cross-section, and buried in SiO_2 cladding, as shown in Fig. 2.3(a). It has a fixed height, $h = 250\,\text{nm}$, but tunable width, w, which offers the possibilities to engineer the optical properties. From theoretical point of view, any dimensions of the

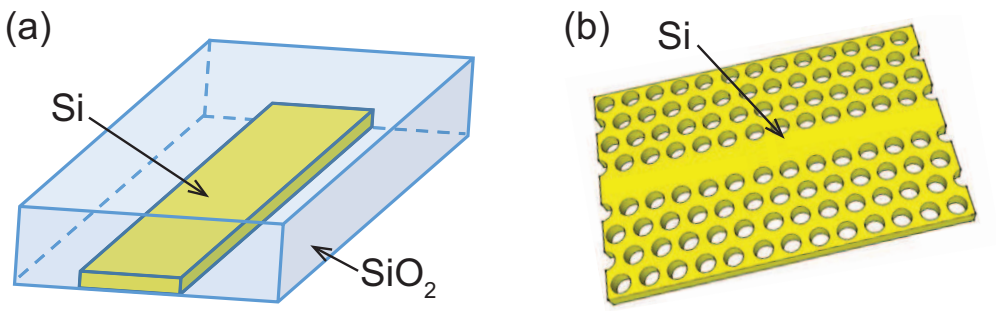

Figure 2.3: (a) A strip Si photonic waveguide with uniform cross section; (b) A Si photonic crystal waveguide.

waveguide cross-section can be simulated. However, our collaborators from Columbia University can validate our simulation results of dispersion coefficients experimentally when the height is 250 nm (a typical height used in the fabrication of Si waveguides). This explains why we choose a fixed height (250 nm) for Si-PhWs. The second waveguide is a Si photonic crystal waveguide (Si-PhCW), which consists of a line defect along the ΓK direction of a PhC slab with hexagonal air hole lattice, as illustrated in Fig. 2.3(b). Its lattice constant, hole radius and slab thickness are a, $r = 0.22a$ and $h = 0.6a$, respectively. In the following sections, both linear and nonlinear optical properties of Si-PhWs and Si-PhCWs will be illustrated.

2.3.1 Strip Silicon Photonic Waveguides

Si-PhWs are classified as one simple case of Si photonic waveguides, whose guiding waveguides are rectangular and the cladding material is SiO_2. In this section, the fundamental optical properties of Si-PhWs, as well as their correlation with the waveguide cross-section and carrier frequencies, will be presented.

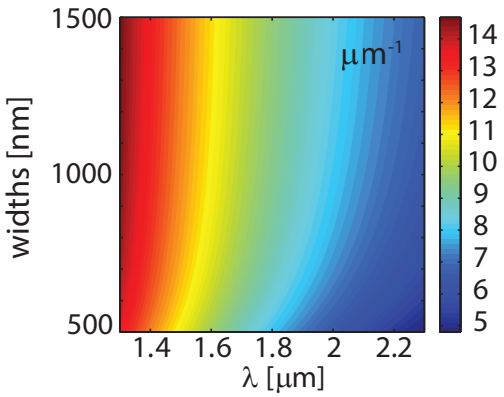

Figure 2.4: Dispersion maps of propagation constant β for certain widths of Si-PhWs with fixed hight of $h = 250$ nm.

The waveguide mode and mode propagation constant are the physical parameters to be studied first. The mode propagation constant β, with the definition of optical signal's phase variation per length during transmission, is often used to measure the evolution of the signal amplitude and phase. Figure. 2.4 shows the modal dispersion of the optical guiding modes within Si-PhWs, accounting for the dependence on waveguide width w and carrier wavelength λ. Specifically, we use a finite-element mode solver (Femsim by Rsoft [36]) to determine β and the fundamental TE-like mode for different wavelength ($1.3\,\mu\text{m} \leq \lambda \leq 2.3\,\mu\text{m}$) and waveguide width ($500\,\text{nm} \leq w \leq 1500\,\text{nm}$). One can easily observe that the propagation constant β changes nonlinearly with the waveguide width w at a fixed carrier wavelength. In addition, this nonlinear dependence becomes stronger when the carrier wavelength turns larger. To conclude, the propagation constant β is determined by the geometry of Si-PhWs at certain frequency.

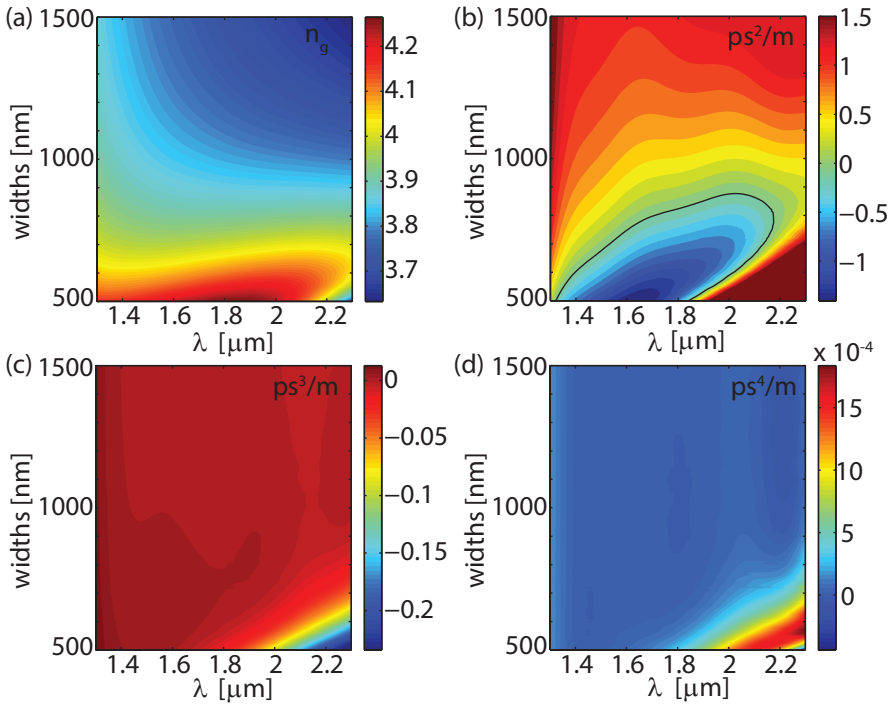

Figure 2.5: Dispersion maps of (a) group index $n_g = c/v_g$; (b) GVD coefficient β_2; (c) TOD coefficient β_3; (d) fourth-order coefficient β_4; for certain widths of Si-PhWs with constant height $h = 250\,\text{nm}$.

Furthermore, the frequency dependence of several other dispersive coefficients on the waveguide geometry is also discussed in this section. To illustrate this, the group index, the GVD coefficient, the TOD coefficient, and the fourth-order dispersion coefficient are displayed in Fig. 2.5. Notably, these high-order dispersion coefficients

are calculated by fitting $\beta(\lambda)$ with a twelfth-order polynomial and then finding the derivatives with respective to λ. One useful finding is that the strong correlation exists between the optical parameters mentioned above and the operational wavelength λ and the waveguide width w. Figure 2.5(b) shows that by tuning λ or w width one can easily switch the nature of pulse propagation from the normal dispersion regime ($\beta_2 > 0$) to anomalous dispersion ($\beta_2 < 0$). For small width, $w \leq 887\,\text{nm}$, and wavelengths, $\lambda \leq 2.187\,\mu\text{m}$, the GVD coefficient β_2 can have large (in absolute value) negative values. The normal and anomalous dispersion regimes are separated by a zero-dispersion curve ($\beta_2 = 0$), depicted in Fig. 2.5(b) by a black line. Note that close to the ZGVD curve, where the effect of GVD is very weak, the third- and fourth-order coefficients, that is, β_3 and β_4 shown in Fig. 2.5(c) and Fig. 2.5(d), respectively, play the dominant role in the dispersion induced pulse reshaping. In addition, the values of β_2, β_3 and β_4 in the Si-PhWs are more than one order of magnitude larger than that of silica fibers, thus resulting in relatively smaller dispersion lengths. This property allows for the dispersion manipulation in the chip-level Si devices.

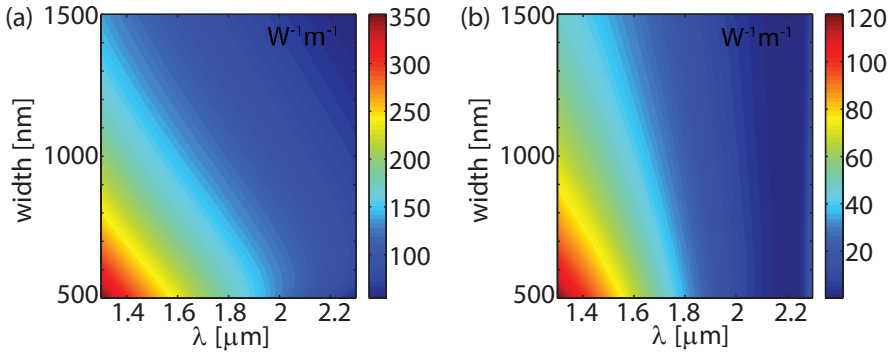

Figure 2.6: Real (a) and imaginary (b) part of nonlinear coefficients for Si-PhW waveguides with several widths and a specific hight of $h = 250\,\text{nm}$.

Similar to the dispersive phenomena, the nonlinear optics in the Si-PhWs is also determined by the waveguide geometry. Figure 2.6 shows the dispersive maps of the real (γ') and imaginary (γ'') part of the nonlinear coefficients in Si-PhWs. It can be easily seen that both values of γ' and γ'' can increase under conditions of either smaller waveguide width or shorter carrier wavelength. More precisely, the magnitude of γ' is at least 3 $\times$ larger than γ'' in the Si-PhWs, with both values much larger than silica fibers. The nonlinearity within Si-PhWs can further reduce the footprint of Si devices.

2.3.2 Silicon Photonic Crystal Waveguides

Photonic crystals, denoted as one-, two- and three- dimensional periodic photonic structures with high refractive index contrast, have become an attractive area for the light manipulations today. A photonic bandgap (PBG) usually exists in such a PhC, which represents a frequency range where the light transmission is prevented in all directions. Thus, the PhCs containing PBGs can be widely employed for light guiding [37]. In particular, by inserting one-dimensional (1D) waveguide into the two-dimensional (2D) photonic crystal structure made of Si, an optical waveguide with new functionality is achieved.

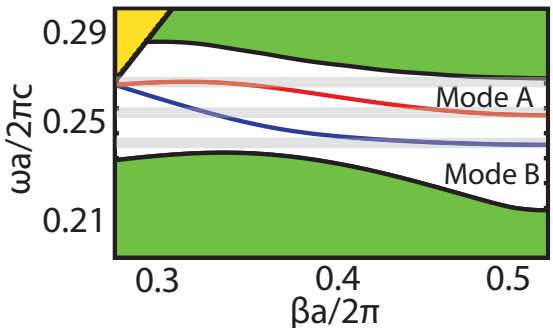

Figure 2.7: Projected band structure. Dark yellow and green ares correspond to slab leaky and guiding modes, respectively. The red and blue curves represent the y-even and y-odd guiding mode of the 1D waveguides. Light grey shaded regions correspond to SL regime, $n_g > 20$.

The Si-PhCWs studied in this dissertation is an hexagonal lattice of air holes within a Si slab, with one row of holes filled by Si in the transmission direction, as illustrated in Fig. 2.3(b). Similarly, the optical properties of Si-PhCWs are also governed by the waveguide geometry, hence the lattice constant a should be carefully designed. This can be illustrated by exploring the projected band structure of Si-PhCWs. In Fig. 2.7, $\beta a/2\pi$ and $\omega a/2\pi c$ stand for the dimensionless wavevector and frequency, respectively. There are two fundamental TE-like guiding modes in the bandgap: Mode A (*y-even*) possesses two flat-curve areas, which represent the SL regimes according to such expression of $v_g = 1/\beta_1 = (d\omega/dk)$; Mode B (*y-odd*) consists of only one SL region. In order to access the switch between the FL and SL regimes with larger flexibility, we select Mode A as the investigated guiding mode for all Si-PhCWs simulations in this dissertation.

Slow-light is an interesting phenomenon that has attracted intensive research ef-

forts in the last decade, where both dispersion and nonlinearity are found to be enhanced. This effect is often applied in the field of pulse reshaping, all-optical memories storage and optical buffers [38]. Particularly, the utilization of SL in nanoscale Si devices can help reduce the power consumption and the resulted operation cost [39]. However, the optical properties of Si waveguides within the SL regimes have to be carefully designed, in order to avoid the dramatically increased waveguide dispersion and nonlinearity. Based on the above circumstances, it is of great importance to extensively investigate the SL spectral domains within Si-PhCWs.

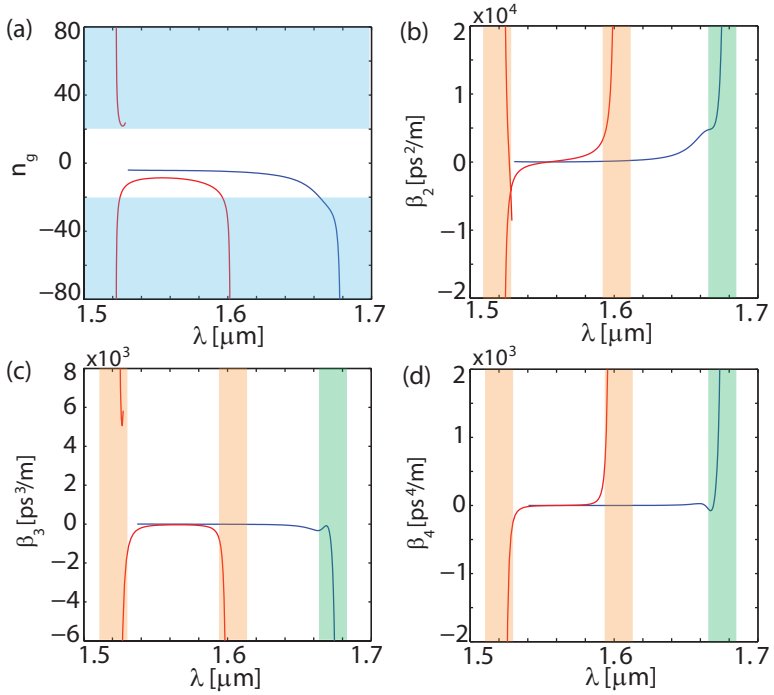

Figure 2.8: (a), (b), (c), and (d) Frequency dependence of waveguide dispersion coefficients $n_g = c/v_g$, β_2, β_3 and β_4, respectively, determined for the Mode A (red) and Mode B (blue). Light green, blue, and brown shaded regions correspond to SL regime, $n_g > 20$.

What follows is the description for the frequency dependence of the first four dispersion coefficients (β_1, β_2, β_3 and β_4) in the Si-PhCWs, considering both Mode A and Mode B. In Fig. 2.8, the shaded areas indicate the spectral SL regions, with the corresponding threshold $n_g > 20$ to reach that region. One major observation is that the two SL regimes of Mode A are located at the band-edge ($\lambda \approx 1.6\ \mu m$) and the area with center wavelength of $\lambda \approx 1.52\ \mu m$. Unlike Mode A, just one SL spectral domain exists in the band-edge of Mode B ($\lambda \approx 1.67 \mu m$). Furthermore, the Mode A can access both positive and negative GVD regions, with the ZGVD placing at $\lambda =$

1.56μm, whereas in Mode B only the normal GVD ($\beta_2 > 0$) is available throughout the whole spectrum. Last but not least, the value of β_2, β_3 and β_4 of Si-PhCWs are several orders of magnitude larger than that of Si-PhWs and silica fibers.

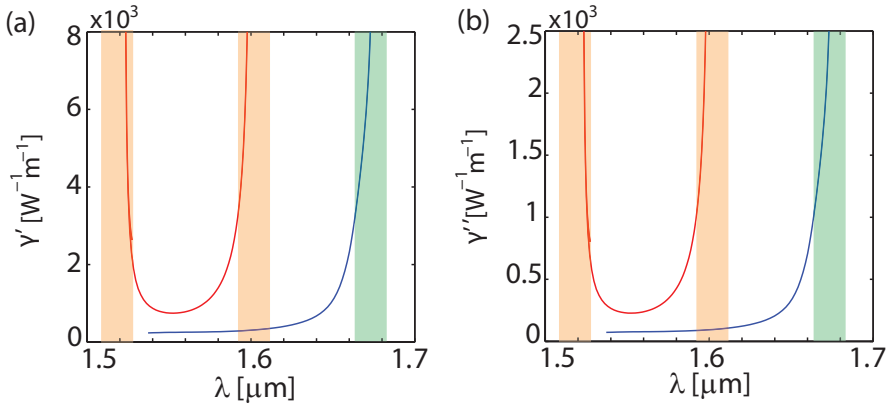

Figure 2.9: Real (a) and imaginary (b) parts of nonlinear coefficients for Si-PhCW waveguides versus wavelength, in cases of Mode A (red) and Mode B (blue). Light green, blue, and brown shaded regions correspond to SL regime, $n_g > 20$.

In terms of optical nonlinearity within Si-PhCWs, we also specify the difference between SL and FL spectral regimes. Several important findings can be derived from Fig. 2.9: firstly, both real and imaginary parts of nonlinear coefficients are much larger in the SL regimes than in the FL regimes; secondly, much stronger nonlinear processes can be observed in Si-PhCWs when compared with Si-PhWs. For instance, in this dissertation, the SL effect only exists in the Si-PhCW instead of the Si-PhW, with the nonlinearity in the SL regimes of the first waveguide two orders of magnitude larger than the latter waveguide; finally, the real value of the nonlinear coefficient (γ') is more than 3 times larger than the imaginary part (γ''). Importantly, the strong nonlinearity of Si-PhCWs can further reduce optical characteristic lengths, and thus providing the functionality of highly-compact on-chip photonic integration.

In conclusion, although both the Si-PhWs and Si-PhCWs are dispersive with carrier frequencies, the essential optical properties of the Si-PhWs are governed by the waveguide cross-section, while the periodicity determines the optical processes within the Si-PhCWs.

2.4 Silicon Photonic System Models

Generally, Si photonic systems consist of similar optical devices as the modern optical fiber transmission systems [40], but with devices made of Si and scaled to subwave-

length size [41, 42]. In fact, all the basic components of photonic NoC have already implemented in the SOI platform, including the optical lasers [43], optical amplifiers [44, 45], modulators [46, 47], multiplexers and demultiplexers [48], optical switches [49–51], receivers [53, 54] and frequency converters [55, 56]. Taking device functionalities and practical requirements into account, modeling of photonic systems must be carefully designed. For instance, the photodiodes are usually modeled to obey the square-law rule. However, the cases like the gain profile and amplified spontaneous emission (ASE) noise [57] require more realistic theoretical analysis. Therefore, the configuration of the investigated photonic systems is presented in this section, acting as the prerequisites of the rigorous theoretical models in this dissertation.

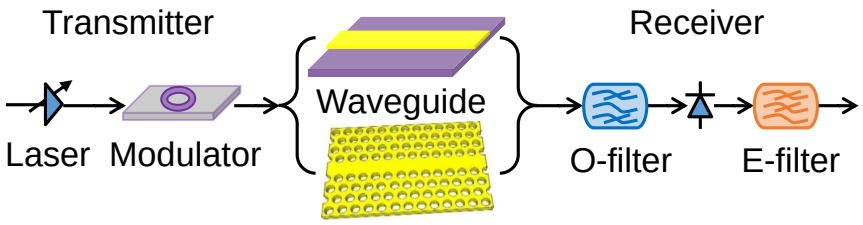

Figure 2.10: (a) Schematic of the single-channel photonic system, containing two types of waveguides: a uniform single-mode Si photonic wire and a Si photonic crystal slab waveguide. The receiver contains an optical filter, an ideal square-law photodetector and an electrical filter.

To start with, a single-channel Si photonic system is investigated in this dissertation, with its schematic shown in Fig. 2.10. This system is composed of a transmitter, a Si waveguide and a direct-detection receiver. Specifically, the receiver is usually composed of an optical filter, an ideal square-law photodetector and an electrical filter. With regard to the transmitter, it is simplified by using several types of optical signals: (1) an OOK modulated NRZ optical CW signal; (2) a PSK modulated optical CW signal; (3) an OOK modulated optical pulsed signal. Even though other formats of signal modulation like frequency-shift keying (FSK) and polarization-shift keying (POLSK) are not studied in this dissertation, they can be easily included by modifying the relevant receiver model. Moreover, we assume that a complex additive white Gaussian noise is placed at the front-end of the waveguide, together with the optical signals mentioned above. The configuration of the input signals enables the observation of the nonlinear interaction between the pure optical signal and noise in the Si waveguides. For simplicity, the inphase and quadrature noise components are assumed to be uncorrelated at the

beginning, a constraint that can be easily relaxed if needed. Further to that, the optical waveguide in the single-channel system is either a Si-PhWs or a Si-PhCW, the optical properties of have already been discussed in Sec. 2.3.

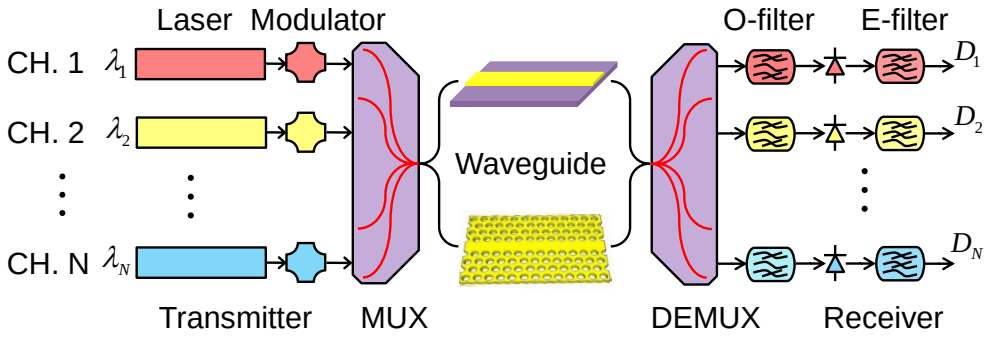

Figure 2.11: Schematic of the multi-channel photonic system, consisting of an array of lasers, a MUX, a Si waveguide, a DEMUX and direct-detection receivers containing an optical band-pass filter, photodetector, and an electrical low-pass filter. Two types of waveguides are investigated: a strip waveguide with uniform cross-section and a specially designed PhC waveguide.

Moreover, the schematic of a multi-channel Si photonic system is shown in Fig. 2.11. This multi-channel system is composed of three blocks–a transmitter (lasers, modulators, a MUX), a Si waveguide and a set of direct-detection receivers (a DEMUX, optical filters, photodiodes and electrical filters). Apart from a MUX and a DEMUX, more than one set of laser source and receiver are needed in the multi-channel system, which corresponds to the number of signal wavelengths. Both Si-PhWs and Si-PhCWs can support multi-wavelength signal transmission, making themselves very attractive to the on-chip interconnects, due to the large capacity and broad bandwidth provided by the WDM techniques.

As mentioned earlier, the theoretical evaluation models for the Si photonic systems should comprise two main aspects, namely, the signal propagation theory and the signal detection theory. Before proceeding to the mathematical details of these theoretical models, the definition of the optical signals will be given in Sec. 2.5, which represents an ideal case that the optical transmitter can generate the desired optical signals. Afterwards, the main signal propagation models will introduced in Sec. 2.6 and Sec. 2.7. And the mathematical models that used in the signal detection will be exhibited in Chapter 3.

2.5 Optical Signal Modulation Formats

The demand to construct the broadband and high-capacity information networks is ever-increasing each year. Some technologies are hopeful to satisfy and maintain such great demand, such as the WDM technology. Apart from the improvement on the device layer, the utilization of advanced optical processing techniques is also viewed as a efficient solution [58]. In particular, advanced optical modulation formats have been intensively investigated over the recent years [59], as they can potentially become viable alternatives to more commonly used OOK modulation. In the context of optical fiber communications it has become clear that, among the advanced modulation formats of optical signals, PSK modulation provides unique advantages, including increased spectral efficiency, superior tolerance to chromatic dispersion and polarization-mode dispersion, and less stringent bandwidth requirements [60, 61]. Moreover, higher spectral efficiency can be achieved by employing PSK modulation schemes with increased complexity, such as quadrature PSK (4PSK) and 8-ary PSK (8PSK) modulation formats, or by combining amplitude-shift keying (ASK) and PSK formats, which we call here ASK-PSK modulation schemes. Importantly, whereas high-order modulation formats have been studied extensively in the context of optical fiber and other communication systems [59, 62, 63], currently a similar theoretical analysis addressing the performance of such modulation schemes when used in photonics systems containing silicon based optical communication links is not available.

Several types of optical signals are introduced in this section, including the OOK modulated CW signals (u_{OOK}), the PSK modulated CW signals (u_{PSK}) and the OOK modulated Gaussian pulsed signals (u_G), in presence of the complex white gaussian noise. Therefore, their explicit expressions for a given bit are illustrated below:

$$u_{OOK}(z,t) = [\sqrt{P(z)} + a(z,t)]e^{-j\Phi(z)}, \tag{2.6a}$$

$$u_{PSK}(z,t) = [\sqrt{P(z)}e^{j\Phi_0} + a(z,t)]e^{-j\Phi(z)}, \tag{2.6b}$$

$$u_G(z,t) = [\sqrt{P(z)}e^{-t^2/2T_0^2} + a(z,t)]e^{-j\Phi(z)}, \tag{2.6c}$$

Here, P represents the peak power of input signal, a is the complex white noise, $\Phi(z)$ stands for the general phase, T_0 is the pulsewidth, and Φ_0 is defined by the PSK signal modulation formats. In particular, $\Phi(z)$ is set to 0 (in unit of rad) when at $z = 0$. It

is important to stress that in our model the pure signal and white noise have different phase. This is so because the noise function, $a(z,t)$, is complex-valued and therefore an additional phase is introduced. As for the ASK-PSK modulation, there would be at least two different power levels involved. More details about the PSK modulation formats will be discussed in Sec. 7.3.

2.6 Theory of Optical Signal Propagation in Silicon Waveguides

Instrumental insights into the optical properties of both Si-PhWs and Si-PhCWs can be obtained by analyzing the evolution of the optical field and FCs in the Si waveguides. Thus, the theory of signal propagation will be presented in this section. Different from the pulse propagation model for silica fibers, the nonlinear optical susceptibilities of Si-PhWs and Si-PhCWs are mathematically described as tensors instead of scalars. Moreover, the FCs dynamcis is included in the case of Si waveguides, but not silica fibers. Generally, this signal propagation model designed for Si waveguides is based on a NLSE describing the optical pulse propagation and a rate equation for FCs [64, 66]. Moreover, the SSFM and a fifth-order Runge-Kutta method are applied in order to derive semi-analytical solutions with regard to the coupled equations mentioned above, with their numerical implementation described in Sec. 2.8.1. Both single- and multi-wavelength pulse propagation will be considered in this dissertation, with the corresponding mathematical models described in Sec. 2.6.1 and Sec. 2.6.2, respectively.

2.6.1 Theory of Single-wavelength Optical Signal Propagation

The strategy for simplifying the evolution of the optical field in Si waveguides, is to divide the waveguide into an unperturbed part and a perturbed part. In particular, the nonlinear effects (SPM, TPA) and the change of the dielectric constant act as the influence sources for the electromagnetic field propagation in the perturbed waveguides [23]. Therefore, we start the mathematical description with the Lorentz reciprocity theorem [67]:

$$\frac{\partial}{\partial z}\int_{A_\infty} \underline{F}\cdot\underline{e_z}dA = \int_{A_\infty} \nabla\cdot\underline{F}dA, \tag{2.7}$$

where the vector field $\underline{F}$ is defined blow:

$$\underline{F} = \underline{E_L}^* \times \underline{H_{NL}} + \underline{E_{NL}} \times \underline{H_L}^*, \tag{2.8}$$

Here, two sets of variables are defined as follows: $(\underline{E_L}, \underline{H_L}) = (\underline{E_0}, \underline{H_0})$ is the guiding mode in the unperturbed waveguides, whereas $(\underline{E_{NL}}, \underline{H_{NL}}) = (\underline{E}, \underline{H})$ represents the mode for the perturbed waveguide. By combining with the source-free Maxwell equations, Eq. (2.7) can cast in the following:

$$\frac{\partial}{\partial z}\int_{A_\infty} \left(\underline{E_L}^* \times \underline{H_{NL}} + \underline{E_{NL}} \times \underline{H_L}^*\right) \cdot \underline{e_z} dA = i\omega \int_{A_\infty} \underline{\delta P} \cdot \underline{E_L} dA \tag{2.9}$$

where $\underline{\delta P}$ is the total mode polarization, which contains a linear and a nonlinear element, namely $\underline{\delta P} = \delta\varepsilon\underline{E} = \underline{\delta P_L} + \underline{\delta P_{NL}}$. To be more specific, $\underline{\delta P_L}$ stands for the change of dielectric constant, according to $\underline{\delta P_L} = \delta\varepsilon_L \underline{E}$. Here, the parameter $\delta\varepsilon_L$ is defined below:

$$\delta\varepsilon_L(\omega) = \frac{i\varepsilon_0 cn\alpha_{in}}{\omega} + 2\varepsilon_0 n\delta n_{FC} + \frac{i\varepsilon_0 cn\alpha_{FC}}{\omega}, \tag{2.10}$$

where ε_0 is the vacuum permittivity and α_{in} is the intrinsic loss coefficient. δn_{FC} and α_{FC} represent the FC-induced change in refractive index and FCA coefficient, respectively, with their mathematical definition given by Eq. (2.5b) and Eq. (2.5a). Furthermore, the nonlinear polarization $\underline{\delta P_{NL}}$ is described by the formula below:

$$\underline{\delta P_{NL}}(\omega) = \frac{3}{4}\varepsilon_0 \underline{\chi}^3(\omega;\omega,-\omega,\omega) \vdots \underline{E}(\omega)\underline{E}^*(\omega)\underline{E}(\omega), \tag{2.11}$$

where $\underline{\chi}^3(\omega;\omega,-\omega,\omega)$ is the third-order susceptibility coefficient. The second step is to extract the explicit expression for the perturbed electromagnetic fields. The unperturbed fields $(\underline{E_0}, \underline{H_0})$ are defined below, with the total power P_0:

$$\underline{E_0} = \frac{1}{2}\sqrt{\frac{Z_0 P_0}{A_0}}\underline{e}(\underline{r_t}, \omega_0)e^{i(\beta_0 z - \omega_0 t)}, \tag{2.12a}$$

$$\underline{H_0} = \frac{1}{2}\sqrt{\frac{P_0}{Z_0 A_0}}\underline{h}(\underline{r_t}, \omega_0)e^{i(\beta_0 z - \omega_0 t)}, \tag{2.12b}$$

where $Z_0 = \sqrt{\mu_0/\varepsilon_0}$, $\underline{e}(\underline{r_t})$ and $\underline{h}(\underline{r_t})$ are the electromagnetic fields in the xy plane. Normalization is then performed on $\underline{e}$ and $\underline{h}$ in our mathematical analysis,

$$\frac{1}{4A_0}\int_{\infty}(\underline{e}\times\underline{h}^{*}+\underline{e}^{*}\times\underline{h})\cdot\underline{e_z}dA = 1. \tag{2.13}$$

For convenience, a slowly varying normalized complex envelope $u(z,\omega)$ is defined, whose input peak amplitude equals to 1 in the time domain. Therefore, in the perturbed part, the electromagnetic field $(\underline{E},\underline{H})$ with total power of $P_0|u(z,\omega)|^2$ are obtained:

$$\underline{E} = \frac{1}{2}\sqrt{\frac{Z_0P_0}{A_0}}u(z,\omega)\underline{e}(\underline{r_t},\omega)e^{i(\beta z-\omega t)}, \tag{2.14a}$$

$$\underline{H} = \frac{1}{2}\sqrt{\frac{P_0}{Z_0A_0}}u(z,\omega)\underline{h}(\underline{r_t},\omega)e^{i(\beta z-\omega t)}, \tag{2.14b}$$

Finally, we can derive the perturbed NLSE for normalized amplitude $u(z,t)$ by combining Eqs. (2.9), (2.10), (2.12), (2.13), (2.14)and performing the Fourier Transform on the resulting equation from the frequency domain to the time-domain:

$$j\left(\frac{\partial u}{\partial z}+\frac{1}{v_g}\frac{\partial u}{\partial t}\right)-\frac{\beta_2}{2}\frac{\partial^2 u}{\partial t^2}-\frac{j\beta_3}{6}\frac{\partial^3 u}{\partial t^3} = -\frac{jc\kappa}{2nv_g}(\alpha_{in}+\alpha_{FC})u-\frac{\omega_0\kappa}{nv_g}\delta n_{FC}u-\gamma|u|^2u, \tag{2.15}$$

The terms in Eq. (2.15) describe well known linear and nonlinear optical effects. Specifically, the second and third terms on the left-side describe the GVD and TOD, respectively. Notably, the dispersion coefficients, $\beta_1 = 1/v_g$, β_2 and β_3 are derived from Eq. (2.1) at the carrier frequency of ω_0. Moreover, from the right-side of Eq. (2.15), the first term corresponds to the intrinsic waveguide loss and FCA, the second term describes the FCD, whereas the last term represents nonlinear effects, namely the SPM and TPA. In terms of the nonlinear parameters, the structures of the Si waveguides need to be taken into account. Particularly, the nonlinearity in the Si-PhWs is determined by their cross-section, while for Si-PhCWs the lattice constant a is the dominant factor. The corresponding nonlinear coefficients are given by:

$$\bar{\gamma} = \frac{3\omega\varepsilon_0}{16v_g^2}\frac{\bar{\Gamma}}{\mathscr{W}^2}, \tag{2.16a}$$

$$\tilde{\gamma} = \frac{3\omega\varepsilon_0 a}{16 v_g^2} \frac{\tilde{\Gamma}}{W^2}, \tag{2.16b}$$

Here and in what follows of this chapter, bar and tilde symbols represent that the physical quantities refer to Si-PhWs and Si-PhCWs, respectively, unless otherwise is specified. $\mathscr{W}$ and W are the optical mode energy per unit length of Si-PhW and optical mode energy contained in a unit cell of Si-PhCW, with the expression listed below:

$$\mathscr{W} = \frac{1}{4}\int_S \left[\varepsilon(\underline{r})|\underline{e}(\underline{r},\omega)|^2 + \mu_0|\underline{h}(\underline{r},\omega)|^2\right] dS, \tag{2.17a}$$

$$W = \frac{1}{4}\int_{V_{\text{cell}}} \left[\varepsilon(\underline{r})|\underline{e}(\underline{r},\omega)|^2 + \mu_0|\underline{h}(\underline{r},\omega)|^2\right] dV. \tag{2.17b}$$

As mentioned earlier, $\underline{e}(\underline{r},\omega)$ and $\underline{h}(\underline{r},\omega)$ are the electric and magnetic field respectively. S and V_{cell} are the cross-section area of Si-PhWs and the unit cell volume of Si-PhCWs, correspondingly. Furthermore, the coefficients $\bar{\Gamma}$ and $\tilde{\Gamma}$ are the mode mediated nonlinear susceptibility for the Si-PhWs and Si-PhCWs, respectively:

$$\bar{\Gamma} = \int_{S_{\text{nl}}} \underline{e}^*(\underline{r}) \cdot \hat{\chi}^{(3)}(\omega,-\omega,\omega) \vdots \underline{e}(\underline{r})\underline{e}^*(\underline{r})\underline{e}(\underline{r}) dS, \tag{2.18a}$$

$$\tilde{\Gamma} = \int_{V_{\text{nl}}} \underline{e}^*(\underline{r}) \cdot \hat{\chi}^{(3)}(\omega,-\omega,\omega) \vdots \underline{e}(\underline{r})\underline{e}^*(\underline{r})\underline{e}(\underline{r}) dV, \tag{2.18b}$$

In order to facilitate a comparison between the optical properties of Si-PhWs and Si-PhCWs, we recast Eqs. (2.3) in a new form of Eqs. (2.16). Furthermore, $\bar{\kappa}$ and $\tilde{\kappa}$ measure the overlap integral between the active area of Si-PhWs and Si-PhCWs and the optical mode, whose mathematical formulae are expressed as:

$$\bar{\kappa} = \frac{n^2 \int_{A_0} |\underline{e}(\underline{r}_t)|^2 dA}{\int_{A_\infty} n^2(\underline{r}_t)|\underline{e}(\underline{r}_t)|^2 dA}, \tag{2.19a}$$

$$\tilde{\kappa} = \frac{a n^2 \int_{A_0} |\underline{e}(\underline{r})|^2 dA}{\int_{V_{Cell}} n^2(\underline{r}_t)|\underline{e}(\underline{r})|^2 dV}, \tag{2.19b}$$

Equations. (2.19) suggest that only a fraction of the power from the electromagnetic mode affects the FCs generation, since the mode profile only partially overlaps with Si waveguides.

A modified rate equation is used to describe the carrier dynamics during the trans-

mission in Si waveguides:

$$\frac{\partial N}{\partial t} = -\frac{N}{\tau_c} + \frac{\gamma''}{\hbar\omega_0 A_{nl}}|u|^4, \tag{2.20}$$

where N represents the FCs density, τ_c is the FC relaxation time, and A_{nl} is the effective mode area. We use $A_{\mathrm{nl}} = wh$ ($A_{\mathrm{nl}} = ah$) for the Si-PhW (Si-PhCW) systems, although more accurate formulae for A_{nl} exist [23, 64, 65, 68]. Since we consider high-index contrast systems, the optical field is strongly confined in the waveguide, so that using the geometrical area for A_{nl} is a reasonable approximation. Here and in what follows ζ' (ζ'') represents the real (imaginary) part of the complex number, ζ. In conclusion, both Eq. (2.15) and Eq. (2.20) are described to describe the single-wavelength pulse propagation.

2.6.2 Theory of Multi-wavelength Optical Signal Propagation

As an expansion of the single-wavelength propagation model, the multi-wavelength propagation model will be presented in this section to fully capture the evolution of multi-wavelength optical fields in coupled with FCs. Note that the FWM terms are not included in our multi-wavelength propagation model, since the phase-match condition is not satisfied with the values of wavelength used in this dissertation. Thus, the multi-wavelength model can be derived by adding the XPM term in Eqs. (2.15) and (2.20) [19, 64, 68]:

$$j\frac{\partial u_i}{\partial z} + j\left(\frac{1}{v_{g,i}} - \frac{1}{v_{g,\mathrm{ref}}}\right)\frac{\partial u_i}{\partial T} - \frac{\beta_{2,i}}{2}\frac{\partial^2 u_i}{\partial T^2} = -\frac{\omega_i \kappa_i}{n v_{g,i}}\delta n_{\mathrm{FC}} u_i - \frac{jc\kappa_i}{2n v_{g,i}}(\alpha_{\mathrm{in}} + \alpha_{\mathrm{FC}})u_i - \left(\gamma_i |u_i|^2 + 2\sum_{k\neq i}\gamma_{ik}|u_k|^2\right)u_i, \tag{2.21a}$$

$$\frac{\partial N}{\partial t} = -\frac{N}{\tau_c} + \sum_{i,k} C_{ik}|u_i|^2|u_k|^2, \tag{2.21b}$$

Here, i and k indicate the transmission channel index with the carrier frequency ω_i and ω_k, and the channel index ranges from 1 to M (M is the total number of channels). $u_i(z,T)$ is the ith pulse envelope, measured in $\sqrt{\mathrm{W}}$, z and T are the distance along the Si waveguide and time in a reference system moving with velocity $v_{g,\mathrm{ref}}$, respectively. Specifically, $T = t - z/v_{g,\mathrm{ref}}$, where t is the physical time. The definitions of $v_{g,i}$, $\beta_{2,i}$, κ_i, δn_{fc}, α_{fc}, α_{in}, γ_i and τ_c can be found in Sec. 2.6.1, with the central frequency to be

ω_i this time. γ_{ik} is the nonlinear coefficient corresponding to the XPM effect in the Si waveguide. For completeness, we present not only the mathematical formula for the γ_{ik} within Si-PhWs and Si-PhCWs, but also for γ_i:

$$\bar{\gamma}_i = \frac{3\omega_i\varepsilon_0}{16v_{g,i}^2}\frac{\bar{\Gamma}_i}{\mathscr{W}_i^2}, \quad \bar{\gamma}_{ik} = \frac{3\omega_i\varepsilon_0}{16v_{g,i}v_{g,k}}\frac{\bar{\Gamma}_{ik}}{\mathscr{W}_i\mathscr{W}_k}, \tag{2.22a}$$

$$\tilde{\gamma}_i = \frac{3\omega_i\varepsilon_0 a}{16v_{g,i}^2}\frac{\tilde{\Gamma}_i}{W_i^2}, \quad \tilde{\gamma}_{ik} = \frac{3\omega_i\varepsilon_0 a}{16v_{g,i}v_{g,k}}\frac{\tilde{\Gamma}_{ik}}{W_iW_k}. \tag{2.22b}$$

The optical mode energy per unit length ($\mathscr{W}_i$) and per unit cell (W_i) at ω_i have been given by Eqs. (2.5). Additionally, the nonlinear susceptibility coefficients, Γ_i and Γ_{ij}, are defined below:

$$\bar{\Gamma}_i = \int_{S_{\mathrm{nl}}} \underline{e}_i^*(\underline{r})\cdot\hat{\chi}^{(3)}(\omega_i,-\omega_i,\omega_i)\vdots\underline{e}_i(\underline{r})\underline{e}_i^*(\underline{r})\underline{e}_i(\underline{r})dS, \tag{2.23a}$$

$$\bar{\Gamma}_{ik} = \int_{S_{\mathrm{nl}}} \underline{e}_i^*(\underline{r})\cdot\hat{\chi}^{(3)}(\omega_k,-\omega_k,\omega_i)\vdots\underline{e}_k(\underline{r})\underline{e}_k^*(\underline{r})\underline{e}_i(\underline{r})dS, \tag{2.23b}$$

$$\tilde{\Gamma}_i = \int_{V_{\mathrm{nl}}} \underline{e}_i^*(\underline{r})\cdot\hat{\chi}^{(3)}(\omega_i,-\omega_i,\omega_i)\vdots\underline{e}_i(\underline{r})\underline{e}_i^*(\underline{r})\underline{e}_i(\underline{r})dV, \tag{2.23c}$$

$$\tilde{\Gamma}_{ik} = \int_{V_{\mathrm{nl}}} \underline{e}_i^*(\underline{r})\cdot\hat{\chi}^{(3)}(\omega_k,-\omega_k,\omega_i)\vdots\underline{e}_k(\underline{r})\underline{e}_k^*(\underline{r})\underline{e}_i(\underline{r})dV, \tag{2.23d}$$

With regard to the carrier dynamics in the multi-wavelength propagation, we use the coefficient C_{ik} in Eq. (2.21b) to quantify the rate at which the optical energy is transferred to FCs. And this important parameter, C_{ik}, is denoted as:

$$C_{ik} = \begin{cases} \dfrac{\gamma_i''}{\hbar\omega_i A_{nl}}, & i = k, \\ \dfrac{4\gamma_{ik}''}{\hbar(\omega_i+\omega_k)A_{nl}}, & i \neq k. \end{cases} \tag{2.24}$$

The explicit description of the effective mode area A_{nl} has been given in the last paragraph of Sec. 2.6.1. More rigorous definitions related to the multi-wavelength propagation can be found in refs. [68, 69].

2.7 Linearized Theoretical Model for CW Noise Dynamics

The linearized models for CW signal propagation in Si waveguides are presented in this section. Similar to the propagation theory introduced in Sec. 2.6, both linearized mod-

els regarding single- and multi-wavelength propagation will be introduced in Sec. 2.7.1 and Sec. 2.7.2, respectively. These models assume that the nonlinear noise-noise interaction during transmission can be negligible [70, 71], due to the fact that the power of noise at the input of waveguides is much smaller than that of optical signal. Thus, two resulting approximations are proposed: firstly, all quadratic and higher-order noise terms are neglected; secondly, δn_{FC} is proportional to carrier density N. Particularly, a numerical ODE solver is employed in the linearized propagation models, in order to reduce the computational time and maintain the simulation reliability, which will be introduced in Sec. 2.8.2.

2.7.1 Single-channel CW Noise Linearization

In single-channel Si waveguides, both an OOK modulated CW signal (u_{OOK}) and a PSK modulated CW signal (u_{PSK}) will be thoroughly studied [72, 73]. After comparing the definition of these two signals via Eq. (2.6a) and Eq. (2.6b), one can tell that PSK signals contain an extra term of Φ_0, which increases the complexity of the linearized propagation model. However, u_{OOK} can be written in the form of u_{PSK} by setting $\Phi_0 = 0$ in Eq. (2.6b). Therefore, one common linearized propagation model is proposed in this section, which is capable of describing the evolution of these two types of CW signals in the single-channel Si waveguides.

Firstly, the FCs dynamics (Eq. (2.20)) is considered in the stationary regime, $\frac{\partial N}{\partial t} = 0$. Then, the steady state FCs density, N_s, is obtained:

$$N_s(z) = \frac{t_c \gamma''}{\hbar \omega_0 A_{nl}} P^2(z) \equiv \xi P^2(z). \tag{2.25}$$

A self-consistency condition for the validity of our model is that the FC induced dispersion is small, namely $\delta n_{\mathrm{fc}} \lesssim 10^{-3}$. In addition, stationary regime can be reached only if the bit window is much smaller than the FC relaxation time, a condition satisfied in all our numerical simulations. This serves as one of the necessary conditions to construct the linearized propagation models. In the small noise limit, Eq. (2.15) can be linearized and transformed to a system of ODEs, which is much less demanding computationally.

The next step is to substitute Eq. (2.6b) into Eq. (2.15), and discard all quadratic and higher-order terms of $a(z,t)$ in the resulted equation. Notably, the TOD and fourth-

order dispersion terms will not be included in the linearized models, since their effects are negligible for pulse widths of picoseconds and larger when compared with the GVD effect. Then, in conjunction with Eq. (2.25), we arrive to the following system of equations for u_{OOK} and u_{PSK}:

$$\frac{dP}{dz} = -\frac{c\kappa}{nv_g}\alpha_{in}P - \frac{c\kappa}{nv_g}\sigma_\alpha \xi P^3 - 2\gamma'' P^2, \tag{2.26a}$$

$$\frac{d\Phi}{dz} = -\frac{\omega_0 \kappa}{nv_g}\sigma_n \xi P^2 - \gamma' P, \tag{2.26b}$$

$$\begin{aligned}\frac{\partial a}{\partial z} =& -j\frac{\beta_2}{2}\frac{\partial^2 a}{\partial t^2} - \frac{c\kappa}{2nv_g}\alpha_{in}a - \gamma'' P a + j2\gamma P e^{j\Phi_0}(\cos\Phi_0 a' + \sin\Phi_0 a'') \\ & - \frac{c\kappa}{2nv_g}\sigma_\alpha \xi P^2[a + 4e^{j\Phi_0}(\cos\Phi_0 a' + \sin\Phi_0 a'')] \\ & + j\frac{4\omega_0\kappa}{nv_g}\sigma_n \xi P^2 e^{j\Phi_0}(\cos\Phi_0 a' + \sin\Phi_0 a'').\end{aligned} \tag{2.26c}$$

Here, σ_n and σ_α quantify the influence of FCs on the linear optical properties of silicon *via* $\delta n_{\text{fc}} = \sigma_n N$ and $\alpha_{\text{fc}} = \sigma_\alpha N$, and have values of $\sigma_\alpha = 1.45 \times 10^{-21}(\lambda/\lambda_0)^2$ (in units of m^2) and $\sigma_n = \sigma(\lambda/\lambda_0)^2$ (in units of m^3), with σ being a power-dependent coefficient [74] and $\lambda_0 = 1550\,\text{nm}$ is a reference wavelength. Here and in what follows $a'(z,t)$ and $a''(z,t)$ represent the real and imaginary parts of the noise $a(z,t)$, respectively. It can be seen from Eqs. (2.26) that the optical power P can be calculated independently of other signal parameters and, as expected, it decays due to intrinsic losses, FC absorption (FCA), and two-photon absorption (TPA). On the other hand, the variation of the global phase, Φ, is determined by the FC dispersion (FCD) and self-phase modulation (SPM) effects. Importantly, the initial phase Φ_0 of PSK modulation formats does not affect the evolution of the signal power and global phase, thus allowing u_{OOK} and u_{PSK} to share the same mathematical formulation for these two physical quantities.

In order to simplify the noise calculations, we transform Eq. (2.26c) to a system of ODEs. For this, we combine this equation with its complex conjugate and Fourier transform the resulting equations for the in-phase and quadrature noise components, $a'(z,t)$ and $a''(z,t)$, respectively. These calculations yield:

$$\begin{aligned}\frac{dA'}{dz} =& -\frac{\beta_2}{2}\Omega^2 A'' - \frac{c\kappa}{2nv_g}\alpha_i A' - \frac{c\kappa}{2nv_g}\sigma_\alpha \xi P^2[A' + 4\cos\Phi_0(\cos\Phi_0 A' + \sin\Phi_0 A'')] \\ & - \frac{4\omega_0\kappa}{nv_g}\sigma_n \xi P^2 \sin\Phi_0(\cos\Phi_0 A' + \sin\Phi_0 A'') - \gamma'' P A'\end{aligned}$$

$$-2(\gamma'\sin\Phi_0+\gamma''\cos\Phi_0)P(\cos\Phi_0 A'+\sin\Phi_0 A''), \tag{2.27a}$$

$$\begin{aligned}\frac{dA''}{dz}=&\frac{\beta_2}{2}\Omega^2 A'-\frac{c\kappa}{2nv_g}\alpha_i A''-\frac{c\kappa}{2nv_g}\sigma_\alpha\xi P^2[A''+4\sin\Phi_0(\cos\Phi_0 A'+\sin\Phi_0 A'')]\\&+\frac{4\omega_0\kappa}{nv_g}\sigma_n\xi P^2\cos\Phi_0(\cos\Phi_0 A'+\sin\Phi_0 A'')-\gamma'' PA''\\&+2(\gamma'\cos\Phi_0-\gamma''\sin\Phi_0)P(\cos\Phi_0 A'+\sin\Phi_0 A'').\end{aligned} \tag{2.27b}$$

where $\Omega=\omega-\omega_0$ and $A'(z,\Omega)=\mathscr{F}\{a'(z,t)\}$ and $A''(z,\Omega)=\mathscr{F}\{a''(z,t)\}$ are the Fourier transforms of the two noise components. Furthermore, a detailed comparison between the full propagation model and its linearized version was carried out for the single-channel systems in Chapter 5, the conclusion being that for practical values of the system parameters the linearized model is accurate.

To this end, both the full propagation model and its linearized version have been derived for the single-channel optical system. In addition, these models can be easily extended to other types of optical waveguides or more complicated optical devices.

2.7.2 Multi-channel CW Noise Linearization

In this section, the linearized approach for multi-wavelength propagation are presented, considering only the OOK CW signal propagation in each channel. To begin with, the superposition of the optical signal and noise propagating in the *i*th channel of a Si-PhW or Si-PhCW photonic system is expressed as [75]:

$$u_i(z,T)=\left[\sqrt{P_i(z)}+a_i(z,T)\right]e^{-j\Phi_i(z)}, \tag{2.28}$$

where $P_i(z)$, $a_i(z,T)$ and $\Phi_i(z)$ represent the power of OOK CW signal, the complex additive white noise, and the global phase shift in the *i*th channel, respectively.

In the stationary regime, $\frac{\partial N}{\partial t}=0$, so that Eq. (2.21b) implies that the steady-state FC density, N_s, is given by:

$$N_s(z)=\sum_{i,k}\xi_{ik}P_i(z)P_k(z), \tag{2.29}$$

where $\xi_{ik}=\tau_c C_{ik}$ and C_{ik} is defined by Eq. (2.24).

In order to linearize Eq. (2.21) w.r.t. the noise amplitudes, $a_i(z,T)$, $i=1,\ldots,M$, we substitute Eq. (2.28) into Eq. (2.21) and discard all quadratic and higher-order

terms in $a_i(z,T)$. Then, in conjunction with Eq. (2.29), the zeroth- and first-order of Eq. (2.21) become:

$$\frac{dP_i}{dz} = -\frac{c\kappa_i}{nv_{g,i}}\big(\alpha_{\text{in}} + \sigma_\alpha N_s\big)P_i - 2\big(\gamma_i'' P_i + 2\sum_{k\neq i}\gamma_{ik}'' P_k\big)P_i \tag{2.30a}$$

$$\frac{d\Phi_i}{dz} = -\frac{\omega_i\kappa_i}{nv_{g,i}}\sigma_n N_s - \gamma_i' P_i - 2\sum_{k\neq i}\gamma_{ik}' P_k, \tag{2.30b}$$

$$\begin{aligned}\frac{\partial a_i}{\partial z} = &-\Big(\frac{1}{v_{g,i}} - \frac{1}{v_{g,\text{ref}}}\Big)\frac{\partial a_i}{\partial T} - \frac{j\beta_{2,i}}{2}\frac{\partial^2 a_i}{\partial T^2} - \frac{c\kappa_i}{2nv_{g,i}} \\ &\times\Big[(\alpha_{\text{in}} + \sigma_\alpha N_s)a_i + 2\sigma_\alpha\sqrt{P_i}\sum_{kl}P_k\sqrt{P_l}(\xi_{kl}+\xi_{lk})a_l'\Big] \\ &+ 2j\frac{\omega_i\kappa_i}{nv_{g,i}}\sigma_n\sqrt{P_i}\sum_{kl}P_k\sqrt{P_l}(\xi_{kl}+\xi_{lk})a_l' + 2j\gamma_i P_i a_i' \\ &- \gamma_i'' P_i a_i + 2\sum_{k\neq i}\sqrt{P_k}(2j\gamma_{ik}\sqrt{P_i}a_k' - \gamma_{ik}''\sqrt{P_k}a_i),\end{aligned} \tag{2.30c}$$

These equations clearly show that the power in a specific channel decays due to intrinsic losses, FCA, TPA, and XAM. Importantly, the terms proportional to N_s in Eqs. (2.30a) and (2.30b) reveal an interchannel cross-talk mechanism that does not have a counterpart in optical fiber systems, namely a FC-mediated interaction between optical signals propagating in different channels. To be more specific, as an optical signal propagates in a certain channel, part of its energy is optically absorbed leading to generation of FCs. As a result, the index of refraction and absorption coefficient of the waveguide changes, which leads to a phase shift and increased optical absorption of an optical signal propagating in a different channel.

By adding to and subtracting Eqs. (2.30) from its complex conjugate, two coupled differential equations are obtained for the in-phase and quadrature noise components, $a_i'(z,T)$ and $a_i''(z,T)$, respectively. Taking the Fourier transform of both sides of the resulting equations leads to the following system of coupled ordinary differential equations:

$$\begin{aligned}\frac{dA_i'}{dz} = &\,j\Big(\frac{1}{v_{g,i}} - \frac{1}{v_{g,\text{ref}}}\Big)\Omega_i A_i' - \frac{\beta_{2,i}}{2}\Omega_i^2 A_i'' - \frac{c\kappa_i}{2nv_{g,i}} \\ &\times\Big[(\alpha_{\text{in}} + \sigma_\alpha N_s)A_i' + 2\sigma_\alpha\sqrt{P_i}\sum_{kl}P_k\sqrt{P_l}(\xi_{kl}+\xi_{lk})A_l'\Big] \\ &- 3\gamma_i'' P_i A_i' - 2\sum_{k\neq i}\sqrt{P_k}(\gamma_{ik}''\sqrt{P_k}A_i' + 2\gamma_{ik}''\sqrt{P_i}A_k'),\end{aligned} \tag{2.31a}$$

$$\frac{dA_i''}{dz} = j\Big(\frac{1}{v_{g,i}} - \frac{1}{v_{g,\text{ref}}}\Big)\Omega_i A_i'' + \frac{\beta_{2,i}}{2}\Omega_i^2 A_i' + 2\frac{\omega_i \kappa_i}{n v_{g,i}}\sigma_n$$
$$\times \sqrt{P_i}\sum_{kl} P_k\sqrt{P_l}(\xi_{kl}+\xi_{lk})A_l' - \frac{c\kappa_i}{2nv_{g,i}}(\alpha_{\text{in}}+\sigma_\alpha N_s)A_i''$$
$$+ (2\gamma_i' A_i' - \gamma_i'' A_i'')P_i - 2\sum_{k\neq i}\sqrt{P_k}(\gamma_{ik}''\sqrt{P_k}A_i'' - 2\gamma_{ik}'\sqrt{P_i}A_k'), \tag{2.31b}$$

where $\Omega_i = \omega - \omega_i$, $A_i'(z,\Omega_i) = \mathscr{F}\{a_i'(z,T)\}$ and $A_i''(z,\Omega_i) = \mathscr{F}\{a_i''(z,T)\}$, $i = 1,\ldots,M$, are the Fourier transforms of the noise components. Moreover, the detailed comparison between the full and linearized models regarding the multi-wavelength signal propagation will be given in Chapter 8.

2.8 Computational Algorithms of Signal Propagation

Computational solvers are often needed in the exploration of the signal propagation in Si waveguides, since the two mathematical models discussed in Sec. 2.6 and Sec. 2.7 will not lead themselves to the analytical solutions. To serve this purpose, many numerical approaches have been developed, with a brief review summarized in Sec. 4.1. Among them, two specific algorithms are utilized in this dissertation, namely, the modified SSFM in Sec. 2.8.1 and the computational solver for ODEs in Sec. 2.8.2.

2.8.1 Split Step Fourier Method

The SSFM method is a pseudospectral method that provides semi-analytical solutions for nonlinear partial equations, such as a NLSE. Particularly, the main strategy of this method is to split the distance into small segments, and then perform the linear and nonlinear operations separately. In this process, the Fast Fourier Transform (FFT) is applied to transfer the optical field between the time- and frequency-domain, in order to improve the computational speed. Importantly, the SSFM method has to be modified for Si waveguides in order to account for the FCs dynamics, which is one of the major differences between Si waveguides and silica fibers.

The SSFM algorithm for Si waveguides is presented as follows. The start point of the SSFM is to separate Eq. (2.15) into the linear and nonlinear parts, which is expressed as:

$$\frac{\partial u}{\partial t} = (\hat{D}+\hat{N})u, \tag{2.32}$$

where

$$\hat{D} = -\frac{i\beta_2}{2}\frac{\partial^2}{\partial t^2} + \frac{\beta_3}{6}\frac{\partial^3}{\partial t^3} - \frac{ic\kappa}{2nv_g}\alpha_{in}, \tag{2.33a}$$

$$\hat{N} = i\gamma|u|^2 - \frac{c\kappa}{2nv_g}\alpha_{FC} + \frac{i\omega\kappa}{nv_g}\delta n_{FC}. \tag{2.33b}$$

Here, $\hat{D}$ represents a differential operator that determines the linear optical effects, and $\hat{N}$ acts as the nonlinear operator that corresponds to the nonlinearity of Si waveguides. In particular, the mathematical terms of FCA (α_{FC}) and FCD (δn_{FC}) in Eq. (2.33b) are related to the FCs dynamics (Eq. (2.20)) in form of Eq. (2.5). Therefore, the evolution of FCs is needed to be measured simultaneously, which can be solved via a fifth-order Runge-Kutta method.

Practically, the optical linear and nonlinear effects mutually interact with each other during transmission. But it is reasonable and realistic to assume that these optical processes are uncorrelated to each other within a small distance segment h, since their mutual interaction are relatively small. Therefore, the numerical solution towards Eq. (2.32) can be derived by performing the linear effects operator $\hat{D}$ alone on the electrical field, followed by the nonlinear effects operator $\hat{N}$. A corresponding mathematical formula is given below:

$$u(z+h,t) = \exp[h(\hat{D}+\hat{N})]\ u(z,t) \approx \exp[h\hat{D}]\exp[h\hat{N}]\ u(z,t) \tag{2.34}$$

This approximation of Eq. (2.34) is made according to the Baker-Hausdorff formula for two independent operators $\hat{a}$ and $\hat{b}$:

$$\exp[\hat{a}]\exp[\hat{b}] = \exp[\hat{a}+\hat{b}+\frac{1}{2}[\hat{a},\hat{b}]+\frac{1}{12}[\hat{a}-\hat{b},[\hat{a},\hat{b}]]+\cdots] \tag{2.35}$$

where $[\hat{a},\hat{b}] = \hat{a}\hat{b}-\hat{b}\hat{a}$. It suggests that Eq. (2.34) provides solution with accuracy of second-order in the segment h.

To improve the accuracy of the SSFM method, an alternative procedure for Eq. (2.34) is proposed:

$$u(z+h,t) \approx \exp[\frac{h}{2}\hat{D}]\exp[\int_z^{z+h}\hat{N}(z_1)dz_1]\exp[\frac{h}{2}\hat{D}]\ u(z,t). \tag{2.36}$$

This numerical process is denoted as the symmetric SSFM, which is accurate to the third order of h. Moreover, the trapezoidal rule is applied to the nonlinear operator in Eq. (2.36):

$$\int_{z}^{z+h} \hat{N}(z_1)dz_1 \approx \frac{h}{2}[\hat{N}(z)+\hat{N}(z+h)] \tag{2.37}$$

Here, two iteration operations are needed to implement Eq. (2.37) in the SSFM method, since $\hat{N}(z+h)$ is unknown at $z+h/2$. Therefore, these two iterations are described as follows: firstly, $\hat{N}(z+h)$ is replaced by $\hat{N}(z)$ at the beginning; secondly, the calculation of $A(z+h,t)$ is performed according to the relation of Eq. (2.36), which provides the new value for $\hat{N}(z+h)$ in turn. This provides the numerical process to capture the nonlinear effects. Till now, all the essential mathematical formula to calculate $u(z+h,t)$ from $u(z,t)$ is achieved.

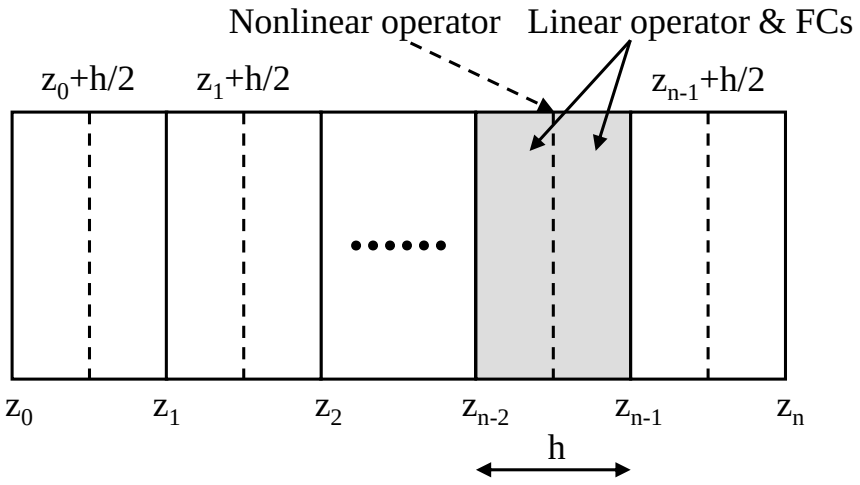

Figure 2.12: Schematic illustration of the symmetric SSFM that introduced for Si waveguides.

To conclude, the main computational procedure of the symmetric SSFM method is demonstrated in Fig. 2.12. The main idea is to divide the distance L into n sections equally ($L = nh$), and then calculate the optical field at each h: firstly, the linear effects operator $\hat{D}$ is carried out on the electrical field in the frequency-domain during a distance segment of $h/2$; next, at the mid-segment of $z+h/2$, the electrical field in the time domain is multiplied by a nonlinear operator $\hat{N}$, which represents the overall waveguide nonlinearity along h; along the second $h/2$, the electrical field only includes the linear effects, where this calculation is done in the frequency domain; furthermore, the FCs evolution is calculated in the above linear effect steps, by means of using the fifth Runge-Kutta technique presented in Appendix B to solve Eq. (2.20). In order to

reduce the computational time, the following expression is used to obtain the output signal after n successive steps:

$$u(L,t) \approx e^{-\frac{h}{2}\hat{D}} \left(\prod_{j=1}^{n} e^{h\hat{D}} e^{h\hat{N}} \right) e^{\frac{h}{2}\hat{D}} u(0,t) \tag{2.38}$$

Additionally, the values of the computational time window, the number of temporal sampling points (or the FFT points) and the distance step, have to be chosen carefully in order to ensure the computational accuracy as well as speed up the computational process. More information about the numerical implementation of this algorithm will be introduced in Sec. 4.3.1.

2.8.2 Computational Solvers for Ordinary Differential Equations

The Matlab standard solver, *ode*45, is employed to calculate the ODEs introduced in Sec. 2.7 [91]. By definition, the Matlab function *ode*45 is designed to implement the fifth-order Runge-Kutta routine to solve the typical mathematical problem as follows:

$$\frac{d\mathbf{y}}{dt} = \mathbf{f}(t,\mathbf{y}), \quad \mathbf{y}(t_0) = \mathbf{y}_0 \tag{2.39}$$

Here, t represents the evaluation points, such as time and distance, and $\mathbf{y}$ is a t-related array waiting to be calculated from Eq. (2.39). In this function, the initial conditions of $\mathbf{y}(t_0) = \mathbf{y}_0$ and the interval of integration $tspan$ are needed to be provided for a specific mathematical problems.

When considering the propagation of a noisy CW signal in the Si waveguides, the Matlab function *ode*45 is used to solve all the coupled first-order ODEs numerically. For instance, with regard to Eqs. (2.26) and (2.27) for single-channel signal propagation, we can firstly select four important vector variables as $A = P$, $B = \Phi$, $C = A'$ and $D = A''$. Then, based on their interrelations explained in such form:

$$D \leftrightarrow C \leftrightarrow A \rightarrow B \tag{2.40}$$

the simplified version of the first-order ODEs (Eqs. (2.26) and (2.27)) can be derived

below, with the evaluation points to be the distance z:

$$\frac{d\mathbf{A}}{dz} = \mathbf{f}_1(\mathbf{A}), \tag{2.41a}$$

$$\frac{d\mathbf{B}}{dz} = \mathbf{f}_2(\mathbf{A}), \tag{2.41b}$$

$$\frac{d\mathbf{C}}{dz} = \mathbf{f}_3(\mathbf{A},\mathbf{C},\mathbf{D}), \tag{2.41c}$$

$$\frac{d\mathbf{D}}{dz} = \mathbf{f}_4(\mathbf{A},\mathbf{C},\mathbf{D}), \tag{2.41d}$$

where the initial conditions, $\mathbf{A}(0) = \mathbf{A}_0$ stands for the input power of CW signals, $\mathbf{B}(0) = \mathbf{B}_0$ represents the initial global phase of optical signal, $\mathbf{C}(0) = \mathbf{C}_0$ and $\mathbf{D}(0) = \mathbf{D}_0$ are the real and imaginary part of the input white noise in the frequency domain. Eventually, with the initial condition of $y_0 = [\mathbf{A}_0;\mathbf{B}_0;\mathbf{C}_0;\mathbf{D}_0]$ and the integration interval of $tspan$, the solver $ode45$ can be performed on a Matlab function that is programmed based on Eq. (2.41). This can facilitate accurate numerical results in an efficient way. Importantly, $tspan$ can be designed in a form of $tspan = [t_0, t_1, t_2, \cdots, t_f]$, in order to control the distance step. In addition, the number of sampling points in y_0 has to be adequately large, aiming at maintaining the accuracy of computation. The mathematical principle of $ode45$ is introduced in Appendix B.

Bibliography

[1] R. A. Soref, and J. P. Lorenzo, "Single-crystal silicon: a new material for 1.3 and 1.6 μm integrated-optical components," Electron. Lett. **21**, 953-954 (1985).

[2] G. V. Treyz, P. G. May and J. M. Halbout, "Silicon optical modulators at 1.3 μm based on free-carrier absorption," IEEE Electron Device Lett. **12**, 276-278 (1991).

[3] B. L. Weiss, Z. Yang, and F. Namavar, "Wavelength dependent propagation loss characteristics of SiGe/Si planar waveguides," Electron. Lett. **28**, 2218-2220 (1992).

[4] S. Y. Chou, and W. Deng, "Subwavelength amorphous silicon transmission gratings and applications in polarizers and waveplates," Appl. Phys. Lett. **67**, 742-745 (1995).

[5] V. S.-Y. Lin, K. Motesharei, K.-P. S. Dancil, M. J. Sailor, and M. R. Chadiri, "A Porous Silicon-Based Optical Interferometric Biosensor," Science **278**, 840-842 (1997).

[6] B. E. Little, J. S. Foresi, G. Steinmeyer, E. R. Thoen, S. T. Chu, H. A. Haus, E. P. Ippen, L. C. Kimerling, and W. Greene, "Ultra-Compact $Si - SiO_2$ Microring Resonator Optical Channel Dropping Filters ," Science **278**, 840-842 (1997).

[7] C. R. Giles, V. Aksyuk, B. Barber, R. Ruel, L. Stulz and D. Bishop, "A silicon MEMS optical switch attenuator and its use in lightwave subsystems," IEEE J. Sel. Top. Quantum Electron. **5**, 18-2 (1999).

[8] T. Shoji, T. Tsuchizawa, T. Watanabe, K. Yamada and H. Morita, "Low loss mode size converter from 0.3 μm square Si wire waveguides to singlemode fibres," Electron. Lett. **38**, 1669-1670 (2002).

[9] S. M. Csutak, J. D. Schaub, W. E. Wu, and J. C. Campbell, "High-speed monolithically integrated silicon optical receiver fabricated in $130 - $ nm CMOS technology," IEEE Photon. Technol. Lett. **24**, 516-518 (2002).

[10] D. Taillaert, P. Bienstman, and R. Baets, "Compact efficient broadband grating coupler for silicon-on-insulator waveguides," Opt. Lett. **29**, 2749-2751 (2004).

[11] I. Kiyat, A. Aydinli, and N. Dagli, "A Compact Silicon-on-Insulator Polarization Splitter," IEEE Photon. Technol. Lett. **17**, 100-102 (2005).

[12] X. Liu, R. M. Osgood, Y. A. Vlasov, and W. M. J. Green, "Mid-infrared optical parametric amplifier using silicon nanophotonic waveguides," Nat. Phot. **4**, 557-560 (2010).

[13] W. Bogaerts, D. Taillaert, B. Luyssaert, P. Dumon, J. Campenhout, P. Bienstman, D. Thourhout, R. Baets, V. Wiaux, and S. Beckx, "Basic structures for photonic integrated circuits in Silicon-on-insulator," Opt. Express **12**, 1583-1591 (2004).

[14] Hui Chen, "Silicon Photonic Devices for On-chip Optical Interconnects," Ph. D. Thesis (Hong Kong University of Science and Technology, 2010).

[15] G. T. Reed, G. Z. Mashanovich, W. R. Headley, B. Timotijevic, F. Y. Gardes, S. P. Chan, P. Waugh, N. G. Emerson, C. E. Png, M. J. Paniccia, A. Liu, D. Hak, and V. M. N. Passaro, "Issues associated with polarization independence in silicon photonics," IEEE J. Sel. Top. Quantum Electron. **12**, 1335-1344 (2006).

[16] Y. A. Vlasov, and S. J. McNab, "Losses in sinlge-mode silicon-on-insulator strip waveguides and bends," Opt. Express **12**, 1622-1631 (2004).

[17] G. Li, J. Yao, Y. Luo, H. Thacker, A. Mekis, X. Zheng, I. Shubin, J.-H. Lee, K. Raj, J. E. Cunningham, and A. V. Krishnamoorthy, "Ultralow-loss, high-density SOI optical waveguide routing for macrochip interconnects," Opt. Express **20**, 12035-12039 (2012).

[18] R. W. Boyd, *Nonlinear Optics* 2nd ed. (2002).

[19] X. Chen, N. C. Panoiu, and R. M. Osgood, "Theory of Raman-mediated pulsed amplification in silicon-wire waveguides," IEEE J. Quantum Electron. **42**, 160-170 (2006).

[20] E. Dulkeith, F. Xia, L. Schares, W. M. J. Green, and Y. A. Vlasov, "Group index and group velocity dispersion in silicon-on-insulator photonic wires," Opt. Express **14**, 3853-3863 (2006).

[21] X. Chen, N. C. Panoiu, I. Hsieh, J. I. Dadap, and R. M. Osgood, "Third-order dispersion and ultrafast pulse propagation in silicon wire waveguides," IEEE Photon. Technol. Lett. **18**, 2617-2619 (2006).

[22] G. P. Agrawal, *Nonlinear Fiber Optics* 4th ed., Academic Press (2006).

[23] R. M. Osgood, N. C. Panoiu, J. I. Dadap, X. Liu, X. Chen, I-W. Hsieh, E. Dulkeith, W. M. J. Green, and Y. A. Vlassov, "Engineering nonlinearities in nanoscale optical systems: physics and applications in dispersion-engineered silicon nanophotonic wires," Adv. Opt. Photon. **1**, 162-235 (2009).

[24] T. R. Taha, and M. J. Ablowitz, "Analytical and numerical aspects of certain nonlinear evolution equations. II. Numerical, nonlinear Schrödinger equation,"J. Comput. Phys. **55**, 203-230 (1984).

[25] J. Zhang, Q. Lin, G. Piredda, R. W. Boyd, G. P. Agrawal, and P. M. Fauchet, " Anisotropic nonlinear response of silicon in the near-infrared region," Appl. Phys. Lett. **91**, 071113 (2007).

[26] M. P. Chethiya, M. Dissanayake, I. D. Rukhlenko, and G. P. Agrawal, "FDTD modeling of anisotropic nonlinear optical phenomena in silicon waveguides," Opt. Express **18**, 21427-21448 (2010).

[27] X. Chen, N. C. Panoiu, and R. M. Osgood, " Theory of Raman-mediated pulsed amplification in silicon- wire waveguides," IEEE J. Quantum Electron. **42**, 2889-2891 (2008).

[28] I.-W. Hsieh, X. Chen, J. I. Dadap, N. C. Panoiu, R. M. Osgood, S. J. McNab, and Y. A. Vlasov, "Ultrafast-pulse self-phase modulation and third-order dispersion in Si photonic wire-waveguides," Opt. Express **14**, 12380-12387 (2006).

[29] L. Y and G. P. Agrawal, "Impact of two-photon absorption on self-phase modulation in silicon waveguides," Opt. Lett. **32**, 2031-2033 (2007).

[30] N. C. Panoiu, J. F. McMillan, and C. W. Wong, "Theoretical analysis of pulse dynamics in silicon photonic crystal wire waveguides," IEEE J. Sel. Top. Quantum Electron. **16**, 257-266 (2010).

[31] I.-W. Hsieh, X. Chen, J. I. Dadap, N. C. Panoiu, R. M. Osgood, S. J. McNab, and Y. A. Vlasov, "Cross-phase modulation-induced spectral and temporal effects on co-propagating femtosecond pulses in silicon photonic wires," Opt. Express **15**, 1135-1146 (2007).

[32] Y. Zhang, C. Husko, S. Lefrancois, I. H. Rey, T. F. Krauss, J. Schr*o*der, and B. J. Eggleton, "Cross-phase modulation-induced spectral broadening in silicon waveguides," Opt. Express **24**, 443C451 (2016).

[33] S. Lavdas, "Optical pulse dynamics in sub-wavelength nano-patterned silicon photonic wires," Ph. D. Thesis (University College London, 2015).

[34] R. A. Soref and B. R. Bennett, "Electro-optical effects in silicon," IEEE J. Quantum Electron. **QE-23**, 123-129 (1987).

[35] P. E. Barclay, K. Srinivasan, and O. Painter, "Nonlinear response of silicon photonic crystal microresonators excited via an integrated waveguide and fiber taper," IEEE J. Quantum Electron. **13**, 801-820 (2005).

[36] Rsoft Design Group, Femsim, `https://optics.synopsys.com/rsoft/rsoft-passive-device-femsim.html`.

[37] J. D. Joannopoulos, S. G. Johnson, J. N. Winnn, and R. D. Meade, *Photonic Crystals: Modeling the Flow of Light* (Princeton University Press, 2008).

[38] T. F. Krauss, "Why do we need slow light?," Nat. Phot. **2**, 448-450 (2008).

[39] T. Baba, "Slow light in photonic crystals," Nat. Phot. **2**, 465-473 (2008).

[40] G. P. Agrawal, *Fiber-Optic Communication Systems* 3rd ed. (Wiley, 2002).

[41] V. R. Almeida, C.A. Barrios, R. R. Panepucci, and M. Lipson, "All-optical control of light on a silicon chip," *Nature* **431**, 1081-1084 (2004).

[42] S. R. Preble, Q. Xu, B. S. Schmidt, and M. Lipson, "Ultrafast all-optical modulation on a silicon chip," *Opt. Lett.* **30**, 2891-2893 (2005).

[43] D. Liang, M. Fiorentino, T. Okumura, H.-H. Chang, D. T. Spencer, Y.-H. Kuo, A. W. Fang, D. Dai, R. G. Beausoleil, and J. E. Bowers,"Electrically-pumped compact hybrid silicon microring lasers for optical interconnects," Opt. Express **17**, 20355-20364 (2009).

[44] R. Claps, D. Dimitropoulos, V. Raghunathan, Y. Han, and B. Jalali, "Observation of stimulated Raman amplification in silicon waveguides," Opt. Express **11**, 1731-1739 (2003).

[45] R. Espinola, J. I. Dadap, R. M. Osgood, S. J. McNab, and Y. A. Vlasov, "Raman amplification in ultrasmall silicon-on-insulator wire waveguides," Opt. Express **12**, 3713-3718 (2004).

[46] A. Liu, R. Jones, L. Liao, D. Samara-Rubio, D. Rubin, O. Cohen, R. Nicolaescu, and M. Paniccia, "A high-speed silicon optical modulator based on a metal-oxide-semiconductor capacitor," Nature **427**, 615-618 (2004).

[47] C. Manolatou, and M. Lipson, "All-optical silicon modulators based on carrier injection by two-photon absorption," *IEEE J. Lightwave Technol.* **24**, 1433-1439 (2006).

[48] P. D. Trinh, S. Yegnanarayanan, F. Coppinger, and B. Jalali, "Silicon-on-Insulator (SOI) Phased-Array Wavelength Multi/Demultiplexer with Extremely Low-Polarization Sensitivity," IEEE Photon. Technol. Lett. **9**, 940-942 (1997).

[49] R. L. Espinola, M.-C. Tsai, J. T. Yardley, and R. M. Osgood Jr., "Fast and low-power thermooptic switch on thin silicon-on-insulator," IEEE Photon. Technol. Lett. **15**, 1366-1368 (2005).

[50] O. Boyraz, P. Koonath, V. Raghunathan, and B. Jalali, "All optical switching and continuum generation in silicon waveguides," Opt. Express **12**, 4094-4102 (2004).

[51] B. G. Lee, A. Biberman, P. Dong, M. Lipson, and K. Bergman, "All-optical comb

switch for multiwavelength message routing in silicon photonic networks," IEEE Photon. Technol. Lett. **20**, 767-769 (2008).

[52] T. Tanabe, M. Notomi, S. Mitsugi, A. Shinya, and E. Kuramochi, "All-optical switches on a silicon chip realized using photonic crystal nanocavities," *Appl. Phys. Lett.* **87**, 151112 (2005).

[53] P. C. P. Chen, A. M. Pappu, and A. B. Apsel, "Monolithic integrated SiGe optical receiver and detector," *Proc. Conf. Lasers and Electro-Optics, Tech. Dig. (CD) (Optical Society of America)* **CTuZ4**, 1-2 (2007).

[54] S. Assefa, F. Xia, W. M. J. Green, C. L. Schow, A. V. Rylyakov, and Y. A. Vlasov, "CMOS-Integrated Optical Receivers for On-Chip Interconnects," IEEE J. Sel. Top. Quantum Electron. **16**, 1376-1385 (2010).

[55] H. Fukuda, K. Yamada, T. Shoji, M. Takahashi, t. Tsuchizawa, T. Watanabe, J. Takahashi, and S. Itabashi, "Four-wave mixing in silicon wire waveguides," Opt. Express **13**, 4629-4637 (2005).

[56] S. Zlatanovic, J. S. Park, S. Moro, J. M. C. Boggio, I. B. Divliansky, N. Alic, S. Mookherjea, and S. Radic, "Mid-infrared wavelength conversion in silicon waveguides using ultracompact telecom-band-derived pump source," Nat. Phot. **4**, 561-564 (2010).

[57] O. V. Sinkin, "Calculation of Bit Error Rates in Optical Fiber Communicatons Systems in the Presence of Nonlinear Distortion and Noise," Ph. D. Thesis (University of Maryland, 2006).

[58] J. Wang, "Performance Evluation of DPSK Optical Fiber Communication system," Ph.D. Thesis (University of California, 2004).

[59] J. P. Winzer and R. J. Essiambre, "Advanced optical modulation formats," Proc. IEEE **94**, 952-985 (2006).

[60] M. Rohde, C. Caspar, N. Heimes, M. Konitzzer, E. J. Bachus, and N. Hanik, "Robustness of DPSK direct detection transmission format in standard fiber WDM systems," Electron. Lett. **36**, 1483-1484 (2000).

[61] J. Wang, and J. M. Kahn, "Impact of Chromatic and Polarization-Mode Dispersions on DPSK Systems Using Interferometric Demodulation and Direct Detection," IEEE J. Lightwave Technol. **22**, 362-371 (2004).

[62] M. Nölle, M. Seimetz, and E. Patzak, "System Performance of High-Order Optical DPSK and Star QAM Modulation for Direct Detection Analyzed by Semi-Analytical BER Estimation," IEEE J. Lightwave Technol. **27**, 4319-4329 (2009).

[63] M. Seimetz, M. Nölle, and E. Patzak, "Optical System With High-Order Optical DPSK and Star QAM Modulation Based on Interferometric Direct Detection," IEEE J. Lightwave Technol. **25**, 1515-1530 (2007).

[64] S. Lavdas and N. C. Panoiu, "Theory of Pulsed Four-Wave-Mixing in One-dimensional Silicon Photonic Crystal Slab Waveguides," Phys. Rev. B **93**, 115435 (2016).

[65] C. Koos, L. Jacome, C. Poulton, J. Leuthold, W. Freude, "Nonlinear silicon-on-insulator waveguides for all-optical signal processing," Opt. Express **15**, 5976-5990 (2007).

[66] J. I. Dadap, N. C. Panoiu, X. G. Chen, I. W. Hsieh, X. P. Liu, C. Y. Chou, E., Dulkeith, S. J., McNab, F. N. Xia, W. M. J. Green, L. Sekaric, Y. A. Vlasov, and R. M. Osgood, "Nonlinear-optical phase modification in dispersion-engineered Si photonic wires," Opt. Express **16**, 1280-1299 (2008).

[67] A. W. Snyder and J. D. Love, *Optical Waveguide Theory* (Chapman & Hall, 1983).

[68] N. C. Panoiu, J. F. McMillan, and C. W. Wong, "Theoretical analysis of pulse dynamics in silicon photonic crystal wire waveguides," IEEE J. Sel. Top. Quantum Electron. **16**, 257-266 (2010).

[69] V. S. Afshar, T. M. Monro, and C. M. de Sterke, "Understanding the contribution of mode area and slow light to the effective Kerr nonlinearity of waveguides," Opt. Express **21**, 18558-18571 (2013).

[70] G. Bosco, A. Carena, V. Curri, R. Caudino, P. Poggiolini, and S. Benedetto, "A

Novel Analytical Method for the BER Evaluation in Optical Systems Affected by Parametric Gain," IEEE Photon. Technol. Lett. **12**, 152-154 (2000).

[71] G. Bosco, A. Carena, V. Curri, R. Caudino, P. Poggiolini, and S. Benedetto, "Parametric Gain in Multiwavelength Systems: A New Approach to Noise Enhancement Analysis," IEEE Photon. Technol. Lett. **11**, 1135-1137 (1999).

[72] J. You, and N. C. Panoiu, "Calculation of Bit Error Rates in Optical Systems with Silicon Photonic Wires," IEEE J. Quantum Electron. **51**, 8400108 (2015).

[73] J. You and N. C. Panoiu, "Exploiting Higher-order Phase-shift Keying Modulation and Direct-detection in Silicon Photonic Systems," Opt. Express **25**, 8611-8624 (2017).

[74] Q. Lin, Oskar J. Painter, and Govind P. Agrawal, "Nonlinear optical phenomena in silicon waveguides: modeling and applications," Opt. Express **15**, 16604-16644 (2007).

[75] J. You, S. Lavdas, and N. C. Panoiu, "Comparison of BER in Multi-channel Systems With Strip and Photonic Crystal Silicon Waveguides," IEEE J. Sel. Top. Quantum Electron. **22**, 4400810 (2016).

[76] R. Hui, D. Chowdhury, M. Newhouse, M. O'Sullivan, and M. Pettcker, "Nonliear amplification of noise in fibers with dispersion and its imipact in optical amplified systems," IEEE Photon. Technol. Lett. **9**, 392-394 (1997).

[77] E. A. Golovchenko, A. N. Pilipetskii, N. S. Bergano, C. R. Davidsen, F. I. Khatri, R. M. Kimball, and V. J. Mazurczyk, "Modeling of transoceanic fiber-optic WDM communications systems," IEEE J. Sel. Top. Quantum Electron. **6**, 337-347 (2000).

[78] R. Holzl*o*hner, V. S. Grigoryan, C. R. Menyuk, and W. L. Kath, "Accurate calculation of eye diagrams and bit error rates in optical transmission systems using linearization," IEEE J. Lightwave Technol. **20**, 389-400 (2002).

[79] E. Forestieri, "Evaluating the error probability in lightwave systems with chromatic dispersion, arbitrary pulse shape and pre- and postdetection filtering," IEEE J. Lightwave Technol. **18**, 1498-1503 (2000).

[80] B. A. Berg and T. Neuhaus, "Multicanonical ensemble: A new approach to simulate first-order phase transitions," Phys. Rev. Lett. **68**, 9-12 (1992).

[81] B. A. Berg , "Algorithmic aspects of multicanonical Monte Carlo simulations," Nucl. Phys. Proc. Suppl. **63**, 982-984 (1998).

[82] G. Bosco, A. Carena, V. Curri, R. Gaudino, P. Poggiolini, and S. Benedetto, "A novel analytical approach to the evaluation of the impact of fiber parametric gain on the bit error rate," IEEE Trans. Commun. **49**, 2154-2163 (2001).

[83] E. Forestieri and M. Secondini, "On the Error Probability Evaluation in Lightwave Systems With Optical Amplification," IEEE J. Lightwave Technol. **27**, 706-717 (2009).

[84] J–S. Lee and C–S. Shim, "Bit-error-rate analysis of optically preamplified receivers using an eigenfunction expansion method in optical frequency domain," IEEE J. Lightwave Technol. **12**, 1224-1229 (1994).

[85] A. Mafi and S. Raghavan, "Nonlinear phase noise in optical communication systems using eigenfunction expansion method," Opt. Engineering **50**, 055003 (2011).

[86] C. W. Helstrom, "Approximate evaluation of detection probabilities in radar and optical communication," *IEEE Trans. Aerosp. Electron. Syst.* **14**, 630-640 (1978).

[87] A. Papoulis, *Probability, Random Variables, and Stochastic Processes* 3rd ed, (McGraw-Hill, New York, 1991).

[88] C. W. Helstrom, *Statistical Theory of Signal Detection* (Pergamon, New York, 1968).

[89] A. M. Mathai and S. B. Provost, *Quadratic Forms in Random Variables* (Marcel Dekker, New York, 1992).

[90] C. W. Helstrom, "Distribution of the Filtered Output of a Quadratic Rectifier Computed by Numberical Contour Integration," **IT-32**, 450-463 (1986).

[91] Matlab version R2016b, ODE45, `https://uk.mathworks.com/help/matlab/ref/ode45.html`.

Chapter 3

Mathematical Concepts Used in BER Calculation

3.1 Introduction

The nonlinearity would normally exist in the current waveguides and receivers, and even in the next-generation optical communication nextworks, which only allow for small bit-rate transmission. This suggests that neither traditional analytical approaches nor standard Monte-Carlo methods are suitable for BER calculation in the systems mentioned above. To date, some new BER calculation methods have been proposed to account for the influence of waveguide nonlinearity, noise and signal patterns. Specifically, these calculation mechanisms can be categorized into four types: (1) CW noise method. This method was initially proposed by Hui et al. [1], and only designed for the CW optical signals. Its main idea is to separate the noise amplification from nonlinear optical effects by using mathematical manipulation. (2) Covariance matrix method. This approach was originally raised by Holzlöehner et al. [2] for the BER estimation in a highly nonlinear optical system via linearization. (3) Receiver model. This numerical algorithm has been developed by Bosco et al. [3] and Forestieri et al. [4] for the calculation of BER in the optical pre-amplified receivers. (4) Multicanonical Monte Carlo method. This numerical scheme was firstly introduced by Berg et al. [5, 6], and is based on the efficient biased Monte Carlo simulations. In this chapter, several KLSE approaches will be presented to compute the BER for both single- and multi-channel optical systems. Specifically, these methods can be performed via the time-domain [7–9], frequency-domain [9–11] and Fourier-series routines [4]. A major advantage of

these KLSE methods is their capability of characterizing various factors that influence the system BER [12], e.g., waveguide nonlinearity.

This chapter is organized as follows. The mathematical formulation of the time-domain KLSE method designed for the CW signals will be introduced in Sec. 3.2. Similarly, Sec. 3.3 will describe another KLSE method for the evaluation of CW signals via the frequency domain. In addition, Sec. 3.4 will present the Fourier-series KLSE method for the analysis of all types of signal modulation formats. In the last section, a specific computational approach, denoted as the saddle-point approximation, will be introduced for the BER calculation. This algorithm is based on the moment-generating function (MGF) from Sec. 3.2, Sec. 3.3 and Sec. 3.4.

3.2 Time-domain Karhunen-Loève Expansion Method

The time-domain KLSE serves as an efficient approach to calculate the transmission BER at the back-end of the receiver. As mentioned earlier, this numerical approach is constructed only for the estimation of CW optical signals. According to the schematic of a single-channel OOK system shown in Fig. 2.10, a generic direct-detection receiver is composed of a Lorentzian optical filter with impulse response, $h_o(t)$, followed by an ideal photodetector and an integrate-and-dump electrical filter, whose impulse response is $h_e(t)$. However, the receiver configuration is more complicated for the PSK optical signals, with more details discussed in Sec. 7.3. Notably, the electrical noises of the receiver have not been taken into account, as in most cases the thermal and shot noises can be negligible in the systems where the white noise enhancement plays the dominant role in limiting the system performance [8, 13]. Moreover, in the WDM system (see Fig. 2.11) we assume that no additional statistical correlations among signal propagating in each channel are introduced during signal demultiplexing. For simplicity, the case of kth channel is selected to stand for both cases of single-channel and multi-channel system detection. Note also that this choice of kth channel representation is also made in the other two KLSE methods described in Sec 3.3 and Sec 3.4.

To start with, we present the complex envelope of the optical signal at the front of the kth receiver as $r_{1,k}(t) = S_k + a_{i,k}(t) + ja_{q,k}(t)$, where $a_{i,k}(t)$ and $a_{q,k}(t)$ are the in-phase and quadrature noise components, respectively, and S_k is the amplitude of the CW signal. We consider that $S_k = 0$ ($S_k^2 = P_k$) when a "0" ("1") is transmitted, where

P_k is the power of optical signals in the kth channel. Moreover, it is assumed that the carrier propagates unchanged through an optical filter, which amounts to $H_o(0) = 1$ with $H_o(f) = \mathscr{F}\{h_o(t)\}$. Hence, the signal after the optical filter can be written as, $r_{2,k}(t) = S_k + v_{i,k}(t) + jv_{q,k}(t)$, where $v_{\mu,k}(t) = h_o(t) \otimes a_{\mu,k}(t)(\mu = i,q)$. After passing through the ideal square-law photodetector and the electrical filter, the electrical signal, $y_k(t) = h_e(t) \otimes |r_{2,k}(t)|^2$, so that at the back-end of the receiver it is given by the following expression:

$$y_k(t) = \int_{-\infty}^{\infty} h_e(t) \left\{ \left[S_k + v_{i,k}(t-t') \right]^2 + v_{q,k}^2(t-t') \right\} dt'. \tag{3.1}$$

The noise components of kth channel at the output of the waveguide are assumed to be stationary and completely determined by their power spectral density matrix [14]:

$$\underline{\underline{\mathscr{G}}}_{a,k}(f) = \begin{pmatrix} \mathscr{G}_{a,k}^{i}(f) & \mathscr{G}_{a,k}^{iq}(f) \\ \mathscr{G}_{a,k}^{qi}(f) & \mathscr{G}_{a,k}^{q}(f) \end{pmatrix}, \tag{3.2}$$

where $\mathscr{G}_{a,k}^{i}$ and $\mathscr{G}_{a,k}^{q}$ are the power spectral densities of the in-phase and quadrature noise components from the kth channel, respectively; $\mathscr{G}_{a,k}^{iq}$ and $\mathscr{G}_{a,k}^{qi}$ symbolize the cross-spectral power density, obeying $\mathscr{G}_{a,k}^{iq} = \mathscr{G}_{a,k}^{qi}$. Note that even if at the input of the Si waveguide the in-phase and quadrature noise components are assumed to be uncorrelated, the mutual interaction mediated by the FCs and optical nonlinearity makes them to become correlated by the time they reach the back-end of the waveguide.

Upon passing through the optical filter, the power spectral density matrix of the noise, $\underline{\underline{\mathscr{G}}}_{v,k}(f)$, becomes [14]:

$$\underline{\underline{\mathscr{G}}}_{v,k}(f) = \underline{\underline{\mathscr{H}}}_{o}(f) \cdot \underline{\underline{\mathscr{G}}}_{a,k}(f) \cdot \underline{\underline{\mathscr{H}}}_{o}^{\dagger}(f), \tag{3.3}$$

where "$\dagger$" represents Hermitian conjugation operation. The real value optical filter matrix $\underline{\underline{\mathscr{H}}}_{o}$ is given by:

$$\underline{\underline{\mathscr{H}}}_{o} = \begin{pmatrix} H_o^{i}(f) & -H_o^{q}(f) \\ H_o^{q}(f) & H_o^{i}(f) \end{pmatrix}. \tag{3.4}$$

where $H_o^{i}(f) = \mathscr{F}\{h_o'(t)\}$ and $H_o^{q}(f) = \mathscr{F}\{h_o''(t)\}$ are the Fourier transform of the real

and imaginary parts of the optical filter impulse response, respectively.

Next, the signal, S_k, and both components of the noise, $v_{i,k}(t)$ and $v_{q,k}(t)$, are expanded in KLSE series. The deterministic functions, $\{\phi_\alpha^k(t)\}$ and $\{\psi_\alpha^k(t)\}$, will be defined in the expansions, and are both orthonormal to $h_e(t)$ [15]:

$$S_k = \sum_{\alpha \geq 1} s_\alpha^k \phi_\alpha^k(t), \tag{3.5a}$$

$$v_{i,k}(t) = \sum_{\alpha \geq 1} p_\alpha^k \phi_\alpha^k(t), \tag{3.5b}$$

$$v_{q,k}(t) = \sum_{\alpha \geq 1} q_\alpha^k \psi_\alpha^k(t), \tag{3.5c}$$

where the expansion coefficients, $\{s_\alpha^k\}$, $\{p_\alpha^k\}$ and $\{q_\alpha^k\}$, are random variables. By applying the orthonormality conditions,

$$\int_{-\infty}^{\infty} h_e(t)\phi_\alpha^k(t)\phi_\beta^{k,*}(t)dt = \delta_{\alpha\beta}, \tag{3.6a}$$

$$\int_{-\infty}^{\infty} h_e(t)\psi_\alpha^k(t)\psi_\beta^{k,*}(t)dt = \delta_{\alpha\beta}, \tag{3.6b}$$

these KLSE expansion coefficients can be proven to be in such forms:

$$s_\alpha^k = S_k \int_{-\infty}^{\infty} h_e(t)\phi_\alpha^{k,*}(t)dt, \tag{3.7a}$$

$$p_\alpha^k = \int_{-\infty}^{\infty} h_e(t)v_{i,k}(t)\phi_\alpha^{k,*}(t)dt, \tag{3.7b}$$

$$q_\alpha^k = \int_{-\infty}^{\infty} h_e(t)v_{q,k}(t)\psi_\alpha^{k,*}(t)dt. \tag{3.7c}$$

What follows is to combine Eqs. (3.1), (3.5) and (3.6) together and use the stationary condition of $v_{i,k}(t)$ and $v_{q,k}(t)$. Thus, the electrical signal can be rewritten as:

$$y_k = \sum_{\alpha \geq 1} |s_\alpha^k + p_\alpha^k|^2 + \sum_{\alpha \geq 1} |q_\alpha^k|^2. \tag{3.8}$$

This equation indicates the fact that the statistics of the electrical signal is completely determined by the probability distributions of the random variables $\{s_\alpha^k\}$, $\{p_\alpha^k\}$ and $\{q_\alpha^k\}$, which in turn are defined by the functions $\{\phi_\alpha^k(t)\}$ and $\{\psi_\alpha^k(t)\}$. Then our emphasis is shifted to compute $\{\phi_\alpha^k(t)\}$ and $\{\psi_\alpha^k(t)\}$. Importantly, the random variables $\{p_\alpha^k\}$ and $\{q_\alpha^k\}$ are mutually uncorrelated, namely, $\mathbb{E}\{p_\alpha^k p_\beta^{k,*}\} = \mu_\alpha^k \delta_{\alpha\beta}$

and $\mathbb{E}\{q_\alpha^k q_\beta^{k,*}\} = \nu_\alpha^k \delta_{\alpha\beta}$. By using simple mathematical manipulations, $\{\phi_\alpha^k(t)\}$ and $\{\psi_\alpha^k(t)\}$ are proven to be eigenfunctions of the second kind homogeneous Fredholm integral equations, with $\{\mu_\alpha^k\}$ and $\{\nu_\alpha^k\}$ to be the corresponding eigenvalues:

$$\int_{-\infty}^{\infty} h_e(\tau)\rho_i^k(t-\tau)\phi_\alpha^k(\tau)d\tau = \mu_\alpha^k \phi_\alpha^k(t), \tag{3.9a}$$

$$\int_{-\infty}^{\infty} h_e(\tau)\rho_q^k(t-\tau)\psi_\alpha^k(\tau)d\tau = \nu_\alpha^k \psi_\alpha^k(t). \tag{3.9b}$$

Here, $\rho_i^k(t)$ and $\rho_q^k(t)$ are the autocorrelation functions of the noise functions $v_{i,k}(t)$ and $v_{q,k}(t)$, respectively, which are symbolized by $\rho_i^k(t) = \mathscr{F}^{-1}\{\mathscr{G}_{v,k}^i\}$ and $\rho_q(t) = \mathscr{F}^{-1}\{\mathscr{G}_{v,k}^q\}$. In order to find numerical solutions for Eqs. (3.9), the Gauss-Hermite quadrature method (see Appendix. A) is employed to calculate the integrals. Simultaneously, the time variable t is discretized over the same grid points as the abscissas τ_l in the Gauss-Hermite quadrature method, namely, $t_l = \tau_l, l = 1,\ldots,M$. To this point, this problem is transferred to find the eigenvalues ($\{\mu_\alpha^k\}$, $\{\nu_\alpha^k\}$) and eigenfunctions ($\{\phi_\alpha^k(t_l)\}$, $\{\psi_\alpha^k(t_l)\}$) for the two resulted matrix. However, the in-phase and quadrature noise components turn to be correlated after propagation, $\mathbb{E}\{p_\alpha^k q_\beta^{k,*}\} \equiv \sigma_{\alpha\beta}^k \neq 0$. which should also be included in the computational analysis. Then, by performing mathematical operations on Eqs. (3.7), we can easily derive the following relation:

$$\int_{-\infty}^{\infty} h_e(t)h_e(\tau)\rho_{iq}^k(\tau-t)\psi_\beta^k(\tau)d\tau = \sum_{\alpha\geq 1} \sigma_{\alpha\beta}^k \phi_\alpha^k(t), \tag{3.10}$$

where $\rho_{iq}^k(t)$ stands for the cross correlation between $v_{i,k}(t)$ and $v_{q,k}(t)$, with the expression of $\rho_{iq}^k(t) = \mathscr{F}^{-1}\{\mathscr{G}_{v,k}^{iq}\}$. Similarly, the Gauss-Hermite quadrature technique is also operated on Eq. (3.10). By solving the resulted linearized equations, we can obtain the matrix $\{\sigma_{\alpha\beta}^k\}$. Hence, the complete form of the noise correlation matrix, $\underline{\underline{R}}^k$, can be derived after direct-detection:

$$\underline{\underline{R}}^k = \begin{pmatrix} \underline{\underline{\Lambda}}_\mu^k & \underline{\underline{\Sigma}}^k \\ \underline{\underline{\Sigma}}^{k,\dagger} & \underline{\underline{\Lambda}}_\nu^k \end{pmatrix}, \tag{3.11}$$

where $\underline{\underline{\Lambda}}_\mu^k = \mathrm{diag}(\mu_\alpha^k)$ and $\underline{\underline{\Lambda}}_\nu^k = \mathrm{diag}(\nu_\alpha^k)$ are diagonal matrices and $\underline{\underline{\Sigma}}_{\alpha\beta}^k = \sigma_{\alpha\beta}^k$.

The last step is to discretize the analytical formula mentioned above, in order

to derive the semi-analytical solution rigorously. First of all, after the optical filter, the complex noise is written as a column vector, $\underline{n_k} = [p_1^k \cdots p_M^k \; q_1^k \cdots q_M^k]^T$ (^{T} is the transpose operation, unless otherwise is specified), containing two random variables ($\{p_\alpha^k\}$ and $\{q_\alpha^k\}$). In the meanwhile, the signal is expressed as $\underline{s_k} = [s_1^k \cdots s_M^k \; 0 \cdots 0]^T$. Thus, the electrical current Eq. (3.8) can be written in a new form:

$$y_k = \underline{x_k}^\dagger \cdot \underline{x_k} = \sum_{\alpha=1}^{2M} |x_\alpha^k|^2, \tag{3.12}$$

where $\underline{x_k} = [x_1^k \cdots x_{2M}^k]^T \equiv \underline{n_k} + \underline{s_k}$. Note that the signal and the noise are uncorrelated, $\mathbb{E}\{n_\alpha^k s_\beta^{k,*}\} = 0$, and also $\mathbb{E}\{n_\alpha^k\} = 0$, $\forall \alpha, \beta = 1 \ldots 2M$. Secondly, a unitary matrix $\underline{\underline{U}}^k$ is used to diagonalize the correlation matrix $\underline{\underline{R}}^k$, obtaining an ideal diagonal matrix $\underline{\underline{\Delta}}^k = \mathrm{diag}(\delta_\alpha^k)$:

$$\underline{\underline{U}}^{k,\dagger} \; \underline{\underline{R}}^k \; \underline{\underline{U}}^k = \underline{\underline{\Delta}}^k, \tag{3.13}$$

where $\{\delta_\alpha^k\}(\alpha = 1 \ldots 2M)$ are the eigenvalues of $\underline{\underline{R}}^k$. Since the unitary matrix $\underline{\underline{U}}^k$ conserves to the norm of vectors, Eq. (3.12) can be recast into:

$$y_k = \underline{w_k}^\dagger \cdot \underline{w_k} = \sum_{\alpha=1}^{2M} |w_\alpha^k|^2, \tag{3.14}$$

where $\underline{w_k} = \underline{\underline{U}}^{k,\dagger} \underline{x_k}$. Then, the statistical properties of $\underline{w_k}$ can be easily obtained:

$$\mathbb{E}\{\underline{w_k}\} = \underline{\underline{U}}^{k,\dagger} \; \mathbb{E}\{\underline{n_k} + \underline{s_k}\} = \underline{\underline{U}}^{k,\dagger} \; \underline{s_k} \equiv \underline{\eta_k} = [\eta_1^k \cdots \eta_{2M}^k]^T, \tag{3.15a}$$

$$\mathbb{E}\{\underline{w_k} \cdot \underline{w_k}^\dagger\} = \underline{\underline{U}}^{k,\dagger} \; \mathbb{E}\{\underline{x_k} \cdot \underline{x_k}^\dagger\} \; \underline{\underline{U}}^k = \underline{\underline{U}}^{k,\dagger} \; \underline{\underline{R}}^k \; \underline{\underline{U}}^k = \underline{\underline{\Delta}}^k. \tag{3.15b}$$

From Eq. (3.15b), one can see that the noise correlation matrix $\{w_\alpha^k\}$ is diagonal. To calculate the BER, the MGF, $\Psi_{y_k}(\zeta)$, is calculated for the random variable y_k [16]:

$$\Psi_{y_k}(\zeta) = \mathbb{E}\{e^{-\zeta y_k}\} = \prod_{\alpha=1}^{2M} \frac{\exp\left(-\frac{|\eta_\alpha^k|^2 \zeta}{1+2\delta_\alpha^k \zeta}\right)}{\sqrt{1+2\delta_\alpha^k \zeta}}, \tag{3.16}$$

where δ_α^k are the eigenvalues of the correlation matrix, and η_α^k are the average values of y_k from Eq. (3.14). The detailed mathematical process of calculating the system BER

from the MGF will be described in Sec. 3.5.

3.3 Frequency-domain Karhunen-Loève Expansion

The frequency-domain KLSE method [11] is presented in this section, aiming at estimating the BER performance of Si photonic systems in a accurate and efficient way. This algorithm is only designed for the CW optical signals, in presence of the complex white noise. When compared with the time-domain method described in Sec 3.2, this method shows strength in its good transferability for more complicated optical systems. Here, the kth channel is selected to be the representative for both cases of single- and multi-channel detection.

Before proceeding to construct the mathematical models, the configuration of the direct-detection receiver is specified in the frequency domain: a lorentzian optical filter, $H_o(f)$, an ideal square-law photodetector and an integrate-and-dump electrical filter, $H_e(f)$. Particularly, $H_o(f)$ and $H_e(f)$ are the Fourier transform of $h_o(t)$ and $h_e(t)$, which are impulse response function of optical and electrical filters mentioned in Sec. 3.2. Here, $X_k(f)$ is defined as the Fourier transform of the receiver input signals $x_k(t)$. Therefore, the photocurrent at the output of the receiver can be written as:

$$y_k(t) = \int_{-\infty}^{\infty}\int_{-\infty}^{\infty} X_k^*(f_1)\underline{\underline{\mathscr{Q}}}(f_1,f_2)X_k(f_2)e^{2\pi j(f_2-f_1)t}df_1df_2 \tag{3.17}$$

where the Hermitian kernel $\underline{\underline{\mathscr{Q}}}$ represents the receiver functionalities, including an optical filter, an electrical filter and a photodetector, which is given by:

$$\underline{\underline{\mathscr{Q}}} = H_o^*(f_1)H_e(f_2-f_1)H_o(f_2), \tag{3.18}$$

As suggested in Sec. 3.2, the derivation of the MGF is indeed the fundamental part of the BER calculation when using the KLSE method. In order to determine the MGF of $y_k(t)$, the crucial step is to compute the correlation matrix $\underline{\underline{R}}^k$ in frequency domain. To fulfil this goal, we firstly discretize the Hermitian kernel and the electrical field with a step δf: $\underline{\underline{\tilde{\mathscr{Q}}}}_{m,n} = \underline{\underline{\mathscr{Q}}}(f_m,f_n)\delta f$, $\tilde{x}_{k,n} = X_k(f_n)e^{2\pi i f_n t}\sqrt{\delta f}$, where $f_m = m\delta f, f_n = n\delta f$ ($m,n = -Q,...,Q$, Q is a large integer). Thus, the Eq. (3.17) can be expressed in a new

form:

$$y_k(t) = \sum_{m,n=-Q}^{Q} \tilde{x}^*_{k,m}\, \underline{\underline{\tilde{\mathscr{D}}}}_{m,n}\, \tilde{x}_{k,n}, \tag{3.19}$$

Secondly, we recast the new electrical field $\tilde{x}_{k,n}$ into a real-value form: $\underline{x_k} = (\tilde{x}'_{k,-Q},...,\tilde{x}'_{k,Q},\tilde{x}''_{k,-Q},...,\tilde{x}''_{k,Q})^T$. In this dissertation, $'$ and $''$ denote the real and imaginary part of a physical variable, unless otherwise is specified. And the real-value receiver matrix is symbolized as $\underline{\underline{\mathscr{W}}} = [\underline{\tilde{\mathscr{D}}}', -\underline{\tilde{\mathscr{D}}}''; \underline{\tilde{\mathscr{D}}}'', \underline{\tilde{\mathscr{D}}}']$. Thus, the decision variable $y_k(t)$ can be written in the new form, $y_k(t) = \underline{x_k}^T \underline{\underline{\mathscr{W}}}\, \underline{x_k}$. Moreover, the optical signal at the input of the receiver is expressed as $x_k(t) = S_k + a_{i,k}(t) + ja_{q,k}(t)$, as mentioned in Sec 3.2. Then, the Fourier transform of the noise $a_{i,k} + ja_{q,k}$ is denoted as $\tilde{A}_{RI} = (\tilde{A}_R, \tilde{A}_I)^T$, where $\tilde{A}_R$ and $\tilde{A}_I$ are real. The Fourier transform of $a_{i,k}$ and $a_{q,k}$ are given by $\check{A}_R$ and $\check{A}_I$, respectively, forming a new complex variable $\check{A}_{RI} = (\check{A}_R, \check{A}_I)^T$. More details about $\tilde{A}_{RI}$ and $\check{A}_{RI}$ can be found in [11]. It can be proved mathematically that the power spectral density matrix $\check{S}_{kk}$ of noise can be expressed in such form:

$$\check{S}_{kk}(z,\omega) = \left\langle \check{A}_{RI}\,(z,\omega)\check{A}_{RI}(z,\omega)^\dagger \right\rangle, \tag{3.20}$$

Note that $\check{S}_{kk}$ obeys such symmetric properties: $\check{S}^\dagger_{kk}(z,\omega) = \check{S}_{kk}(z,\omega)$, $\check{S}^*_{kk}(z,\omega) = \check{S}_{kk}(z,-\omega)$. Regarding the new noise form, $\tilde{A}^{\pm}_{RI} = [\tilde{A}_R(\omega), \tilde{A}_R(-\omega), \tilde{A}_I(\omega), \tilde{A}_I(-\omega)]^T$, the cross correlation matrix is derived mathematically:

$$\mathscr{F}_k(\omega) = \langle \tilde{A}^{\pm}_{RI}\, \tilde{A}^{\pm T}_{RI} \rangle = \begin{pmatrix} s^+ & t \\ t & s^- \end{pmatrix}, \tag{3.21}$$

where $s^{\pm} = \check{S}^{11}_{kk}(\omega)\frac{1\pm\sigma_1}{2} + \check{S}^{22}_{kk}(\omega)\frac{1\mp\sigma_1}{2} + Im[\check{S}^{12}_{kk}(\omega)]\sigma_3$, $t = Re[\check{S}^{12}_{kk}(\omega)]\sigma_1$. Here, σ_1, σ_2 and σ_3 stand for 2×2 Pauli matrices. Due to the symmetry properties of $\check{S}_{kk}$, we only need to calculate the elements of Eq. (3.21) with $\omega \geq 0$. To this end, the correlation matrix $\underline{\underline{R}}^k$ can be obtained by using mathematical manipulation of $\mathscr{F}_k$, according to relation listed below:

$$\left(\underline{\underline{R}}^k\right)_{\rho_a,\rho_b} = (\mathscr{F}_k)_{ab|\omega=2\pi f_n}$$

$$\rho_a = (1+n, 2Q+1-n, 2Q+2+n, 4Q+2-n),$$

$$\begin{aligned} n &= 0,...,2Q, \\ a,b &= 1,...,4 \end{aligned} \tag{3.22}$$

Furthermore, the Cholesky factorization is utilized to decompose the correlation matrix $\underline{\underline{R}}^k$ in form of a lower triangular matrix $\underline{\underline{\mathscr{L}}}$, i.e., $\underline{\underline{R}}^k = \underline{\underline{\mathscr{L}}}\,\underline{\underline{\mathscr{L}}}^T$. To diagonalize the real symmetric matrix $\underline{\underline{\mathscr{L}}}^T\,\underline{\underline{\mathscr{W}}}\,\underline{\underline{\mathscr{L}}}$, an orthogonal matrix $\underline{\underline{\mathscr{U}}}$ is used to obtain eigenfunctions and eigenvalues:

$$(\underline{\underline{\mathscr{U}}}^T\,\underline{\underline{\mathscr{L}}}^T\,\underline{\underline{\mathscr{W}}}\,\underline{\underline{\mathscr{L}}}\,\underline{\underline{\mathscr{U}}})_{p,q} = \underline{\underline{\Lambda}} \tag{3.23}$$

where $\underline{\underline{\Lambda}} = diag(\lambda_1,...,\lambda_{4Q+2})$, with λ_p $(p = 1,...,4Q+2)$ real value. Moreover, the total electric field $\underline{x_k}$ is composed of signal $\underline{s_k}$ and noise $\underline{n_k}$, where $\langle \underline{n_k} \rangle = 0$ and $\langle \underline{x_k} \rangle = \underline{s_k}$. Thus, according to Eq. (3.23), the new signal and noise elements can be obtained:

$$z_k = \underline{\underline{\mathscr{U}}}^T\,\underline{\underline{\mathscr{L}}}^{-1}(\underline{x_k} - \underline{s_k}), \tag{3.24a}$$

$$\zeta_k = \underline{\underline{\mathscr{U}}}^T\,\underline{\underline{\mathscr{L}}}^{-1}\underline{s_k}, \tag{3.24b}$$

Hence, the decision variable $i_k(t)$ can be rewritten in a simple form:

$$y_k(t) = \sum_{n=1}^{4Q+2} \lambda_n (z_{k,n} + \zeta_{k,n})^2, \tag{3.25}$$

Therefore, by combining the analysis towards the signal $\bar{s}_k$, the noise $\bar{n}_k$, the shift variable ζ_k, the decision variable $y_k(t)$ and the correlation matrix $\underline{\underline{R}}^k$, the MGF in frequency domain, $\Psi_{y_k}(s)$, is obtained:

$$\Psi_{y_k}(s) = \prod_{n=1}^{4Q+2} \frac{\exp\left(\frac{\lambda_n |\zeta_{k,n}|^2 s}{\sqrt{1-2\lambda_n s}}\right)}{\sqrt{1-2\lambda_n s}}, \tag{3.26}$$

In the end, the system BER can be computed by applying the mathematical technique introduced in Sec. 3.5 on Eq. (3.26).

3.4 Fourier-series Karhunen-Loève Expansion

The Fourier-series KLSE approach [4] is described in this section to quantify the system BER after the direct-detection receivers. As a complementary, the perturbation theory is first used to characterize the transmission matrix and further the noise correlation matrix in the central channel of single- and multi-channel transmission systems. In this section, we select the kth channel to be the central channel, and carry out the BER calculation in the kth channel to represent both single- and multi-channel systems. Specifically, the central channel refers to the kth channel for the $\bar{M}$-channel photonic systems, where $k = \bar{M}/2$ when $\bar{M}$ is an even integer, or $k = (\bar{M}-1)/2$ when $\bar{M}$ is odd. As for the single-channel systems, the central channel is itself.

Before we describe the mathematical approach for system BER calculation, we present the perturbation theory used to determine the noise dynamics in Si waveguides. To this end, we express the complex envelope of the optical field at the input of the waveguide as $x_k(t) = s_k(t) + w_k(t)$, where $s_k(t) = \langle x_k(t) \rangle$ represents the noise-free signal and $w_k(t)$ is the complex additive white Gaussian noise. Here, the symbol $\langle \cdot \rangle$ denotes the statistical expectation operator. Furthermore, the noise w_k is expanded in Fourier series, namely, $w_k = \sum_{l=-N/2}^{N/2-1} n_{l,k} e^{j\Omega_l t}$, where $\Omega_l = 2\pi l/T_{tot}$ and $T_{tot} = N_{tot} T_0$, with N_{tot} being the total number of transmitted bits. Then, a $(4Q+2)$-dimensional noise Fourier vector is defined as, $\underline{w_k} = (n'_{-Q,k}, \ldots, n'_{Q,k}, n''_{-Q,k}, ..., n''_{Q,k})^T$, where x^T denotes the transpose of x. Importantly, in order to reduce the computational time, Q is chosen such that $2Q+1$ is more than 100 times smaller than N. The reason why this is a valid choice is that most of the information pertaining to the noise can be collected from the central part of the spectra.

The next step of the algorithm is to calculate the noise covariance matrix, $\underline{\underline{R}}^k = \left\langle \underline{w_k}\, \underline{w_k}^T \right\rangle$, at the output of the waveguide. This can be expressed in terms of $\underline{\underline{R}}^k(0)$ as:

$$\underline{\underline{R}}^k(L) = \underline{\underline{\mathscr{R}}}\, \underline{\underline{R}}^k(0)\, \underline{\underline{\mathscr{R}}}^T, \tag{3.27}$$

where $\underline{\underline{\mathscr{R}}}$ is the transmission matrix of the Si waveguide. To calculate $\underline{\underline{R}}^k(L)$, it is necessary to compute first $\underline{\underline{\mathscr{R}}}$. To this end, we perturb the input noise-free optical signal, $s^0(t,0)$, by a small amount proportional to the β-th frequency mode, $\Delta e^{j\Omega_{\beta-Q-1}t}$, with

$\beta = 1,\ldots,(2Q+1)$ and Δ a small quantity. This perturbed optical signal,

$$s^{\beta}(t,0) = s^{0}(t,0) + \Delta e^{j\Omega_{\beta-Q-1}t}, \tag{3.28}$$

is then launched into the waveguide. By numerically solving Eq. (2.15), we compute the corresponding optical signal at the back-end of the waveguide, denoted as $s^{\beta}(t,L)$. We then calculate the Fourier coefficients vector, $\underline{w}^{\beta}$, of the difference $\delta s^{\beta}(t) = s^{\beta}(t,L) - s^{0}(t,L)$ and subsequently the matrix elements $\underline{\underline{\mathscr{R}}}_{\alpha\beta}$ of the transmission matrix via the relation:

$$\underline{\underline{\mathscr{R}}}_{\alpha\beta} = \underline{w}_{\alpha}^{\beta}/\Delta, \tag{3.29}$$

where $\alpha = 1,\ldots,(4Q+2)$. In these calculations, Δ is chosen to be a real positive number when $\alpha \leq (2Q+1)$ and an imaginary number with $\Delta'' > 0$ if $\alpha > (2Q+1)$. Finally, the $(4Q+2)\times(2Q+1)$ complex transmission matrix $\underline{\underline{\mathscr{R}}}$ is extended to a $(4Q+2)\times(4Q+2)$ real matrix defined as $\underline{\underline{\tilde{\mathscr{R}}}} = [\underline{\underline{\mathscr{R}}}', \underline{\underline{\mathscr{R}}}'']$.

Following this procedure, the noise covariance matrix $\underline{\underline{\mathscr{G}}}(L)$ can be determined using Eq. (3.27), since the matrix $\underline{\underline{\mathscr{G}}}(0)$ can be calculated directly from the input noise. Once the noise correlation matrix at the output of the Si waveguide has been calculated, the Fourier-series KLSE is applied to compute the BER at the back-end of the direct-detection receiver. Similar to the frequency-domain method presented in Sec. 3.3, the first step of the Fourier-series KLSE is based on Eqs. (3.17), where $X_k(f)$ is the Fourier transform of the signals at the input of the receiver and the Hermitian kernel is given by $\underline{\underline{\mathscr{Q}}}(f_1,f_2) = H_o^*(f_1)H_e(f_2-f_1)H_o(f_2)$. Then, we define the real receiver matrix as $\underline{\underline{\mathscr{W}}} = [\underline{\underline{\mathscr{Q}}}', -\underline{\underline{\mathscr{Q}}}''; \underline{\underline{\mathscr{Q}}}'', \underline{\underline{\mathscr{Q}}}']$.

We now move to the main part of this algorithm, that is we compute the MGF of $y(t)$. To begin with, we use the Cholesky factorization to decompose the covariance matrix as $\underline{\underline{R}}^{k} = \underline{\underline{\mathscr{L}}}\,\underline{\underline{\mathscr{L}}}^{T}$, where $\underline{\underline{\mathscr{L}}}$ is a lower-triangular matrix. For the sake of simplicity, we introduce a real symmetric matrix, $\underline{\underline{\mathscr{L}}}^{T}\underline{\underline{\mathscr{W}}}\,\underline{\underline{\mathscr{L}}}$, which contains all the information about the receiver matrix and the correlation matrix, and diagonalize this newly introduced matrix via an orthogonal matrix, $\underline{\underline{\mathscr{U}}}$ [11]:

$$\underline{\underline{\mathscr{U}}}^{T}\,\underline{\underline{\mathscr{L}}}^{T}\,\underline{\underline{\mathscr{W}}}\,\underline{\underline{\mathscr{L}}}\,\underline{\underline{\mathscr{U}}} = \Sigma, \tag{3.30}$$

where $\Sigma = \mathrm{diag}(\sigma_1, \ldots, \sigma_{4Q+2})$ is a real-valued matrix. Since the receiver and noise are characterized in the frequency domain, we describe the noise-free signal, $s_k^0(t)$, after propagation in the waveguide in the frequency domain, too. Thus, we expand in Fourier series $s_k^0(t)$ taken in the interval $[t_0 - T_0/2, t_0 + T_0/2]$, with t_0 an arbitrary time,

$$s_k^0(t) = \sum_{p=-\infty}^{\infty} \tilde{s}_{p,k}\, e^{j2\pi pt/T_0},\ t_0 - T_0/2 < t < t_0 + T_0/2 \tag{3.31}$$

and define a $(2Q+1)$-dimensional column-vector, $\underline{\bar{s}}_q$, associated with the noise-free signal Fourier coefficients $\{\tilde{s}_p\}$ at the time spot t_q [9]:

$$\underline{\bar{s}}_{p,q} = \tilde{s}_{p-Q-1,k}\, e^{j2\pi(p-Mo-1)t_q/T_0},\ p = 1, \ldots, 2Q+1 \tag{3.32}$$

This $(2Q+1)$-dimensional complex-valued vector is extended to a $(4Q+2)$-dimensional real-valued vector by separating the real and imaginary parts, that is $\underline{\tilde{s}}_q = [\underline{\bar{s}}_q{}', \underline{\bar{s}}_q{}'']^T$. With these definitions, the transformed signal is given by:

$$\chi_q = \underline{\underline{\mathscr{U}}}^T\, \underline{\underline{\mathscr{L}}}^{-1}\, \underline{\tilde{s}}_q. \tag{3.33}$$

This transformed signal and the matrix Σ are then used to calculate the MGF of $y_k(t)$ using the following formula:

$$\Psi_{y_k}(s) = \prod_{p=1}^{4Q+2} \frac{\exp\left(\frac{\sigma_p |\chi_q|^2 s}{\sqrt{1-2\sigma_p s}}\right)}{\sqrt{1-2\sigma_p s}}. \tag{3.34}$$

Importantly, we set the detection clock time, t_q, at the middle of each bit interval, which is also the place where the peak pulse is located. Finally, by applying the saddle-points approximation that will be introduced in Sec. 3.5, the BER contributions of a "0" bit and a "1" bit can be calculated in a rigorous and efficient way.

3.5 Saddle-point Approximation Approach for Probability Density Function Calculation

The saddlepoint approximation method is a mathematical technique that evaluates the integral of the MGF in the complex plane, in order to derive the probability density

function (PDF) of a distribution with great accuracy. It was originally proposed by Daniels [17], and successive research of this method has been carried out intensively, in aspects of the extensions and applications [12, 18–20]. In this section, the mathematical description of the saddle-point approximation approach in the BER calculation will be presented. Considering the difference of the MGF between Eq. (3.16) (time-domain KLSE method) and Eq. (3.26) (frequency-domain KLSE method) and Eq. (3.34) (Fourier-series KLSE method), the strategy of mathematical description here is to first provide semi-analytical solutions for BER derived from Eq. (3.16), and then make a complementary for BER calculated from the other two MGFs (Eq. (3.26) and Eq. (3.34)). Note also the kth channel is the selected to represent the cases of single- and multi-channel BER detection in this section. To start with, we use the following relation to derive the system BER calculation:

$$\mathscr{P} = \frac{1}{2}\left[\mathscr{P}(y_k > y_{th,k}|S_k = 0) + \mathscr{P}(y_k < y_{th,k}|S_k = \sqrt{P_k})\right], \tag{3.35}$$

where the first (second) term represents the probability for an error to occur when a "0" ("1") bit is transmitted in the kth channel and $y_{th,k}$ is the decision threshold. Then the PDF $\mathscr{P}_{y_k}(t)$ can be calculated by applying the Riemann-Fourier inversion formula on the MGF $\Psi_{y_k}(\zeta)$

$$\mathscr{P}_{y_k}(t) = \int_{\zeta_0 - j\infty}^{\zeta_0 + j\infty} \frac{\Psi_{y_k}(\zeta)}{2\pi j\zeta}\, e^{\zeta t} d\zeta \tag{3.36}$$

Then, the explicit expressions of the probabilities for signal "1" and signal "0" can be acquired for the MGF of Eq.(3.16) [21]:

$$\mathscr{P}(y_k > y_{th,k}|S_k = 0) = -\int_{-|\zeta_0|-\infty}^{-|\zeta_0|+\infty} \frac{\Psi_{y_k}(\zeta|S_k = 0)}{2\pi j\zeta}\, e^{\zeta y_{th,k}} d\zeta, \tag{3.37a}$$

$$\mathscr{P}(y_k < y_{th,k}|S_k = \sqrt{P_k}) = \int_{|\zeta_0|-\infty}^{|\zeta_0|+\infty} \frac{\Psi_{y_k}(\zeta|S_k = \sqrt{P_k})}{2\pi j\zeta}\, e^{\zeta y_{th,k}} d\zeta, \tag{3.37b}$$

where ζ_0 is a real constant that defines the integration path in the complex plane, ζ. Importantly, by employing the saddle-point approximation, the simpler mathematical

formulae for the probabilities are obtained [9]:

$$\mathscr{P}(y_k > y_{th,k}|S_k = 0) = \frac{\exp[\Phi_{y_k}(s_o^-)]}{\sqrt{2\pi\Phi''_{i_k}(s_o^-)}}, \tag{3.38a}$$

$$\mathscr{P}(y_k < y_{th,k}|S_k = \sqrt{P_k}) = \frac{\exp[\Phi_{y_k}(s_o^+)]}{\sqrt{2\pi\Phi''_{y_k}(s_o^+)}}, \tag{3.38b}$$

where Φ''_{y_k} denotes as the second-order derivative of the phase function Φ_{y_k}, whose mathematical formula is given by:

$$\Phi_{y_k}(s) = ln\left[\Psi_{y_k}(s)\frac{\exp(y_{th,k}s)}{|s|}\right], \quad s \in \mathscr{R} \tag{3.39}$$

where s_o^+ and s_o^- correspond to the positive and negative saddle points on the real s axis of $\exp[\Phi_{y_k}(s)]$. And their values can be calculated by minimizing $\exp[\Phi_{y_k}(s)]$, with this process numerically solved by using the Golden Section Algorithm. More details about this algorithm is presented in Appendix C.

Similar mathematical expressions of the PDFs can also be derived by using the Riemann-Fourier inversion on the MGFs of Eq. (3.26) and Eq. (3.34), which correspond to the frequency-domain and Fourier-series KLSE methods, respectively:

$$\mathscr{P}(y_k > y_{th,k}|S_k = 0) = -\int_{|\zeta_0|-\infty}^{|\zeta_0|+\infty} \frac{\Psi_{y_k}(\zeta|S_k = 0)}{2\pi j\zeta}\, e^{-\zeta y_{th,k}} d\zeta, \tag{3.40a}$$

$$\mathscr{P}(y_k < y_{th,k}|S_k = \sqrt{P_k}) = \int_{-|\zeta_0|-\infty}^{-|\zeta_0|+\infty} \frac{\Psi_{y_k}(\zeta|S_k = \sqrt{P_k})}{2\pi j\zeta}\, e^{-\zeta y_{th,k}} d\zeta, \tag{3.40b}$$

And by applying the saddle-point approximation, these formula of the PDFs can be simplified as:

$$\mathscr{P}(y_k > y_{th,k}|S_k = 0) = \frac{\exp[\Phi_{y_k}(s_o^+)]}{\sqrt{2\pi\Phi''_{i_k}(s_o^+)}}, \tag{3.41a}$$

$$\mathscr{P}(y_k < y_{th,k}|S_k = \sqrt{P_k}) = \frac{\exp[\Phi_{y_k}(s_o^-)]}{\sqrt{2\pi\Phi''_{y_k}(s_o^-)}}, \tag{3.41b}$$

where the phase function Φ_{y_k} has a different analytical expression:

$$\Phi_{y_k}(s) = ln\left[\Psi_{y_k}(s)\frac{\exp(-y_{th,k}s)}{|s|}\right], \quad s \in \mathscr{R} \tag{3.42}$$

It is obvious that the value of saddle points (s_o) changes from negative to positive, when the method that measures the PDF for signal "0" switches from the time-domain KLSE to the frequency-domain and Fourier-series KLSE. And a similar situation can observed in the case of signal "1". This is caused by the sign of eigenvalues in the square-root term of Eq. (3.16), Eq. (3.26) and Eq. (3.34), but will not affect the computational accuracy and efficiency of these KLSE approaches.

Bibliography

[1] R. Hui, D. Chowdhury, M. Newhouse, M. O'Sullivan, and M. Pettcker, "Nonliear amplification of noise in fibers with dispersion and its imipact in optical amplified systems," IEEE Photon. Technol. Lett. **9**, 392-394 (1997).

[2] R. Holzl*o*hner, V. S. Grigoryan, C. R. Menyuk, and W. L. Kath, "Accurate calculation of eye diagrams and bit error rates in optical transmission systems using linearization," IEEE J. Lightwave Technol. **20**, 389-400 (2002).

[3] G. Bosco, A. Carena, V. Curri, R. Gaudino, P. Poggiolini, and S. Benedetto, "A novel analytical method for the BER evaluation in optical systems affected by parametric gain," IEEE Photon. Technol. Lett. **12**, 152-154 (2000).

[4] E. Forestieri, "Evaluating the error probability in lightwave systems with chromatic dispersion, arbitrary pulse shape and pre- and postdetection filtering," IEEE J. Lightwave Technol. **18**, 1498-1503 (2000).

[5] B. A. Berg and T. Neuhaus, "Multicanonical ensemble: A new approach to simulate first-order phase transitions," Phys. Rev. Lett. **68**, 9-12 (1992).

[6] B. A. Berg , "Algorithmic aspects of multicanonical Monte Carlo simulations," Nucl. Phys. Proc. Suppl. **63**, 982-984 (1998).

[7] J. You, and N. C. Panoiu, "Calculation of Bit Error Rates in Optical Systems with Silicon Photonic Wires," IEEE J. Quantum Electron. **51**, 8400108 (2015).

[8] G. Bosco, A. Carena, V. Curri, R. Gaudino, P. Poggiolini, and S. Benedetto, "A novel analytical approach to the evaluation of the impact of fiber parametric gain on the bit error rate," IEEE Trans. Commun. **49**, 2154-2163 (2001).

[9] E. Forestieri and M. Secondini, "On the Error Probability Evaluation in Lightwave Systems With Optical Amplification," IEEE J. Lightwave Technol. **27**, 706-717 (2009).

[10] J–S. Lee and C–S. Shim, "Bit-error-rate analysis of optically preamplified receivers using an eigenfunction expansion method in optical frequency domain," IEEE J. Lightwave Technol. **12**, 1224-1229 (1994).

[11] A. Mafi and S. Raghavan, "Nonlinear phase noise in optical communication systems using eigenfunction expansion method," Opt. Engineering **50**, 055003 (2011).

[12] C. W. Helstrom, "Approximate evaluation of detection probabilities in radar and optical communication," IEEE Trans. Aerosp. Electron. Syst. **14**, 630-640 (1978).

[13] A. Carena, V. Curri, R. Gaudino, P. Poggiolini, and S. Benedetto, "New Analytical Results on Fiber Parametric Gain and Its Effects on ASE Noise," IEEE Photon. Technol. Lett. **9**, 535-537 (1997).

[14] A. Papoulis, *Probability, Random Variables, and Stochastic Processes* 3rd ed, (McGraw-Hill, New York, 1991).

[15] C. W. Helstrom, *Statistical Theory of Signal Detection* (Pergamon, New York, 1968).

[16] A. M. Mathai and S. B. Provost, *Quadratic Forms in Random Variables* (Marcel Dekker, New York, 1992).

[17] H. E. Daniels, "Saddlepoint Approximations in Statistics," Ann. Math. Statist. **25**, 631-650 (1954).

[18] S. O. Rice, "Uniform asymptotic expansions for saddle point integrals-Application to a probability distribution occurring in noise theory," Bell Syst. Tech J. **47**, 1971-2013 (1968).

[19] L. Wang, "Numerical Calculation of cumulative probability from the moment-generating function," Proc. IEEE **60**, 1452-1453 (1972).

[20] C. W. Helstrom and J. A. Ritcey, "Evaluating radar detection probabilities by steepest descent integrationi," IEEE Trans. Aerosp. Electron. Syst. **20**, 624-634 (1984).

[21] C. W. Helstrom, "Distribution of the Filtered Output of a Quadratic Rectifier Computed by Numberical Contour Integration," ***IT-32**, 450-463 (1986).*

Chapter 4

Numerical Implementation of Main Computational Methods

4.1 Introduction

The numerical implementation of the complete system evaluation models will be described in this chapter. It is a Matlab tool [1] based on the signal propagation theory in Sec. 2 and the BER calculation approaches in Sec. 3. This numerical tool can support accurate modeling for Si-based photonic systems, accounting for single- and multi-wavelength propagation, various signal modulation formats and different types of Si waveguides.

The optical signal propagation simulators are essential parts in the characterization and design of optical waveguides and other optical devices. A number of numerical algorithms have been developed for the signal propagation. There are two big branches: the first branch is based on the time-domain methods, whose representatives are the SSFM [2], the FEM [3], and the Finite-Difference Time-Domain Method [4]; the other branch is built in the frequency domain, including the Eigenmode Expansion Method [5], the Transfer Matrix Method [6], and the Beam Propagation Method [7]. Among these algorithms, the SSFM is such a straightforward routine that can be easily implemented in numerical codes, and incorporating all the essential linear and nonlinear optical effects within the optical waveguides. The currently available SSFM softwares comprise the Nonlinear Schrödinger Equation Solver [2], the OptSim by Rsoft [8] and SSPROP [9]. Even though they are of high reliability, these SSFM softwares are developed only for optical fibers.

Furthermore, regarding the performance evaluation (i.e., BER, eye-diagrams) of optical systems, a number of ready-to-use softwares have been developed in the last two decades. The freely available software like SIMFOCS [10], and the commercial softwares, such as OptSim by Rsoft [11]and PHOTOSS [12], can all provide accurate system evaluation, which are extremely useful for the construction and characterization of the optical networks in practice. However, some of these tools are designed for optical fibers, and may not provide platforms for users to customize the types of optical waveguides and modify the underlying computational routines. On the other hand, what is appealing about the self-developed numerical routine is that it can not only provide full access to the original codes, but also flexibility and extendability to include more complicated optical systems.

The rest of this chapter is organized as follows. Sec. 4.2 presents the program flow of the system analysis model and discuss the details of its numerical implementation. Additionally, several specific numerical algorithms and their correlation with the mathematical formulae will be explained in Sec. 4.3. In the last section, the key features of this numerical tool for Si photonic systems will be summarized.

4.2 Program Flow for System Analysis Models

The goal of the computational tool presented in this dissertation is to facilitate the design and optimization of different optical waveguides, waveguide-based devices and sophisticated optical systems. In the process of constructing this numerical engine, the mathematical algorithms and numerical parameters are needed to be carefully selected, in order to ensure the computational precision and reliability. In this section, the architecture of this theoretical and numerical tool will be described.

According to the program flow shown in Fig. 4.1, every simulation towards the performance analysis encompasses the following main steps, namely, simulation setup, system evaluation and output. To be more specific, the first step is of great importance but relatively simple, because it is supposed to guarantee the accuracy of the simulated results by initializing all the essential parameters. As for the third step, the results are programmed to generated automatically. Furthermore, the key part of the whole computational process is the second step, which comprises the modules of the preparation engine, the propagation simulator and the BER calculator. Notably, the

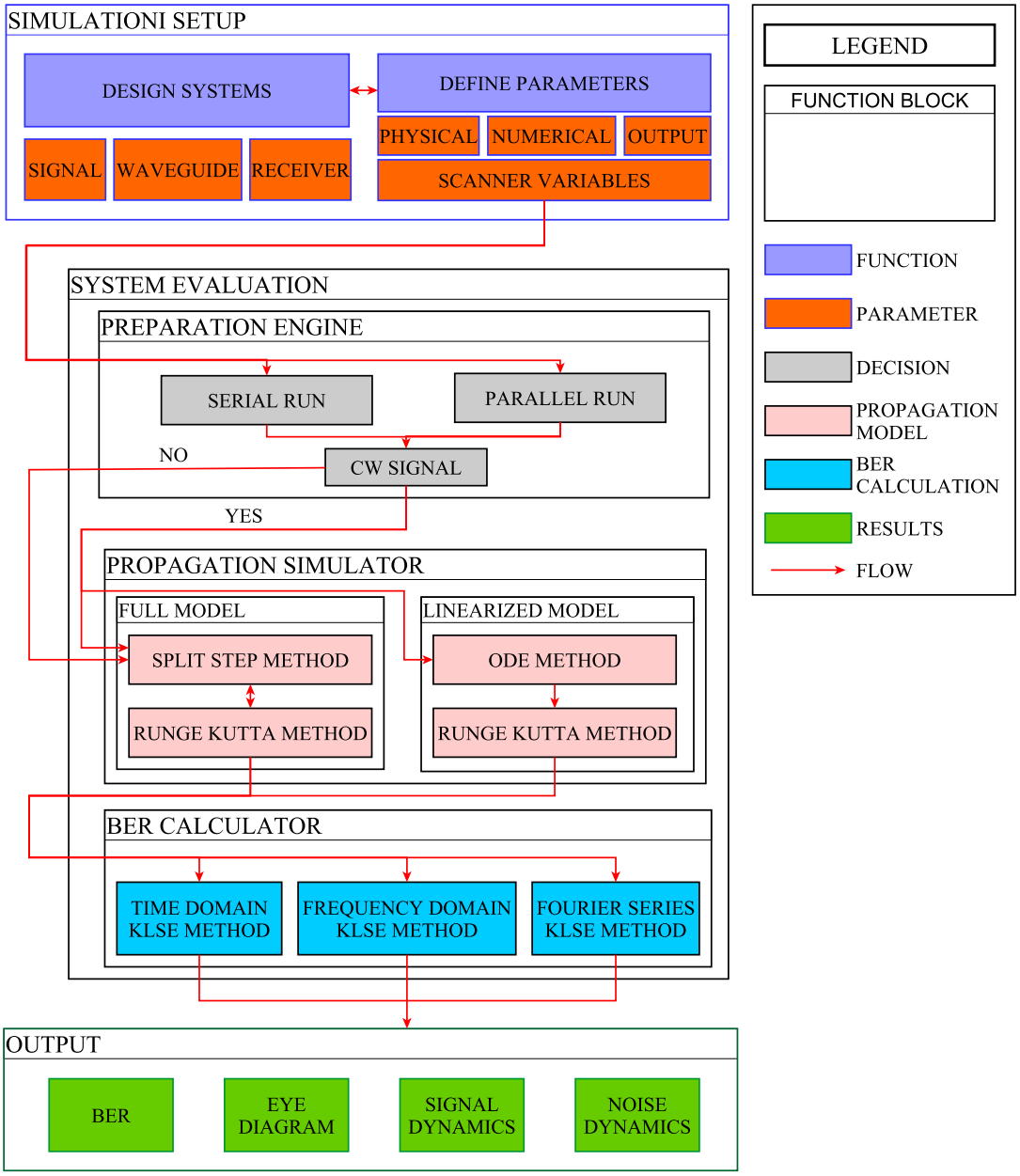

Figure 4.1: Program flow of the system evaluation model.

method of error counting is not used to verify the BER results calculated via the KLSE approaches, since this method is extremely time-consuming and subsequently makes itself infeasible especially at larger values of BER. However, the verification tests regarding BERs have been carried out, with more details described in Sec. 4.3.6. In the following paragraphs, the thorough computational procedures of this implementation will be presented.

In the first step, the initial conditions of the whole simulation process are prepared, including the specific components of a Si photonic system and the simulation parame-

ters. To start with, a photonic system can be constructed by defining several groups of physical parameters illustrated in the first stage of Fig. 4.1: (1) Optical signal parameters. Generally, the signal modulation formats, the central carrier frequency, the signal power and the bit sequence pattern, as well as the white noise, all have to be properly selected in order to fulfill the research purpose; (2) Waveguides optical parameters and dimensions. In particular, the dispersion and nonlinear coefficients of Si waveguides are required to be calculated. In this dissertation, we obtain the waveguide parameters of Si-PhWs and Si-PhCWs by using Femsim by Rsoft [13] and MIT Photonic Bands (MPB) [14], respectively; (3) Receiver schematics. The mathematical expressions will be given for the direct-detection optical receiver, which contains an band-pass optical filter, an ideal photodetector and a low-pass electrical filter. As for a $\bar{M}$-channel system, the $\bar{M}$ sets of optical filters, photodetectors and electrical filters, as well as a demultiplexer are used in the direct-detection.

Another significant aspect of the simulation setup is the numerical parameters. Basically, they can be divided into the following groups according to different numerical algorithms: (1) the temporal sampling points (or FFT points), the distance step and the time window for the SSFM method and the ODE model; (2) the Cash-Karp parameters [15] and Dormand-Prince parameters [16] for the fifth-order Runge-Kutta method (see Appendix. B); (3) the temporal sampling points, bit-rate (or bit interval), weights and abscissas of Gaussian-Hermite rule for the time-domain KLSE method; (4) the number of frequency points for both the frequency-domain and Fourier-series KLSE methods. Moreover, the output parameters determines the types of results. Apart from the essential simulation parameters, we also define the scanner variables. One or more input parameters can be automatically scanned in the simulation process, such as the signal power, the pulsewidth, the bit-rate and the waveguide length. Notably, the numerical parameters are not suggested to be scanned. Since the computational accuracy can only be ensured by choosing suitable values of these parameters, there is no point to continue the simulation if this condition can not be satisfied. Importantly, the values of all the relevant parameters are given in Sec. 4.3.6.

Moving on now to consider the core of the numerical scheme – the system evaluation. The system evaluation process is composed of three stages. In particular, the first stage is the preparation engine. In this stage, two decision operations will be per-

formed: one is to choose the types of simulators (or *run*s), i.e., the *serial run* and the *parallel run*; the other is to identify the shape of the optical signals, namely, CW and pulse. To be more specific, the *parallel run* is often employed in the variable scanning, in order to speed up the whole computational process. The *parallel run* refers to the Matlab built-in function $parfor$ [17], where these simulations will be treated as independent tasks and then a specific number of tasks will be performed simultaneously. Additionally, the *serial run* is adopted in the single simulation operation or the case where the computational environment (e.g, a single processor) can not support parallel operations. Furthermore, the shape of optical signals decides a specific numerical routine used in the propagation section, which will be demonstrated in the next stage.

The second stage of the system evaluation engine is the propagation simulator. Take the case of single-wavelength propagation for instance. Firstly, the optical signals of Eqs. (2.6) will be placed at the input of Si waveguides. Then, the semi-analytical solutions regarding the output signals can be derived by using either the full propagation algorithm (Eqs. (2.15) and (2.20)) or the linearized version (Eqs. (2.26) and (2.27)). Precisely, both types of simulators can be selected for the CW signals (u_{OOK}, u_{PSK}), whereas only the first simulator is capable of simulating the pulsed signal (u_G). In case of the multi-wavelength co-propagation, the analysis is carried out by first extracting the mathematical expression for signals in each channel (e.g., Eq. (2.28)), and then modifying the single-channel numerical routines to the multi-channel case by using Eqs. (2.21) and Eqs. (2.30), (2.31), respectively. Therefore, the explicit numerical implementation details for full and linearized propagation models will be presented in Sec. 4.3.1 and Sec. 4.3.2, respectively.

Another important stage is the BER calculator. From Fig. 4.1, we can see that the time-domain, frequency-domain and Fourier-series KLSE calculators are available in the BER estimation. The system BERs are determined by Eqs. (3.35), (3.38) and (3.41). The numerical procedures to implement these calculators will be explained in Sec. 4.3.3, Sec. 4.3.4 and Sec. 4.3.5. Particularly, the time- and frequency-domain KLSE calculators are only suitable for CW signals, while the third KLSE calculator can be applied to all shape of optical signals. At this stage, the numerical discretization must be carefully performed in order to guarantee the convergence and accuracy. Once the simulation operation is completed, the whole evaluation will enter the output stage.

Last but not least, the output of the whole system evaluation is illustrated in the final part of Fig. 4.1. Specifically, four important output characteristics will be generated, namely BER, eye diagrams, signal dynamics and noise dynamics. The BER results are exported in form of DAT files, and can be viewed via softwares like Matlab and Python. Moreover, the eye diagrams can be inspected either at the output of optical filters or at the back-end of the receiver. In addition, the signal dynamics and the noise dynamics can be exported by utilizing either the propagation simulator or the entire simulation engine, with the difference existing between the optical dynamics and the electrical dynamics correspondingly.

4.3 Algorithms in the System Evaluation Engine

In this section, different numerical algorithms employed in the system evaluation engine will be presented. Moreover, the complementary explanation regarding the KLSE computational routines will be made for the case of multi-channel system performance analysis.

4.3.1 Full Algorithm of Signal Propagation

The full signal propagation models provide an accurate description for the evolution of the optical field and FCs in Si waveguides, which incorporate all the essential linear and nonlinear optical effects, as shown in Sec. 2.6. Note that the theoretical algorithm of SSFM has been introduced in Sec. 2.8.1. Before proceeding to the SSFM implementation, it is also important to briefly discuss the choice of time and distance steps. For convergence, we first choose a specific time and distance steps, and get the result data. Then we test with smaller values of both steps until the results are matchable with previous one. Eventually, we will choose certain values for both time and distance steps according to the computational accuracy and efficiency. In this section, I will first introduce the numerical procedure to construct full model of the single-wavelength signal propagation, followed by the implementation of full propagation model with regard to the multi-wavelength optical signals.

Firstly, the full details of implementing single-channel model numerically are explained as follows:

1. Obtain the linear operator $\hat{D}$ and nonlinear operator $\hat{N}$ in forms of Eq. (2.33a)

and Eq. (2.33b), respectively.

2. Choose a distance step h and calculate the optical field at each h. h can be obtained by dividing the transmission distance L into n segments, namely, $h = L/n$. Then, the output optical field is computed via Eq. (2.38). Importantly, the calculation of FCs density is operated in the linear step, where the fifth-order Runge Kutta method in AppendixB is employed.

3. Record the simulation results in a DAT file.

When compared with the case of single-wavelength signal propagation, the numerical implementation of multi-wavelength signal propagation model requires more steps:

1. Derive the linear operator $\hat{D}_i$ and nonlinear operator $\hat{N}_i$ in the i channel ($i = 1, ..., \bar{M}$, $\bar{M}$ is the total number of signal wavelengths), by using Eqs. (2.21a) and (2.32).

2. Divide the transmission distance L into n segments, with distance step h. According to Eq. (2.38), the linear operator $\hat{D}_i$ will be performed on the electrical field of the i channel in the frequency domain, during a distance of $h/2$. Importantly, this process must be carried out by using a loop, in order to construct the $\bar{M}$ coupled NLSE. Then, calculate the overall FCs density at $h/2$ by applying the fifth-order Runge Kutta method on Eq. (2.21b).

3. Build a distance loop to derive the semi-analytical solutions for the optical signal u_i at the distance point $z_j = jh,\ j = 0, ..., n-1$:

   (a) Repeat step 2 during a distance from z_j to $z_j + h/2$.

   (b) Compute the nonlinear operator $\hat{N}_i$ at $z_j + h/2$, by using the FCs density calculated from last step. Then multiply the electrical field of the ith channel with $\hat{N}_i$ in the time domain, and repeat this operation for the remaining channels in a loop.

   (c) Repeat step 2 during a distance from $z_j + h/2$ to z_{j+1}.

4. Inverse step 2 by using $-\hat{D}$, and write the results of each channel in a separate DAT file.

In both procedures mentioned above, the FFT technique is applied for the conversion of optical signal between frequency-domain and time-domain.

4.3.2 Linearized Algorithm of Signal Propagation

The linearized propagation algorithms are designed for the CW signals, which requires less computational time but with high accuracy. As mentioned in Sec. 2.7, two assumptions are made for the linearization: one is that the terms containing quadratic and higher-order noise are discarded under low noise power condition; the other is that the FC-mediated coefficients α_{fc} and δn_{FC} are assumed to be related to the carrier density N under this approximation: $\delta n_{\text{fc}} = \sigma_n N$ and $\alpha_{\text{fc}} = \sigma_\alpha N$, where N is the FC density, $\sigma_\alpha = 1.45 \times 10^{-21}(\lambda/\lambda_0)^2$ (in units of m^2), and $\sigma_n = \sigma(\lambda/\lambda_0)^2$ (in units of m^3), with σ and $\lambda_0 = 1550\,\text{nm}$ being a power dependent coefficient [18] and a reference wavelength, respectively. Two numerical routines regarding the linearized propagation models will be described in this section.

The first numerical routine is developed for the single-channel CW signal propagation. This routine works for both the OOK modulated CW signal ($\Phi_0 = 0$) and the PSK modulated CW signal. The main steps are listed as follows:

1. Recast Eqs. (2.26) and (2.27) in forms of Eqs. (2.41), where $A = P$, $B = \Phi$, $C = A'$ and $D = A''$. Then implement these ODEs in a Matlab function.

2. Obtain the initial conditions of input field $y_0 = [\mathbf{A}_0; \mathbf{B}_0; \mathbf{C}_0; \mathbf{D}_0]$ and distance steps $tspan = [t_0, t_1, t_2, \cdots, t_f]$.

3. Use the Matlab function *ode*45 to compute the optical field evolution.

4. Write the output data in a DAT file, including signal power, global phase, in-phase and quadrature noise components.

Furthermore, the second routine is designed for the multi-wavelength signal co-propagation. The formulae of the multi-wavelength OOK optical signal propagation are given in Sec. 2.7.2. It is important to mention that these mathematical expressions are ODEs. Therefore, the computational procedure regarding $\bar{M}$-wavelength linearized model is illustrated below:

1. Derive the $\bar{M}$ coupled ODEs from Eqs. (2.30) and (2.31), and write up the corresponding Matlab functions. As an expansion of the single-channel CW signal case, these functions are organized by a loop, with the iteration number equaling to the total channel number. Inside of this loop, the numerical operations are the same as the numerical implementations for single-channel CW signal case. Note also that the coefficients of these ODEs have to be calculated simultaneously inside the loop.

2. Perform the Matlab function *ode*45 on the functions obtained from Step 1, and use the initial conditions, which contain the $\bar{M}$-channel input field, distance steps and total channel number.

3. Record the results of signal power, global phase, in-phase and quadrature noise components in a DAT file, for all channels.

Numerical tests shows that this algorithm has good agreement with the full propagation models.

4.3.3 Time-domain KLSE Algorithm in BER Calculation

The computational algorithm of the time-domain KLSE method is illustrated here to evaluate the transmission BER in Si waveguides. Implemented as the Matlab codes, this numerical routine is relatively simple to construct, due to its logic consistency. However, the difficult part of the time-domain method is the derivation of the noise correlation matrix at output of the receiver. The whole process regarding the noisy CW signal transmission and detection are briefly summarized below:

1. Run the main simulation loop for the noisy signal propagation in the Si waveguides.

   (a) Setup the essential simulation condition by loading a input file which includes all necessary physical and numerical parameters, namely, the signal properties (e.g., input power, bit sequence and pulsewidth), the waveguide linear and nonlinear optical parameters, as well as the computational time window, FFT points and distance step;

   (b) Use either the SSFM demonstrated in Sec. 4.3.1 or the ODEs solvers presented in Sec. 4.3.2 to derive the output signal from the waveguides.

2. Calculate the receiver-output noise correlation matrix in the time-domain, and compute the new signal-related variable.

   (a) Separate the noise and signal at the input of the receiver;

   (b) Calculate the noise correlation matrix before and after the optical receiver, by applying Eqs. (3.2) and (3.3);

   (c) Apply the Gauss-Hermite technique by deriving the explicit formulas for Eqs. (A.2), (A.3) and (A.4), and then obtain the correlation matrix at the end of the receiver according to Eq. (3.11);

   (d) Expand the signal and complex noise components after the optical filter in form of Eqs. (3.5), and use the relevant expansion coefficients, $\{s_\alpha^k\}$, $\{p_\alpha^k\}$, and $\{q_\alpha^k\}$ to construct new vector variables $\underline{s_k}$ and $\underline{n_k}$.

3. Compute the system BER according to the time-domain noise correlation matrix and the related MGF:

   (a) Diagonalize the correlation matrix by using Eq. (3.13), and recast the signal vector in new form of Eq. (3.15a);

   (b) Derive the MGF function format based on Eq. (3.16);

   (c) Calculate BER by applying the saddle-point approximation in Sec. 3.5 on the MGF function via Eqs. (3.35) and (3.38);

   (d) Record the BER in a DAT file.

With regard to the multi-channel system, the computational process is quite similar to the algorithm mentioned above. However, there are two major difference between the multi-channel and single-channel numerical implementation. One is that the input files, the SSFM simulator and the ODEs simulator in Step 1 all have to be switched to the multi-channel case. In addition, the signal detection (Step 2 and Step 3) is applied in each receiver that corresponds to one independent channel, and then the overall system BER is calculated by averaging the BER from each channel. This implementation is reasonable, due to the fact that the functionality of a demultiplexer in our model is to separate the signals with different wavelength, but without inducing any electrical noise.

4.3.4 Frequency-domain KLSE Algorithm in BER Calculation

Similar to the time-domain KLSE routine, the full computational algorithm of the frequency-domain KLSE method is also implemented in Matlab. Moreover, this algorithm is focused on the noisy CW signal as well. In particular, the frequency-domain KLSE is numerically easy to be extended to other applications, such as WDM systems and the optical systems that employ advanced modulation formats. The numerical process for the frequency-domain KLSE is described below:

1. Start a simulation loop for the signal transmission, similar to the first step in Sec. 4.3.3. Here, we need to specify a new central frequency points $2Q+1$ for the noisy signal.

2. Simulate the receiver-output noise correlation matrix in the frequency domain, and compute the related phase-shifted signal variable.

   (a) Derive the photocurrent at the end of the receiver and the related Hermitian kernal, in forms of Eqs. (3.17) and (3.18), repsectively;

   (b) Discretize the Hermitian kernel and then multiply the with frequency step δf, yielding new forms of the receiver matrix and the electrical field, as well as the photocurrent that is expressed as Eqs. (3.19);

   (c) Rewrite the receiver matrix and the electrical field into real-valued matrixes.

   (d) Compute the correlation matrix in frequency-domain by applying Eqs. (3.20), (3.21) and (3.22);

3. Compute the final BER by deriving the noise correlation matrix in frequency-domain and further the MGF:

   (a) Derive the eigenfunction and eigenvalues by using an orthogonal matrix to diagonalize the noise correlation matrix at the receiver output, according to Eq. (3.23);

   (b) Calculate the phase-shift signal vector by using the expansion in Eq. (3.24b);

   (c) Compute the MGF by using Eq. (3.26);

(d) Derive the transmission BER by using the saddle-point approximation on the MGF, obtaining Eqs. (3.35) and (3.41), as illustrated in Sec. 3.5;

(e) Save all the BER results in an easily-traceable file.

As was pointed out in Sec. 4.3.3, there are also two changes in the numerical scheme for the multi-channel system analysis in the frequency domain, when compared with the single-channel case. Therefore, the corresponding implementation regarding multi-channel systems in frequency domain can refer to the last paragraph in Sec. 4.3.3.

4.3.5 Fourier-series KLSE Algorithm in BER Calculation

The numerical calculations of the PDFs for Signal "1" and Signal "0" can also be done by using the Fourier-series KLSE method in combination with the perturbation theory. Specifically, the optical signal propagation in Si waveguides and the followed BER detection and calculation are all implemented in Matlab. The implementation routine for the single-channel systems is presented as follows:

1. Setup a main simulation process for the noise-free optical signal ($s^0(t,0)$) transmission in Si waveguides:

   (a) Read a input file with initial conditions for all necessary physical and numerical parameters;

   (b) Run the SSFM numerical simulator according to Sec. 4.3.1. Then obtain the output signal in the central channel as $s^0(t,L)$, and save it.

2. Calculate the noise correlation matrix at the end of the Si waveguide. To start with, compute the correlation matrix $\underline{\underline{R}}^k(0)$ based on the input complex white noise, with the matrix dimension of $(4Q+2)\times(4Q+2)$. After obtaining the noise free signal $s^0(t,L)$ in the central channel at $z=L$, we then continue with the simulation process for different input signal in the same channel:

   (a) Obtain $s^\beta(t,0)$ by perturbing $s_0(t,0)$ in the β-th frequency mode with an extremely small amount Δ, in correspondence to Eq. (3.28). Here, $\beta = 1,...,(2Q+1)$, $(2Q+1)$ is the chosen frequency points in the central part of signal spectrum. Particularly, we use two values of Δ in the signal initialization, which are a real positive number and an imaginary positive

number for the same 1 to $(2Q+1)$ frequency components. Then launch $s^{\beta}(t,0)$ at input of the Si waveguide;

(b) Calculate the waveguide output signal $s^{\beta}(t,L)$ by solving Eqs. (2.15) and (2.20);

(c) Compute $\delta s^{\beta}(t) = s^{\beta}(t,L) - s_0(t,L)$ and its Fourier coefficients, $\underline{w}^{\beta}$;

(d) Find the $(4Q+2)\times(2Q+1)$ transmission matrix $\mathscr{R}$ by using Eq. (3.29). Then recast $\mathscr{R}$ into a $(4Q+2)\times(4Q+2)$ real-valued matrix.

(e) Obtain the noise correlation matrix after transmission according to Eq. (3.27).

3. Computation of the System BER based on the Noise Correlation Matrix:

(a) Read the output noise-free signal and transfer it into the frequency domain. And then load the noise correlation matrix at the output of Si waveguide, $\underline{\underline{R}}^{k}$.

(b) Calculate the real receiver matrix $\underline{\underline{\mathscr{W}}}$ from $\underline{\underline{\mathscr{W}}} = [\underline{\underline{\mathscr{D}}}', -\underline{\underline{\mathscr{D}}}''; \underline{\underline{\mathscr{D}}}'', \underline{\underline{\mathscr{D}}}']$, where $\underline{\underline{\mathscr{D}}}$ is a Hermitian kernel.

(c) Diagonalize the combined matrix of the $\underline{\underline{R}}^{k}(L)$ and $\underline{\underline{\mathscr{W}}}$;

(d) Calculate the signal shift variable χ_q based on Eqs. (3.31), (3.32) and (3.33);

(e) Compute the MGF function from Eq. (3.34);

(f) Calculate BER by performing the saddle-point approximation presented in Sec. 3.5 on the MGF, referring to Eqs. (3.35) and (3.41);

(g) Save BER and write them into a recorded file.

Importantly, the correlation matrix calculation in multi-channel systems are slight different from that of single-channel systems. The basic idea is to compute only the noise correlation matrix in the central channel, by perturbing the signal in the central channel and leaving the other channels to be noise free. It has been verified that the cross correlation between the noise in the investigated channel and the noise from the rest channels can be neglected, when compared with noise correlation in the central channel. The remaining part of BER calculation is identical to that of single-channel.

4.3.6 Comparative Study of Alternative Algorithms

As mentioned earlier, the theory of signal propagation and the KLSE-based BER calculation approaches are two fundamental components of this dissertation. Importantly, only by carefully choosing the numerical parameters can the validation of these theoretical methods be guaranteed. In this section, I will present the values of simulation parameters used in this dissertation and prove the consistency of the relevant algorithms in each computational branch.

In terms of signal propagation, the number of temporal sampling points for one bit is set to 1024, the number of distance steps is 512, and the time-window is usually chosen to be $20\times$ larger than the signal pulsewidth. The above condition is applied to both full and linearized propagation algorithms, but in the first algorithm additional Cash-Karp parameters, presented in Table B.1, are need for the calculation of FC density. Notably, the utilization of the linearized propagation model in this dissertation is due to its high computational accuracy and faster convergence when compared with the full model. Even though suitable to simulate different types of optical signals, the full propagation model is only adopted in the detailed performance analysis of systems using pulsed signals, which is presented in Chapter 9. Furthermore, a detailed comparison between the full propagation model and its linearized version was carried out for both single-channel and multi-channel systems, with the results illustrated in Fig. 5.3 and Fig. 8.4, respectively. This proves that for practical values of the system parameters the linearized model is accurate.

With regard to the KLSE-base BER calculation methods, the configuration of the numerical parameters is described as follows. The number of temporal sampling points within one bit is determined by the same parameter from the signal propagation theory, namely 1024, and bit-rate will be given in latter chapters for a specific case. Additionally, in the time KLSE algorithm the number of weights used in the Gaussian Hermite rule is 58, whereas the number of frequency points is chosen to be 201 in both the frequency-domain and Fourier-series KLSE methods. In order to prove the accuracy of these KLSE methods with the above parameters, we first illustrate BER results calculated for a simple case of CW signal along with a real additive white Gaussian noise, in comparison with the method of Gaussian approximation [19]. The corresponding conclusions are summarized in Fig. 4.2, where

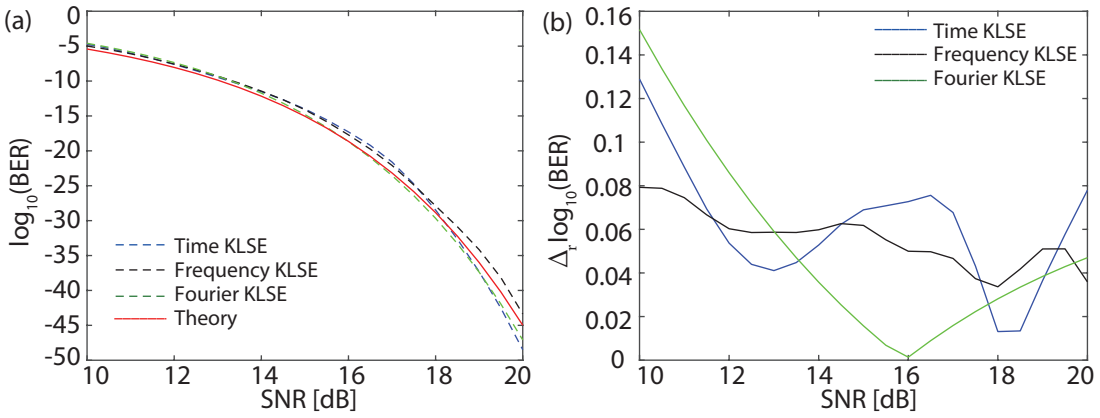

Figure 4.2: (a) Comparison of the system BER calculated via the time-domain (TD), frequency-domain (FD) and Fourier-series (FS) KLSE approaches, as well as the Gaussian approximation method (red line). (b) The relative BER difference between these KLSE approaches and Gaussian approximation. This agreement is quantified by $\Delta_r \log_{10}(\mathrm{BER}) = |[\log_{10}(\mathrm{BER})_{ii} - \log_{10}(\mathrm{BER})_{Gaussian}]/\log_{10}(\mathrm{BER})_{Gaussian}|$, where $ii = 1,2,3$, with each value representing the TD, FD and FS, respectively. The plots correspond to a CW signal in presence with a real additive white Gaussian noise, with a initial signal power of $P = 5\,\mathrm{mW}$. Note that no waveguide is included in this case.

we plot the BER of the absolute value and the relative difference between the BERs calculated via the above four methods. This quantity of relative difference is defined as $\Delta_r \log_{10}(\mathrm{BER}) = |[\log_{10}(\mathrm{BER})_{ii} - \log_{10}(\mathrm{BER})_{Gaussian}]/\log_{10}(\mathrm{BER})_{Gaussian}|$, where $ii = 1,2,3$, with each value representing the time-domain, frequency-domain and Fourier-series KLSE, respectively. In addition, the method of Gaussian approximation is selected as the reference. The curves presented in Fig. 4.2 show that the predictions of the four algorithms are in good agreement, which proves the accuracy of the KLSE approaches. Notably, though the BER range of 10^{-1} to 10^{-15} is more meaningful for the practical optical systems, the plots in Fig. 4.2(a) provide the validation of the KLSE approaches over a large scale of SNRs.

For completeness, we also include a second comparison of BER results calculated via the three KLSE methods in a system containing the Si waveguide, where the nonlinear noise dynamics has to be taken into account. As illustrated in Fig. 4.3(a), one can see the absolute value of BERs derived from the time-domain, frequency-domain and Fourier-series KLSE methods, in case of a single-channel photonic system that consists of a SPW and a direct-detection receiver. The initial power of the optical CW signal is $P = 5\,\mathrm{mW}$, the bit-rate is $B_r = 10Gb/s$, and the length of a Si-SPW is $L = 5\,\mathrm{cm}$, with other waveguide parameters listed in Table 4.1. In addition, a

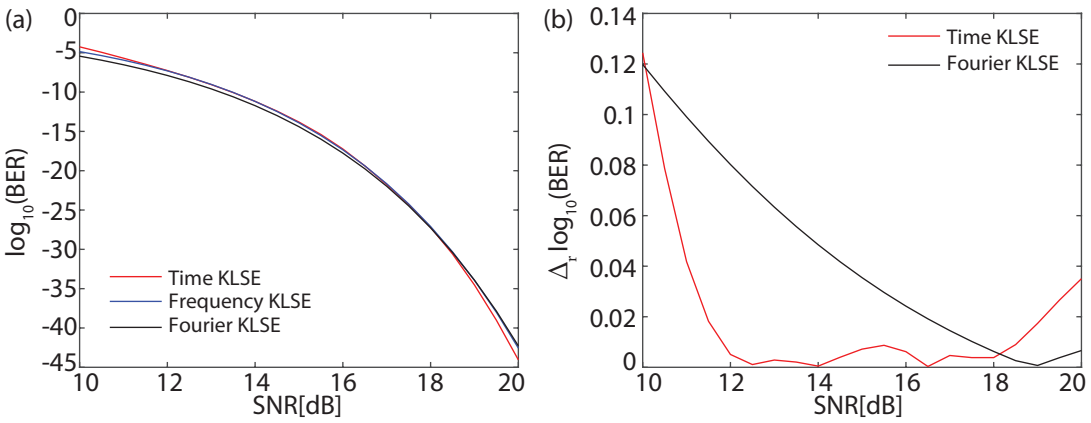

Figure 4.3: (a) Comparison of the system BER calculated via the time-domain (TD), frequency-domain (FD) and Fourier-series (FS) KLSE approaches. (b) The relative BER difference between the frequency-domain KLSE and the other two KLSE emthods. This agreement is quantified by $\Delta_r \log_{10}(\text{BER}) = |[\log_{10}(\text{BER})_{ii} - \log_{10}(\text{BER})_{FD}]/\log_{10}(\text{BER})_{FD}|$, where $ii = 1,2$, with each value representing the TD and FS, respectively. The plots correspond to a single-channel Si-PhW system using a NRZ CW signal together with a complex additive white Gaussian noise. The initial power of the CW signal is $P = 5\,\text{mW}$, $B_r = 10Gb/s$, $L = 5\,\text{cm}$ and the other waveguide parameters is illustrated in Table 4.1.

vivider picture about the difference of these three KLSE methods is shown in Fig. 4.3 (b), where the evaluation quantity is denoted as $\Delta_r \log_{10}(\text{BER}) = |[\log_{10}(\text{BER})_{ii} - \log_{10}(\text{BER})_{FD}]/\log_{10}(\text{BER})_{FD}|$, where $ii = 1,2$, with each value representing the time-domain and Fourier-series KLSE, respectively. Here, the frequency-domain KLSE is selected as the reference. To conclude, these curves in Fig. 4.3 suggest that the time-domain, frequency-domain, and Fourier-series KLSE methods are matching with each other very well, which in turn ensures the accuracy of simulation results in the latter chapters.

Table 4.1: Main parameters for a Si-PhW used in Fig. 4.3.

w [nm]	h [nm]	λ [nm]	β_2 [ps^2 m^{-1}]	κ	γ' [W^{-1} m^{-1}]	γ'' [W^{-1} m^{-1}]
900	250	1550	0.54	0.9685	166.8403	50.8236

Last but not least, we also validate the accuracy of the KLSE methods in multi-channel photonic systems. Thus, another comparison of BERs calculated by employing the time- and frequency-domain methods for three different 8-channel Si photonic systems is presented in Fig. 8.6. The information that conveys in Fig. 8.6 strengthens the idea that these two KLSE algorithms are in agreement with each other. As stated earlier, the Fourier-series KLSE method is only utilized for the single-channel

performance analysis in this dissertation, which is the reason why this algorithm is not included in the multi-channel BER comparison.

4.4 Conclusions

In this chapter, the computational implementation details of the entire system evaluation model is discussed. This numerical tool can support not only accurate investigations of the signal propagation in Si waveguides, but also precise evaluation of the overall system performance. Moreover, the current numerical algorithms are also of excellent expandability, which can be applied in other optical devices and more sophisticated photonic systems. To our knowledge, this is the first time to provide the complete numerical implementation of the linearized propagation models for Si waveguides.

Bibliography

[1] Matlab version R2016b, https://uk.mathworks.com/products/matlab.html.

[2] G. P. Agrawal, *Nonlinear Fiber Optics* 4th ed., (Academic Press, 2006).

[3] J. N. Reddy, *An introduction to the finite element method*, (New York: McGraw-Hill, 1993).

[4] A. Taflove and S. Hagness, *Computational Electrodynamics, The finite-difference time-domain method*, 3rd ed., (Artech House, 2005).

[5] D. F. G. Gallagher and T. P. Felici, "Eigenmode Expansion Method for Simulation of Optical Propgation in Photonics - Pros and Cons," Proc. SPIE **4987**, 69-82 (2003).

[6] L. Wang, and S.I. Rokhlin, "Stable reformulation of transfer matrix method for wave propagation in layered anisotropic media," Ultrasonics **39**, 413-424 (2001).

[7] K. Okamoto, *Fundamentals of optical waveguides*, (Academic press, 2010).

[8] A. Carena, V. Curri, R. Gaudino, P. Poggiolini, and S. Benedetto. "A time-domain optical transmission system simulation package accounting for nonlinear and polarization-related effects in fiber," IEEE J. Sel. Areas Commun. **15**, 751-765 (1997).

[9] SSPROP, develped by Ross Pleban (NCSU), Afrouz Azari (UMD), Reza Salem (UMD) and T. E. Murphy (UMD). `http://www.photonics.umd.edu/software/ssprop/`.

[10] SIMFOCS, developed by Dr. Siegfried Geckeler, Horwitzstr.1, D-81739 Munich, Germany. `http://www.geckeler.homepage.t-online.de/simfocs/smfe.htm`.

[11] Rsoft Design Group, Optsim, `https://optics.synopsys.com/rsoft/rsoft-system-network-optsim.html`.

[12] PHOTOSS, `http://www.lenge.de/english/`.

[13] Rsoft Design Group, Femsim, https://optics.synopsys.com/rsoft/rsoft-passive-device-femsim.html.

[14] MIT Photoinc Bands, http://ab-initio.mit.edu/wiki/index.php/MIT_Photonic_Bands.

[15] W. H. Press, S. A. Teukolsky, W. T. Vetterling, and B. P. Flannery, "Numerical Receipes in C: The Art of Scientific Computing," Cambridge University Press (1992).

[16] J. R. Dormand, and P. J. Prince, "A family of embedded Runge-Kutta formulae," J. Computational and Applied Mathsmatics **6**, 19-26 (1980).

[17] Matlab version R2016b, PARFOR, https://uk.mathworks.com/help/distcomp/parfor.html.

[18] Q. Lin, O. J. Painter, and G. P. Agrawal, "Nonlinear optical phenomena in silicon waveguides: Modeling and applications," Opt. Express **15**, 16604-16644 (2007).

[19] P. Sun, M. M. Hayat, B. E. A. Saleh, and M. C. Teich, "Statistical correlation of gain and buildup time in APDs and its effects on receiver performance," IEEE J. Lightwave Technol. **24**, 755-768 (2006).

Chapter 5

Calculation of Bit Error Rates in Optical Systems with Strip Silicon Photonic Wires

5.1 Introduction

In this chapter, we perform a theoretical analysis of the transmission BER in a system consisting of a Si-PhW linked with a direct-detection optical receiver containing an optical filter, an ideal square-law photodetector, and an electrical filter (see Fig. 5.1). We assume that the bandwidth of the optical filter is larger than the bit rate of the optical signal, whereas the bandwidth of the electrical filter is close to the bit rate. In particular, an integrate-and-dump electrical filter is employed in this work, which can be viewed as a matched filter for the nonreturn-to-zero (NRZ) signals. At the front-end of the system the optical field is assumed to be a superposition of an ON-OFF keying (OOK) modulated NRZ optical signal, with ON and OFF power values of P_0 and zero, respectively, and a stationary additive white Gaussian noise containing an in-phase and a quadrature component. For simplicity, we assume that these two noise components are uncorrelated, a constraint that can be easily relaxed if needed. To describe the optical field propagation in the Si-PhW we use a rigorous model [1] that incorporates linear and nonlinear optical effects, including free-carrier (FC) dispersion (FCD), FC absorption (FCA), self-phase modulation (SPM), and two-photon absorption (TPA), as well as the FCs dynamics and the interaction between the FCs and the optical field. A linearized system governing the optical noise dynamics in the presence of FCs is

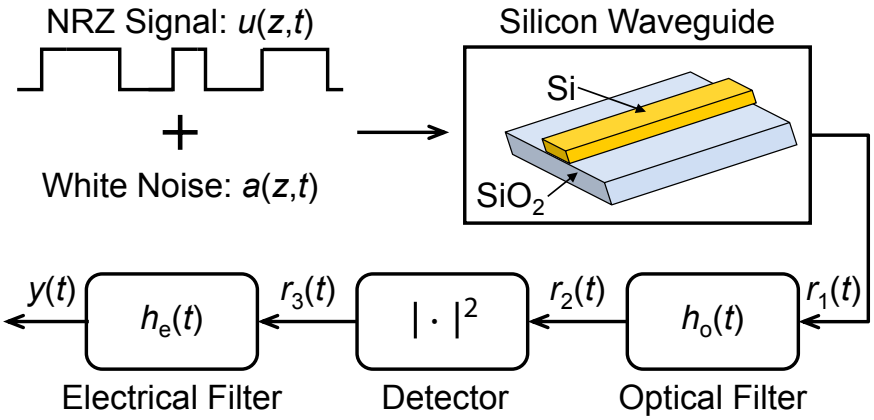

Figure 5.1: Schematic of the investigated photonic system, consisting of a Si-PhW linked to a receiver containing an optical filter with impulse response function, $h_o(t)$, a photodetector, and an electrical filter with impulse response function, $h_e(t)$.

also derived and used to analyze the noise propagation in Si-PhWs. The system BER is calculated using the time domain Karhunen-Loève (KL) series expansion (KLSE) method [2], an algorithm that has also been used to analyze the performance of optical fiber communication systems [3, 4].

The remaining of the paper is organized as follows. In Sec. 5.2 we present the theoretical model that describes the propagation of the optical signal in the Si-PhW, whereas in Sec. 5.3 we briefly summarize the time domain KL expansion method used to evaluate the BER. The results of our analysis are presented in Sec. 5.4, the main conclusions of our study being summarized in the last section.

5.2 Theoretical Signal Propagation Model in Strip Silicon Photonic Wires

The mathematical description for the single-wavlength optical signal propagation in a Si-PhW, is based on the coupled dynamics of the optical signal and FCs, which are governed by Eq. (2.15) and Eq. (2.20). The terms in Eq. (2.15) describe well known linear and nonlinear optical effects. Specifically, on the left-hand side, the second term describes the GVD, while on the right-hand side, the first term corresponds to the intrinsic waveguide loss and FCA, the second term describes the FCD, and the last term represents the nonlinear effect of SPM. Since all the relevant optical parameters have been defined in Sec. 2.6.1, their actual values will be specified here for the simulations in this chapter. In particular, the intrinsic loss coefficient α_i was set to $0.2\,\mathrm{dB\,cm^{-1}}$

Table 5.1: Main parameters for the Si-PhWs used in our simulations.

Type	w [nm]	β_2 [ps^2 m^{-1}]	β_3 [ps^3 m^{-1}]	κ	γ' [W^{-1} m^{-1}]	γ'' [W^{-1} m^{-1}]
A	800	0.26	2.8×10^{-3}	0.9663	183.1	55.8
B	675	-0.2	3.8×10^{-3}	0.9611	207.7	63.3

unless otherwise specified, the FC relaxation time t_c was assumed to be $t_c = 0.5$ ns, FC-induced refractive index change ($\delta n_{\rm fc}$) and FC loss coefficient ($\alpha_{\rm fc}$) and are given by $\delta n_{\rm fc} = \sigma_n N$ and $\alpha_{\rm fc} = \sigma_\alpha N$, where N is the FC density, $\sigma_n = -2.68\times10^{-26}(\lambda/\bar{\lambda})^2$ (in units of m^3), and $\sigma_\alpha = 1.45\times10^{-21}(\lambda/\bar{\lambda})^2$ (in units of m^2) [5], the reference wavelength being $\bar{\lambda} = 1550$ nm.

The superposition of the optical signal and noise propagating in the Si-PhW can be expressed as,

$$u(z,t) = [\sqrt{P(z)} + a(z,t)]e^{-j\Phi(z)}, \tag{5.1}$$

where $P(z)$ is the power of the CW signal, $a(z,t)$ is the complex additive Gaussian noise, and $\Phi(z)$ is a global phase shift. Also, a linearized model of Eqs. (2.26a), (2.26b) (2.27) is utilized for the simulations investigated in this chapter. Notably, the global phase is set to be $\Phi_0 = 0$ for all the simulations in this chapter. It is also worth to mention that the full model Eq. (2.15), and its linearized version Eq. (2.27) can be extended to other devices, too, the main difference being that the resulting mathematical description could potentially become much more intricate. For example, waveguide splitters, ring modulators coupled to a waveguide, multi-wavelength signals propagating in single- or multi-mode waveguides can all be described by systems of coupled equations similar to Eq. (2.15) and its linearized version Eq. (2.27). Therefore, the approach presented in this study can be applied to a multitude of chip-level photonic devices, thus underlying the generality of our approach.

We have determined the optical field at the output of the Si-PhW both by integrating the full system (Eqs. (2.15), (2.20)), using a standard SSFM, and also by solving the linearized system (Eqs. (2.26a), (2.26b), (2.27)) via a fifth-order Runge-Kutta method, with the numerical implementation details demonstrated in Sec. 2.8. In the latter case, we first found the spectra of the noise components, then by inverse Fourier transforming these spectra we calculated the optical noise in the time domain. Moreover, in order to gain a more complete understanding of the factors that affect the BER,

we considered Si-PhWs with both normal and anomalous dispersion. Thus, since the linear and nonlinear properties of stripe Si-PhWs depend strongly on the waveguide geometry [1], the waveguide parameters (dispersion and nonlinear coefficients) can be varied over a wide range of values by properly choosing the waveguide height, h, and its width, w. In particular, unless otherwise specified, we assumed that the Si-PhW has constant height $h = 250\,\text{nm}$ [6] and width, its optical waveguide parameters being

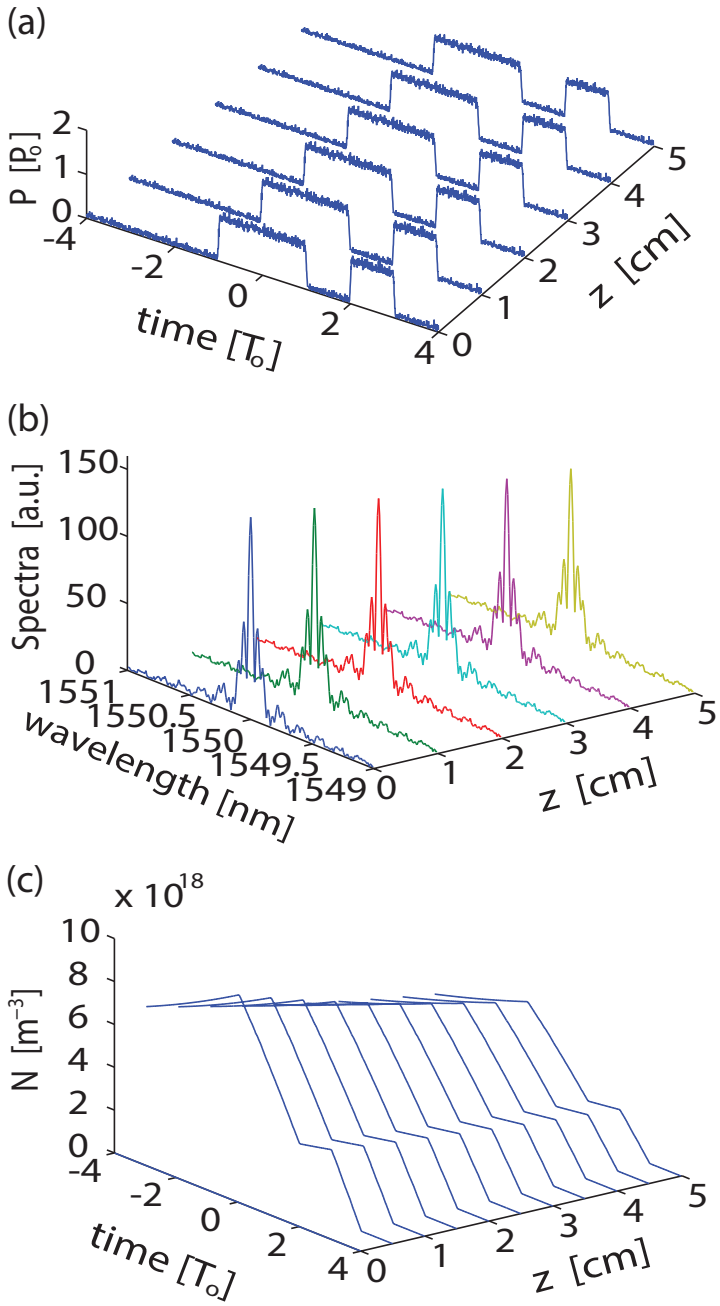

Figure 5.2: (a) Time and (b) spectral domain evolution of a noisy signal with $P_0 = 5\,\text{mW}$ and $T_0 = 100\,\text{ps}$ in a 5 cm-long Si-PhW with anomalous dispersion (see the text for the values of β_2, β_3, and γ). (c) Carrier density variation along the waveguide.

thus independent of the distance along the waveguide, z. By adjusting the width w of Si-PhWs, it can be easily achieved the switch from the normal dispersion region to the anomalous dispersion. The main waveguide parameters are listed in Table 5.1.

An example of time and wavelength domain evolution of a noisy signal in a 5 cm-long Si-PhW with anomalous dispersion is shown in Fig. 5.2, the bit sequence being "01011000". For completeness, we also show in Fig. 5.2(c) the dynamics of the photogenerated FCs. It can be seen that the optical field is fairly weakly distorted during propagation, which means that for the optical power considered in these simulations the nonlinear effects are small. The most notable feature revealed by these plots is the signal decay, which is due to the intrinsic losses, FCA, and TPA. The generation of the FCs that produce FCA is illustrated in Fig. 5.2(c), where the increase in the FC density induced by each "1"-bit can be clearly seen.

In order to determine the accuracy with which the linearized system (Eq. (2.26)) describes the propagation of the optical field in the Si-PhW, we calculated the signal and noise at the back-end of the waveguide by using both the linearized model and full system Eqs. (2.15), (2.20). The conclusions of this analysis, summarized in Fig. 5.3, suggest that the linearized system describes fairly accurately the dynamics of the CW signal and noise, especially when the noise power is small. Thus, Figs. 5.3(b) and 5.3(c) show that both models predict a larger parametric amplification of the quadrature noise (a finding also supported by the power spectral densities of the two noises, not shown here) and similar values of the average phase, ϑ, of the noise, which is equal to the slope of the red lines in these plots. This is a known effect, a larger parametric gain amplification of the quadrature noise being observed in optical fiber systems, too [7]. In the case when the linearized system was used, the phase ϑ was calculated from the relation, $\vartheta = \mathbb{E}\{\arg[a(z,t)]\}$, where $\mathbb{E}\{\cdot\}$ denotes the statistical expectation operator. When the full system was used, the CW signal parameters were extracted from the relation, $\sqrt{P(z)}e^{-j\Phi(z)} = \mathbb{E}\{u(z,t)\}$, and then the noise was found as $a(z,t) = [u(z,t) - \mathbb{E}\{u(z,t)\}]e^{j\Phi(z)}$. Note that in Figs. 5.3(b) and 5.3(c) we plot $a(z,t)e^{-j\Phi(z)}$, calculated at $z = L = 5\,\text{cm}$.

A good agreement between the two models can also be observed in their predictions of the dependence of the CW signal power and phase on the distance, z, as per Fig. 5.3(d). Expectedly, the differences between the results inferred from the two mod-

els decrease with the signal-to-noise ratio (SNR) as the effects due to the nonlinear noise propagation and noise interaction with FCs, which are neglected in the linearized model, become less important as the SNR increases. In particular, as compared to the full system, the linearized system overestimates the power of the CW signal and underestimates its phase. In our simulations we define the SNR of the optical signal at the front-end of the Si-PhW as the ratio between the power of the CW signal, P_0, and the average of the sum of the powers of the in-phase and quadrature noise components,

$$\mathrm{SNR} = \frac{P_0}{\mathbb{E}\left\{a'^2 + a''^2\right\}\Big|_{z=0}}, \tag{5.2}$$

Additionally, the resolution bandwith of the SNR measurement is 0.1 nm.

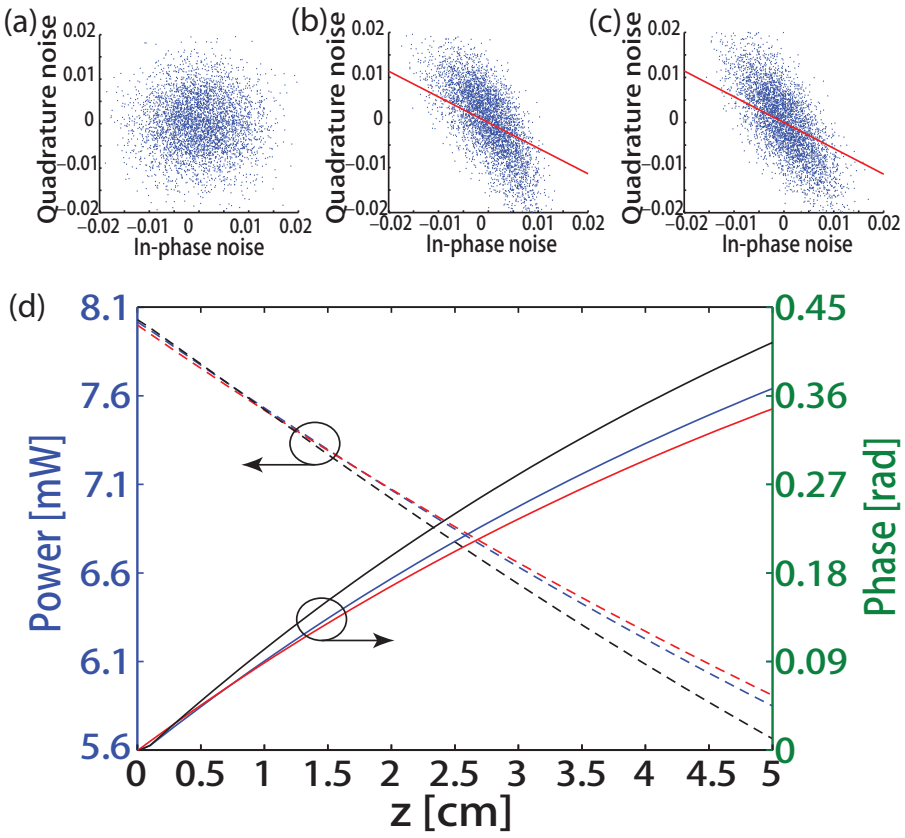

Figure 5.3: (a) In-phase and quadrature noise components at the input of the Si-PhW and (b), (c) waveguide output, determined from the full system (Eqs. (2.15), (2.20)) and linearized system (Eq. (2.26)), respectively. The propagation length, $L = 5\,\mathrm{cm}$, and $\mathrm{SNR} = 20\,\mathrm{dB}$. The red lines indicate the average phase of the noise. The Si-PhW is the same as in Fig. 5.2. (d) Power $P(z)$ and phase $\Phi(z)$ calculated using the linearized system (red lines) and full system for $\mathrm{SNR} = 20\,\mathrm{dB}$ (blue lines) and $\mathrm{SNR} = 15\,\mathrm{dB}$ (black lines).

5.3 Calculation of BER

The time-domain KLSE method that demonstrated in Sec. 3.2 is employed to calculate the transmission BER at the back-end of the receiver, with the numerical routine clearly described in Sec. 4.3.3. Particularly, in this chapter, we assume that the direct-detection receiver is composed of a Lorentzian optical filter with impulse response, $h_o(t)$, followed by an ideal photodetector, and an integrate-and-dump electrical filter, whose impulse response is $h_e(t)$. The electrical noise of the receiver has not been taken into account, as in most cases it can be neglected. These considerations are extremely important when implementing the time-domain KLSE algorithm. As a final note on the BER calculation, we stress that this KL-based method produces significantly more accurate results when the parametric gain amplification of the noise cannot be neglected, as compared to the commonly used Gaussian approximation [3].

5.4 Results and Discussion

In order to illustrate how our approach can be applied in practical cases to calculate the system BER, we consider a single-channel OOK system ($\lambda_0 = 1550\,\text{nm}$) with NRZ pulses in a back-to-back configuration, the bit window being $T_0 = 100\,\text{ps}$ throughout our investigations. Here, a PRBS of $2^9 - 1$ bits plus a zero bit is employed, which contains possible 9-bit sequence patterns. To model the direct-detection receiver, we assume that the electrical filter is a low-pass integrate-and-dump filter with the 3-dB bandwidth equal to $B_e = 10\,\text{Gb}\,\text{s}^{-1}$, whereas the optical filter is a bandpass Lorentzian with 3-dB bandwidth, $B_o = 4B_e$. Specifically, the two filters are described by the following transfer functions,

$$H_o^i(f) = \frac{\Gamma_o^2}{f^2 + \Gamma_o^2}, \quad H_o^q(f) = -\frac{\Gamma_o f}{f^2 + \Gamma_o^2}, \tag{5.3a}$$

$$H_e^i(f) = \begin{cases} 1, & |f| \le B_e/2 \\ 0, & |f| > B_e/2 \end{cases} \quad H_e^q(f) = 0, \tag{5.3b}$$

where $\Gamma_o = B_o/2$.

In our calculations of the system BER, we considered Si-PhWs with both normal and anomalous dispersion and in both cases we assumed that the waveguide length, $L = 5\,\text{cm}$. For comparison, we also examined the case of a system without the Si-PhW,

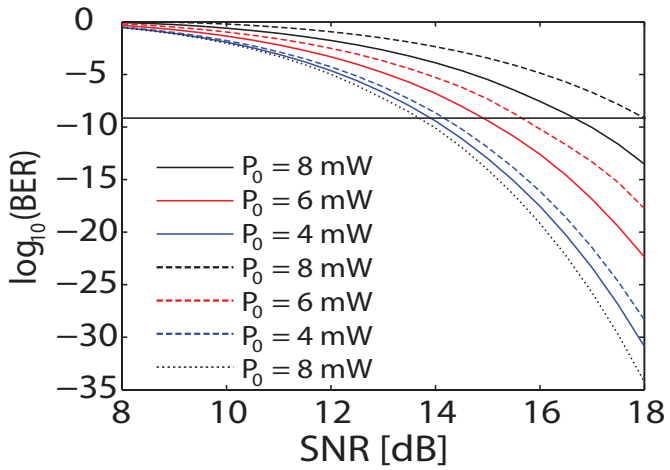

Figure 5.4: System BER vs. SNR, calculated for Si-PhWs with normal (solid line) and anomalous (dashed line) dispersion (see the text for the values of β_2, β_3, and γ). The waveguide length, $L = 5$ cm. The dotted line indicates the BER in the case of a system without the silicon waveguide. The horizontal black solid line corresponds to a BER of 10^{-9}.

so that the contribution of the waveguide to the system BER can be easily assessed. The dependence of the system BER on the SNR, calculated for several values of the input power, P_0, is presented in Fig. 5.4. The results summarized in Fig. 5.4 demonstrate that a better system performance is achieved in the normal dispersion regime, which is primarily due to the fact that the Si-PhW with anomalous dispersion has a larger nonlinear coefficient and consequently it generates a larger parametric gain amplification of the noise. Moreover, because the parametric gain also increases with the optical power, one expects that increasing P_0 would lead to larger BER, a conclusion fully validated by the plots in Fig. 5.4. This figure also shows that the Si-PhW has a significant contribution

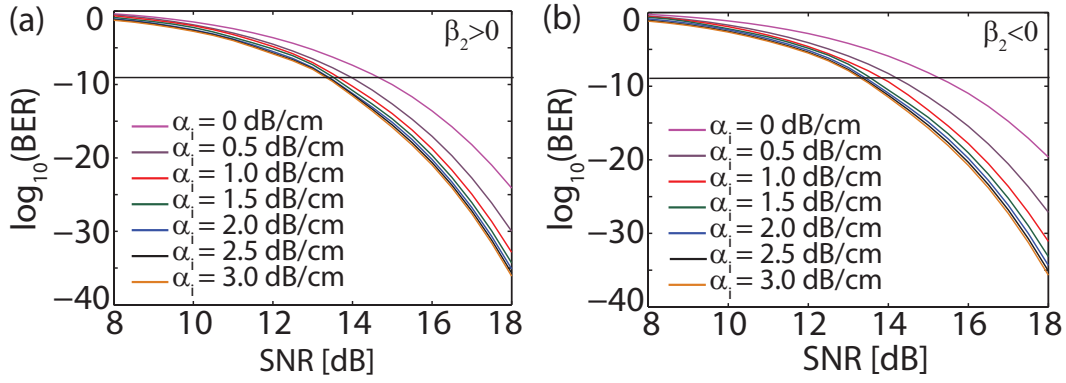

Figure 5.5: System BER vs. SNR, calculated for several different values of the waveguide loss coefficient, α_i. The panels (a) and (b) correspond to waveguides A ($\beta_2 > 0$) and B ($\beta_2 < 0$), respectively. In all simulations $P_0 = 5$ mW and $L = 5$ cm. The horizontal black solid line corresponds to a BER of 10^{-9}.

to the signal degradation, especially for large SNR, when compared with the simulation result for the system without no Si-PhW included (black-dotted line).

Depending on the width of the waveguide and specific fabrication processes, the intrinsic loss coefficient, α_i, can usually vary from $0.03\,\mathrm{dB\,cm^{-1}}$ to more than $3\,\mathrm{dB\,cm^{-1}}$. We therefore considered the two Si-PhWs with positive and negative dispersion coefficient and in both cases calculated the system BER for several values of α_i. In all these calculations we chose $P_0 = 5\,\mathrm{mW}$ and $L = 5\,\mathrm{cm}$. The results of these simulations, plotted in Fig. 5.5, demonstrate that as the waveguide loss coefficient increases the system performance improves, which is reflected in a smaller transmission BER. This conclusion is in agreement with the dependence of BER on pulse power illustrated in Fig. 5.4. To be more specific, when α_i increases the power of the signal upon its propagation in the Si-PhW decreases and therefore a smaller parametric gain amplification of the noise is produced. This results in a larger SNR at the output facet of the waveguide and consequently a reduced BER. Note also that, similarly to the dependence illustrated in Fig. 5.4, the variation of the BER with α_i, for the same value of the SNR, is smaller for the waveguide A ($\beta_2 > 0$) as compared to the case of waveguide B ($\beta_2 < 0$).

Due to the strong confinement of light in Si-PhWs with submicrometer transverse size, the waveguide parameters characterizing their linear and nonlinear optical properties are strongly dependent on the waveguide width. It is therefore of particular interest to investigate the dependence on the waveguide width of the system BER. To this end, we considered several Si-PhWs with widths ranging from 500 nm to 1000 nm and constant height, $h = 250\,\mathrm{nm}$, and for all these waveguides we determined their waveguide parameters; the corresponding values are presented in Table 5.2. We stress that for the range of widths considered here the waveguides are single-mode [6]. Note that as the waveguide width varies within the specified bounds, the second-order dispersion coefficient, β_2, changes from anomalous to normal dispersion regime.

After the waveguide parameters have been determined, we have calculated the system BER corresponding to each of the waveguides considered. In all cases we set $P_0 = 5\,\mathrm{mW}$ and $L = 5\,\mathrm{cm}$. As illustrated in Fig. 5.6, the main conclusion that can be drawn from this analysis is that the BER decreases as the waveguide width increases. This result can be readily understood if one considers the variation of the waveguide

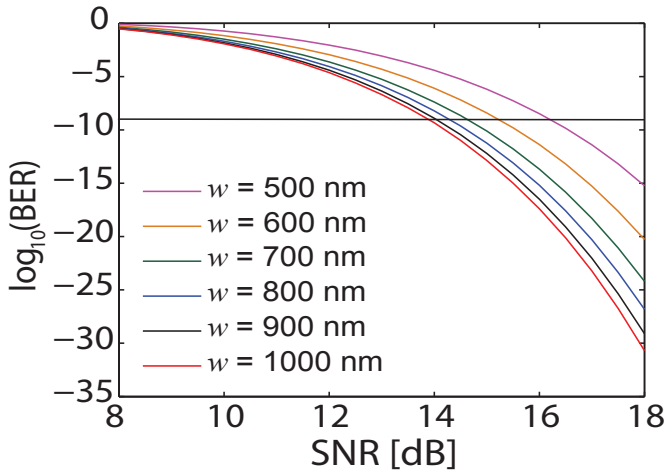

Figure 5.6: System BER vs. SNR, calculated for Si-PhWs with different width, w. The waveguide parameters for all widths are given in Table 5.2. In all cases $P_0 = 5\,\text{mW}$ and $L = 5\,\text{cm}$. The horizontal black solid line indicates a BER of 10^{-9}.

Table 5.2: Waveguide parameters used to obtain the results presented in Fig. 5.6

w [nm]	c/v_g	β_2 [ps^2 m^{-1}]	β_3 [ps^3 m^{-1}]	κ	γ' [W^{-1} m^{-1}]	γ'' [W^{-1} m^{-1}]
500	4.2	-1.2455	3.73×10^{-3}	0.9399	251.64	76.68
600	4.05	-0.595	4.33×10^{-3}	0.9552	225.16	68.60
700	3.96	-0.0921	3.57×10^{-3}	0.9624	202.29	61.63
800	3.93	0.258	2.80×10^{-3}	0.9663	183.08	55.77
900	3.87	0.504	2.21×10^{-3}	0.9685	166.84	50.83
1000	3.84	0.684	1.73×10^{-3}	0.9699	153.02	46.62

nonlinear coefficient, γ', with the waveguide width, w (see Table 5.2). Thus, it can be seen that as w increases the waveguide nonlinearity decreases, and therefore the parametric gain amplification is weaker. As a result, the SNR increases, which leads to a smaller BER.

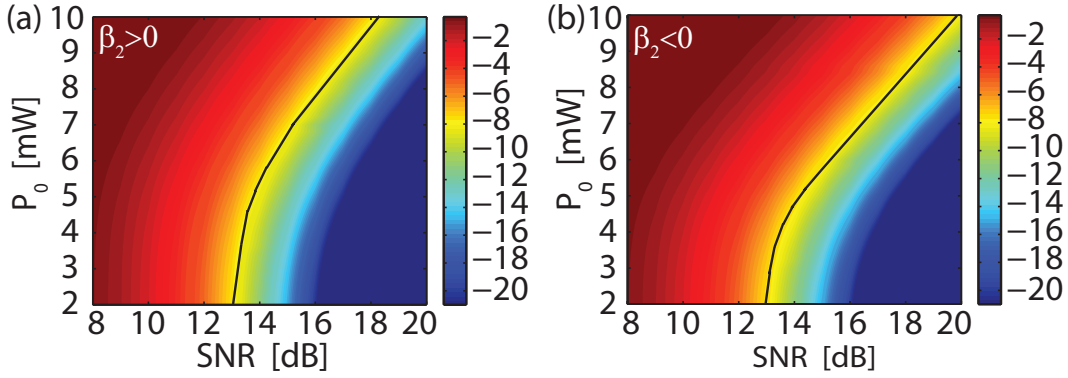

Figure 5.7: Contour maps of $\log_{10}(\text{BER})$ vs. power and SNR. (a), (b) correspond to Si-PhWs with normal and anomalous dispersion, respectively, the waveguides being the same as in Fig. 5.4. The black contours correspond to BER $= 10^{-9}$.

Since both the nonlinear optical effects and FC dynamics are mainly determined by the optical power, we proceeded to analyze in more in-depth the dependence of the system BER on the input power of the CW signal. The results of this study, determined for the waveguides *A* and *B* described in Sec. 5.2, are presented in Fig. 5.7 as contour maps of $\log_{10}(\mathrm{BER})$. While confirming the conclusions illustrated in Fig. 5.4, it can be seen that the maps in Fig. 5.7 reveal additional features. Thus, at low power the BER is almost independent of P_0, which is explained by the fact that in this situation the signal and noise propagates in the linear regime. If the power increases beyond $P_0 \approx 5\,\mathrm{mW}$, however, the FCs generated via TPA as well as the nonlinear effects begin to strongly affect the signal propagation and as a result the BER varies nonlinearly with P_0. Moreover, as expected, low signal degradation is observed at small P_0 and large SNR (the boundary of the domain where the BER has values that are tolerable in regular practical systems, namely $\log_{10}(\mathrm{BER}) \leq -9$, is shown as the black contour in Fig. 5.7).

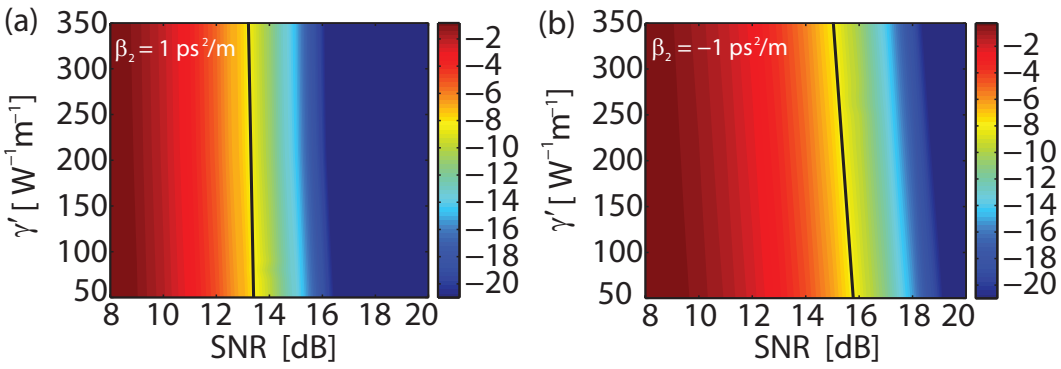

Figure 5.8: Maps of $\log_{10}(\mathrm{BER})$ vs. γ' and SNR. (a), (b) correspond to Si-PhWs with normal and anomalous dispersion, respectively. In both cases $\gamma''/\gamma' = 0.3$, $P_0 = 5\,\mathrm{mW}$, and $L = 5\,\mathrm{cm}$. The black contours indicate a BER of 10^{-9}.

Additional insights into the contribution of nonlinear effects to the system signal degradation are provided by the dependence of the system BER on the waveguide nonlinear coefficient, the corresponding contour maps being presented in Fig. 5.8. We have investigated Si-PhWs with normal ($\beta_2 = 1\,\mathrm{ps}^2\,\mathrm{m}^{-1}$) and anomalous ($\beta_2 = -1\,\mathrm{ps}^2\,\mathrm{m}^{-1}$) dispersion, in both cases the ratio $\gamma''/\gamma' = 0.3$ being kept constant. A comparison between the results shown in Fig. 5.8(a) and Fig. 5.8(b) reveals several interesting features of the system BER. Thus, for Si-PhWs with normal dispersion the BER depends only slightly on γ', as in this case the parametric gain is relatively small. By contrast, the

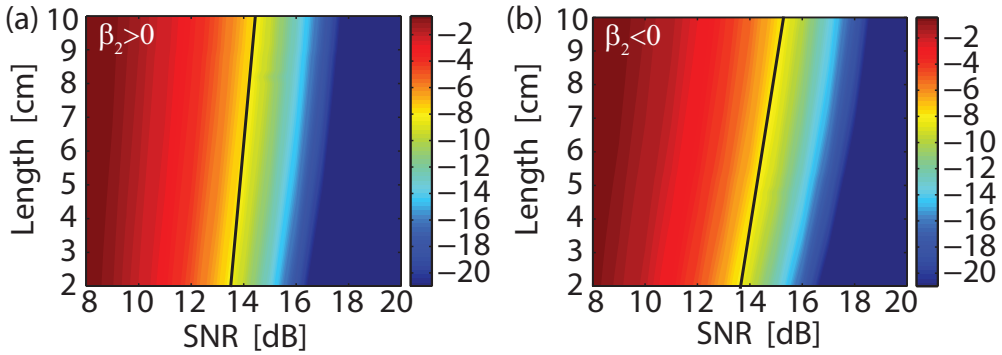

Figure 5.9: Contour maps of $\log_{10}(\mathrm{BER})$ vs. waveguide length and SNR. Panels (a) and (b) correspond to Si-PhWs with normal and anomalous dispersion, respectively, the waveguides being the same as in Fig. 5.4. The input power is $P_0 = 5\,\mathrm{mW}$. The black contours correspond to a BER of 10^{-9}.

BER in the anomalous dispersion regime depends much stronger on γ', due to a much larger parametric gain amplification of the noise. In particular, for the same waveguide (γ) and optical signal (P_0 and SNR) parameters, the system signal degradation is more pronounced in the anomalous dispersion regime.

A key property one employs when assessing the feasibility of using Si-PhWs as on-chip optical interconnects is the relationship between the waveguide transmission BER and the waveguide length, L. In order to characterize this dependence, we have determined the system BER as a function of L, the main results of this study being summarized in Fig. 5.9. We considered Si-PhWs with normal and anomalous dispersion, the calculations being performed for a CW signal with power, $P_0 = 5\,\mathrm{mW}$. One important result illustrated by this figure is that a BER smaller than 10^{-9} can be achieved even when the waveguide length is as large as 10 cm, provided that the SNR is suitably large, namely $\mathrm{SNR} \gtrsim 15\,\mathrm{dB}$. Moreover, as before, it can be seen that the system signal degradation is larger in the case of waveguides with anomalous dispersion.

5.5 Conclusion

In conclusion, we have introduced a novel approach to the evaluation of bit error rates in optical systems containing silicon photonic wires. In order to describe the evolution of the mutually interacting optical field and free-carriers in the silicon photonic wire we employed both a rigorous theoretical model that incorporates all the linear and nonlinear physical effects and the linearized version of this full model, valid in the low noise power limit. The signal degradation in a link containing such a waveguide and a

direct-detection optical receiver made of an optical filter, an ideal square-law photodetector, and an electrical filter was evaluated by using the time domain Karhunen-Loève expansion method. This approach was used to study the dependence of the bit error rate on waveguide and optical signal parameters. In particular, we have determined the domain in the system parameters space in which the signal degradation remains below a certain threshold used in practical settings to assess the fidelity of detected signals. It should be noted that the method introduced here can be easily extended to other silicon based components of on-chip and chip-to-chip optical networks, including modulators, amplifiers, optical switches, and frequency converters. Equally important, our formalism can be applied to physical settings in which additional optical effects can become important. For example, our approach could readily incorporate nonlinear effects such as four-wave mixing and stimulated Raman scattering, which can become large enough to affect the bit error rate in properly designed waveguides or for shorter optical pulses.

In the next chapter, the comparative study of the fast-light and SL regimes within the single-channel silicon photonic crystal systems will be demonstrated, with the system using OOK modulated CW signals.

Bibliography

[1] X. Chen, N. C. Panoiu, and R. M. Osgood, "Theory of Raman-mediated pulsed amplification in silicon-wire waveguides," IEEE J. Quantum Electron. **42**, 160-170 (2006).

[2] A. Papoulis, *Probability, Random Variables, and Stochastic Processes* 3rd ed, (McGraw-Hill, New York, 1991).

[3] G. Bosco, A. Carena, V. Curri, R. Gaudino, P. Poggiolini, and S. Benedetto, "A novel analytical approach to the evaluation of the impact of fiber parametric gain on the bit error rate," IEEE Trans. Commun. **49**, 2154-2163 (2001).

[4] E. Forestieri and M. Secondini, "On the Error Probability Evaluation in Lightwave Systems With Optical Amplification," IEEE J. Lightwave Technol. **27**, 706-717 (2009).

[5] Q. Lin, O. J. Painter, and G. P. Agrawal, "Nonlinear optical phenomena in silicon waveguides: Modeling and applications," Opt. Express **15**, 16604-16644 (2007).

[6] S. Lavdas, J. B. Driscoll, R. R. Grote, R. M. Osgood, and N. C. Panoiu, "Pulse compression in adiabatically tapered silicon photonic wires," Opt. Express **22**, 6296-6312 (2014).

[7] K. Kikuchi, "Enhancement of optical-amplifier noise by nonlinear refractive index and group-velocity dispersion of optical fibers," IEEE Photon. Technol. Lett. **5**, 221-223 (1993).

Chapter 6

Slow-light and Fast-light Regimes of Silicon Photonic Crystal Waveguides: A Comparative Study

6.1 Introduction

In this chapter, we present a detailed analysis of the BER in Si-PhCWs, highlighting the key differences between the dependence of the BER on the parameters defining the optical signal and waveguide when the signal propagates in the FL or SL regime. With emphasis on the characteristics of BER in silicon optical interconnects, we consider a photonic system containing only a Si-PhCW, whose input and output are connected, respectively, to a transmitter and a direct-detection optical receiver, shown in Fig. 6.1(a). However, our model can easily implement other optical components like the ring resonators and multiplexers. We use a pseudorandom bit sequence (PRBS) of $2^9 - 1$ bits plus a zero bit, thus including all possible 9-bit sequence patterns, where each bit is superimposed of an ON-OFF keying (OOK) modulated nonreturn-to-zero (NRZ) optical signal together with a stationary additive white Gaussian noise. To reveal the statistical properties of the transmitted signal we employ the time domain Karhunen-Loève (KL) series expansion (KLSE) method [1–3], whereas the coupled dynamics of the optical field and FCs are described by using a rigorous theoretical model that incorporates both the linear and nonlinear optical effects pertaining to optical signal propagation in Si-PhCWs [4]. Importantly, the KL expansion method allows one to use significantly shorter PRBSs: whereas this method already converges for PRBS-9, Monte-Carlo type

methods could require PRBSs as long as 2^{32} to reach convergence.

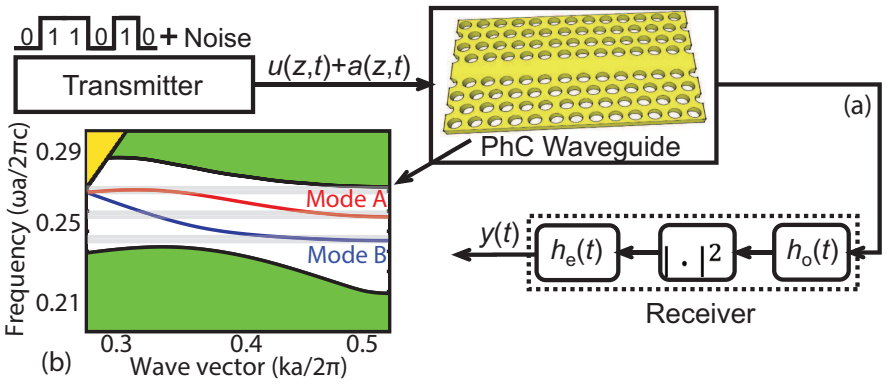

Figure 6.1: (a) Schematic of the photonic system, containing a Si-PhCW and a direct-detection receiver composed of an optical filter, $h_o(t)$, a photodetector, and an electrical filter, $h_e(t)$. (b) Mode dispersion diagram of the Si-PhCW, with grey bands indicating the SL spectral domains $n_g > 20$.

6.2 Optical Properties of Silicon Photonic Crystal Waveguides

The PhC slab waveguide considered here consists of a line defect created by filling in a line of holes oriented along the ΓK direction of a hexagonal hole lattice in a silicon slab [see Fig. 6.1(a)]. The PhC has the lattice constant, $a = 412\,\text{nm}$, hole radius, $r = 0.22a$, and slab thickness, $h = 0.6a$. The photonic band structure of the Si-PhCW, shown in Fig. 6.1(b), shows that the waveguide has two guiding modes, which are SL modes within certain spectral domains shown as grey bands in Fig. 6.1(b). In particular, the mode A has two SL spectral domains, whereas mode B only has one. In these SL regions the group index, $n_g = c/v_g$, second-order dispersion coefficient, $\beta_2 = d^2\beta/d\omega^2$, where β is the mode propagation constant, and nonlinear coefficient, $\gamma = 3\varepsilon_0 a\omega_c\Gamma/(4v_g W)^2$ [5], with ω_c, Γ, and W being the carrier frequency of the signal, effective waveguide nonlinear susceptibility, and mode energy in the unit cell, respectively, have very large absolute values (see Fig. 6.2). This indicates that in the SL regime the linear and nonlinear optical effects are strongly enhanced. In particular, we denote the Si-PhCWs in the FL and SL regime as Si-PhCW-FLs and Si-PhCW-SLs, respectively. Moreover, the all essential parameters of Si-PhCWs that used the simulations of this chapter, are demonstrated in Table 6.1 and Table 6.2.

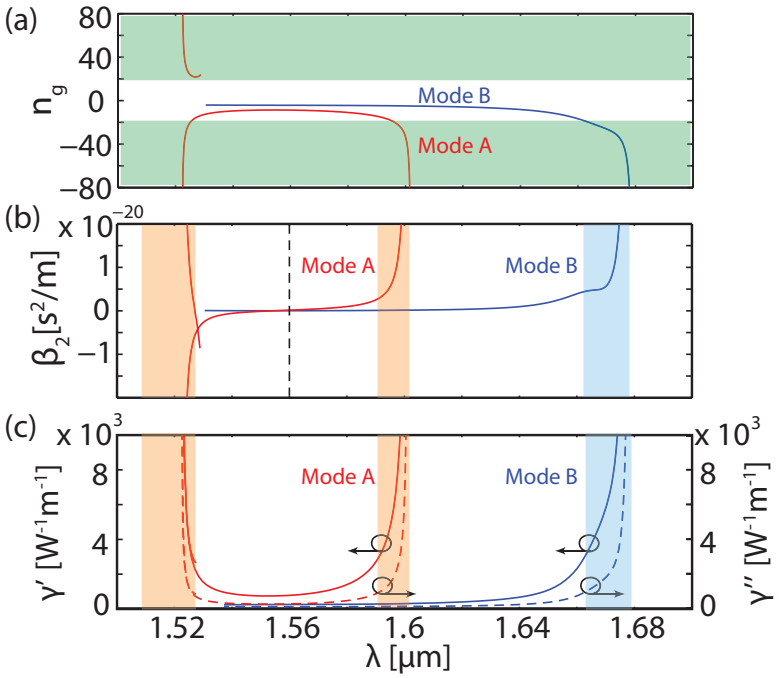

Figure 6.2: (a), (b), (c) Wavelength dependence of n_g, β_2, and γ' and γ'', respectively, determined for mode A (red lines) and mode B (blue lines). The shaded areas correspond to the SL regime, defined by the relation $n_g > 20$.

6.3 Optical Signal Propagation Approach

The full mathematical analysis for the signal propagation in the Si-PhCWs is described by a modified nonlinear Schrödinger equation (Eq. (2.15)), coupled to a rate equation (Eq. (2.20)) for the FCs. Similarly, several optical parameters will be assigned here. The intrinsic loss coefficient α_{in} was set to $\alpha_{\text{in}} = 50\,\text{dB}\,\text{cm}^{-1}$, whose value is chosen due to the roughness of Si-PhCWs. However, the intrinsic loss indeed vary with different values of group index v_g in our model, which is suggested by the first term on the right side of Eq. (2.15). The FC absorption (FCA) coefficient is $\alpha_{\text{fc}} = \sigma_\alpha N$, and the FC-induced refractive index change is assumed to be $\delta n_{\text{fc}} = \sigma_n N$, where $\bar{\lambda} = 1550\,\text{nm}$, N is the FC density, $\sigma_\alpha = 1.45 \times 10^{-21}(\lambda/\bar{\lambda})^2$ (in units of m^2). $\sigma_n = \sigma_0(\lambda/\bar{\lambda})^2$ (in units of m^3), with σ_0 being a power dependent coefficient [6]. The FC relaxation time t_c is 0.5 ns in our analysis. Moreover, all dispersive and nonlinear coefficients of Si-PhCWs are much larger than that of Si-PhWs, which explains the reason why the waveguide length of Si-PhCWs is far shorter than the Si-PhWs.

The input noisy signal is expressed as Eq. (5.1), which consists of the optical CW signal with power $P(z)$ and a complex additive Gaussian noise $a(z,t)$. We have used two methods to determine the optical field at the output of the Si-PhCW. In the first

approach we solved numerically the system of Eq. (2.15) and Eq. (2.20), whereas in the alternative approach we use a computational routine to derive solutions for the linearized model (Eqs. (2.26a)). Note also that the global phase is $\Phi_0 = 0$ in this chapter. The linearized model shows that the power is independent of the phase and noise amplitude, its decay being due to intrinsic losses, FCA, and two-photon absorption (TPA). In addition, the variation of the total phase of the optical field is determined by the FC dispersion (FCD) and nonlinearly induced phase shift. Note also that due to the SL effects ($\gamma \sim v_g^{-2}$), both P and Φ vary much stronger with z in the SL regime.

Table 6.1: Main parameters for the Si-PhCW-FLs used in our simulations.

Parameters	$n_g = 8.64$	$n_g = 10.3$	$n_g = 14.7$	$n_g = 16.1$
λ $[nm]$	1559.2	1538.2	1528.3	1527.1
β_2 $[ps^2/m]$	-5.09·10^1	-1.18·10^3	-5.65·10^3	-7.95·10^3
κ	0.9930	0.9947	0.9954	0.9954
γ' $[W^{-1}m^{-1}]$	755.67	880.7671	1.77·10^3	2.16 ·10^3
γ'' $[W^{-1}m^{-1}]$	230.28	268.3963	539.89	656.97
α_{in} $[dB/cm]$	50	50	50	50
L $[\mu m]$	500	500	500	500

Table 6.2: Main parameters for the Si-PhCW-SLs used in our simulations.

Parameters	$n_g = 20.2$	$n_g = 23.3$	$n_g = 27.7$	$n_g = 34.3$
λ $[nm]$	1525.1	1524.2	1523.6	1523.1
β_2 $[ps^2/m]$	-1.8·10^4	-2.98·10^4	-5.45·10^4	-1.15·10^5
κ	0.9954	0.9953	0.9952	0.9951
γ' $[W^{-1}m^{-1}]$	3.6 ·10^3	5.05 ·10^3	7.7 ·10^3	1.35·10^4
γ'' $[W^{-1}m^{-1}]$	1.1 ·10^3	1.54 ·10^3	2.35 ·10^3	4.12 ·10^3
α_{in} $[dB/cm]$	50	50	50	50
L $[\mu m]$	500	500	500	500

The key differences between the characteristics of the propagation of the optical signal in the FL and SL regimes are illustrated by Fig. 6.3. Thus, we have determined the time and wavelength domain evolution of a noisy signal in a 500 µm-long Si-PhCW, both in the FL ($n_g = 10.3$) and SL ($n_g = 20.2$) regimes, the bit sequence being "01101100". For completeness, we also show in Figs. 6.3(h) and 6.3(i) the dynamics of the photogenerated FCs for one occurrence of the above 8-bit signals. It can be seen that despite the fact that the bit sequence is preserved upon propagation in both cases, the optical signal and noise are distorted much more in the SL regime. In particular, the in-phase noise is strongly compressed in the SL regime, whereas the increased influence of intrinsic losses, FCA, and TPA on the optical field leads to much

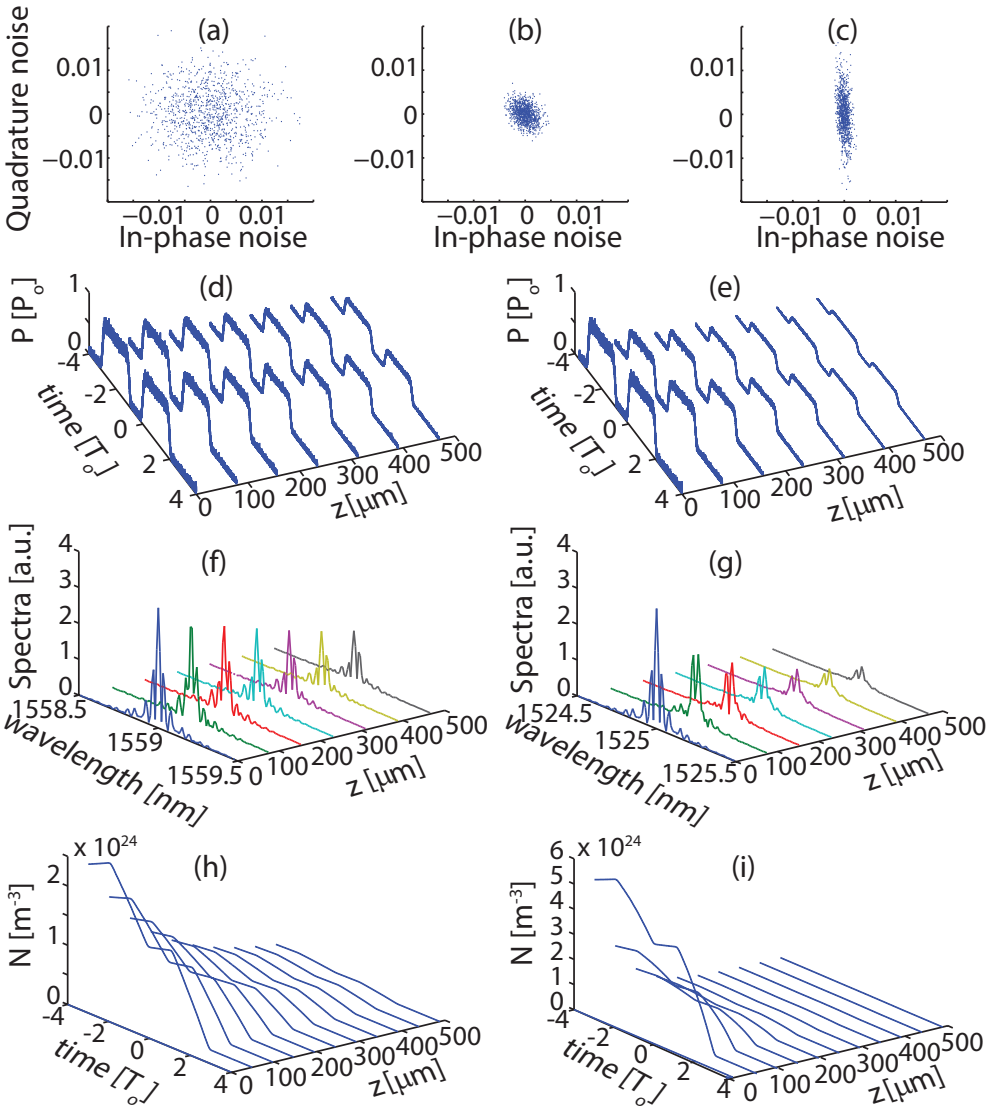

Figure 6.3: (a) In-phase and quadrature noise components at the input of the Si-PhCW. (b), (c) the same as in (a), but determined at the waveguide output in the FL and SL regimes. Second, third, and fourth row of panels show the time domain, spectral domain, and carrier density evolution of a noisy signal with $P_0 = 10\,\text{mW}$ and $T_0 = 100\,\text{ps}$ in a $500\,\mu\text{m}$-long Si-PhCW, respectively, with the left (right) panels corresponding to the FL (SL) regime.

more rapid decay of the optical signal in the SL regime. As a result of enhanced linear and nonlinear optical effects, more than a double amount of FCs is generated in the SL regime, as per Figs. 6.3(h) and 6.3(i). As we will show in what follows, these qualitative differences in the dynamics of the optical signal have direct implications on the BER.

6.4 Results and Anaylsis

In order to compare the system transmission BER in SL and FL regimes we assumed a noisy signal propagating in mode A, the carrier frequency, ω_c, being chosen in such a way that the group index varied from $n_g = 8.64$ in the FL regime to $n_g = 34.3$ in SL case. The signal is assumed to be OOK modulated, with NRZ pulses in a back-to-back configuration and bit window of $T_0 = 100\,\text{ps}$ throughout our investigations. To calculate the transmission BER, we first propagated the optical signal in the Si-PhCW using linearized model, then determined the signal at the back-end of the direct-detection receiver, and finally used the time-domain KL series expansion method to evaluate the BER. Importantly, the linearized model is accurate for the task at hand, and much less computationally demanding as compared to the full model. Full details of this approach can be found in Sec. 3.2 and Sec. 4.3.3. To model the direct-detection receiver, we assumed that the electrical filter is a low-pass integrate-and-dump filter with the 3-dB bandwidth equal to $B_e = 10\,\text{Gb}\,\text{s}^{-1}$, whereas the optical filter is a bandpass Lorentzian with 3-dB bandwidth, $B_o = 4B_e$. Specifically, the two filters are described by the following transfer functions, with $\Gamma_o = B_o/2$:

$$H_o^i(f) = \frac{\Gamma_o^2}{f^2+\Gamma_o^2}, \quad H_o^q(f) = -\frac{\Gamma_o f}{f^2+\Gamma_o^2}, \tag{6.1a}$$

$$H_e^i(f) = \begin{cases} 1, & |f| \le B_e/2 \\ 0, & |f| > B_e/2 \end{cases} \quad H_e^q(f) = 0. \tag{6.1b}$$

The main parameter that determines the transmission BER is the GV, as both the linear and nonlinear optical effects affecting the optical signal propagation strongly depend on it. In particular, by simply varying the frequency of the signal one can tune v_g so as the optical signal propagation changes from the FL to the SL regime. To illustrate this, we varied the signal frequency while keeping constant the input power, $P_0 = 10\,\text{mW}$, and waveguide length, $L = 500\,\mu\text{m}$, and determined the dependence of BER on the signal-to-noise ratio (SNR). The outcomes of this analysis, summarized in Fig. 6.4(a), show that as the signal is tuned deeper into the SL regime by changing n_g from 8.64 to 34.3 the signal impairments increase dramatically, the BER change of 60 dB when SNR = 25 dB. Since in the back-to-back system configuration the BER is independent of the properties of optical signals (e.g., carrier frequency) and waveg-

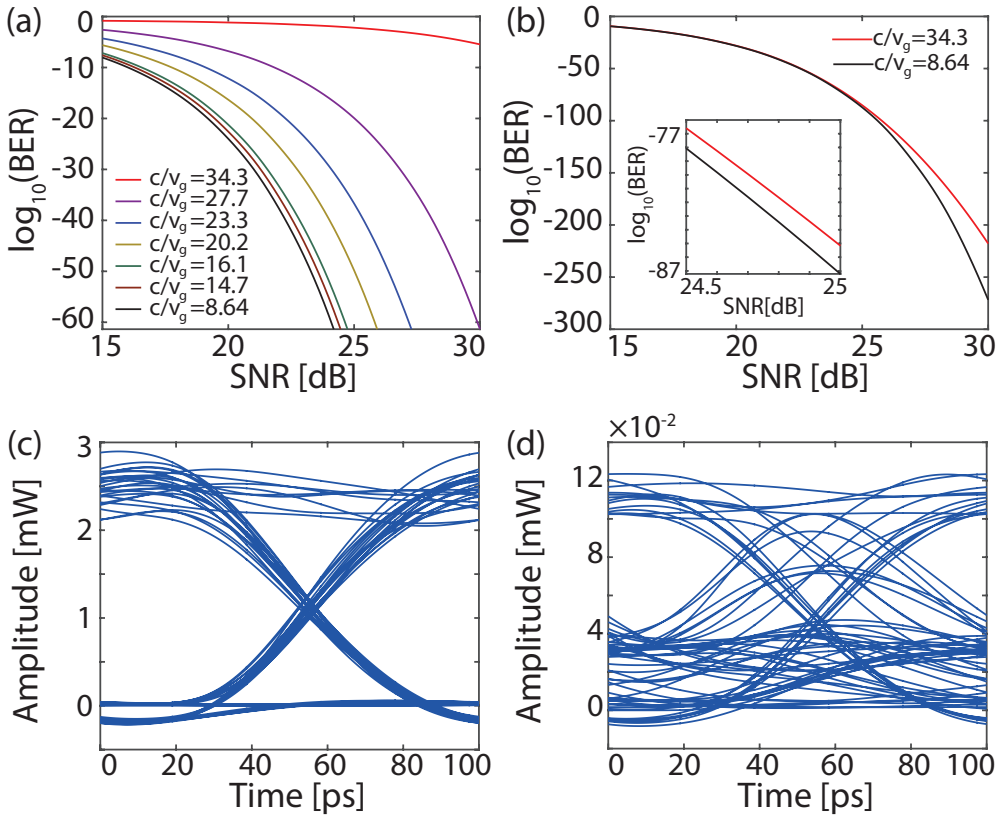

Figure 6.4: Top panels show the system BER calculated for the Si-PhCW with FC dynamics included (left) and by neglecting them (right). Bottom panels show the eye diagrams corresponding to $n_g = 8.64$ (left) and $n_g = 27.7$ (right), both at SNR $= 25$ dB. In all panels, $P_0 = 10$ mW and $L = 500$ µm.

uide coefficients, one can determine the penalty caused by inserting the Si-PhCW after comparing Fig. 6.4(a) with Fig. 4.2(a) (BER calculated for the system without a Si waveguide).

Table 6.3: Characteristic length of FCA and TPA for different group-index.

n_g	L_{FCA} [m]	L_{TPA} [m]
34.3	0.0044	0.0226
27.7	0.0095	0.0397
23.3	0.0172	0.0606
20.2	0.0278	0.0851
16.1	0.0583	0.1425
14.7	0.0777	0.1737
8.64	0.3034	0.4231

These results raise a key question: is this signal degradation primarily related to the linear and nonlinear optical effects in the Si-PhCW or it is due the influence of the generated FCs on the signal propagation? To answer this question, we investigated two cases of optical signal propagation in the Si-PhCW, in both instances setting the

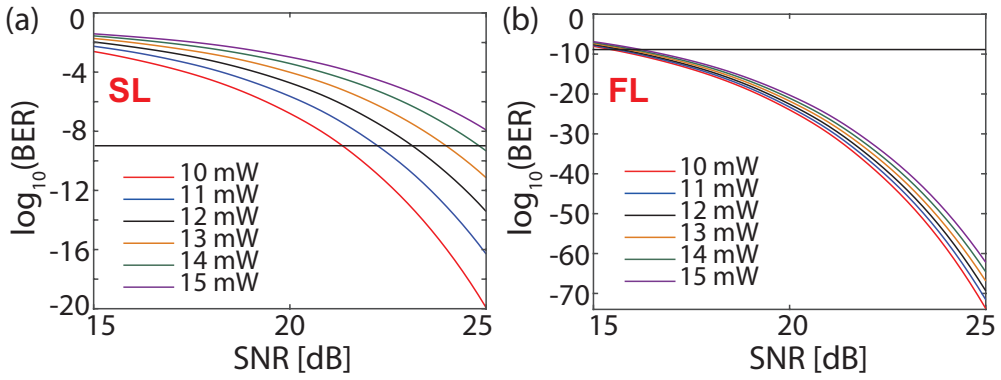

Figure 6.5: (a), (b) System BER vs. SNR, calculated for different P_0, in the SL ($n_g = 27.7$) and FL ($n_g = 8.64$) regimes, respectively. The horizontal black line indicates a BER of 10^{-9}.

FC density to zero by imposing $\gamma'' = 0$. For a better illustration of the conclusion of this study, we performed the simulations for the largest and smallest value of n_g in Fig. 6.4(a), the results being shown in Fig. 6.4(b). Thus, it can be seen that the variation of BER with SNR is extremely weakly dependent on n_g, a result that suggests that, unlike the case of optical fibers, the transmission BER is primarily determined by the FCs. In order to explore the in-depth physical mechanism for the BER degradation in Fig. 6.4, we show in Table 6.3 the characteristic lengths of FCA and TPA, L_{FCA} and L_{TPA}, respectively, calculated for several values of n_g and for power $P_0 = 10\,\text{mW}$ and $T_0 = 100\,\text{ps}$. In particular, it can be seen that for all values of n_g, $L_{FCA} < L_{TPA}$. Therefore, FCA effects play the main role in BER degradation. Moreover, note that although apparently FCA is a linear effect, because of the implicit dependence of the FCA coefficient on the FCs density (and consequently on optical power), FCA depends nonlinearly on the optical power - see also Eq. (2.26a). In addition, the system performance without FCs is far better than in the case when FCs dynamics are included, especially in the SL regime. The degradation of the transmitted signal when the Si-PhCW operation is shifted from the FL to the SL regime is illustrated by the eye diagrams presented in Figs. 6.4(c) and 6.4(d), too. In particular, due to increased optical interactions in the SL regime, the eye diagram almost completely closes as n_g increases from 8.64 to 27.7, with both strong power fluctuations and bit window shifts being observed in the SL regime.

Since the optical power is the main parameter that determines the strength of the nonlinear optical effects, including the TPA as the source of FCs, we have calculated

the dependence of the BER on the SNR, for different values of P_0. The results of these calculations, presented in Fig. 6.5, show that, irrespective of P_0, a much better system performance is achieved in the FL regime ($n_g = 8.64$) than in the SL regime ($n_g = 27.7$). This is primarily due to the fact that the Si-PhCW operating in the SL regime has a much larger nonlinear coefficient, which leads both to a larger parametric gain amplification of the noise and to increased amount of FCs. To be more specific, γ is proportional to v_g^{-2} and therefore in the SL regime the parametric gain responsible for noise amplification ($\sim\gamma'$) and TPA ($\sim\gamma''$) are enhanced. Consequently, the signal degradation increases, leading to larger BER. In addition, TPA increases with P_0, too, which explains why the BER increases with P_0. One last idea illustrated by Fig. 6.5 is that in the SL regime the BER varies much stronger with P_0 as compared to this power variation in the FL regime.

6.5 Conclusion

In conclusion, we studied the transmission BER in silicon photonic crystal waveguides and contrasted the results obtained in two relevant cases, namely when the optical signal propagates in the fast- and slow-light regimes. Our analysis revealed that although slow-light effects provide the key advantage of increased nonlinearity, they also lead to detrimental consequences, including a significant degradation of the transmission BER. Theoretical and computational investigations showed that the signal impairments are primarily due to the generation of free carriers.

When compared with the OOK modulation, the PSK modulated signals have advantage in increasing the spectral efficiency and enlarging the system capacity. Therefore, the study of single-channel Si photonic systems that utilizing higher-order PSK modulation will be described in the next chapter.

Bibliography

[1] A. Papoulis, *Probability, Random Variables, and Stochastic Processes* 3rd ed, (McGraw-Hill, New York, 1991).

[2] G. Bosco, A. Carena, V. Curri, R. Gaudino, P. Poggiolini, and S. Benedetto, "A novel analytical approach to the evaluation of the impact of fiber parametric gain on the bit error rate," IEEE Trans. Commun. **49**, 2154-2163 (2001).

[3] J. You, and N. C. Panoiu, "Calculation of Bit Error Rates in Optical Systems with Silicon Photonic Wires," IEEE J. Quantum Electron. **51**, 8400108 (2015).

[4] N. C. Panoiu, J. F. McMillan, and C. W. Wong, "Theoretical Analysis of Pulse Dynamics in Silicon Photonic Crystal Wire Waveguides," IEEE J. Sel. Top. Quantum Electron. **16**, 257-266 (2010).

[5] S. Lavdas and N. C. Panoiu, "Theory of Pulsed Four-Wave-Mixing in One-dimensional Silicon Photonic Crystal Slab Waveguides," Phys. Rev. B **93**, 115435 (2016).

[6] Q. Lin, O. J. Painter, and G. P. Agrawal,"Nonlinear optical phenomena in silicon waveguides: Modeling and applications," Opt. Express **15**, 16604-16644 (2007).

Chapter 7

Exploiting Higher-order PSK Modulation and Direct-detection in Single-channel Silicon Photonic Systems

7.1 Introduction

In this chapter, we study theoretically the performance of photonic systems containing single-channel Si-PhWs or Si-PhCWs and utilizing PSK, OOK, and ASK-PSK modulated signals. The system investigated in this work consists of a single-mode Si-PhW or Si-PhCW, the latter being operated either in the fast-light (FL) or slow-light (SL) regime, linked to a direct-detection receiver containing an intensity-detect branch and phase-detect branch (see Fig. 7.1). The system dynamics was described by a modified nonlinear Schrödinger equation governing the propagation of the optical field coupled to a standard rate equation describing the evolution of free-carriers (FCs) [1–5]. Moreover, the statistical properties of the transmitted signal were analyzed using the frequency-domain Karhunen-Loève (KL) method [6, 7]. This analysis was performed for different values of key system parameters and for several modulation formats.

The chapter is organized as follows. In Sec. 7.2, we introduce the models that govern the propagation of the noisy signal in the Si waveguides. Then, in Sec. 7.3, we describe the advanced modulation formats and the details of direct-detection receivers considered in this work. This is followed by the description of the bit-error rate (BER)

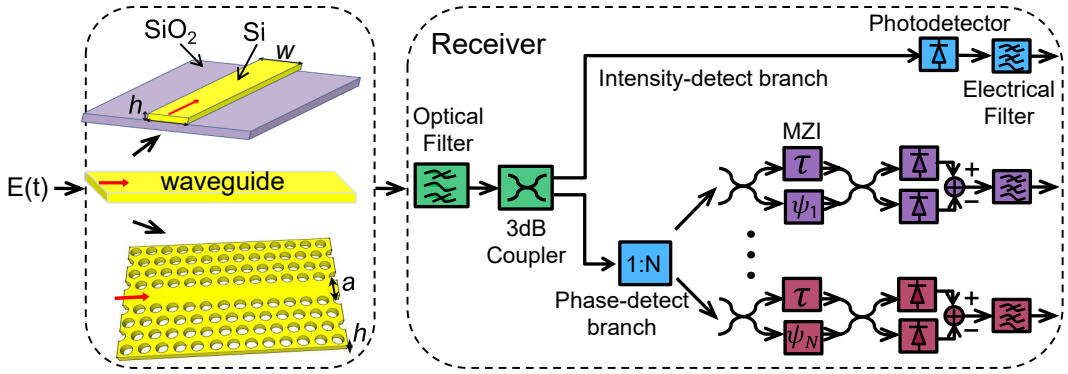

Figure 7.1: Schematics of the Si photonic system investigated in this work. It contains a Si waveguide and a direct-detection receiver with bi-level electrical decisions. The receiver has two branches, an intensity-detection and a phase-detection branch, with the latter consisting of N Mach-Zehnder interferometers. Two types of waveguides are investigated: one is a strip waveguide with uniform cross-section with height, $h = 250\,\text{nm}$, and width, $w = 900\,\text{nm}$ and the other one is a PhC waveguide with lattice constant, $a = 412\,\text{nm}$, hole radius, $r = 0.22a$, and slab thickness, $h = 0.6a$.

calculation method, which is presented in Sec. 7.4. These theoretical and computational tools are used in Sec. 7.5 to analyze the system performance corresponding to several modulation formats, for different values of the main system parameters. Finally, the main results are summarized in the last section.

7.2 Theory of Propagation of Optical Signals in Silicon Waveguides

In this section, a rigorous theoretical model (Eq. (2.15) and Eq. (2.20)) is utilized to describe the coupled dynamics of the optical field and FCs in Si waveguides. In this analysis, the input optical field is assumed to consist of a superposition between the PSK signal and complex additive white Gaussian noise (AWGN), and the mutual interaction between the optical signal and noise is mediated by FCs and nonlinear optical effects. In order to reduce the computational time, a linearized model of the full propagation model (Eqs. (2.26a)) is also employed, which is derived in the vanishingly small noise limit.

Two types of Si waveguides are considered in this work, as illustrated in the first block of Fig. 7.1. Thus, one is a single-mode Si-PhW buried in SiO_2, with uniform cross-section of height, $h = 250\,\text{nm}$, and width, $w = 900\,\text{nm}$. The other one is a Si-PhCW consisting of a line defect along the ΓK direction of a PhC slab waveguide with

Table 7.1: The optical parameters of silicon waveguides used in numerical simulations.

Waveguide type	λ	α_i [dB cm^{-1}]	β_2 [ps^2 m^{-1}]	γ' [W^{-1} m^{-1}]	γ'' [W^{-1} m^{-1}]
Si-PhW	1550	1	0.5	166.8	50.8
Si-PhCW-FL	1550	50	-3.3×10^2	750.1	228.6
Si-PhCW-SL	1524	50	-4.3×10^4	6.94×10^3	2.12×10^3

honeycomb air hole lattice with lattice constant, $a = 412\,\text{nm}$, hole radius, $r = 0.22a$, and slab thickness, $h = 0.6a$. The Si-PhCW is designed to possess both FL and SL spectral regions [8], referred to as Si-PhCW-FL and Si-PhCW-SL, respectively, so as to facilitate the study of the dependence of the system performance on the linear and nonlinear optical coefficients of the waveguide. More specifically, due to their strong dependence on the GV, in the SL regime both the linear and nonlinear optical effects are significantly enhanced as compared to the FL regime. The optical coefficients of the silicon waveguides are given in Table 7.1, whereas t_c is set to 0.5 ns [9] in all our calculations.

7.3 Optical Direct-detection Receivers for High-order PSK Modulated Signals

In this section, we introduce and briefly discuss the constellation diagrams of PSK and ASK-PSK signal modulation formats as these tools play a central role in our study. To this end, we show in Fig. 7.2 the symbols of 2PSK and high-order PSK (4PSK, 8PSK, and 16PSK), as well as those of ASK-PSK (A2PSK and A4PSK). As can be seen in these diagrams, in the case of PSK modulation formats all symbols have the same power, whereas for A2PSK and A4PSK each of the two and four symbols are located on two different power rings.

Let us consider now how the functionality of direct-detection receivers for high-order PSK signals is implemented using Mach-Zehnder interferometers (MZIs) [10, 11], that is how to convert phase modulation into intensity modulation before the photodiode square-law detection stage. To be more specific, in Fig. 7.1 we schematically illustrate a phase detection scheme employing N MZIs with properly chosen phase shifts, N representing half of the number of phase states ($N = m/2$ for mPSK signals). For each MZI, the delay time is one symbol interval and the particular value of the phase shift depends on the particular PSK format.

The direct-detection process pertaining to PSK signals can be briefly summarized as follows: The received optical signal is filtered by an optical bandpass filter and subsequently passed on to N MZIs, which demodulate the received PSK signal. Then, the demodulated signals pass through ideal photodiodes yielding photocurrents proportional to the difference between the intensities at the output ports of the previous MZI. Finally, these photocurrents are lowpass filtered by electrical filters. By performing bilevel electrical decisions on the resulting N photocurrents, the direct-detection process of the optical signal is completed. When applied to ASK-PSK signals, an additional branch for intensity detection must be used for a separate evaluation of the signal intensity. For example, for 4PSK and 8PSK modulation formats, two and four MZIs are needed for the direct-detection process, respectively [12–14].

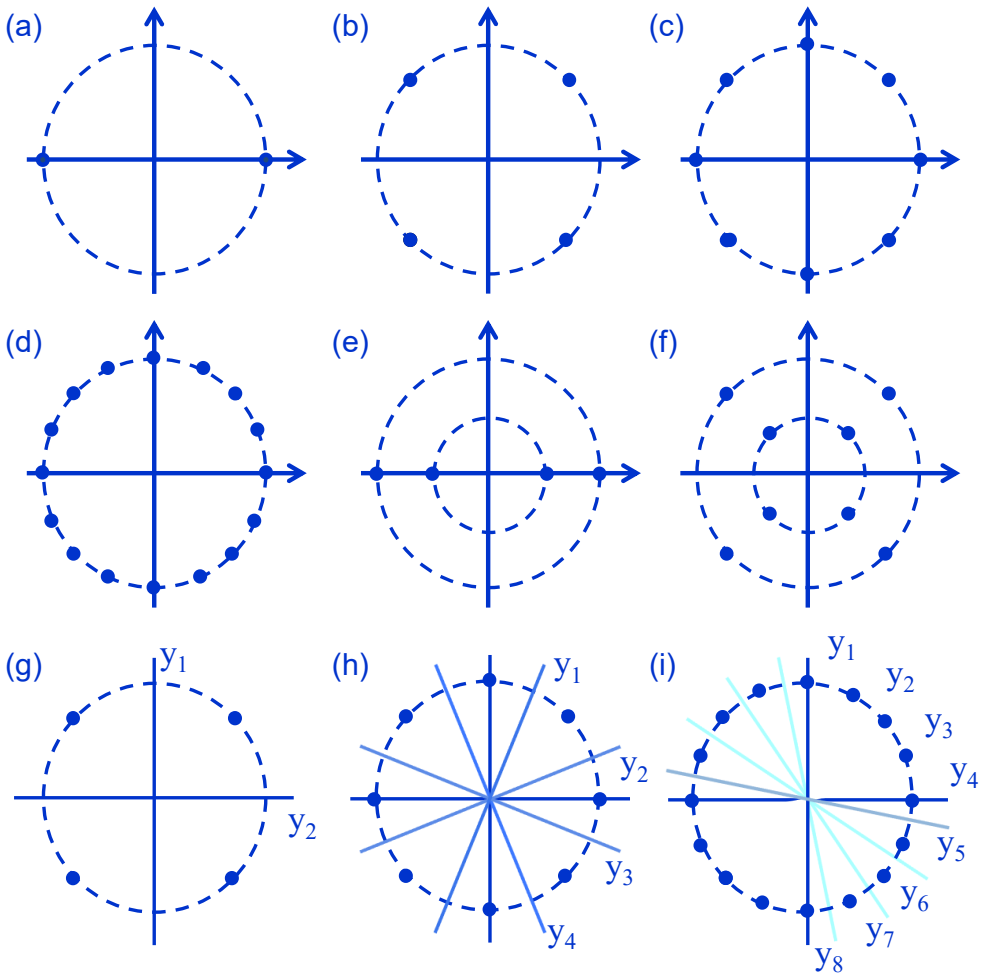

Figure 7.2: Constellation diagrams of the investigated signal modulation formats. (a), (b), (c), (d), (e), (f), are for 2PSK, 4PSK, 8PSK, 16PSK, A2PSK, and A4PSK modulation, respectively. (g), (h), (i) The decision boundaries for 4PSK, 8PSK, and 16PSK modulation formats.

7.4 Methods for Analysis of Direct-detection of PSK and ASK-PSK Signals

In this section we present a general formalism for the characterization of direct-detection of PSK and ASK-PSK signals with particular emphasis on BER calculations. As an illustration of the general formalism, we show how it applies to the 8PSK modulation format.

7.4.1 General Case

Our general approach to BER calculations is based on the frequency-domain KL series expansion of the transmitted signal. Importantly, the KL expansion method allows one to use much shorter pseudorandom bit sequences (PRBSs): whereas it already converges for PRBS-9, Monte-Carlo type methods could require PRBSs as long as 2^{32} to reach convergence [11].

The basic idea of KL expansion is to obtain the decision variable as a sum of uncorrelated and independent random variables *via* a set of orthonormal functions. Thus, starting from the frequency-domain signal at the output of the waveguide, $X(f)$, the decision variable for the nth port, $n = 1,\ldots,N$, is expressed as a double Fourier transform:

$$y_n(t) = \int_{-\infty}^{\infty}\int_{-\infty}^{\infty} X^*(f_1)K_n(f_1,f_2)X(f_2)e^{2\pi i(f_2-f_1)t}df_1df_2, \tag{7.1}$$

where the kernel $K_n(f_1,f_2)$ is

$$K_n(f_1,f_2) = H_o^*(f_2)H_o(f_1)H_e(f_1-f_2)[H_{n,U}^*(f_2)H_{n,U}(f_1) - H_{n,L}^*(f_2)H_{n,L}(f_1)]. \tag{7.2}$$

Here, $H_o(f)$, $H_e(f)$, $H_{n,U}$, and $H_{n,L}$ are the transfer functions of the bandpass optical filter, lowpass electrical filter, and the upper and lower branch of the nth MZI with the corresponding couplers included, respectively [12]. The specific forms of $H_{n,U}$ and $H_{n,L}$ depend on the type of the PSK signal. Thus, for mPSK, neglecting the phase error in MZIs, these functions are:

$$H_{n,U}(f) = \frac{1}{2}C_r\left(e^{-2\pi ifT_s} + e^{i\phi_n}\right), \tag{7.3a}$$

$$H_{n,L}(f) = \frac{1}{2}C_r\left(e^{-2\pi ifT_s} - e^{i\phi_n}\right), \tag{7.3b}$$

where T_s is the symbol duration, ϕ_n is the phase shift of the nth MZI, and C_r represents the coupler coefficients for mPSK and are given by $C_r = (\sqrt{2}/2)^r$, $r = \log_2 m - 1$.

The BER calculation for each MZI port is performed by using discrete Fourier transform. Thus, the frequency interval is discretized to a discrete-frequency vector with equally spaced values separated by Δf. Then, the decision variable in Eq. (7.1) can be written as a double sum,

$$y(t) = \sum_{\alpha=1}^{2M+1} \sum_{\beta=1}^{2M+1} x_\alpha^* K_{\alpha\beta} x_\beta, \tag{7.4}$$

where for convenience the port index n has been dropped and

$$x_\alpha = X(f_\alpha) e^{2\pi i f_\alpha t} \sqrt{\Delta f}, \tag{7.5a}$$

$$K_{\alpha\beta} = K(f_\alpha, f_\beta) \Delta f. \tag{7.5b}$$

Here, M is an integer chosen such that the entire relevant frequency interval is covered and $f_\alpha = (\alpha - 1 - M)\Delta f$, $\alpha = 1, \ldots, 2M+1$.

For later convenience, we now recast Eq. (7.4) into a real-valued equation. For this, the signal is converted to a real column vector by concatenating the real and imaginary parts of the vector, $\{x_\alpha\}$, namely $\mathbf{x} = [x' \;\; x'']^T$, and the kernel K is similarly converted to a $(4M+2) \times (4M+2)$ real matrix, $\mathbf{K} = [K' \;\; -K''; \; K'' \;\; K']$. As a result of these manipulations, the decision variable $y(t)$ can be expressed as:

$$y(t) = \mathbf{x}^T \mathbf{K} \mathbf{x}. \tag{7.6}$$

The covariance matrix associated to statistical variable $\mathbf{x}$, $\mathbf{R} = \mathbb{E}\{\mathbf{x}\mathbf{x}^T\}$ where $\mathbb{E}\{\cdot\}$ denotes the statistical expectation operator, can be factorized in Cholesky decomposition as $\mathbf{R} = \Sigma\Sigma^T$, where Σ is a lower-triangular matrix. An orthogonal matrix, Λ, is then constructed so as to diagonalize the real symmetric matrix $\Sigma^T \mathbf{K} \Sigma$, namely:

$$\left\{\Lambda^T \Sigma^T \mathbf{K} \Sigma \Lambda\right\}_{\alpha,\beta} = \eta_\alpha \delta_{\alpha,\beta}, \tag{7.7}$$

where $\eta_\alpha, \alpha = 1, \ldots, 4M+2$, are real-valued eigenvalues. If we introduce the new multivariate random variable $\mathbf{w} = \Lambda^T \Sigma^{-1} \mathbf{x} \equiv \Lambda^T \Sigma^{-1} \mathbf{s} + \Lambda^T \Sigma^{-1} \mathbf{n}$, where $\mathbf{s}$ and $\mathbf{n}$ are

the signal and noise part of **x**, respectively, the decision variable becomes:

$$y(t) = \sum_{\alpha=1}^{4M+2} \eta_\alpha w_\alpha^2. \tag{7.8}$$

The statistical properties of **w** can be easily derived from those of **x**, as follows:

$$\mathbb{E}\{\mathbf{w}\} = \Lambda^T \Sigma^{-1} \mathbb{E}\{\mathbf{s}+\mathbf{n}\} = \Lambda^T \Sigma^{-1} \mathbb{E}\{\mathbf{s}\} \equiv \sigma, \tag{7.9a}$$

$$\mathbb{E}\{\mathbf{w}\mathbf{w}^T\} = \mathbb{E}\{\Lambda^T \Sigma^{-1} \mathbf{x}\mathbf{x}^T {\Sigma^{-1}}^T \Lambda\} \equiv I, \tag{7.9b}$$

where we have used the fact that $\mathbb{E}\{\mathbf{n}\} = 0$ and the variable σ is defined as $\Lambda^T \Sigma^{-1} \mathbb{E}\{\mathbf{s}\}$. These relations show that the correlation matrix of the multivariate random variable **w** is diagonal, which means that its components are mutually uncorrelated. Using these results, the moment-generation function Ψ_y of the decision variable $y(t)$ can be written as:

$$\Psi_y(s) = \mathbb{E}\{e^{-sy}\} = \prod_{\alpha=1}^{4M+2} \frac{\exp\left(\frac{\eta_\alpha \sigma_\alpha^2 s}{\sqrt{1-2\eta_\alpha s}}\right)}{\sqrt{1-2\eta_\alpha s}}. \tag{7.10}$$

By using the saddlepoint approximation, we can calculate the probability $\mathscr{P}(y > y_{th}|s=0)$ [$\mathscr{P}(y < y_{th}|s=\sqrt{P})$] for an error to occur when a "0" ["1"] bit is detected. Finally, the transmission BER for the nth port can be evaluated from the following relation:

$$\mathscr{P} = \frac{1}{2}\left[\mathscr{P}(y > y_{th}|s=0) + \mathscr{P}(y < y_{th}|s=\sqrt{P})\right]. \tag{7.11}$$

7.4.2 Application to 8PSK Modulation Format

We now illustrate how the formalism just presented can be applied to the 8PSK modulation formats. Four MZIs and bi-level electrical decision are used in 8PSK receiver, amounting to four decision currents [6]. The Hermitian kernels $K_n(f_1, f_2)$, $n = 1, ..., 4$ are calculated using Eq. (7.3), with $n \in \{1,2,3,4\}$, MZI phase shift $\phi_n \in \{3\pi/8, \pi/8, -\pi/8, -3\pi/8\}$, $C_r = 1/2$, $T_s = 3T_0$, with T_0 being the bit window.

The decision thresholds in the signal space, which are required to decide whether an error has occurred during the signal transmission, are illustrated in Fig. 7.2(h). There are four decision boundaries, labeled by y_1, y_2, y_3, and y_4, the angles of their directions

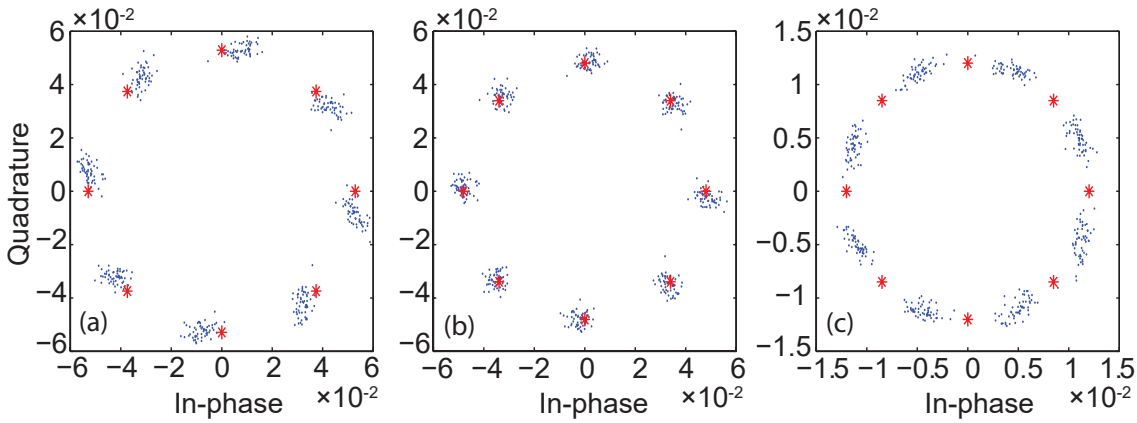

Figure 7.3: (a), (b), (c) Signal constellation of 8PSK signals with SNR = 25 dB and P = 10 mW, at the output of a Si-PhW, Si-PhCW-FL, and Si-PhCW-SL, respectively. The dots indicate the noisy signals and the asterisks represent the ideal output signal without noise and phase shift.

being chosen to be consistent with the four MZI phase-shift values. Note that there are alternative choices for decision boundaries for 8PSK modulated signals, their advantages and disadvantages being thoroughly discussed in [14]. We also provide the threshold boundaries for 4PSK and 16PSK signals in Figs. 7.2(g) and 7.2(i), respectively, since they are important when performing the signal decoding and BER estimation. One common feature of threshold-boundary diagrams is that all decision axes coincide with constant phase lines and, in order to ensure optimum performance, are chosen in such a way that they are located at the maximum distance from adjacent symbols. This type of decision threshold is referred to "arg-decision" [10]. Finally, the overall BER is calculated by combining the BER obtained at each output port and is given by [13]:

$$BER = \frac{1 - \prod_{n=1}^{4}(1 - BER_n)}{3}. \tag{7.12}$$

It is instructive to explore the location in signal space and eye diagrams of 8PSK signals before being converted into electrical currents. We start with the distribution of the 8PSK signals at the output of the Si waveguides and plot it in Fig. 7.3. In these calculations we assumed that the power is $P = 10\,\text{mW}$ and the length of the Si-PhW (Si-PhCW) is $L = 5\,\text{cm}$ ($L = 500\,\mu\text{m}$). Note that in what follows we used these same values of the system parameters, unless otherwise specified. One important conclusion revealed by these calculations is that the phase spread is similar for Si-PhCW-FL and Si-PhW but is significantly smaller as compared to that of Si-PhCW-SL. On the other

hand, the signal amplitude spread in the three cases has similar values. One possible explanation of this finding is that for Si γ'' is about an order of magnitude smaller than γ', meaning that TPA has a weaker effect on the power, as compared to the extent to which SPM affects the phase. We see that even though the length of Si-PhCW is $100\times$ shorter than that of the Si-PhW, the Si-PhCW operating in the FL regime leads to much less degraded signals.

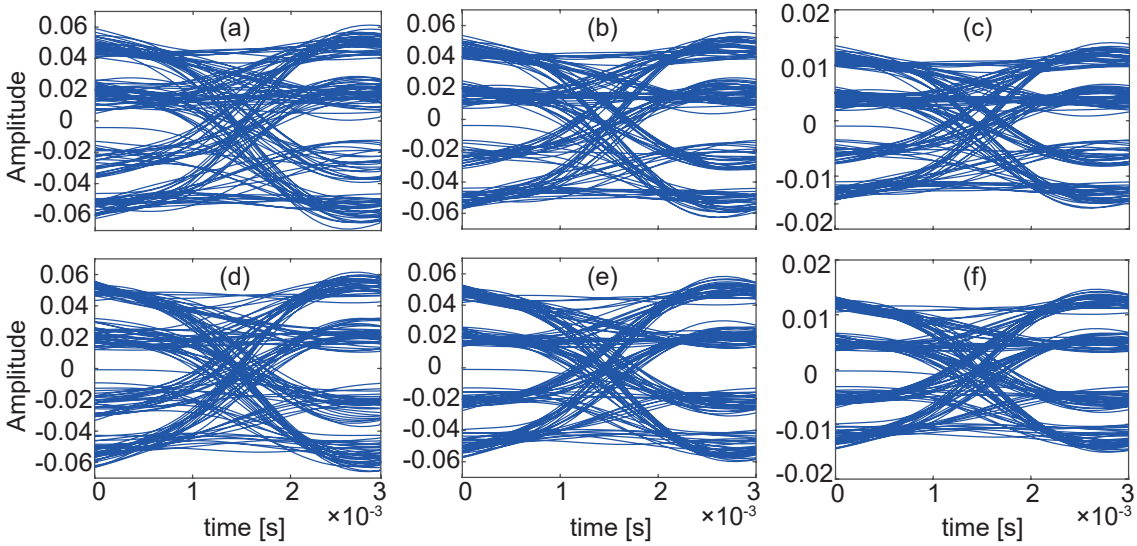

Figure 7.4: Top and bottom panels show the eye diagrams of real and imaginary part of received 8PSK signals after fifth-order Butterworth optical filter, respectively. From left to right, the panels correspond to the Si-PhW, Si-PhCW-FL, and Si-PhCW-SL. The input power $P = 10\,\text{mW}$, SNR $= 25\,\text{dB}$, and lengths of Si-PhW and Si-PhCW are 5 cm and 500 µm, respectively.

The eye diagrams of the real and imaginary parts of 8PSK signals, after passing through fifth-order Butterworth optical filter, are shown in Fig. 7.4. The top and bottom panels represent the real and imaginary part of signals, respectively. These eye diagrams show that the amplitude decay is comparable in the Si-PhW and Si-PhCW-FL systems, but is much larger in the Si-PhCW-SL system, a fact explained by increased linear and nonlinear losses in the SL regime. Moreover, the eye opening is the smallest in the Si-PhCW-SL system when the eye diagrams are normalized so that a fair comparison can be made. This conclusion agrees with the results presented in Fig. 7.3.

7.5 Results and Discussion

We begin this section by describing the set-up of the numerical simulations. Thus, we use a PRBS of $2^9 - 1$ bits plus a zero bit, hence including all possible 9-bit sequence

patterns. The bit window is $T_0 = 100\,\text{ps}$ and all MZIs in the direct-detection receivers have a time delay of $T_s = 3T_0$ and modulation-type related phase shifts. Note that the FC relaxation time (0.5 ns) is much shorter than the total time of the bit sequence (51.2 ns), which means that steady state is reached in our calculations. In addition, we choose low-pass integrate-and-dump electrical filters with the 3-dB bandwidth, $B_e = 10\,\text{Gb}\,\text{s}^{-1}$, and bandpass Lorentzian optical filters with the 3-dB bandwidth, $B_o = 4B_e$ [15]. In order to illustrate the capabilities of our model, other types of filter configurations are considered, too.

Before presenting the main results of our analysis of the system performance, we discuss the physical conditions in which our theoretical model is valid as well as the main physical effects that influence the BER. Thus, if we assume that the signal power is $P = 5\,\text{mW}$, the corresponding FC loss coefficient of the Si waveguides, α_{fc}, is $1.4 \times 10^{-3}\,\text{dB}\,\text{cm}^{-1}$, $1.38 \times 10^{-2}\,\text{dB}\,\text{cm}^{-1}$, and $1.24 \times 10^{-1}\,\text{dB}\,\text{cm}^{-1}$ for the Si-PhW, Si-PhCW-FL, and Si-PhCW-SL, respectively, all these values being very small compared to the intrinsic loss coefficient of the Si-PhW ($1\,\text{dB}\,\text{cm}^{-1}$) and Si-PhCW ($50\,\text{dB}\,\text{cm}^{-1}$). The same conclusion holds for δn_{fc}, the corresponding values being -7.91×10^{-7}, -7.73×10^{-6}, and -6.93×10^{-5}, that is well within the bounds where FC response is linear. We now turn our attention to the relative strength of dispersive and nonlinear effects. Using the values in Table 7.1, we find that for $P = 10\,\text{mW}$ and $T_0 = 100\,\text{ps}$ the dispersion length is $L_D = 2 \times 10^4\,\text{m}$, $L_D = 30\,\text{m}$, and $L_D = 0.24\,\text{m}$ for the Si-PhW, Si-PhCW-FL, and Si-PhCW-SL, respectively, whereas the corresponding nonlinear lengths are $L_{NL} = 1.97\,\text{m}$, $L_{NL} = 0.13\,\text{m}$, and $L_{NL} = 0.014\,\text{m}$. This shows that nonlinearity plays a much more important role than the waveguide dispersion in defining the optical signal dynamics.

The BER for all modulation formats was simulated for different values of the signal-to-noise ratio (SNR), for the Si-PhW, Si-PhCW-FL, and Si-PhCW-SL systems depicted in Fig. 7.1, the results being summarized in Fig. 7.5. A first conclusion of these numerical investigations is that the system BER increases as the order of PSK signal increases. In particular, ranked from the highest to lowest BER, the modulation formats are 16PSK, 8PSK, A4PSK, A2PSK, 4PSK, and 2PSK. Note that in the case of A4PSK and A2PSK signals, the power in the outer circle was chosen to be twice as large as that in the inner one and since we set the average power to be the same in

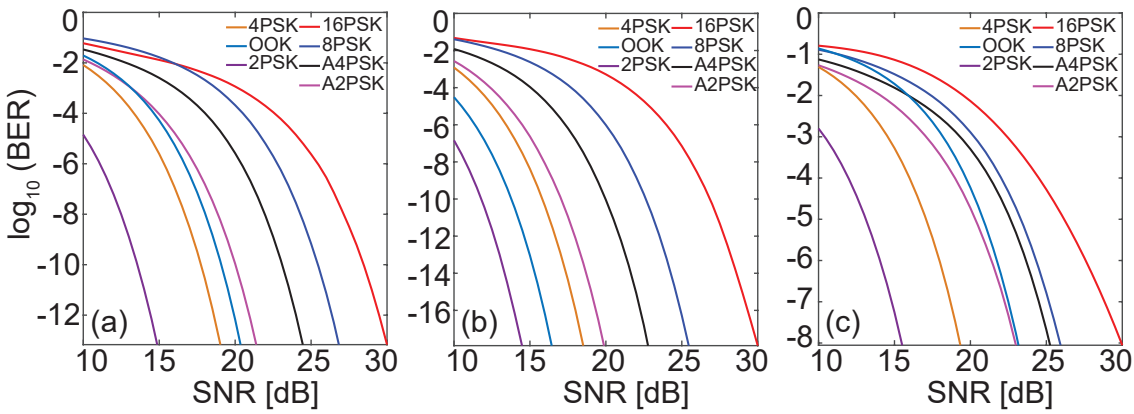

Figure 7.5: System BER of various modulation formats for direct-detection receivers with bi-level decision. From left to right, the panels correspond to a Si-PhW, a Si-PhCW operated in the FL regime, and a Si-PhCW operated in the SL regime. Here, $P =$ 10 mW, and lengths of Si-PhW and Si-PhCW are 5 cm and 500 µm, respectively.

all simulations, the power of OOK for bit "1" is twice as large as the average power. Moreover, these power considerations make it easy to understand why OOK and PSK signals have different signal quality after detection, namely because the average not the peak optical power is the power parameter directly related to the transmission BER [15].

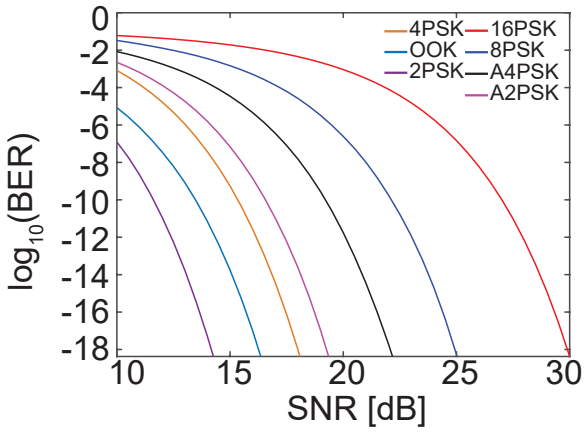

Figure 7.6: System BER of various modulation formats in the back-to-back system where no waveguide link is contained. Here, the average power is $P = 10$ mW.

Another significant idea revealed by the plots in Fig. 7.5 is that, for all types of PSK signals, the Si-PhCW-SL system shows the worst performance. This result implies that the advantages associated to SL operation, namely enhanced nonlinear optical interactions and consequently reduced device footprint, could be outweighed by poor BER. On the other hand, the best BER performance is achieved using the same Si-PhCW but when operated in the FL regime, as per Fig. 7.5(b). This clearly under-

lines the importance of the interplay between the favorable role played by enhanced dispersive and nonlinear effects in the SL regime in reducing the device size and their detrimental influence on transmission BER. As a reference, we also illustrate the BER curves for the above PSK modulation formats employed in systems where the transmitter is connected directly to the receiver, which are shown in Fig. 7.6.

A key parameter on which the performance of optical communication systems depends is the signal power. In the case of Si optical interconnects with subwavelength cross-section this influence is particularly critical due to tight light confinement and SL effects. Therefore, we have investigated the dependence of transmission BER on the input power and its relationship with the type of signal modulation format. To illustrate the main findings of this analysis, we show in Fig. 7.7 the variation of BER with the SNR for A2PSK, 4PSK, and 2PSK signals, determined for different values of the input power.

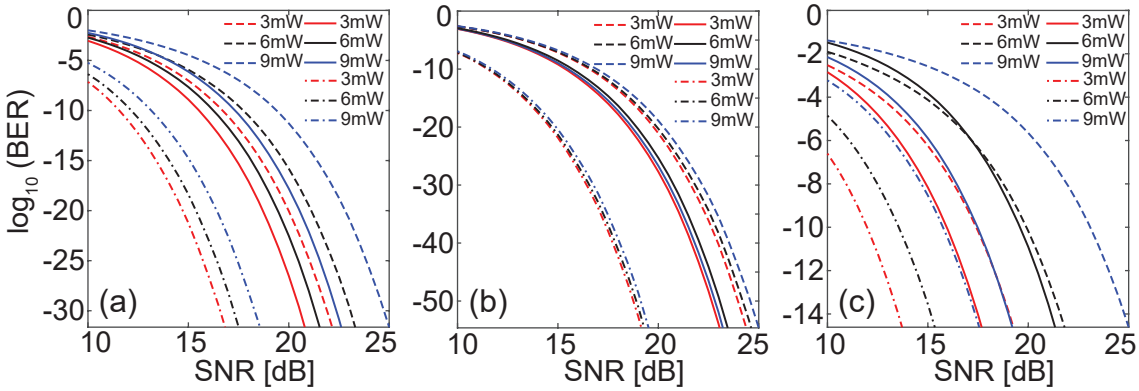

Figure 7.7: System BER vs SNR with different initial input power, calculated for three different single-channel systems: From left to right, the panels indicate the case of a Si-PhW, a Si-PhCW operating in the FL regime, and Si-PhCW operating in the SL regime. The dashed lines, solid lines and dash-dot lines represent the cases of A2PSK, 4PSK and 2PSK modulated signals, respectively. For these curves, the lengths of Si-PhW and Si-PhCW are 5 cm and 500 µm, respectively.

As expected, this figure shows that BER increases with the optical power, irrespective of the signal format. We can also see that the Si-PhCW-FL system is characterized by the weakest dependence of BER on power, chiefly because only a small nonlinear phase accumulates over the short length of this waveguide. In addition, as the signal propagates over a short distance, the FC phase-shift is small, too. These results agree with the data plotted in Fig. 7.3(b), which shows that indeed the smallest phase-shift corresponds to the Si-PhCW-FL system. By contrast, the phase variations at the output

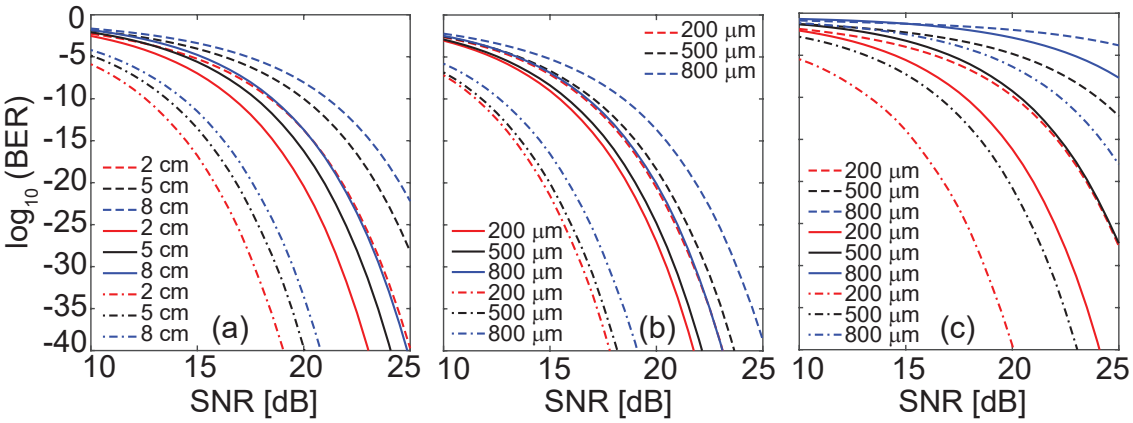

Figure 7.8: System BER vs SNR, calculated for different waveguide lengths. From left to right, the panels correspond to a Si-PhW, a Si-PhCW operating in the FL regime, and Si-PhCW operating in the SL regime. The dashed lines, solid lines and dash-dot lines represent the cases of A2PSK, 4PSK and 2PSK modulated signals, respectively. The average power is $P = 10\,\mathrm{mW}$.

of the Si waveguides are the largest when the PhC waveguide is operated in the SL regime, which in this case is reflected in a strong power dependence of the BER. As a conclusion to this discussion, the Si-PhCW operated in the FL regime represents the optimum choice for on-chip Si optical interconnects, due to the best transmission BER and its relatively small dimensions. Importantly, however, all three systems are suitable for chip-level optical communication networks using PSK modulation formats, as for properly chosen SNR the BER is below a quasi-error free level, e.g. BER $< 10^{-9}$.

The results presented so far show that the transmission BER depends not only on the optical power and type of signal modulation format but also on the waveguide length. In order to further clarify this length dependence of BER, we varied the length of the two types of waveguides but kept constant and equal to 100 the ratio between the lengths of the Si-PhW and Si-PhCW. The corresponding BER curves, calculated for A2PSK, 4PSK, and 2PSK signals and $P = 10\,\mathrm{mW}$, are depicted in Fig. 7.8. As expected, in all cases investigated, the signal impairments increase as the waveguide length increases, this variation being the steepest in the case of Si-PhCW-SL systems. If on the other hand we compare the system performance corresponding to the three modulation formats, one concludes that the strongest dependence of BER on the waveguide length is observed in the case of 2PSK signal, the overall system performance being the worst in this case, too. In addition, it can be seen in Fig. 7.8 that the Si-PhCW-FL system shows weakest length dependence of BER, which again is consistent with the

results presented in Fig. 7.7(b).

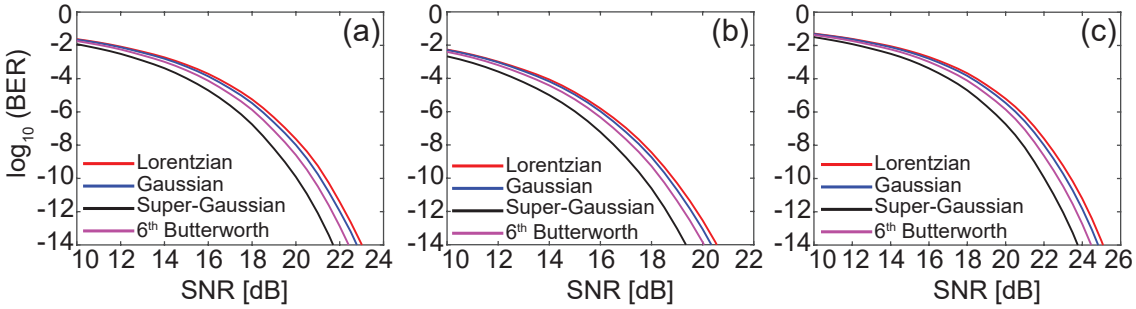

Figure 7.9: BER calculated for several system receiver configurations. From left to right, the panels correspond to a Si-PhW, a Si-PhCW operated in the FL regime, and Si-PhCW operated in the SL regime. In all cases, an 8PSK modulation format is considered. The electrical filter is chosen as fifth Bessel filter, whereas the optical filter is a Lorentzian filter (red line), Gaussian filter (black line), super-Gaussian filter (blue line), and sixth-order Butterworth filter (purple line). For these curves, $P = 10\,\mathrm{mW}$, and $L = 5\,\mathrm{cm}$ ($L = 500\,\mu\mathrm{m}$) for the Si-PhW (Si-PhCW).

For completeness, we also studied the extent to which the transmission BER depends on the system configuration, namely the type of optical and electrical filters used. In this analysis, we considered an 8PSK signal modulation and calculated the dependence of BER on SNR for the three waveguide systems, namely Si-PhW, Si-PhCW-FL, and Si-PhCW-SL, for different types of filters. More specifically, the electrical filter was a fifth-order Bessel filter with bandwidth of $10\,\mathrm{Gb\,s^{-1}}$, whereas the optical filters were a Lorentzian filter, Gaussian filter, second-order super-Gaussian filter, and sixth-order Butterworth filters, all with bandwidth of $40\,\mathrm{Gb\,s^{-1}}$. The results of these calculations are summarized in Fig. 7.9. The main conclusion of these investigations is that, in all cases, the optimum choice is the second-order super-Gaussian filter, whereas the worst performance corresponds to the Lorentzian one. The variation of the system performance with the type of filter, however, is relatively small for all waveguides considered.

7.6 Conclusion

In conclusion, we have presented a comprehensive theoretical and computational analysis of the performance of photonic systems containing silicon based optical interconnects and employing high-order phase-shift keying modulation formats. The systems consisted of optical waveguides made of silicon and direct-detection receivers. The silicon optical interconnects were designed so as to possess fast- and slow-light prop-

agation regimes, which allowed us to investigate the relationships between the system performance and the linear and nonlinear optical coefficients of the optical waveguides. Importantly, by considering different types of phase-shift keying modulation formats, we have identified those most suitable to be used in photonic systems containing silicon based optical interconnects. In addition, using the theoretical models and computational methods introduced in this study we have investigated the dependence of the performance of systems employing high-order modulation formats on the optical properties of silicon interconnects and signal characteristics. In particular, this analysis has revealed that the higher the order of the signal modulation format is, the worse the bit-error ratio is.

For completeness, the investigation regarding the multi-channel silicon photonic systems using OOK modulated CW signals will be presented in the next chapter.

Bibliography

[1] R. M. Osgood, N. C. Panoiu, J. I. Dadap, X. Liu, X. Chen, I-W. Hsieh, E. Dulkeith, W. M. J. Green, and Y. A. Vlassov, "Engineering nonlinearities in nanoscale optical systems: physics and applications in dispersion-engineered silicon nanophotonic wires," Adv. Opt. Photon. **1**, 162-235 (2009).

[2] X. Chen, N. C. Panoiu, and R. M. Osgood, "Theory of Raman-mediated pulsed amplification in silicon-wire waveguides," IEEE J. Quantum Electron. **42**, 160-170 (2006).

[3] N. C. Panoiu, J. F. McMillan, and C. W. Wong, "Theoretical Analysis of Pulse Dynamics in Silicon Photonic Crystal Wire Waveguides," IEEE J. Sel. Top. Quantum Electron. **16**, 257-266 (2010).

[4] S. Lavdas and N. C. Panoiu, "Theory of pulsed four-wave mixing in one-dimensional silicon photonic crystal slab waveguides," Phys. Rev. B **93**, 115435 (2016).

[5] C. Koos, L. Jacome, C. Poulton, J. Leuthold, W. Freude, "Nonlinear silicon-on-insulator waveguides for all-optical signal processing," Opt. Express **15**, 5976-5990 (2007).

[6] A. Mafi and S. Raghavan, "Nonlinear phase noise in optical communication systems using eigenfunction expansion method," Opt. Eng. **50**, 055003 (2011).

[7] E. Forestieri and M. Secondini, "On the Error Probability Evaluation in Lightwave Systems With Optical Amplification," IEEE J. Lightwave Technol. **27**, 706-717 (2009).

[8] J. You, S. Lavdas, and N. C. Panoiu, "Theoretical Comparative Analysis of BER in Multi-Channel Systems With Strip and Photonic Crystal Silicon Waveguides," IEEE J. Sel. Top. Quantum Electron. **22**, 4400810 (2016).

[9] P. E. Barclay, K. Srinivasan, and O. Painter, "Nonlinear response of silicon photonic crystal microresonators excited via an integrated waveguide and fiber taper," Opt. Express **13**, 801-820 (2005).

[10] M. Seimetz, M. Nölle, and E. Patzak, "Optical System With High-Order Optical DPSK and Star QAM Modulation Based on Interferometric Direct Detection," IEEE J. Lightwave Technol. **25**, 1515-1530 (2007).

[11] M. Nölle, M. Seimetz, and E. Patzak, "System Performance of High-Order Optical DPSK and Star QAM Modulation for Direct Detection Analyzed by Semi-Analytical BER Estimation," IEEE J. Lightwave Technol. **27**, 4319-4329 (2009).

[12] J. Wang, and J. M. Kahn, "Impact of Chromatic and Polarization-Mode Dispersions on DPSK Systems Using Interferometric Demodulation and Direct Detection," IEEE J. Lightwave Technol. **22**, 362-371 (2004).

[13] H. Yoon, D. Lee, and N. Park, "Performance comparison of optical 8-ary differential phase-shift keying systems with different decision schemes," Opt. Express **13**, 371-376 (2005).

[14] E. Agrell, and M. Karlsson, "Performance comparison of optical 8-ary differential phase-shift keying systems with different decision schemes: Comment," Opt. Express **14**, 1700-1701 (2006).

[15] J. You and N. C. Panoiu, "Calculation of Bit Error Rates in Optical Systems with Silicon Photonic Wires," IEEE J. Quantum Electron. **51**, 8400108 (2015).

Chapter 8

Performance Evaluation in Multi-channel Systems With Strip and Photonic Crystal Silicon Waveguides

8.1 Introduction

In this chapter, we perform a theoretical analysis of the performance of a WDM photonic system consisting of a noisy optical signal represented as a superposition of M communication channels, a Si optical interconnect, which can be either a strip single-mode silicon photonic waveguide (Si-PhW) or a Si PhC waveguide (Si-PhCW), and a set of direct-detection receivers that analyze the content of the demultiplexed output signal, cf. Fig. 8.1. To describe the optical field propagation in each channel, we use a rigorous model [1–3] that incorporates linear and nonlinear optical effects, including FC dispersion (FCD), FC absorption (FCA), SPM, XPM, TPA, and cross-absorption modulation (XAM), as well as the FCs dynamics and coupling between FCs and the optical field. Importantly, the dependence on GV of these linear and nonlinear effects is naturally incorporated in our theoretical model, so that a comparative analysis of the signal degradation in the SL and fast-light (FL) regimes can conveniently be performed. A simplified, linearized theoretical model is also used to study the noise dynamics. In order to assess the performance of our multichannel photonic system we calculate the transmitted bit-error rate (BER) using two Karhunen-Loève (KL) eigenfunction expansion methods.

The remaining of the chapter is organized as follows. The two types of opti-

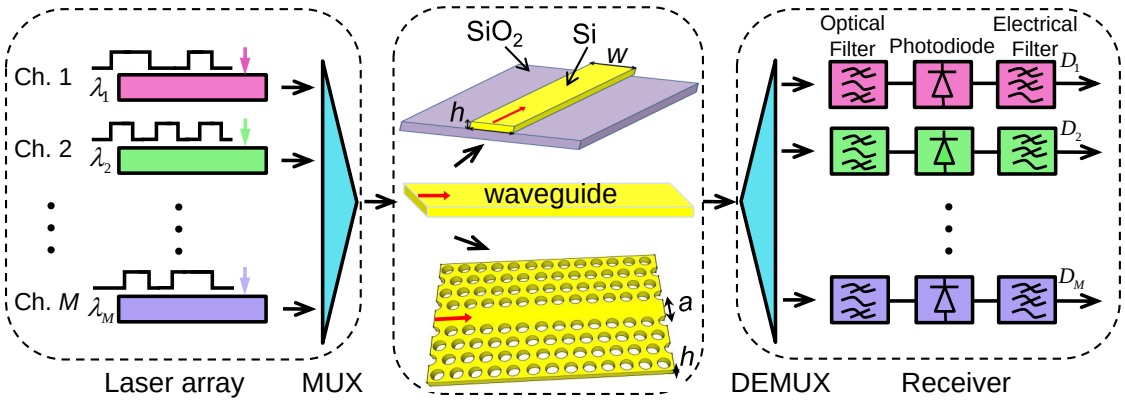

Figure 8.1: Schematic of the multi-channel photonic system, consisting of an array of lasers, MUX, silicon waveguides, DEMUX and direct-detection receivers containing an optical band-pass filter, photodetector, and an electrical low-pass filter. Two types of waveguides are investigated: a strip waveguide with uniform cross-section and a PhC waveguide that possesses slow-light spectral regions.

cal interconnects considered in this study, strip and PhC waveguides, are described in Sec. 8.2. In Sec. 8.3 we present the system of equations that governs the propagation of a multi-wavelength noisy signal in the two types of Si waveguides, whereas in Sec. 8.4 we briefly outline the general time- and frequency-domain formulations of the KL expansion method. We then use these theoretical tools to investigate the impact of white Gaussian noise, in the presence of Kerr nonlinearity, frequency dispersion, and FCs, on BER. The results of this analysis are presented in Sec. 8.5, the main conclusions of our study being summarized in the last section [4], implemented in the time and spectral domains [5, 6].

8.2 Description of the Photonic Waveguides

In this study we consider two types of Si waveguides, depicted schematically in the central block of Fig. 8.1. The first waveguide is a single-mode Si-PhW with uniform cross-section, buried in SiO_2 cladding. We assume that the waveguide height is fixed to $h = 250\,\text{nm}$ and consider that its width, w, can be varied, so that its optical properties can be tuned. The second waveguide is a Si-PhCW, namely a line defect in a two-dimensional PhC slab waveguide consisting of a hexagonal lattice of air holes in a Si slab with thickness, $h = 0.6a$, the lattice constant and hole radius being $a = 412\,\text{nm}$ and $r = 0.22a$, respectively. The line defect is created by filling in a row of holes oriented along the ΓK direction of the PhC. The modal dispersion of the optical guiding modes supported by the Si-PhW and Si-PhCW is presented in Figs. 8.2(a) and 8.2(b),

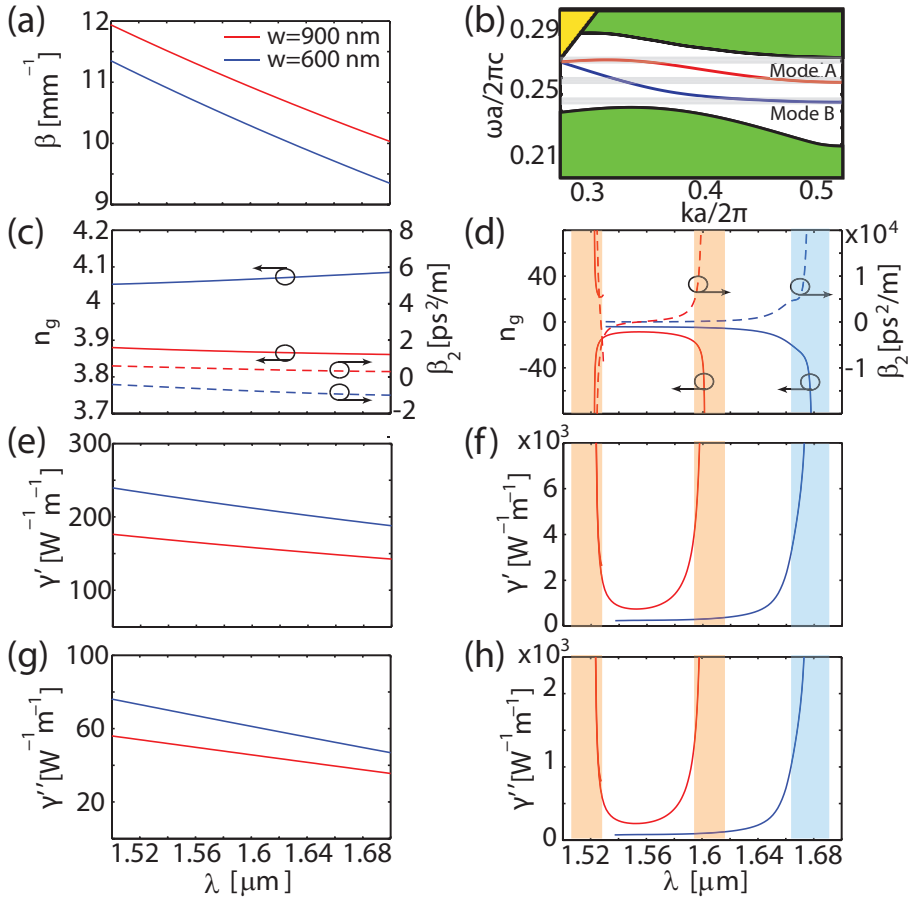

Figure 8.2: Left (right) panels show dispersion diagrams of linear and nonlinear waveguide coefficients of the Si-PhW (Si-PhCW). The Si-PhW has $h = 247\,\text{nm}$, whereas the Si-PhCW has $r = 0.22a$ and $h = 0.6a$, the lattice constant being $a = 412\,\text{nm}$. The grey, red, and blue shaded areas indicate slow-light domains defined by $n_g = c/v_g > 20$.

respectively, whereas in Figs. 8.2(c) and 8.2(d) we summarize the corresponding frequency dispersion of the group-index, $n_g = c/v_g$, and second-order dispersion coefficient, $\beta_2 = d^2\beta/d\omega^2$, where $\beta(\omega)$ is the mode propagation constant. Thus, in the case of the Si-PhW, we show the wavelength dependence $\beta(\lambda)$, determined for $w = 900\,\text{nm}$ and $w = 600\,\text{nm}$. In the first case the waveguide has normal dispersion ($\beta_2 > 0$) at $\lambda_0 = 1550\,\text{nm}$, whereas the second waveguide has anomalous dispersion ($\beta_2 < 0$) at this wavelength. Note that in this study we only consider the waveguide with width $w = 900\,\text{nm}$.

The Si-PhCW, on the other hand, possesses two TE-like guiding modes, modes *A* and *B*, which contain either two SL regions (mode *A*) or only one such domain (mode *B*). In quantitative terms, we define the SL spectral regions as the domains where the relation $n_g = c/v_g > 20$ is satisfied. Importantly, as per Fig. 8.2, in the SL regime

of optical signal propagation the characteristic lengths of both linear and nonlinear effects can be reduced by several orders of magnitude as compared to their values in the FL regime. Moreover, we assume that the Si-PhCW is operated in the FL and SL domains of mode A; for convenience, we refer to these two configurations as Si-PhCW-FL and Si-PhCW-SL, respectively. This choice is guided by the fact that in practice it is much more convenient to access a SL region located in the middle of a photonic band, as at frequencies close to the band-edge the optical signal experiences strong back-scattering. Particularly, all important parameters of the silicon waveguides used in this chapter are presented in Table 8.1, Table 8.2 and Table 8.3. Moreover, the operating wavelength can be changed to any required value by simply scaling a while keeping the ratio a/λ constant.

Table 8.1: Main parameters for the 8-channel Si-PhW waveguide used in our simulations.

Index	1	2	3	4	5	6	7	8
λ $[nm]$	1549.4	1549.6	1549.8	1550	1550.2	1550.4	1550.6	1550.8
β_1 $[ns/m]$	12.92	12.92	12.92	12.92	12.92	12.92	12.92	12.92
β_2 $[ps^2/m]$	0.505	0.505	0.505	0.504	0.504	0.503	0.503	0.503
κ	0.9985	0.9985	0.9985	0.9985	0.9985	0.9985	0.9985	0.9985
γ' $[W^{-1}m^{-1}]$	166.95	166.91	166.88	166.84	166.81	166.77	166.73	166.70
γ'' $[W^{-1}m^{-1}]$	50.89	50.87	50.85	50.83	50.81	50.78	50.76	50.74
α_{in} $[dBcm^{-1}]$	1	1	1	1	1	1	1	1

Table 8.2: Main parameters for the 8-channel Si-PhCW-FL waveguide used in our simulations.

Index	1	2	3	4	5	6	7	8
λ $[nm]$	1524.5	1524.3	1524.1	1523.9	1523.7	1523.5	1523.2	1523.0
β_1 $[ns/m]$	74.60	77.51	81.52	85.61	89.71	94.50	107.47	123.22
β_2 $[ps^2/m]$	-358	-350	-342	-333	-325	-317	-309	-302
κ	0.9938	0.9938	0.9938	0.9937	0.9937	0.9937	0.9937	0.9937
γ' $[W^{-1}m^{-1}]$	752.40	751.64	750.87	750.11	749.35	748.58	748.03	747.88
γ'' $[W^{-1}m^{-1}]$	229.28	229.05	228.81	228.58	228.35	228.12	227.95	227.90
α_{in} $[dBcm^{-1}]$	50	50	50	50	50	50	50	50

Table 8.3: Main parameters for the 8-channel Si-PhCW-SL waveguide used in our simulations.

Index	1	2	3	4	5	6	7	8
λ $[nm]$	1549.4	1549.6	1549.8	1550	1550.2	1550.4	1550.6	1550.8
β_1 $[ns/m]$	29.87	29.83	29.79	29.75	29.71	29.67	29.63	29.60
β_2 $[ps^2/m]$	$-2.63\cdot10^4$	$-2.96\cdot10^4$	$-3.62\cdot10^4$	$-4.31\cdot10^4$	$-5\cdot10^4$	$-6.03\cdot10^4$	$-9.6\cdot10^4$	$-1.62\cdot10^5$
κ	0.9954	0.9953	0.9953	0.9953	0.9953	0.9952	0.9952	0.9951
γ' $[W^{-1}m^{-1}]$	$4.95\cdot10^3$	$5.38\cdot10^3$	$6.15\cdot10^3$	$6.94\cdot10^3$	$7.74\cdot10^3$	$8.86\cdot10^3$	$1.26\cdot10^4$	$1.88\cdot10^4$
γ'' $[W^{-1}m^{-1}]$	$1.51\cdot10^3$	$1.64\cdot10^3$	$1.87\cdot10^3$	$2.12\cdot10^3$	$2.36\cdot10^3$	$2.70\cdot10^3$	$3.82\cdot10^3$	$5.72\cdot10^3$
α_{in} $[dBcm^{-1}]$	50	50	50	50	50	50	50	50

8.3 Theory of Multi-wavelength Optical Signal Propagation in Silicon Wires

In this section, the full theoretical model in Sec. 2.6.2 is used to investigate the propagation of a multi-wavelength optical signal in both Si-PhWs and Si-PhCWs. This model rigorously describes the evolution of the optical field in the presence of FCs as well as the dynamics of FC density. Specifically, the coupled dynamics of the optical signal and FCs are governed by Eqs. (2.21). Particularly, in Eqs. (2.21), τ_c is the FC relaxation time (in our analysis we assumed $\tau_c = 0.5\,\text{ns}$), δn_{fc} and α_{fc} are the FC-induced refractive index change and FC loss coefficient, respectively, and are given by $\delta n_{\text{fc}} = \sigma_n N$ and $\alpha_{\text{fc}} = \sigma_\alpha N$, where N is the FC density, $\sigma_\alpha = 1.45 \times 10^{-21}(\lambda/\lambda_0)^2$ (in units of m^2), and $\sigma_n = \sigma(\lambda/\lambda_0)^2$ (in units of m^3), with σ and $\lambda_0 = 1550\,\text{nm}$ being a power dependent coefficient [7] and a reference wavelength, respectively. Moreover, the frequency dispersion of the real and imaginary part of the nonlinear coefficient γ is presented in Figs. 8.2(e) through 8.2(h). As these figures illustrate, the nonlinear coefficient in the case of Si-PhCWs can be more than two orders of magnitude larger than that of Si-PhWs, being particularly large in the SL domain. In addition, in the spectral region considered in this work γ' is more than $10\times$ larger than γ'', which suggests that SPM is the dominant nonlinear effect. For all multi-channel photonic systems considered in this study, we assume that the bit window is $T_0 = 100\,\text{ps}$, the channel spacing is $\Delta\omega = 25\,\text{GHz}$, and the reference wavelength (the wavelength of channel 1) for the Si-PhW, Si-PhCW-FL, and Si-PhCW-SL systems is 1550 nm, 1550 nm, and 1523.9 nm, respectively.

The superposition of the optical signal and noise propagating in the ith channel of a Si-PhW or Si-PhCW photonic system is selected to be:

$$u_i(z,T) = \left[\sqrt{P_i(z)} + a_i(z,T)\right] e^{-j\Phi_i(z)}, \tag{8.1}$$

where $P_i(z)$ is the power of the CW signal in the ith channel, $a_i(z,T)$ is the complex additive Gaussian noise, and $\Phi_i(z)$ is a global phase shift associated with the ith channel. We also assume that the noise components at the input of the waveguide are statistically

independent,

$$\mathbb{E}\left\{a_i(0,T)a_k(0,T')\right\} = \delta_{ik}\delta(T-T'), \quad i,k=1,\ldots,M, \tag{8.2}$$

where $\mathbb{E}\{\cdot\}$ is the statistical expectation operator. The more general case of statistically correlated noise functions can be considered by introducing in our analysis the corresponding matrix correlation of these noise functions. Importantly, the linearized model of Eqs. (2.30) and (2.31) are utilized in this chapter for the CW signal propagation in the WDM system.

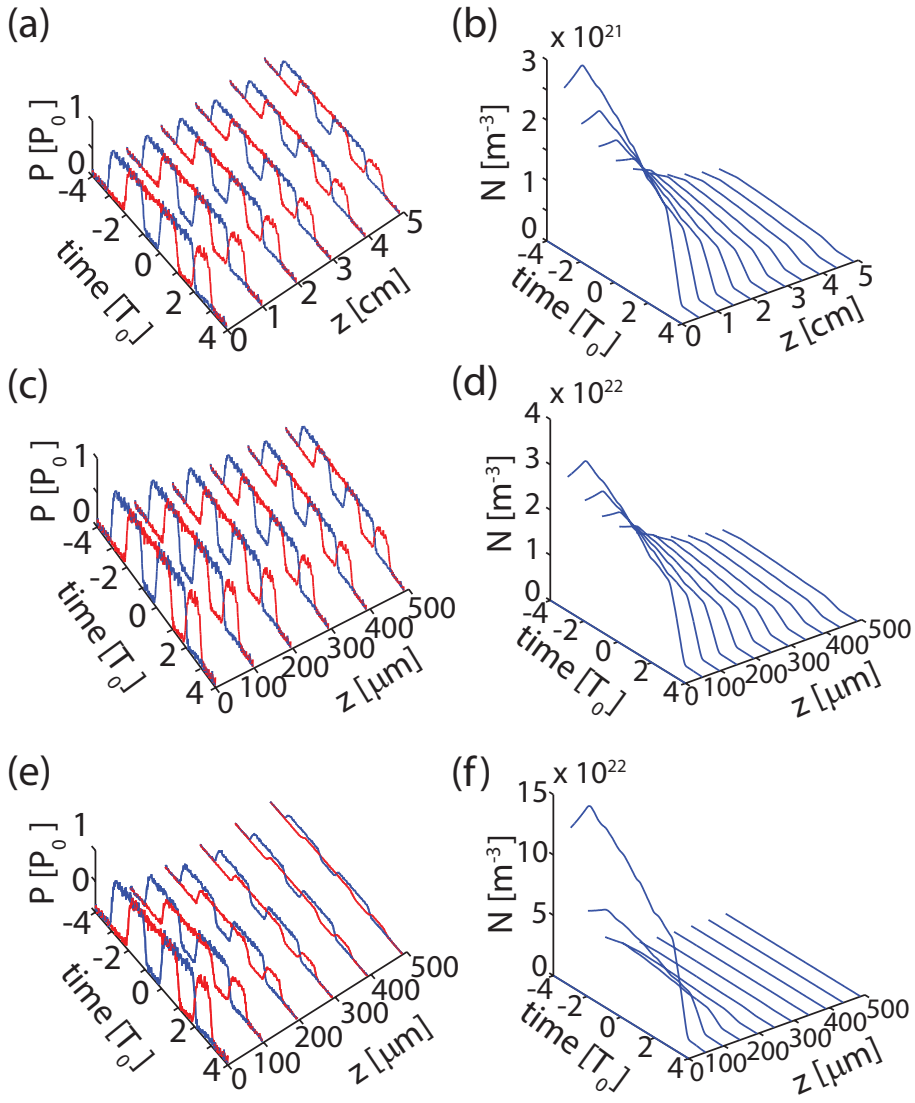

Figure 8.3: Time-domain evolution of a noisy signal in channel 1 (blue) and channel 6 (red) of a 10-channel photonic system. The plots correspond to: (a), a Si-PhW; (c), a Si-PhCW operating in the FL regime; and (e), a Si-PhCW operating in the SL regime. Left panels show the corresponding FC dynamics. In each channel of the three systems $P = 10\,\text{mW}$.

In order to illustrate how the full model Eq. (2.21) can be used to study the propagation of a multi-wavelength optical signal in a Si waveguide, we show in Fig. 8.3 the time evolution of a noisy signal in channels 1 and 6 of a 10-channel photonic system. The optical field and FC density were calculated by integrating the system Eqs. (2.21) using a standard split-step Fourier transform numerical method. These calculations were performed for both the Si-PhW and Si-PhCW, the latter case being investigated both in the FL and SL regimes. In this and all the following examples, the length of the Si-PhW (Si-PhCW) is $\bar{L} = 5\,\mathrm{cm}$ ($\tilde{L} = 500\,\mu\mathrm{m}$). The bit sequence in each channel is the same in all three photonic systems but for each system it depends on the channel; specifically, in our example the bit sequences in channels 1 and 6 are "00110110" and "01011100", respectively. Moreover, we assume that the input power of the noise and signal is the same for each channel, meaning that the signal-to-noise ratio (SNR) is independent of the channel. Note that in our simulations we define the SNR of the optical signal at the front-end of each channel as the ratio between the power of the CW signal, P_i, and the average of the sum of the powers of the in-phase and quadrature noise components,

$$\mathrm{SNR}(i) = \frac{P_i}{\mathbb{E}\left\{a_i'^2 + a_i''^2\right\}\Big|_{z=0}}, \quad i = 1, \ldots, M. \tag{8.3}$$

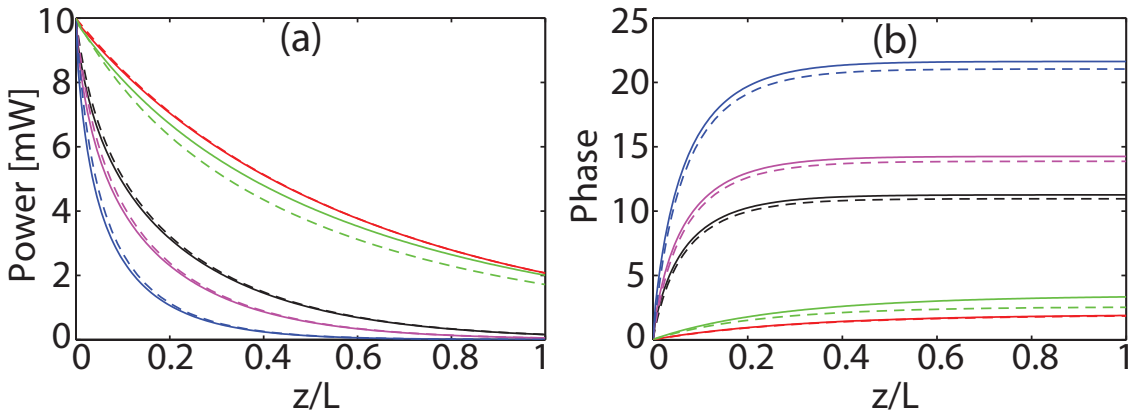

Figure 8.4: (a), (b) Power and phase, respectively, calculated using the full (solid lines) and linearized system (dashed lines) for a 10-channel system. The photonic wire is a Si-PhW (green, channel 1), Si-PhCW-FL (red, channel 1), and Si-PhCW-SL. In the last case the three lines correspond to: channel 1 (black), channel 6 (purple), and channel 10 (blue). SNR = 30 dB. The system conditions are the same as in Fig. 8.3.

The main conclusion revealed by these calculations is that the optical field is distorted much stronger in the Si-PhCW system, with a more pronounced signal degradation being observed in the SL regime of this waveguide as compared to the FL case. These results are not surprising, as the largest values of the linear and nonlinear waveguide coefficients are achieved in the SL regime of the Si-PhCW (see Fig. 8.2). For completeness, we also show in Figs. 8.3(b), 8.3(d) and 8.3(f) the dynamics of FCs. Similar to the case of the optical field, it can be seen that SL effects strongly influence the FCs dynamics as well. More specifically, our calculations show that, for the same optical power, in the SL regime of Si-PhCW the FC density is about $5\times$ larger than in the FL case and about $50\times$ larger than in the case of the Si-PhW. This is a direct consequence of the enhanced TPA and XAM in the former case, an effect that is proportional to v_g^{-2}.

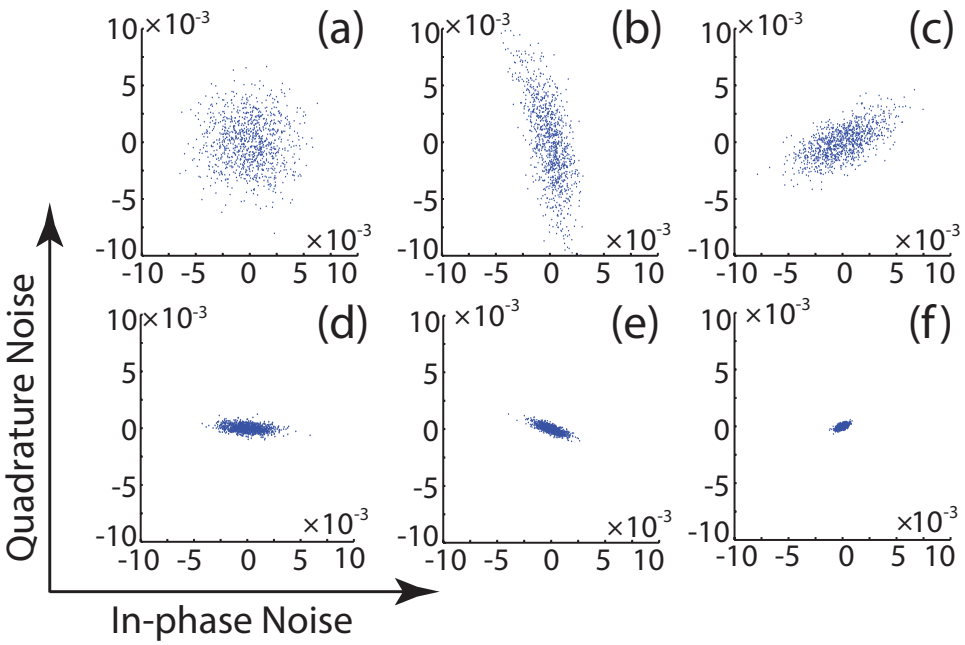

Figure 8.5: (a) In-phase and quadrature noise components at the input of the 10-channel Si-PhW, Si-PhCW-FL and Si-PhCW-SL systems. (b), (c) Noise components at the output of channel 1 of the Si-PhW and Si-PhCW-FL systems, respectively, determined from the linearized system Eq. (2.30). (d), (e), (f) Noise output in channel 1, channel 6, and channel 10, respectively, in the Si-PhCW-SL system. SNR = 30 dB. The system conditions are the same as in Fig. 8.3.

A clear picture about the reliability of the linearized system Eq. (2.30) is revealed by a comparison between the optical field at the back-end of the Si waveguides considered in this work, calculated using this linearized model and the full system Eqs. (2.21). The solution of the linearized model was calculated by using a standard

5th order Runge-Kutta method. The conclusions of such a comparison are summarized in Fig. 8.4, where we plot the evolution of the optical power and phase of a multi-wavelength optical signal corresponding to three different regimes of propagation in Si waveguides. In particular, we considered the same 10-channels system as above, the three waveguides being a Si-PhW, a Si-PhCW-FL, and a Si-PhCW-SL. The first conclusion we can derive from the results presented in Fig. 8.4 is that for all systems and all channels the linearized system describes fairly accurately the dynamics of the optical field.

Our simulations show that in the case of the Si-PhW and Si-PhCW-FL systems the power and phase of the optical signal are nearly the same across all 10 channels and as such we plot in Fig. 8.4 only the quantities that correspond to channel 1. This is an expected result because in these two cases the linear and nonlinear waveguide coefficients are only weakly dispersive, so that in the case of small inter-channel separation they do not vary much from channel to channel. This picture changes markedly if one considers the case of the Si-PhCW-SL system. Thus, in the SL regime, as a consequence of SL effects, the waveguide coefficients are enhanced and become much more dispersive. This results in a large spread of the values of the parameters that characterize the propagation of optical signals in the SL multi-channel system.

The linearized system Eq. (2.30) also allows one to determine the evolution of the noise components of the optical field. This is illustrated in Fig. 8.5, where we present the noise components at the back-end of the Si waveguides investigated above. Note that in this figure we plot $a_i(z,t)e^{-j\Phi_i(z)}$, calculated at $z=\bar{L}=5\,\text{cm}$ and $z=\tilde{L}=500\,\mu\text{m}$ for the Si-PhW and Si-PhCW systems, respectively, where $\Phi_i(z)$ is the phase defined by Eq. (8.1). The statistical properties of the input additive white Gaussian noise do not depend on the channel nor the particular system considered. Comparing Figs. 8.5(b) and 8.5(c), which correspond to channel 1 of the Si-PhW and Si-PhCW-FL systems, respectively, it can be seen that our model predicts a larger parametric amplification of the quadrature noise. Moreover, the output noise in channel 1, channel 6, and channel 10 of the Si-PhCW-SL system is shown in Figs. 8.5(d), 8.5(e), and 8.5(f), respectively. Interestingly enough, it can be seen not only that, similar to the case of the optical signal, there is a large noise variation with the transmission channel, but also that the noise amplitude rapidly decreases with the channel number. This latter dependence is

explained by the fact that the channels indexed by larger numbers are located deeper in the SL spectral domain, namely in a spectral region with larger linear and nonlinear optical losses.

8.4 Time and Frequency Domain Karhunen-Loève Series Expansion Methods

In this section, both the time- and frequency-domain KLSE methods are used to calculate the transmission BER of multi-channel Si-PhW and Si-PhCW systems at the back-end of the waveguide. We assume that the output signal is first demultiplexed and then the signal content in each channel is analyzed. We performed these calculations both in the time and frequency domain, with the explicit algorithms introduced in Sec. 3.2 and Sec. 3.3, respectively, followed by the comparison of the results obtained by the two methods. As a final note on the BER calculation, we stress that KL-based methods produce significantly more accurate results in the strong nonlinear regime, as compared to the commonly used Gaussian approximation [8]. This becomes particularly important when BER calculations are performed in the SL regime of the Si-PhCW, as in this case intra- and inter-channel signal-noise interactions mediated by the optical nonlinearity of the waveguide and FCs increase significantly.

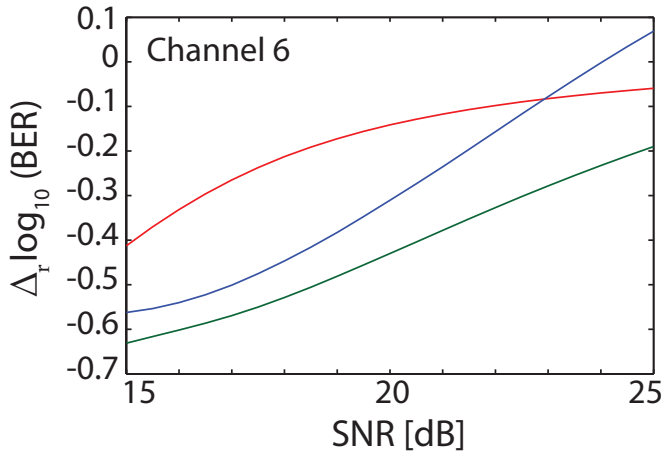

Figure 8.6: Comparison of the system BER calculated via the time- and frequency-domain KL expansion method. The plots correspond to channel 6 in an 8-channel system containing a Si-PhW (green), Si-PhCW operating in the FL regime (red), and a Si-PhCW operating in the FL regime (blue). Initial signal power in each channel is $P = 5\,\mathrm{mW}$. The agreement between the two methods is quantified by $\Delta_r \log_{10}(\mathrm{BER}) = [\log_{10}(\mathrm{BER})_{FD} - \log_{10}(\mathrm{BER})_{TD}]/\log_{10}(\mathrm{BER})_{FD}$.

In order to evaluate the computational accuracy of the two approaches, we used them to analyze the transmission BER of several system configurations and then compared the results. More specifically, we considered 8-channel Si-PhW, Si-PhCW-FL, and Si-PhCW-SL systems and in all cases calculated the BER for each channel. The power in each channel was $P = 5\,\mathrm{mW}$. In this example and all those that follow we assume that the electrical filter is a low-pass integrate-and-dump filter with the 3-dB bandwidth equal to $B_e = 10\,\mathrm{Gb\,s^{-1}}$, whereas the optical filter is a bandpass Lorentzian with 3-dB bandwidth, $B_o = 4B_e$. Specifically, the two filters are described by the following transfer functions,

$$H_o^i(f) = \frac{\Gamma_o^2}{f^2+\Gamma_o^2}, \quad H_o^q(f) = -\frac{\Gamma_o f}{f^2+\Gamma_o^2}, \tag{8.4a}$$

$$H_e^i(f) = \begin{cases} 1, & |f| \le B_e/2 \\ 0, & |f| > B_e/2 \end{cases} \quad H_e^q(f) = 0, \tag{8.4b}$$

where $\Gamma_o = B_o/2$. These parameters are the same as those used in [9], where the single-channel transmission BER in Si-PhWs was investigated. This choice makes it easy to compare the performance of single- and multi-channel systems.

The conclusions of these calculations are summarized in Fig. 8.6, where we plot the dependence on BER of the relative difference between the BERs calculated by employing the time- and frequency-domain methods. This quantity is defined as $\Delta_r \log_{10}(\mathrm{BER}) = [\log_{10}(\mathrm{BER})_{FD} - \log_{10}(\mathrm{BER})_{TD}]/\log_{10}(\mathrm{BER})_{FD}$. We show here only the results corresponding to channel 6, as the results are rather independent of the channel number. The plots presented in Fig. 8.6 show that the predictions of the two algorithms are are in good agreement, especially at large SNR.

8.5 Performance Evaluation for Multi-channel Systems

Armed with these theoretical and computational tools, we performed a comparative study of transmission BER in Si waveguides with uniform cross-section and PhC Si waveguides, the main results being presented in this section. In the latter case we considered both FL and SL regimes, so that we could assess the extent to which enhanced linear and nonlinear optical effects degrade the transmitted optical signal.

To begin with, we assume that our system contains a variable number of channels,

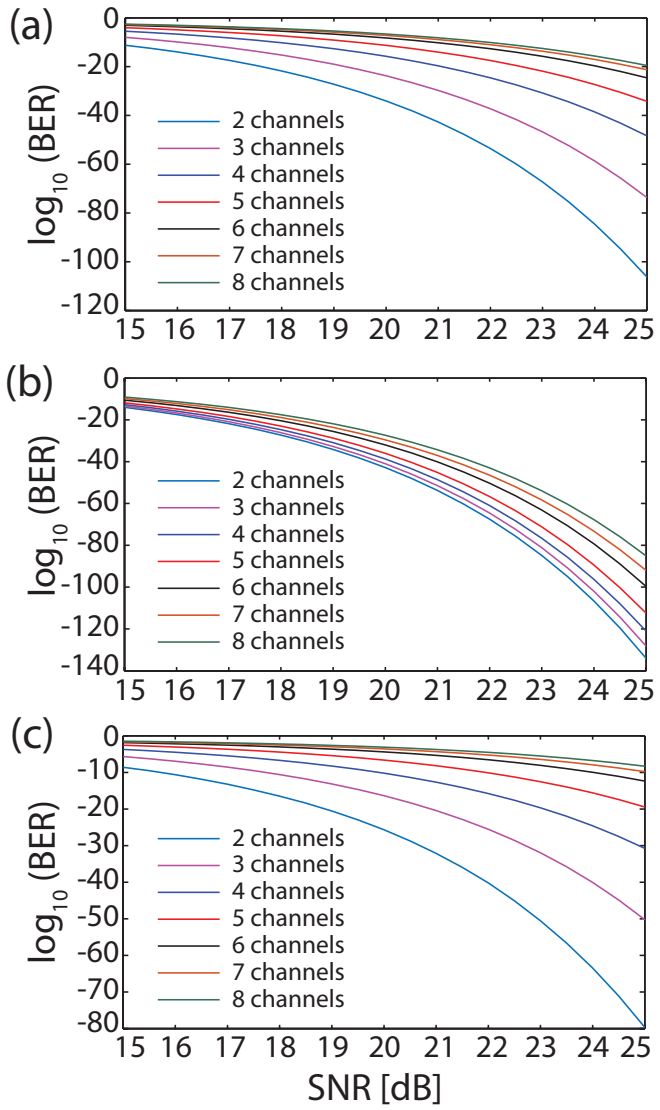

Figure 8.7: System BER for channel 2 vs. SNR, calculated for systems with different number of channels. From top to bottom, the panels correspond to a Si-PhW, a Si-PhCW operating in the FL regime, and a Si-PhCW operating in the SL regime.

each channel consisting of a NRZ bit stream. We start our analysis by investigating in each of the three cases the correlation between the transmission BER and the number of channels as well as the dependence of the calculated BER on the SNR. The dependence of the transmission BER on the number of channels is illustrated in Fig. 8.7, where we plot the BER corresponding to channel 2 of a system containing a number of channels that varies from 2 to 8. In all cases we assume that the input power is $P = 5\,\mathrm{mW}$ in each channel. These calculations, which can provide valuable insights into the limits of WDM silicon photonic systems, suggest that the BER increases with the number of channels, most strongly in the case of a Si-PhCW operating in the SL regime. This is an

expected conclusion because as the number of channels increases the strength of inter-channel interactions mediated by optical nonlinearity and FCs increases, which results in a degradation of the system performance. Moreover, as linear and nonlinear optical effects are enhanced in the SL regime, a more pronounced deterioration of the system performance is observed in this case. Last but not least, the influence of number of channels would be extremely small in systems where a Si waveguide is not contained, under the assumption that neither the receivers or the DEMUX would induce noise. Thus, when considering the BER performance in this case, one can refer to the BER plots for single-channel back-to-back system configuration, as shown in Fig. 4.2(a).

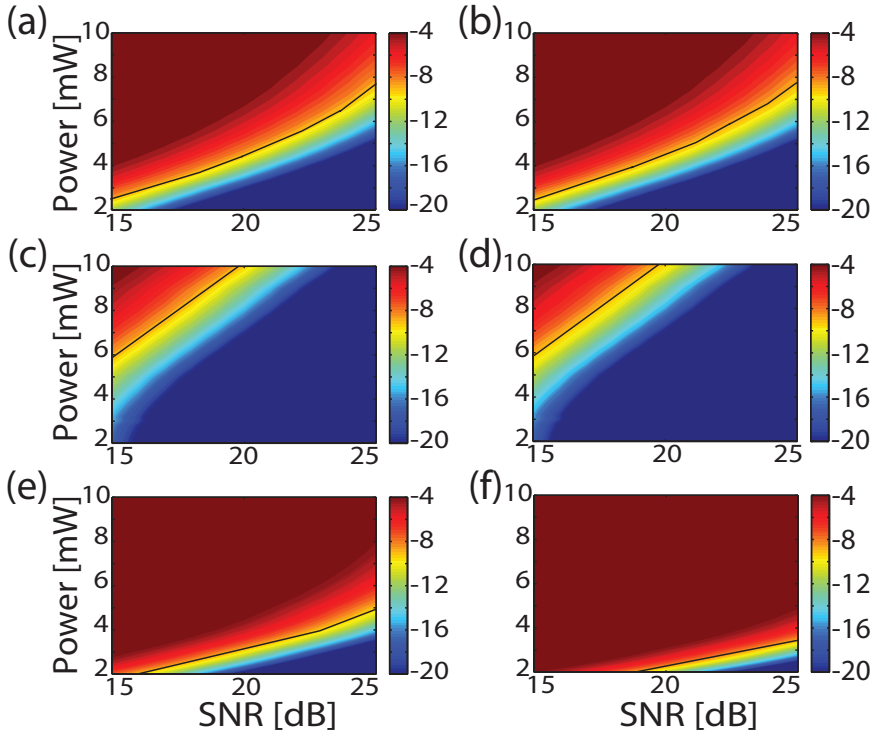

Figure 8.8: Maps of $\log_{10}(\text{BER})$ vs. power and SNR, calculated for three different 8-channel systems: from top to bottom, the panels correspond to a Si-PhW, a Si-PhCW operating in the FL regime, and a Si-PhCW operating in the SL regime. Left and right panels correspond to channel 1 and channel 8, respectively. Black curves correspond to $\log_{10}(\text{BER}) = -9$.

The physical parameter that most critically affects the system performance is the optical power of the signal. Indeed, the optical field induces nonlinear effects that affect the signal propagation in the Si waveguide and generates FCs that modify the optical properties of the waveguide. Therefore, in the next part of our study, we investigate the dependence of the performance of the 8-channel system described above on the optical power contained in each channel, at the front-end of the three type of waveguides

considered in this work. The results of this analysis are presented in Fig. 8.8, where the BERs corresponding to channel 1 and channel 8 are presented. Similar to our previous findings, it can be seen that the system performance decreases as the power is increased, irrespective of the value of the SNR. Moreover, this figure shows that although it is 100× shorter than the Si-PhW, the Si-PhCW operating in the FL regime provides a larger parameter space where the system BER is smaller than an upper-bound limit commonly used in optical communications systems, namely BER $< 10^{-9}$. This situation changes markedly if the same PhC waveguide is operated in the SL regime, namely the power must be decreased considerably if the BER is to remain smaller than 10^{-9}. In addition, one can observe that in this regime the transmission BER experiences the strongest variation with the channel number.

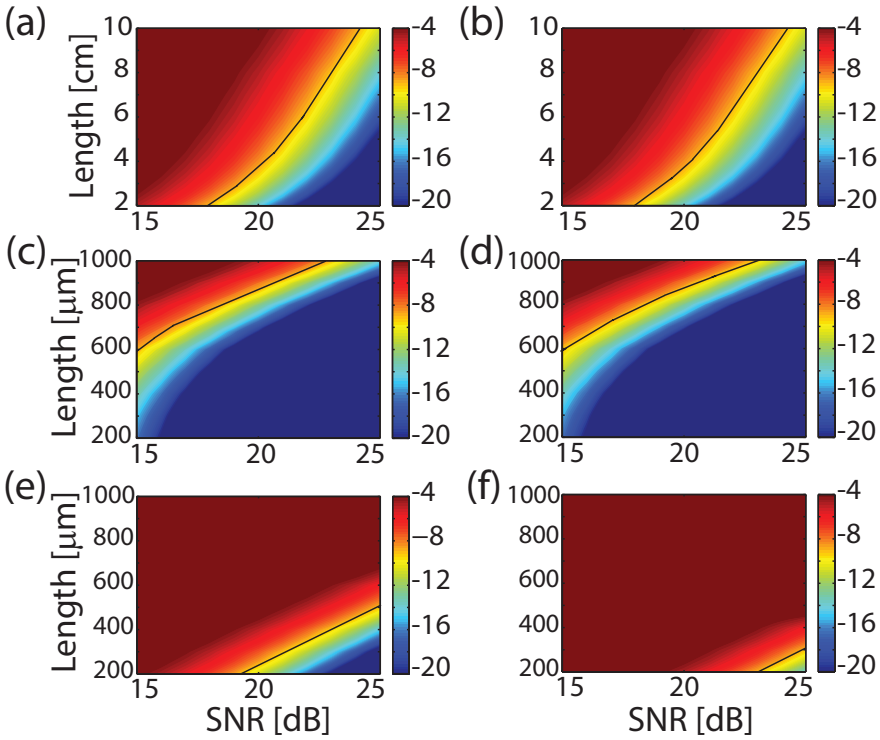

Figure 8.9: Maps of $\log_{10}(\mathrm{BER})$ vs. waveguide length and SNR, calculated for three different 8-channel systems: from top to bottom, the panels correspond to a Si-PhW, a Si-PhCW operating in the FL regime, and a Si-PhCW operating in the SL regime. Left and right panels correspond to channel 1 and channel 8, respectively. The input power in each channel is $P = 5\,\mathrm{mW}$. Black curves correspond to $\log_{10}(\mathrm{BER}) = -9$.

Let us now consider the dependence of the transmission BER on the length of the waveguide. This is a particularly important issue if one assesses the feasibility of using Si waveguides for on-chip optical interconnects. We therefore considered

Si-PhWs and Si-PhCWs with different length but in order to be able to compare the findings of this investigation to the conclusions drawn so far we assumed that the ratio of the lengths of the two waveguides is fixed to 100. The system BER determined under these circumstances, for the same 8-channel system and power $P = 5\,\mathrm{mW}$, is plotted in Fig. 8.9. One important result illustrated by this figure is that, among the three cases investigated, the Si-PhCW operated in the FL regime provides the optimum performance. When the same waveguide is operated in the SL regime, on the other hand, the BER is larger than the threshold of 10^{-9} in almost the entire parameter space considered in Fig. 8.9.

8.6 Conclusion

In conclusion, we have presented a comprehensive analysis of bit-error rates in multi-channel photonic systems containing silicon waveguides. We have considered two types of such photonic devices, namely a strip waveguide with uniform cross-section and a photonic crystal waveguide. The latter photonic waveguide allowed us to extend our analysis to the important case of slow-light propagation where both linear and nonlinear optical effects are enhanced. Our calculations of the bit-error rate have demonstrated that using photonic crystal waveguides in the fast light regime allows one to reduce the device footprint by as much as two orders of magnitude while maintaining the system performance to an almost unchanged level. However, if the photonic crystal is operated in the slow-light regime at similar power levels, a significant degradation of the system performance is observed.

The theoretical formalism introduced in this study can also be applied to other, more complex devices of practical interest. For example, our theoretical approach can be applied to taper, slot and other types of waveguides by simply using the corresponding linear and nonlinear waveguide optical coefficients. Moreover, after properly modifying the system of equations governing the optical field dynamics in silicon waveguides, a similar theoretical formalism can be employed to study the transmission bit-error rate of photonic systems containing, e.g, splitters, ring modulators coupled to a waveguide, and multi-mode waveguides. Equally important, the generality of the theoretical methods used in this study makes it easy to adapt them to tackle much more advanced signal modulation formats and detection schemes than those considered in

this chapter.

In the next chapter, the research emphasis will shift to the single-channel silicon photonic interconnect that operating in the pulsed regime.

Bibliography

[1] X. Chen, N. C. Panoiu, and R. M. Osgood, "Theory of Raman-mediated pulsed amplification in silicon-wire waveguides," IEEE J. Quantum Electron. **42**, 160-170 (2006).

[2] N. C. Panoiu, J. F. McMillan, and C. W. Wong, "Theoretical analysis of pulse dynamics in silicon photonic crystal wire waveguides," IEEE J. Sel. Top. Quantum Electron. **16**, 257-266 (2010).

[3] S. Lavdas and N. C. Panoiu, "Theory of Pulsed Four-Wave-Mixing in One-dimensional Silicon Photonic Crystal Slab Waveguides," Phys. Rev. B **93**, 115435 (2016).

[4] A. Papoulis, *Probability, Random Variables, and Stochastic Processes* 3rd ed, (McGraw-Hill, New York, 1991).

[5] A. Mafi and S. Raghavan, "Nonlinear phase noise in optical communication systems using eigenfunction expansion method," Opt. Eng. **50**, 055003 (2011).

[6] E. Forestieri and M. Secondini, "On the Error Probability Evaluation in Lightwave Systems With Optical Amplification," IEEE J. Lightwave Technol. **27**, 706-717 (2009).

[7] Q. Lin, O. J. Painter, and G. P. Agrawal, "Nonlinear optical phenomena in silicon waveguides: Modeling and applications," Opt. Express **15**, 16604-16644 (2007).

[8] G. Bosco, A. Carena, V. Curri, R. Gaudino, P. Poggiolini, and S. Benedetto, "A novel analytical approach to the evaluation of the impact of fiber parametric gain on the bit error rate," IEEE Trans. Commun. **49**, 2154-2163 (2001).

[9] J. You and N. C. Panoiu, "Calculation of Bit Error Rates in Optical Systems with Silicon Photonic Wires," IEEE J. Quantum Electron. **51**, 8400108 (2015).

Chapter 9

Single-channel Silicon Photonic Interconnects Utilizing RZ Pulsed Signals

9.1 Introduction

In this chapter, we analyze the transmission BER in single-channel Si photonic systems operated in the RZ regime. The photonic systems investigated in this study consist of an optical transmitter, a Si optical waveguide, and a direct-detection receiver, as shown in Fig. 9.1. The optical link can be either a single-mode Si-PhW with uniform cross-section or a Si-PhCW, and is connected to a direct-detection receiver consisting of a Lorentzian bandpass optical filter, an ideal square-law photodetector, and an integrate-and-dump low-pass electrical filter. An ON-OFF keying (OOK) modulated Gaussian pulses with a 512-bit pseudorandom binary sequence (PRBS) pattern, together with complex additive white noise, form the input signal. To characterize the pulse dynamics upon transmission, we use a theoretical model, which incorporates all the significant optical effects, including the linear loss, GV dispersion (GVD), free-carrier (FC) dispersion (FCD), FC absorption (FCA), self-phase modulation (SPM), two-photon absorption (TPA), and the mutual interaction between the FCs and the optical field [1–4]. Moreover, the Fourier-series Karhunen-Loève (KL) expansion approach is employed in conjunction with a perturbation theory for the calculation of the noise covariance matrix [5], to evaluate the system BER at the back-end of the receiver.

The rest of the chapter is organized as follows. The rigorous theoretical model that

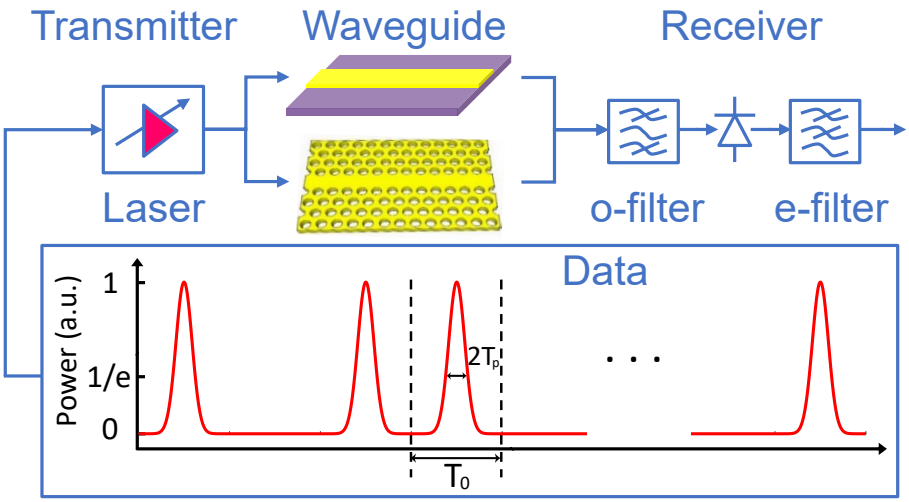

Figure 9.1: Schematic of the investigated Si photonic system. It consists of a transmitter (a laser and a PRBS generator), a Si waveguide, and a direct-detection receiver (an optical filter, a photodetector, and an electrical filter). The optical link is either a strip or a PhC Si waveguide. In the PRBS generator the bit window is T_0 and each bit consists of a Gaussian pulse with half-width (at $1/e$-intensity point), T_p.

describes the pulse propagation in Si waveguides is introduced in Sec. 9.2. Then, in Sec. 9.3, we present the general formulation of the perturbation theory and the Fourier-series KL expansion method that we used to evaluate the system BER. The simulation results and their discussion are presented in Sec. 9.4, followed by the main conclusions of this work summarized in the final section.

9.2 Theory of PRBS Optical Pulse Propagation in Silicon Waveguides

In this section, a rigorous theoretical and computational model is exploited to describe the propagation of optical pulses in Si waveguides. This model consists of a modified NLSE (Eq. (2.15)), which governs the dynamics of the optical field, coupled to a rate equation for the FCs (Eq. (2.20)).

Two types of Si waveguides are considered in this work, as illustrated in the middle block of Fig. 9.1. One is a single-mode Si-PhW with uniform cross-section, buried in SiO_2 cladding. The optical properties of such Si-PhWs are fully determined by the waveguide height, h, and width, w. The second waveguide is a Si-PhCW, consisting of a line defect in a two-dimensional honeycomb lattice of air holes in a Si slab. The geometrical parameters of Si-PhCWs are the lattice constant a, thickness, $h = 0.6a$,

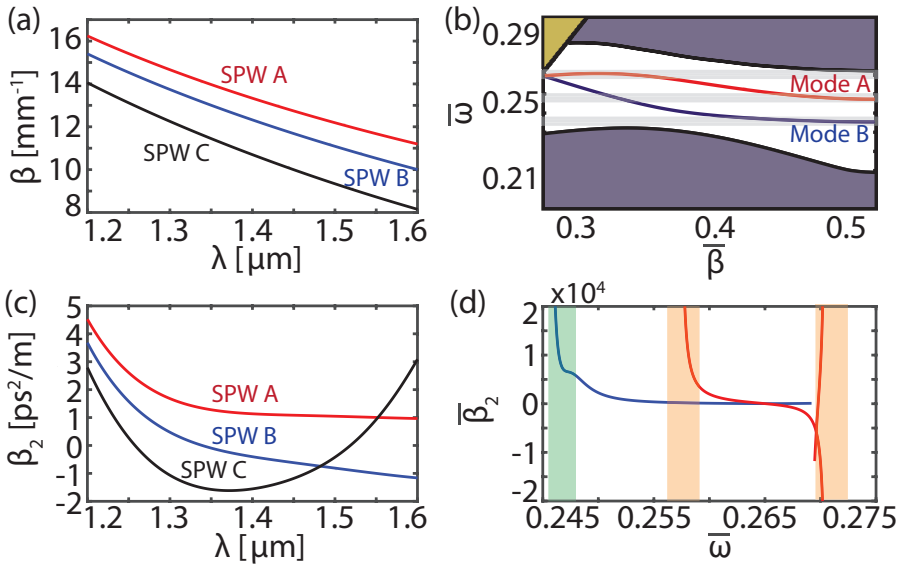

Figure 9.2: (a) Waveguide dispersion of strip waveguides with a fixed height, $h = 250\,\text{nm}$, and widths of $w = 1310\,\text{nm}$ (red line), $w = 537\,\text{nm}$ (blue line), and $w = 350\,\text{nm}$ (black line). (b) Projected photonic band structure of a Si-PhCW with $h = 0.6a$ and $r = 0.22a$. (c), (d) Second-order dispersion coefficient vs. wavelength, determined for the modes in (a) and (b), respectively. In (d), normalized quantities, $\bar{\omega} = \omega a/2\pi c$, $\bar{\beta} = \beta a/2\pi$, and $\bar{\beta}_2 = d^2\bar{\beta}/d\bar{\omega}^2$, are used. The grey bands in (b) and the green and orange bands in (d) indicate SL spectral domains defined as $n_g > 20$.

and hole radius, $r = 0.22a$. In this work, we consider both the telecommunication wavelength, $\lambda = 1550\,\text{nm}$, and the wavelength, $\lambda = 1300\,\text{nm}$, commonly used in data centers. For both wavelengths we design waveguides that have both normal and anomalous dispersion, so that the influence of dispersion on the system performance can be analyzed. Moreover, in the case of Si-PhCWs, the dispersion is engineered so that the waveguide possesses both fast-light (FL) and SL regimes, denoted as Si-PhCW-FL and Si-PhCW-SL, respectively.

The waveguide dispersion is tuned by simply changing the waveguide geometry. Thus, let us consider first the Si-PhWs. For this type of waveguide, we choose the height $h = 250\,\text{nm}$ and three widths, $w = 1310\,\text{nm}$ (called *Si-PhW-A*), $w = 537\,\text{nm}$ (called *Si-PhW-B*), and $w = 350\,\text{nm}$ (called *Si-PhW-C*), their propagation constant and second-order dispersion coefficient being plotted in Figs. 9.2(a) and 9.2(c), respectively. With this choice, at $\lambda = 1550\,\text{nm}$, *Si-PhW-A* (*Si-PhW-B*) has normal (anomalous) dispersion, whereas at $\lambda = 1300\,\text{nm}$ we used *Si-PhW-A* and *Si-PhW-C*, which have normal and anomalous dispersion, respectively. Moreover, dispersion properties of Si-PhCWs are summarized in Figs. 9.2(b) and 9.2(d). It can be seen from this fig-

Table 9.1: Silicon waveguide parameters used to in all our simulations

Waveguide type	λ	$w(a)$ [nm]	c/v_g	β_2 [ps^2 m^{-1}]	κ	γ' [W^{-1} m^{-1}]	γ'' [W^{-1} m^{-1}]
Si-PhW-1	1550	537	4.14	-1.0002	0.9469	241.4872	73.5711
Si-PhW-2	1550	1310	3.79	1.0042	0.9718	121.0340	36.8340
Si-PhW-3	1300	350	4.48	-1.0736	0.9281	379.50	152.68
Si-PhW-4	1300	1310	3.88	1.6796	0.9820	158.3060	54.1422
Si-PhCW-FL-1	1550	412	8.91	-330.75	0.9937	724.2573	220.7031
Si-PhCW-FL-2	1550	405.94	9.28	368.30	0.9919	1102.9	336.1006
Si-PhCW-FL-3	1300	345.55	8.91	-277.41	0.9937	1227.6	374.0825
Si-PhCW-FL-4	1300	340.45	9.28	308.88	0.9919	1869.7	569.7637
Si-PhCW-SL-1	1550	418.9	22.40	-1.76×10^4	0.9954	4388.1	1337.2
Si-PhCW-SL-2	1550	400.06	20.19	6.36×10^3	0.9902	6608.6	2013.8
Si-PhCW-SL-3	1300	351.34	22.40	-1.48×10^4	0.9954	7437.4	2266.4
Si-PhCW-SL-4	1300	335.54	20.19	5.33×10^3	0.9902	1.12×10^4	3413.3

ure that if one considers mode A, which depending on wavelength has either normal or anomalous dispersion, it is possible to tune the dispersion from normal to anomalous at chosen wavelengths simply by varying the lattice constant while keeping constant the ratio $\omega a/2\pi c = a/\lambda$. Following this procedure, for both the FL and SL regimes, we designed Si-PhCWs that have both normal and anomalous dispersion at 1550 nm and 1300 nm. As a result we can group our waveguides in four classes, denoted as class 1 ($\lambda = 1550$ nm, $\beta_2 < 0$), class 2 ($\lambda = 1550$ nm, $\beta_2 > 0$), class 3 ($\lambda = 1300$ nm, $\beta_2 < 0$), and class 4 ($\lambda = 1300$ nm, $\beta_2 > 0$). The resulting waveguide parameters, for both types of waveguides, are summarized in Table 9.1.

9.3 Theoretical Approach for BER Calculation

The BER calculation approach presented in Sec. 3.4 is applied to evaluate the performance of systems operating in the pulsed regime and which contain Si-PhW and Si-PhCW. The key underlying method, which is used in conjunction with a perturbation theory, is the Fourier-series KLSE of the optical field. The main advantage of this approach is its computational efficiency and accuracy. Specifically, we use a perturbative theory to construct the noise covariance matrix after propagation in the Si waveguides, whereas the Fourier-series KL expansion is used to determine a semi-analytical solution for the BER at the back-end of the direct-detection receiver. In our calculations, we assume that the receiver contains a Lorentzian optical filter described by the transfer function, $h_o(t)$, an ideal photodetector, and an integrate-and-dump electrical filter defined by the transfer function, $h_e(t)$. The electrical noise has not been included in

the receiver model, a reasonable approximation considering that the electrical noise is much smaller than the accumulated noise in the waveguide. Here, the bit-rate and bit window are denoted as B_r and T_0, respectively.

9.4 Results and Discussion

In this section, we present the results of a comprehensive performance analysis of systems containing the two types of Si waveguides. To begin with, we describe the computational setup of our numerical simulations. Thus, we utilize a PRBS of Gaussian-shaped pulses containing 2^9-1 bits together with a zero bit, which includes all possible 9-bit sequence patterns. The average power of the optical pulse is $P = 10\,\text{mW}$, with the relation between the peak power, P_0, and the average power per gaussian pulse being $PT_0 = \sqrt{\pi}P_0T_p$. The waveguide length for Si-PhWs, Si-PhCW-FLs, and Si-PhCW-SLs is $L = 5\,\text{cm}$, $L = 500\,\mu\text{m}$, and $L = 250\,\mu\text{m}$, respectively, unless otherwise is specified. Moreover, the number of frequency points used within one bit is $2Q+1 = 201$, which is relatively small as compared to the number of temporal sampling points, $N = 1024$, within the same bit, whereas the bit-rate and signal pulse width are chosen according to the following rules: *i*) When different values of the bit-rate, B_r, are used, the pulse width is fixed at $T_p = 9\,\text{ps}$. *ii*) When the duty-cycle $d_{cycle} = T_p \times (2B_r)$ is varied, the signal bit-rate is kept unchanged at $B_r = 10\,\text{Gb/s}$. Note that when keeping constant the average power, P, the smaller the B_r (d_{cycle}) is, the larger the peak power P_0 of a pulse is. Moreover, in the BER calculations, we select fixed detection thresholds for each type of Si waveguides.

A clear picture of the signal dynamics in the optical and electrical domains is provided by Fig. 9.3, where we show the amplitude of Gaussian pulses at the output of different types of Si waveguides, normalized to the input amplitude (left panels), and the eye diagrams of the electrical signal after the direct-detection receiver determined for class 1 ($\lambda = 1550\,\text{nm}$ and $\beta_2 < 0$) waveguides (right panels). As different types of Si-PhWs and Si-PhCWs have been considered in these simulations, Fig. 9.3 illustrates how the waveguide parameters influence the output signal. One main finding is that the signal degradation is larger in the anomalous dispersion regime for Si-PhWs and Si-PhCW-SLs as compared to normal dispersion regime, whereas the opposite is true in Si-PhCW-FLs, as per Figs. 9.3(a), 9.3(c), and 9.3(e). This is explained by the magnitude

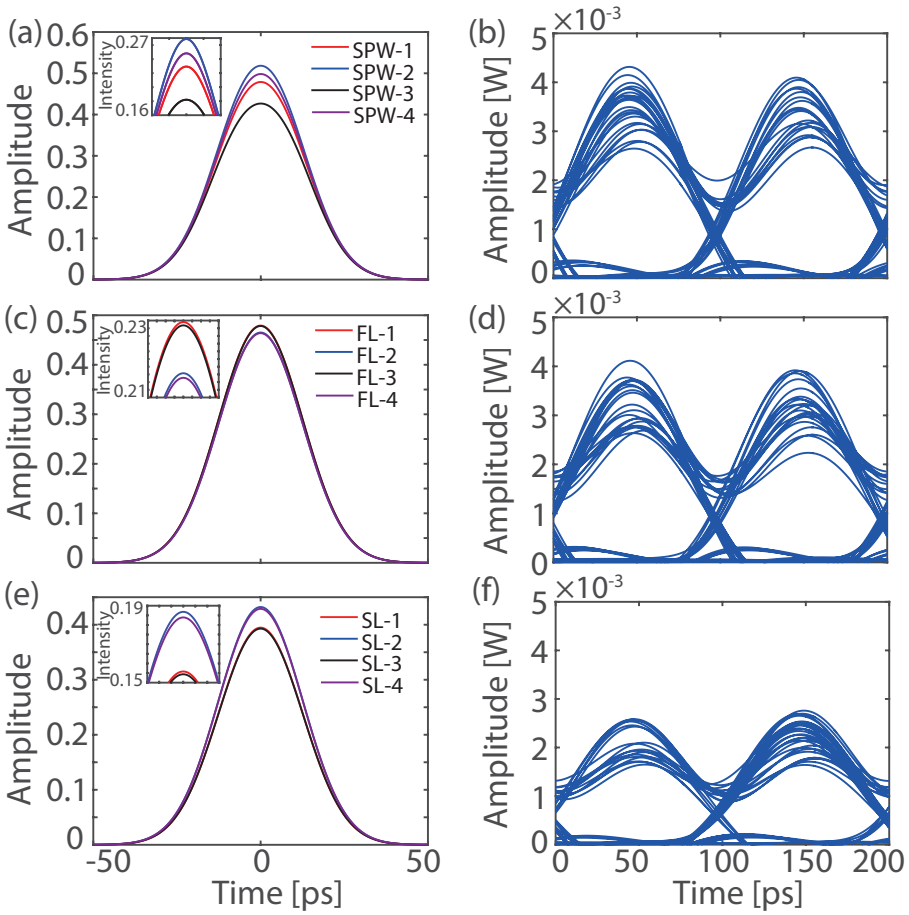

Figure 9.3: Output amplitude of Gaussian pulses corresponding to different types of Si waveguides, normalized to the input pulse (left panels) and the eye diagrams corresponding to the class 1 ($\lambda = 1550\,\text{nm}$ and $\beta_2 < 0$) waveguides (right panels). From top to bottom, the panels correspond to Si-PhWs, Si-PhCW-FLs, and Si-PhCW-SLs, respectively. In these simulations, $P = 10\,\text{mW}$, $d_{cycle} = 0.25$, and SNR $= 10\,\text{dB}$.

of the GV, namely the smaller the GV is the larger the linear and nonlinear losses are and consequently the larger the pulse decay is. The GV also influences the eye diagrams. In particular, Figs. 9.3(d) and 9.3(f) show that the eye diagram closes as the pulse propagation is tuned from the FL to the SL regime.

Duty-cycle is a key parameter of a train of Gaussian pulses that would directly influence the signal quality in Si photonic systems. In particular, for a given average power of the input signal, the smaller the duty-cycle, the higher the pulse peak power, and consequently the larger optical nonlinearity and amount of generated FCs would the optical pulses probe. To gain a deeper insight into these dependencies, we present in Fig. 9.4 the dependence of the BER on the pulse duty-cycle and SNR, determined for different types of Si photonic waveguides. In this analysis, the average power and

bit-rate are $P = 10\,\text{mW}$ and $B_r = 10\,\text{Gb/s}$, respectively. Note that some values of BER are unrealistically small; however, to make it easier to compare the results obtained for different waveguides, we used the same range of SNR. It can be seen that in all cases the system BER increases with the duty-cycle. In addition, when considering the Si waveguides with anomalous dispersion, the performance of class 3 waveguides is worse than that of class 1 waveguides, as shown in the left panels of Fig. 9.4. Moreover, this figure shows that the difference between BER in class 2 and class 4 Si-PhCWs is relatively small, with this difference being larger in the SL regime.

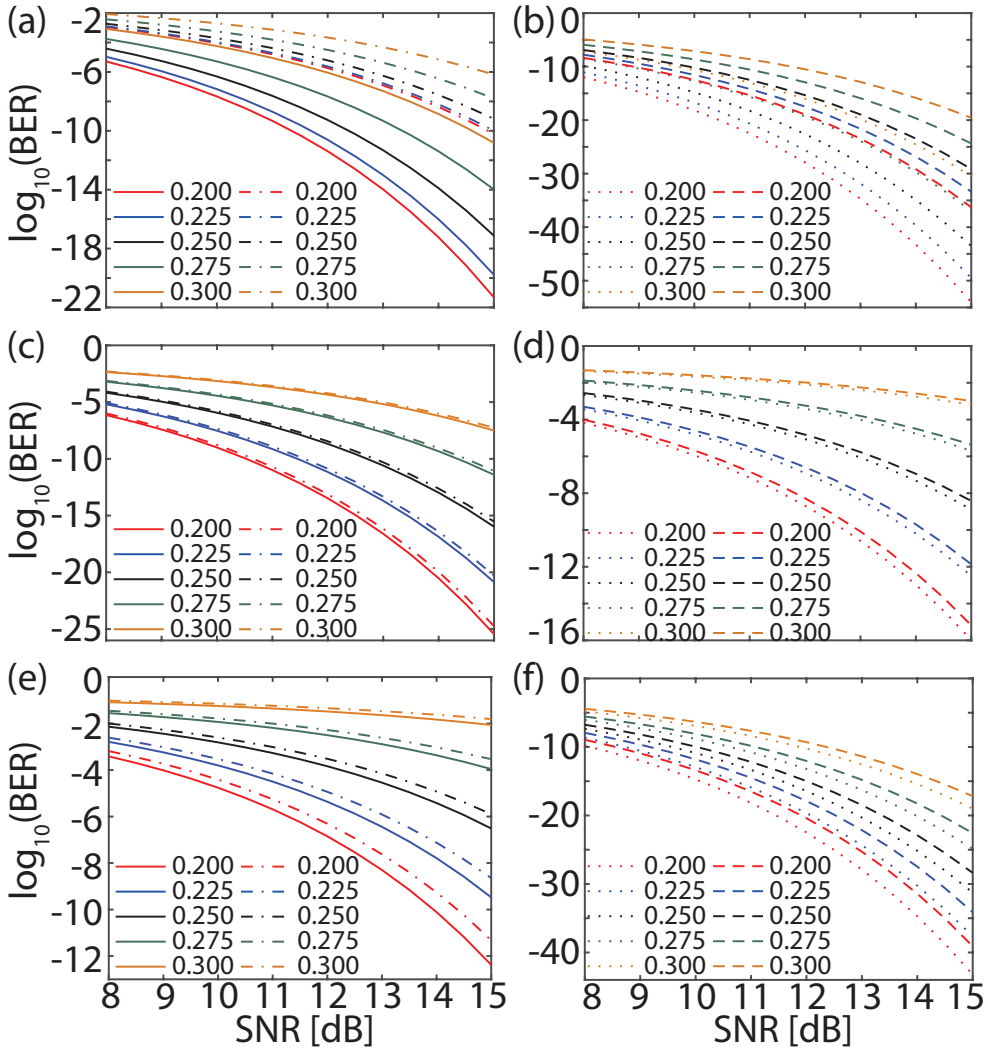

Figure 9.4: System BER vs. SNR, calculated for several values of d_{cycle} and for three types of Si photonic systems. The investigated waveguides and their length are Si-PhW (top, $L = 5\,\text{cm}$), Si-PhCW-FL (middle, $L = 500\,\mu\text{m}$), and Si-PhCW-SL (bottom, $L = 250\,\mu\text{m}$). In the left panels, the solid (dash-dot) lines correspond to class 1 (class 3) waveguides, whereas the dotted (dashed) lines in the right panels represent class 2 (class 4) waveguides. In these simulations, $P = 10\,\text{mW}$ and $B_r = 10\,\text{Gb/s}$.

Figures 9.4(c), 9.4(d), 9.4(e), and 9.4(f) also show that in the case of Si-PhCWs, BER increases as the wavelength decreases, when comparing two groups of Si-PhCWs, namely class 1 vs. class 3 and class 2 vs. class 4. To understand this phenomenon, let us consider the dependence of the waveguide parameters on wavelength. Thus, it can be easily proven that β_2 and γ are proportional to a and a^{-3}, respectively. Therefore, if one operates at a certain point on the normalized dispersion band of a mode (fixed a/λ), β_2 increases as the wavelength increases, whereas the opposite is true in the case of γ. Note, however, that γ decreases with a much faster than β_2 increases with a, and therefore its variation with λ has the dominant influence on the variation of BER with λ, resulting in an increase of BER when the wavelength decreases. On the other hand, the BER for Si-PhWs are not in such relation, since their linear and nonlinear parameters do not scale with wavelength in a self-similar way. Last but not least, the BER curves with different values of duty-cycle, calculated for the system where the transmitter is directly connected to the receiver, are plot in Fig. 9.5. After comparing Fig. 9.5(a) with Fig. 9.4, one can get the penalty information caused by inserting Si waveguides at each pulsewidth.

We now consider the transmission BER at different bit-rates, for Si-PhWs, Si-PhCW-FLs, and Si-PhCW-SLs. We investigate both anomalous and normal dispersion regimes, the wavelengths being 1550 nm and 1300 nm, the average power $P = 10$ mW, and $T_p = 9$ ps. The transmission BER calculated under these conditions is shown in Fig. 9.6. This figure suggests that, as expected, smaller bit-rates lead to improved sys-

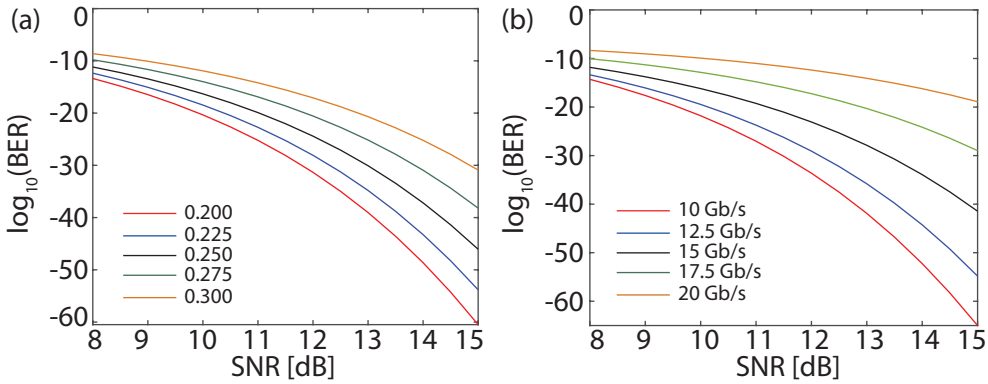

Figure 9.5: System BER vs. SNR in the system where no Si waveguide link is contained, considering different values of duty-cycle (a) and bit-rate (b). In these simulations, the average power is $P = 10$ mW. Additionally, in (a) the bit-rate is $B_r = 10$ Gb/s, whereas in (b) the pulsewidth is fixed with $T_p = 9$ ps.

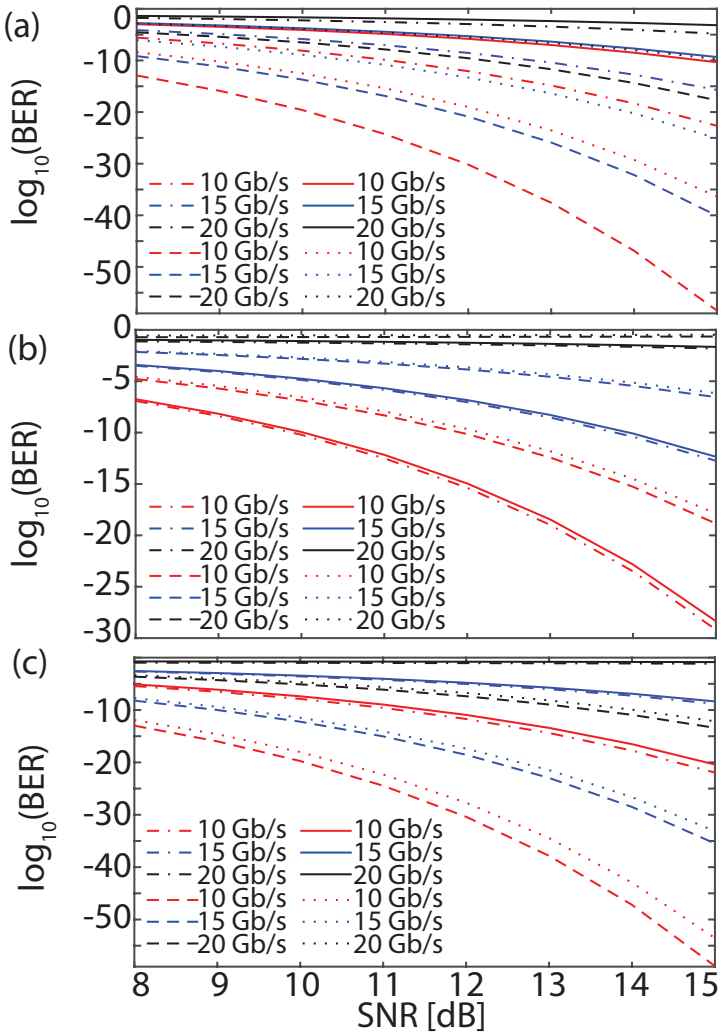

Figure 9.6: BER vs. SNR, determined for different B_r and Si photonic systems. From top to bottom, the panels correspond to Si-PhWs ($L = 5\,\text{cm}$), Si-PhCW-FLs ($L = 500\,\mu\text{m}$), and Si-PhCW-SLs ($L = 250\,\mu\text{m}$). The dash-dot, dashed, solid, and dotted lines correspond to class 1, class 2, class 3, and class 4 waveguides, respectively. In all cases, $P = 10\,\text{mW}$ and $T_p = 9\,\text{ps}$.

tem performance for all Si waveguides. Another important result illustrated in Fig. 9.6 is that the difference between BER in the normal and anomalous regime is much smaller in the Si-PhW-FL regime as compared to that in the Si-PhW-SL regime and in Si-PhWs. This can be explained as follows: the signal propagates in the Si-PhW over a much larger distance so that larger variation of BER occurs, whereas in the case of the Si-PhW-SL the increase in the strength of the linear and nonlinear effects leads to smaller BER. Also related to this finding, it can be seen that the overall BER performance is better in the normal dispersion regime of Si-PhWs and Si-PhW-SLs as compared to BER performance in the case of anomalous dispersion, whereas the opposite situation

holds in the cease of Si-PhCW-FLs. Specifically, the best system performance can be found in the class 2 of Si-PhWs and Si-PhW-SLs, as well as class 1 of Si-PhW-FLs, when comparing the same types of Si waveguides. Similarly, the BERs in the system where the Si waveguide is not contained, accounting for different values of bit-rate, are shown in Fig. 9.5(b). This figure is provided as a reference to determine the penalty after inserting the Si waveguide.

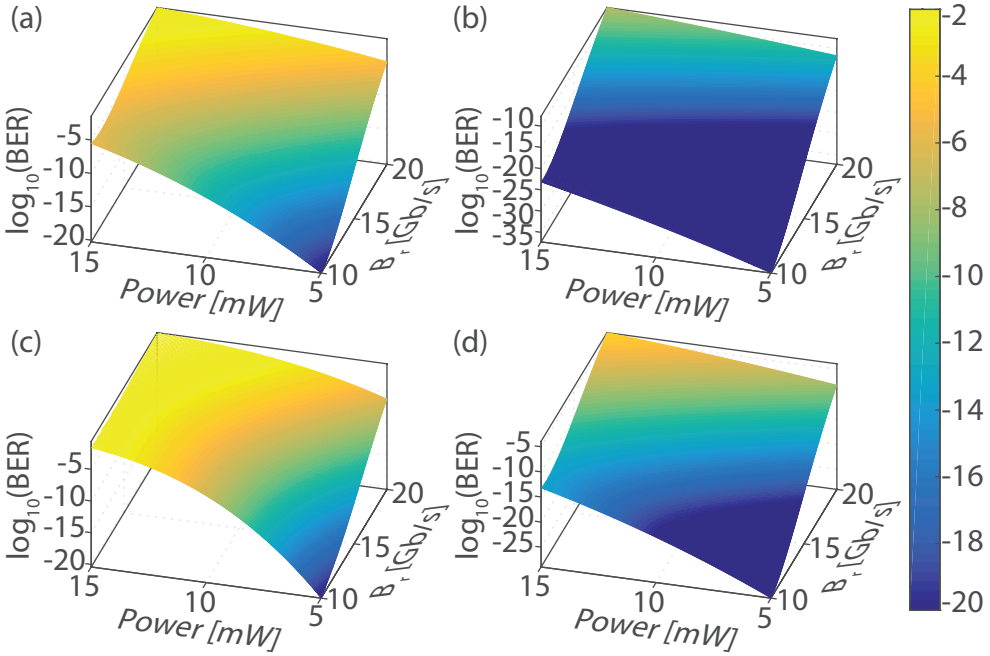

Figure 9.7: Dependence of BER on the input power and bit-rate for four strip waveguide systems: (a) Si-PhW-1, (b) Si-PhW-2, (c) Si-PhW-3, and (d) Si-PhW-4. In all cases, SNR $= 12\,$dB, $L = 5\,$cm, and $T_p = 9\,$ps.

Another key parameter that influences the system performance is the optical power, as it determines the strength of nonlinear optical effects, such as SPM and TPA. Therefore, we investigated the dependence of the transmission BER of Si photonic systems on the average optical power. The first systems we considered contain Si-PhWs. More specifically, we calculated the BER for four 5 cm-long Si-PhWs, for different values of the input power and bit-rate. These calculations were performed for the two wavelengths of interest, $\lambda = 1550\,$nm and $\lambda = 1300\,$nm, and both normal and anomalous waveguide dispersion cases were studied.

The results of this investigation are summarized in Fig. 9.7. It can be seen from this figure that, as expected, BER decreases when either the average power or bit-rate decreases. In addition, if one compares the two waveguides whose dispersion has oppo-

site signs at $\lambda = 1550\,\text{nm}$, namely Si-PhW-1 and Si-PhW-2, one can see that although the absolute value of β_2 is the same for both waveguides, the BER is much smaller for the latter one. This is explained by the fact that the nonlinear coefficient of Si-PhW-1 is almost twice as large as that of Si-PhW-2, meaning that for the pulse parameters considered in this analysis the optical nonlinearity plays the dominant role in determining the BER. This conclusion is further supported by the comparison of the BER corresponding to the Si-PhW-2 and Si-PhW-4 waveguides, which both have normal dispersion. A similar conclusion can be derived by comparing the BERs calculated for Si-PhW-3 and Si-PhW-4, which are the waveguides that have anomalous and normal dispersion at $\lambda = 1300\,\text{nm}$, respectively. Thus, it can be seen that again the smaller BER corresponds to the waveguide with smaller γ. Moreover, among these four different photonics systems, the best performance is achieved in the case of Si-PhW-2 and the worse one corresponds to Si-PhW-3.

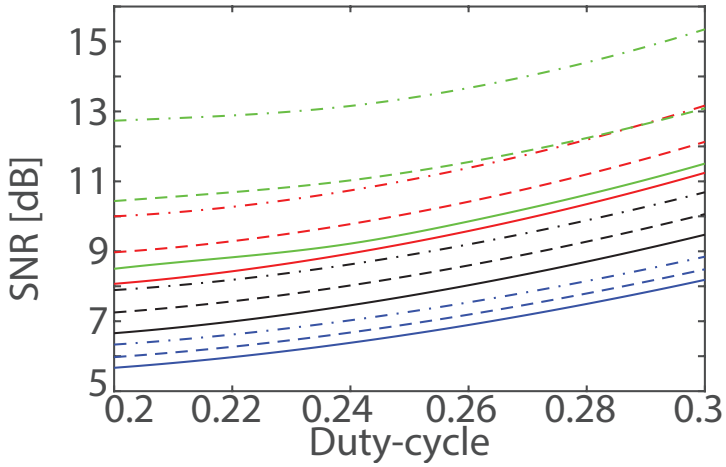

Figure 9.8: Constant-level curves corresponding to BER $= 10^{-9}$. The average power is 5 mW (solid lines), 7 mW (dashed lines), and 9 mW (dash-dot lines). The red, blue, green, and black curves correspond to Si-PhW-1, Si-PhW-2, Si-PhW-3, and Si-PhW-4 cases, respectively. In all calculation, $L = 5\,\text{cm}$ and $B_r = 10\,\text{Gb/s}$.

In order to gain a deeper insight into the system performance, we determined the values of the SNR and duty-cycle for which the BER is lower than a certain threshold, that is BER $< 10^{-9}$. The results of this investigation are summarized in Fig. 9.8. In this analysis, we consider the same four Si-PhW systems investigated in Fig. 9.7, the corresponding average power being 5 mW, 7 mW, and 9 mW and the bit-rate, $B_r = 10\,\text{Gb/s}$. One conclusion of these simulations is that the larger parameter space where the condition BER $< 10^{-9}$ holds corresponds to the Si-PhW-2 case (blue curves in

Fig. 9.8), namely the waveguide with the smallest γ. In addition, it can also be seen that as γ increases, the shift of the constant-BER curves with the variation of the average power increases as well. Moreover, one can observe in Fig. 9.8 that as the duty-cycle increases one has to increase the SNR in order to maintain BER constant. This is explained by the fact that larger values of the duty-cycle lead to the worse signal quality when the same detection threshold is used, and therefore to keep constant the BER one has to reduce the noise content of the optical signal.

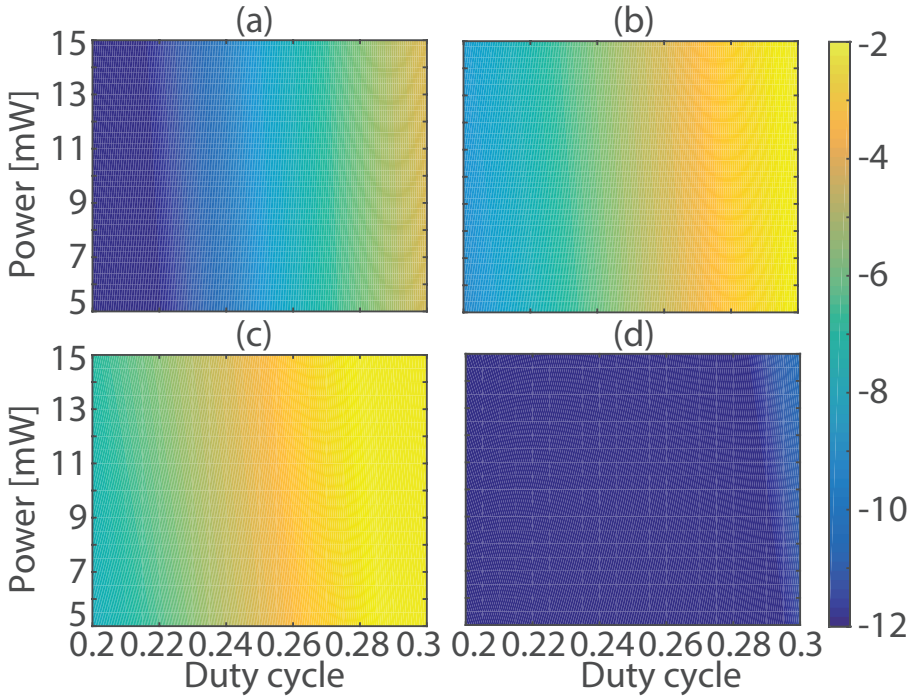

Figure 9.9: Contour maps of $\log_{10}(\text{BER})$ vs. power and pulse duty-cycle, calculated for four Si-PhCW systems at $\lambda = 1550\,\text{nm}$. The top (bottom) panels correspond to Si-PhCW-FLs with $L = 500\,\mu\text{m}$ (Si-PhCW-SLs with $L = 250\,\mu\text{m}$), whereas the left (right) panels correspond to class 1 (class 2) Si-PhCWs. In all case, SNR $= 12\,\text{dB}$, $P = 10\,\text{mW}$, and $B_r = 10\,\text{Gb/s}$.

Since both the linear and nonlinear optical effects depend on the GV, a pertinent question is how the system performance is affected by changes of this parameter. To answer this question, we considered Si-PhCWs operated in the FL and SL regimes. In particular, we calculated the BER maps vs. power and duty-cycle for Si-PhCWs with normal and anomalous dispersion at $\lambda = 1550\,\text{nm}$, the results being presented in Fig. 9.9. Similar to the previous analysis, the transmission BER in the anomalous dispersion region of Si-PhCW-FL is smaller than in the normal dispersion region, whereas the influence of the waveguide dispersion on the system performance is much stronger

in Si-PhCW-SLs. Moreover, it can be seen in Fig. 9.9 that smaller duty-cycle leads to better BERs when the same detection threshold is uded, even though more FCs are generated when the duty-cycle decreases. Importantly, the results presented in Fig. 9.9 suggest that similar transmission BER is achieved in FL and SL regimes, although in the latter case the waveguide is twice as short. This proves that by operating the system in the SL regime, one can reduce the device footprint.

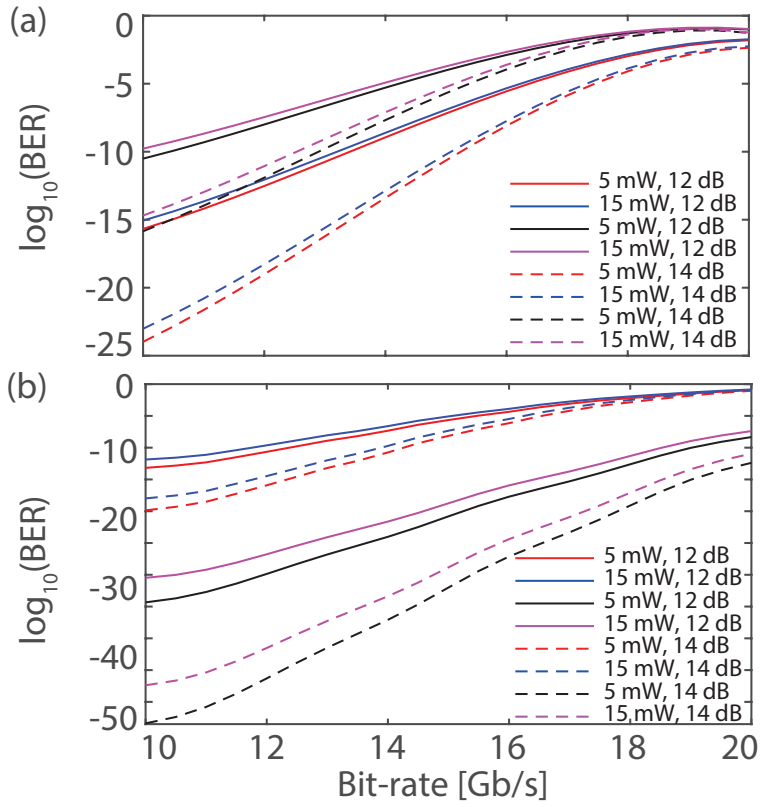

Figure 9.10: Variation of the system BER with the bit-rate. Top (bottom) panel corresponds to FL (SL) regime, in both cases the wavelength being $\lambda = 1550\,\text{nm}$. The red and blue curves correspond to class 1 Si-PhCWs, whereas black and magenta curves to class 2 Si-PhCWs. The values of SNR and average power are indicated in the legends, whereas $T_p = 9\,\text{ps}$.

Additional insights into the influence of the average power on the signal degradation in Si-PhCWs are provided by data plotted in Fig. 9.10, where the dependence of the system BER on the bit-rate is presented. In particular, we considered the largest and smallest average power used in Fig. 9.9, for both class 1 and class 2 Si-PhCWs ($\lambda = 1550\,\text{nm}$). This figure shows that BER increases monotonously with B_r in the SL regime, whereas in the FL regime it appears to peak at $B_r \sim 19\,\text{Gb/s}$. Moreover, it can be seen that of the four Si-PhCW systems, only in the case of class 2 Si-PhCW oper-

ated in the SL regime is the system BER below the threshold of 10^{-9}, for all values of B_r in the range of 10 Gb/s to 20 Gb/s. Further validating our previous conclusions, the results presented in Fig. 9.10 also demonstrate a stronger dependence of BER on the average power in the SL regime as compared to the FL one. Finally, in agreement with previous results, it can be seen that the $2\times$ shorter Si-PhCW-SL provides better system performance than the Si-PhCW-FL, meaning that there is large potential for designing extremely compact Si optical interconnects that operate at high bit-rate.

9.5 Conclusion

In conclusion, we have performed an extensive and in-depth study of transmission bit-error ratio in silicon photonic systems utilizing return-to-zero optical signals consisting of trains of Gaussian pulses. The photonic systems are composed of silicon photonic waveguides and direct-detection receivers. A rigorous theoretical model is developed and applied to characterize all the key optical effects during pulse propagation in silicon waveguides, and the Fourier-series Karhunen-Loève expansion method in conjunction with a perturbation theory are employed to evaluate the system bit-error ratio after direct-detection. In order to fully assess the influence of the waveguide parameters on the system performance, we considered in this work both strip silicon photonic wires and silicon photonic crystal waveguides, with each waveguide possessing normal and anomalous dispersion. In addition, the silicon photonic crystal waveguides studied in this work possessed slow- and fast-light dispersion regimes, so that we could investigate the influence of the group-velocity on the bit-error ratio. We also explored the relationships between the bit-error ratio and other key system parameters, including the pulse wavelength and temporal width, power, and bit-rate.

Our computational results suggest that suitable and commensurate system bit-error ratios can be achieved in silicon photonic wires and photonic crystal waveguides, but in the latter case the waveguide length is about $100\times$ shorter when operating in the fast-light regime and about $200\times$ shorter when the optical signal propagates in the slow-light regime. Importantly for future studies of the performance of silicon-based photonic systems, the mathematical formalism introduced in this paper can also be applied to other optical waveguides and more sophisticated photonic integrated circuits, thus providing a basis for future technological advancements in silicon-based on-chip

and chip-to-chip optical networks.

Bibliography

[1] X. Chen, N. C. Panoiu, and R. M. Osgood, "Theory of Raman-mediated pulsed amplification in silicon-wire waveguides," IEEE J. Quantum Electron. **42**, 160-170 (2006).

[2] J. You and N. C. Panoiu, "Calculation of Bit Error Rates in Optical Systems with Silicon Photonic Wires," IEEE J. Quantum Electron. **51**, 8400108 (2015).

[3] N. C. Panoiu, J. F. McMillan, and C. W. Wong, "Theoretical analysis of pulse dynamics in silicon photonic crystal wire waveguides," IEEE J. Sel. Top. Quantum Electron. **16**, 257-266 (2010).

[4] S. Lavdas and N. C. Panoiu, "Theory of Pulsed Four-Wave-Mixing in One-dimensional Silicon Photonic Crystal Slab Waveguides," Phys. Rev. B **93**, 115435 (2016).

[5] R. Holzlöhner, C. R. Menyuk, W. L. Kath, and V. S. Grigoryan, "Efficient and Accurate Computation of Eye Diagrams and Bit-Error Rates in a Single-Channel CRZ System," IEEE Photon. Technol. Lett. **14**, 1079-1081, (2002).

Chapter 10

Conclusions and Future work

Silicon photonic waveguides have attracted extensive research efforts during the last two decades, due to their abilities of facilitating ultrafast optical interconnects and ultra-dense passive and active photonic devices. The outstanding properties of silicon photonic waveguides, including the large transparency window, subwavelength cross-sections, strong dispersion and nonlinearity, as well as the good compatibility with CMOS circuitries, provide great opportunities to the next-generation information networks. Even though all the essential parts of silicon photonics have been investigated nowadays, including the scientific exploration, design, fabless, foundries, devices and systems, the whole silicon photonics ecosystem is under research and development stage. Therefore, it is extremely important to study the underlying physics of silicon photonic waveguides, by means of the theoretical and computational approaches. This would not only allow the engineering of more complicated silicon photonic systems, but also enable the implementation of the most up-to-date photonic materials and devices in practice.

This dissertation serves as a promising solution to settle the realistic issues raised above. The emphasis of this work is put on the investigation and demonstration of the nonlinear signal processing in the photonic systems containing nanoscale silicon waveguides. More precisely, two sets of mathematical models have been proposed in this dissertation, namely, the optical signal propagation models for silicon waveguides and the accurate BER calculation models. In particular, regarding the first set of theoretical models, a linearized version of the full propagation models is derived, which is specified for the photonic systems utilizing continuous-wave (CW) signals. These two propagation models accurately characterize all the linear and nonlinear optical effects

within silicon photonic waveguides. Furthermore, the second set of mathematical models are based on the Karhunen-Loève series expansion methods, which can be applied to calculate the system BER in an accurate and efficient way. Therefore, the theoretical models and numerical algorithms introduced in this dissertation can be very useful to design high-performance photonic devices and integrated photonic circuitries, as well as provide a complete induction of the significant optical phenomena within the silicon photonic waveguides.

The following sections will present my original contributions to the field of silicon photonics and the future prospectives to the area of photonics.

10.1 Contributions

The main contributions of this dissertation in the development of silicon photonics can be divided into two aspects: firstly, this work helps provide the rigorous theoretical and numerical models for the investigation of nonlinear signal propagation in silicon photonic waveguides; secondly, the accurate BER evaluation approaches are recommended to deal with the nonlinear interaction between the signal and the noise in particular. Importantly, the complete system analysis model has been numerically implemented as a Matlab tool. Furthermore, the accurate analysis towards silicon photonic systems, which is obtained by using this Matlab tool, has shown that it is of great importance to employ the theoretical and computational approaches in the design of silicon interconnects and optical devices, and the corroboration and optimization of the experimental work.

To be more specific, an accurate computational model is developed to simulate the the optical signal propagation in two specially designed silicon waveguides, namely the single-mode strip silicon photonic waveguides and the photonic crystal silicon waveguides. Both cases of single- and multi-wavelength input signals have been taken into account, thus two sets of the full propagation models are yielded. Furthermore, the linearized models are extracted from the full propagation approaches for the CW input signals, by means of discarding all quadratic and higher-order noise terms in the original formulations. Notably, these two types of propagation models are mathematically and numerically proved that they can accurately incorporate all important optical effects, including the waveguide loss, GVD, SPM, XPM, FCA and FCD, as well as the

mutual interaction between free carriers and the optical field. Moreover, two groups of comprehensive investigations are carried out: one is the detailed comparison between the normal and anomalous dispersion regions of silicon photonic waveguides, with the other being the comparison between the fast-light and slow-light spectral regimes. In this process, the noise dynamics is studied in combination with different types of signal modulation formats. Last but not least, the numerical implementation of the full and linearized algorithms for optical signal propagation is also provided in this dissertation, which allows for extensively investigation regarding nonlinear optical response in silicon photonic waveguides.

Furthermore, accurate and efficient theoretical models are constructed for BER calculation in this dissertation. Specifically, three BER calculation approaches based on the time-domain, frequency-domain and Fourier-series Karhunen-Loève series expansion, are presented, in order to fully capture the waveguide nonlinearity in silicon photonic systems. Moreover, the discussion with regard to the applications and advantages of these expansion methods is also presented. Particularly, the time- and frequency-domain Karhunen-Loève series expansion methods are selected for the evaluation of BER with regard to CW optical signals, whereas the Fourier-series Karhunen-Loève series expansion method is employed for the case of optical pulsed signals. In addition, rigorous computational procedures are included for the implementation of these Karhunen-Loève expansion methods in the system performance evaluation, considering both single- and multi-channel silicon photonic systems.

Apart from the major contributions of establishing the performance evaluation engine for silicon photonic systems, literature reviews in the aspect of silicon photonics, optical interconnects, silicon waveguides and BER calculation methods, are also provided in this dissertation. These concise summaries can help one better understand the background, connections between each of those fields, and the importance of this work.

Equipped with this theoretical and computational tools, the comprehensive analysis are performed for the single-channel and multi-channel photonic systems. Several valuable and remarkable findings can be drawn from this PhD project, which definitely contributes to the development of silicon photonics:

- In terms of the single-channel strip silicon photonic systems with the OOK CW signals, the geometry of silicon waveguides and the power of optical signal play

an important role when determining the system BER. In addition, the BER dependence on these two factors becomes more transparent in the anomalous dispersion region of silicon waveguide, where the nonlinearity is much larger than that of normal dispersion.

- The analysis of the single-channel silicon photonic crystal systems reveals that although slow-light effects can enhance the waveguide nonlinearity, they also cause a significant degradation of the transmission BER.

- With regard to the higher-order PSK modulation formats, the studies of the single-channel strip and photonic crystal systems indicate that the optical power, type of PSK modulation, waveguide length, and group-velocity are key factors characterizing the system BER, their influence on BER being more significant in a photonic system with larger nonlinearity. In particular, due to the reduced Euclidean spacing between points in the constellation of PSK signals, the higher-order PSK modulated signals would induce larger system BERs, and thus the balance between the high information capacity (orders of PSK modulation) and good signal quality (BER) must be reached.

- The rigorous mathematical algorithms are developed for the N-channel signal co-propagation and the receiver detection. The relevant simulations show that the BER affecting factors in the multi-channel system performance include the dispersion regimes, group-velocity, the waveguide length, the channel number and the signal power.

- The case of single-channel silicon photonic systems utilizing arbitrary Gaussian pulsed signals is also investigated in this dissertation. The simulation results suggest that a good system performance is achieved in centimeter-long Si-PhWs, and a similar case of BER is also realized in Si-PhCWs but with their length $100\times$ and $200\times$ shorter when operating in the fast- and slow-light regimes, respectively. However, the pulse width of Gaussian-pulse signals is the dominant parameter to influence the BER in Si-PhWs, while for Si-PhCWs the main factor turns out to be the waveguide properties via the pulse group-velocity.

- The complete system evaluation model is implemented in Matlab. This Matlab

engine has the scan function, which can be run in serial or in parallel. It is beneficial to use the parallel run, considering the computational time.

10.2 Future Prospects

Silicon photonics are promising to settle the bottlenecks of ultra-broad bandwidth and highly integrated supercomputers and data centers, thus substantial research efforts have been and will be contributed to this field. As mentioned before, a full supply of silicon photonics is under the stage of research and development, requiring loads of improvements to enable the commercialization of silicon photonic products in the near future. The theoretical and computational models demonstrated in this dissertation definitely provide a valuable and efficient tool for the design of chip-scale optical interconnects. Apart from the goals presented earlier, the signal propagation models and BER calculation approaches can be widely applied in abundant aspects, which I will give a detailed explanation in the next few paragraphs.

Firstly, it would be very beneficial to include more complicated nonlinear effects like FWM and Raman scattering in the signal propagation models. An interesting example is to consider the Raman effect in a two-channel silicon photonic system, where one channel contains a CW signal and the white noise, while the other channel only consisting of the white noise. The first channel will behaves as the pump to yield the signal generation in the other channel. Moreover, their nonlinear interaction during transmission may bring out some new phenomena. Therefore, a signal propagation model that owns the flexibility to engineer the optical properties of silicon waveguides, will absolutely offer more possibilities to the functionalities of photonic devices.

Secondly, from practical point of view, all types of system noise can be taken into account in the BER calculation that based on the Karhunen-Loève series expansion, including the laser phase noise, the spontaneous emission noise, receiver thermal noise and signal shot noise. In general, this all-inclusive evaluation is usually carried out by using the Monte-Carlo method, with the accuracy guaranteed by the computational time. But when compared with the newly-proposed BER calculation method, the Monte-Carlo method is lack of the advantage in the computational cost.

Furthermore, the theoretical formalism introduced in this dissertation can also be applied to other types of waveguides or more complex devices practical interest.

For example, our theoretical approach can applied to tapered, slot, and other types of waveguides by simply using the corresponding linear and nonlinear waveguide optical coefficients. Moreover, after properly modifying the system of equations governing the optical field dynamics in silicon waveguides, a similar theoretical formalism can be employed study the transmission BER of photonic systems containing, e.g., splitters, ring modulators coupled to a waveguide, and multi-mode waveguides. Equally important, the generality the theoretical methods used in this study makes it easy to adapt them to tackle much more advanced signal modulation formats and detection schemes than those considered in this work.

Last but not least, a more sophisticated modeling platform can be built based on the evaluation engine provided in this dissertation. To be more specific, the current engine will serves as the physical layer, with the other two layers to be the network and the application. Even though large amount of theoretical and numerical investigations are required to carry out, such a integrated simulation platform can definitely contribute to the revolution of the next-generation information network.

Appendix A

Gauss-Hermite Algorithm

The Gauss-Hermite algorithm is applied in this dissertation to handle the convolution of Eqs. (3.9) and (3.10). A general form of Gauss-Hermite quadrature is illustrated below to approximate such integral:

$$\int_{-\infty}^{\infty} e^{(-\tau^2)}\mathbf{f}(\tau)d\tau \approx \sum_{j=1}^{M} \omega_j \mathbf{f}(\tau_j), \tag{A.1}$$

where τ_j and ω_j are the abscissas and associated weights, respectively. By operating the Gauss-Hermite technique to Eqs. (3.9) and (3.10) and choosing the same time step of τ_j, the discretized formulas are yield:

$$\sum_{j=1}^{M} \omega_j h_e(\tau_j)\rho_i^k(t_m-\tau_j)\phi_\alpha^k(\tau_j) = \mu_\alpha^k \phi_\alpha^k(t_m), \tag{A.2a}$$

$$\sum_{j=1}^{M} \omega_j h_e(\tau_j)\rho_q^k(t_m-\tau_j)\psi_\alpha^k(\tau_j) = \nu_\alpha^k \psi_\alpha^k(t_m), \tag{A.2b}$$

$$\sum_{j=1}^{M} \omega_j h_e(t_m)h_e(\tau_j)\rho_{iq}^k(\tau_j-t_m)\psi_\beta^k(\tau_j) = \sigma_{\alpha\beta}^k \phi_\alpha^k(t_m), \tag{A.2c}$$

where $m, j = 1, ..., M$. Then, solving Eqs. (3.9) and (3.10) is transferred to find the eigenvalues and eigenfunctions, based on the relations below:

$$\underline{\underline{C}}_i \cdot \underline{\underline{F}}^1 = \underline{\underline{\Lambda}}_\mu^k \cdot \underline{\underline{F}}^1, \tag{A.3a}$$

$$\underline{\underline{C}}_q \cdot \underline{\underline{F}}^2 = \underline{\underline{\Lambda}}_\nu^k \cdot \underline{\underline{F}}^2, \tag{A.3b}$$

$$\underline{\underline{C}}_{iq} \cdot \underline{\underline{F}}^1 = \underline{\underline{\Sigma}}^k \cdot \underline{\underline{F}}^1, \tag{A.3c}$$

with the explicit expressions of the related matrixes listed below:

$$(\underline{\underline{F}}^1)_{j\alpha} = \phi_\alpha^k(t_m), \quad \underline{\underline{F}}^2_{j\alpha} = \psi_\alpha^k(t_m), \tag{A.4a}$$

$$(\underline{\underline{C}}_{i/q})_{mj} = \omega_j h_e(\tau_j)\rho^k_{i/q}(t_m - \tau_j),$$

$$(\underline{\underline{C}}_{iq})_{mj} = \omega_j h_e(t_m)h_e(\tau_j)\rho^k_{iq}(\tau_j - t_m), \tag{A.4b}$$

$$(\underline{\underline{\Lambda}}^k_\mu)_{mj} = \mu^k_\alpha \delta_{mj}, \quad (\underline{\underline{\Lambda}}^k_\nu)_{mj} = \nu^k_\alpha \delta_{mj}, \quad (\underline{\underline{\Sigma}}^k)_{mj} = \sigma^k_{\alpha\beta}|_{\alpha=m,\beta=j}. \tag{A.4c}$$

To this end, the mathematical solutions for Eqs. (3.9) and (3.10) are ready to be derived.

Appendix B

Fifth-order Runge-Kutta Algorithm

The Runge-Kutta method is usually applied in the ODEs, in order to extract the semi-analytical solutions. Its mathematical process is to first collect data from a few Euler-steps, with each step accounting for one calculation of the right-hand side of the ODE, and then utilize the data to approach a desired Taylor series expansion. Here, the numerical implementation of the fifth-order Runge-Kutta algorithm in Matlab will be presented. In particular, a self-constructed Matlab code based on the fifth-order Runge-Kutta algorithm is applied, in order to calculate the FCs density for the full propagation model, whereas the Matlab built-in function *ode*45 is utilized for the evaluation of the ODEs in the linearized model. Moreover, these two approaches share exactly the same mathematical formulae.

Table B.1: Cash-Karp paramters for embedded Runge-Kutta method.

j	a_j	b_{jm}					c_j
1	0	0	0	0	0	0	$\frac{37}{378}$
2	$\frac{1}{5}$	$\frac{1}{5}$	0	0	0	0	0
3	$\frac{3}{10}$	$\frac{3}{40}$	$\frac{9}{40}$	0	0	0	$\frac{250}{621}$
4	$\frac{3}{5}$	$\frac{3}{10}$	$-\frac{9}{10}$	$\frac{6}{5}$	0	0	$\frac{125}{594}$
5	1	$-\frac{11}{54}$	$-\frac{5}{2}$	$-\frac{70}{27}$	$\frac{35}{27}$	0	0
6	$\frac{7}{8}$	$\frac{1631}{55296}$	$\frac{175}{512}$	$\frac{575}{13824}$	$\frac{44275}{110592}$	$-\frac{253}{4096}$	$\frac{512}{1771}$
$m=$		1	2	3	4	5	

The start point is to select the suitable points t_n for Eq. (2.39), where both conditions of continuity and differentiability are satisfied, in order to approximate $\mathbf{y}(t_n)$ with

Table B.2: Dormand-Prince paramters for embedded Runge-Kutta method.

j	a_j	b_{jm}					c_j
1	0	0	0	0	0	0	$\frac{71}{57600}$
2	$\frac{1}{5}$	$\frac{1}{5}$	0	0	0	0	0
3	$\frac{3}{10}$	$\frac{3}{40}$	$\frac{9}{40}$	0	0	0	$\frac{-71}{16695}$
4	$\frac{4}{5}$	$\frac{44}{45}$	$-\frac{56}{15}$	$\frac{32}{9}$	0	0	$\frac{71}{1920}$
5	$\frac{8}{9}$	$\frac{19372}{6561}$	$-\frac{25360}{2187}$	$\frac{64448}{6561}$	$\frac{-212}{729}$	0	$\frac{-17253}{339200}$
6	1	$\frac{35}{384}$	0	$\frac{500}{1113}$	$\frac{125}{192}$	$-\frac{5103}{18656}$	$\frac{22}{525}$
$m=$		1	2	3	4	5	

$\mathbf{y_n}$:

$$t_{n+1} = t_n + h_n, \quad h_n = \delta(t_n)h \tag{B.1}$$

where $0 < \delta(t_n) \leq 1$ and $n = 0, 1, 2, \cdots$. Then an analytical Runge-Kutta formula is given by

$$\mathbf{y_{n+1}} = \mathbf{y_n} + h_n\Theta(y_n, h_n) = \mathbf{y_n} + \sum_{j=1}^{\varpi} c_j k_j \tag{B.2}$$

where

$$k_1 = h_n\mathbf{f}(t_n, y_n) \tag{B.3a}$$

$$k_j = h_n\mathbf{f}(t_n + a_j h, y_n + \sum_{m=1}^{j-1} b_{jm}k_m), \quad j = 2, 3, ..., \varpi$$

Here ϖ is the number of Euler-style step. Importantly, two groups of parameters (a_j, b_{jm}, and c_j) are used in the fifth-order Runge-Kutta method: (1) the Cash-Karp parameters for the calculation of the FCs density, see Table B.1; (2) the Dormand-Prince (4,5) parameters for the Matlab function *ode*45, see Table B.2.

Appendix C

Golden Section Algorithm

Golden Section Algorithm is a numerical scheme that often used in search of the maximum or minimum value of a function over an interval. Its mathematical process is to continuously reduce the interval until the extremum point of the function is located. To simply mathematical discussion, I will take the minimization problem for example, which also coincide with the issue of saddle points raised in Sec. 3.5.

To start with, a function $\mathbf{f}(x)$ with the variable x is defined. Specifically, $\mathbf{f}(x)$ is assumed to be continuous over the integral of $[a,b]$ and have only one minimum in this range. Aiming at using a constant fraction to narrow the search range and reduce the number of function evaluation as much as possible, the main steps of Golden Section Algorithm are demonstrated as follows. Notably the constant fraction is referred as golden ratio, with the value of $w_{gold} = (3-\sqrt{5})/2$.

1. Select two specific points x_1 and x_2 inside the interval $[a,b]$. These two points are defined as $x_1 = a+d$ and $x_2 = b-d$, where $d = w_{gold}(b-a)$.

2. Calculate the functions of $\mathbf{f}(x_1)$ and $\mathbf{f}(x_2)$.

3. Make a decision based on the relative value between $\mathbf{f}(x_1)$ and $\mathbf{f}(x_2)$.

   (a) If $\mathbf{f}(x_1) > \mathbf{f}(x_2)$, the minimum of $\mathbf{f}(x)$ must be located at the right of x_1. The new value is given to a according to such relation of $a = x_1$, while the value of b is kept unchanged.

   (b) If $\mathbf{f}(x_1) < \mathbf{f}(x_2)$, the minimum of $\mathbf{f}(x)$ must be located at the left of x_2. The new value is given to b according to such relation of $b = x_2$, while the value of a remains the same.

4. Determine if the minimum of $\mathbf{f}(x)$ is found under the condition of $b-a<\sigma$, where σ is the tolerance of this algorithm. If so, the minimum occurs at $(a+b)/2$ and stop the iteration. Otherwise repeat the procedure from Step 1.

In this dissertation, the tolerance of the Golden Section Algorithm is set to $\sigma = 10^{-8}$. With regard to the process of deriving the saddle points, as mentioned in Sec. 3.5, it can be classified into two categories. In particular, the first procedure relates to the time-domain KLSE method, while the second one corresponds to the frequency-domain and Fourier-series KLSE approaches, with the difference being the function $\mathbf{f}(x)$. To be more specific, referring to Eq. (3.39) (time-domain KLSE), the saddle point s_o^- for signal "0" is extracted, by using the Golden Section Algorithm to find the minimum of $\exp[\Phi_{y_k}(s)]$ over the interval of $[-1/(\max|2\delta_\alpha^{k,-}|),0]$. And the same numerical routine is applied on $\exp[\Phi_{y_k}(s)]$ in the interval $[0,+\infty]$, in order to find the second saddle point s_o^+ for signal "1". However, the search for saddle points in the frequency-domain and Fourier-series KLSE is based on Eq. (3.42). Thus, the calculation of the saddle point s_o^+ for signal "0" is carried out by using the algorithm proposed in this section over the interval of $[0,1/(\max|2\lambda_n^+|)]$ and $[0,1/(\max|2\varepsilon_p^+|)]$, which correspond to the frequency-domain and Fourier-series KLSE approaches, respectively. In the meanwhile, the value of s_o^- for signal "1" is extracted by using the same technique but in the range of $[-\infty,0]$, validated in both frequency-domain and Fourier-series KLSE methods. To this end, the saddle points used in all the KLSE methods have been settled.